

UNIVERSITY OF BIRMINGHAM

MODELLING GRAVITATIONAL WAVES FROM ECCENTRIC BINARY BLACK HOLE MERGERS

by

ALICE BONINO

A thesis submitted to the University of Birmingham for the degree of

DOCTOR OF PHILOSOPHY

Astrophysics & Space Research Group

School of Physics and Astronomy

College of Engineering and Physical Science

University of Birmingham

July 2025

UNIVERSITY OF
BIRMINGHAM

University of Birmingham Research Archive

e-theses repository

This unpublished thesis/dissertation is copyright of the author and/or third parties. The intellectual property rights of the author or third parties in respect of this work are as defined by The Copyright Designs and Patents Act 1988 or as modified by any successor legislation.

Any use made of information contained in this thesis/dissertation must be in accordance with that legislation and must be properly acknowledged. Further distribution or reproduction in any format is prohibited without the permission of the copyright holder.

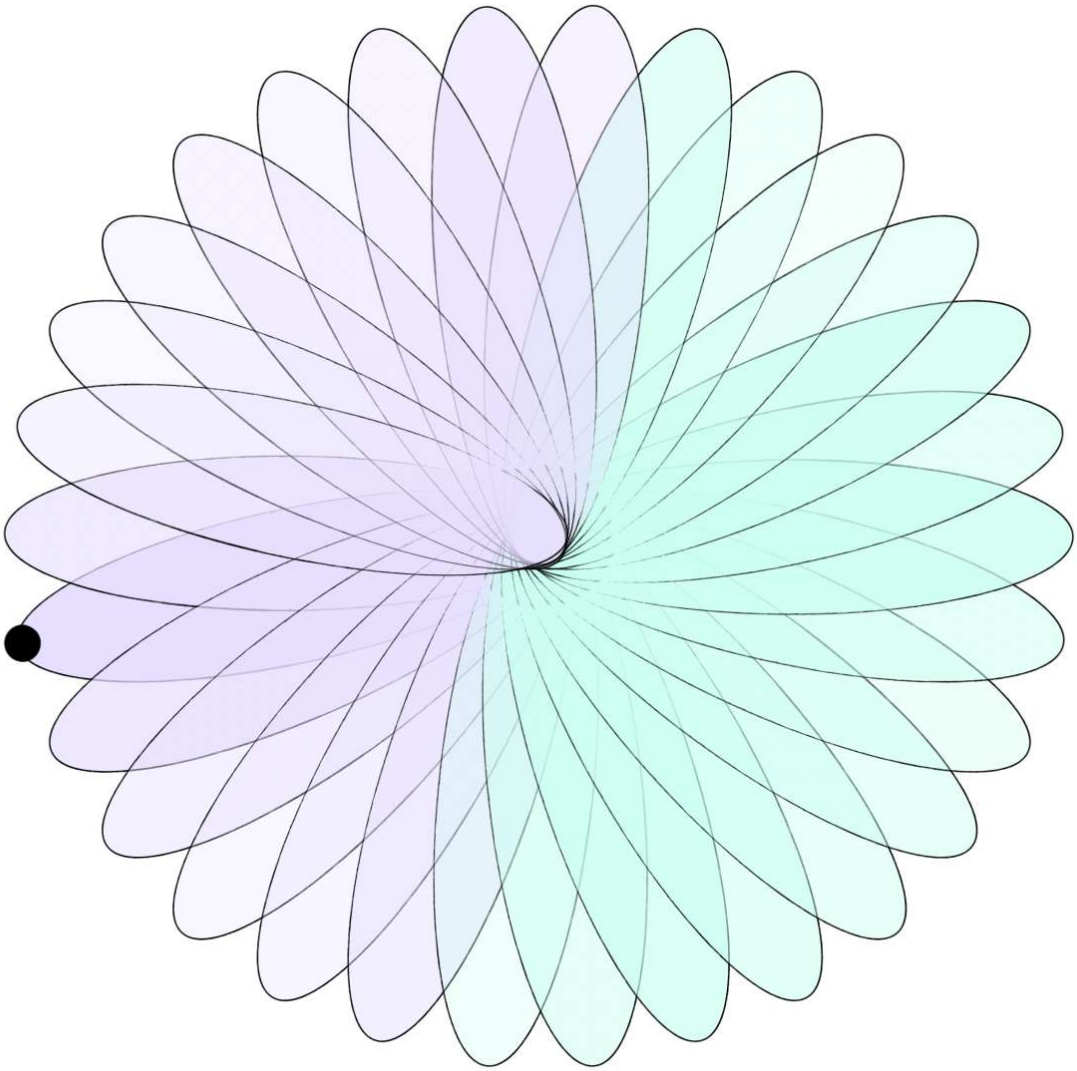


Figure 1: Artistic representation of the apsidal precession.

Abstract

The detection of gravitational waves from the coalescence of compact binary objects has provided a powerful tool to probe the origin of such systems and inferring their properties. Although binary systems are expected to circularise their orbit through gravitational wave emission, they can still retain a significant degree of orbital eccentricity when entering the sensitivity band of gravitational wave detectors. Orbital eccentricity is considered a key tracer for constraining the formation pathways and dynamical evolution of binary systems. In order to reliably measure eccentricity in gravitational wave signals, it is crucial to develop accurate waveform models and routines to measure eccentricity from the data. In recent years, cosiderable effort has been invested in incorporating eccentricity into waveform models. However, substantial work remains to improve the accuracy of eccentric waveform models. In this thesis we first perform parameter estimation of a gravitational wave event and validate the efficacy of an effective-one-body model in distinguishing between circular and eccentric signals as well as explore the correlations between eccentricity and other parameters characterising the binary. We then present a robust pipeline to reliably measure eccentricity from gravitational wave data and a map between eccentricity evolutions in numerical relativity and effective-one-body waveforms. Finally, we present comparisons between numerical relativity and effective-one-body quantities and establish a method enabling direct comparison of fluxes and energetics for eccentric binaries in the comparable mass regime that can be used as a baseline for future studies.

"Why do you tend a flock of sheep?" "Because I like to travel"

- The Alchemist, Paulo Coelho

Acknowledgements

First of all, I would like to thank all the scientific and administrative staff members of the Astrophysics group at the University of Birmingham and Alberto, the director of the Institute of Gravitational Wave Astronomy. I am grateful to all my mentors and collaborators, who have contributed to shape the person I am today. This PhD journey has profoundly transformed me, marking a period of significant personal growth. In particular, I would like to thank Patricia, my PhD supervisor, and Geraint for their mentorship and guidance through my PhD, their constant advice and all the inspiring and insightful scientific discussions we had. I am grateful for everything I have learned from you. I would then like to thank all the people in G26 and G27, who have been part of my daily life in the office. Each of you has been unique in their way of being and has brought joy and light to my days. This PhD has been not only a period of scientific growth but but also a journey enriched by deep friendships, for which I am deeply grateful. I will truly miss you all a lot. Thank you Simona for all the things we have done together and for the time we have shared. Even if I am not your desk neighbour anymore I am happy that Alastair has inherited my desk, and that you can both keep enjoying the only two desks in the office that get a glance sunlight (sigh). Also, keep our Italian traditions alive in the office and make sure to teach two steps in the sun to all of these British people. Thanks Adam and Shaun for the amazing Theory Journal Club that has has been a true source of enthusiasm and passion for science. Thanks both for all your jokes that have

made my days always funny. Diolch Shaun, I don't think I can find words to express my gratitude for you, so I will just say thank you for your constant presence, I am very happy that we ended up sharing my last (your first) years of the PhD. Thank you Dimple for your kindness and support and for teaching me how to make parhantas. Thank you Felicia for your supportive friendship, Joscha for the music sessions and you both for the many nice moments we shared with Simona, the MAC, the breakfasts, the hikings under the rain. Thank you Gonzalo for your constant friendship even from far away and for sharing the hard moment of postdoc applications. Thanks to Diganta especially for sharing the intense moment of thesis writing and for all the jokes that made this period more enjoyable. Thank you Xinyue for your friendship, for caring and coming back to Birmingham just for celebrating my viva. Thanks to Alastair and Luke (the LA moving company), Christian, the G27 sofa mascotte (thanks for teaching me how to say stir fried noodles properly), Natalie for the long PhD journey we have shared and for letting me opening the blinds when I needed the Sun, Issie, Alex, Owen, Emily, Andres, Makenzie, Nichola, Tom and all the other PhD fellows. Thanks also to Penny for our new journey together, Khun Sang, Hannah, Swetha, Julian, Martin, Gregorio, Lucy, Piero, Markos and all the others that I didn't mention here and that, through the years, have shared this journey with me. Thanks to the members of my capoeira group, in particular to my teachers Joyce and Mascote, from which I learned that discipline and hard work are the key to achieve life goals and for making me discover this amazing discipline that I hope to continue in the future. Thanks to Nicola for being my crazy friend, for your delicious dishes, the fire nights, capoeira, concerts and the tomato seeds. Thanks to all the friends that I have made in Birmingham through the years. Gracias también a Grecia y Valentina por su bienvenida en España. Infine, vorrei ringraziare i miei amici di vita e familiari. Grazie a tutti voi per il vostro infinito amore e supporto che mi ha permesso di arrivare fin qui anche da lontano. Un particolare grazie va a Sarah, grazie per la tua

grande amicizia e sorellanza, per avermi fatto compagnia durante la scrittura tesi e aver condiviso una parte importante del mio percorso, per la tua presenza costante e per farmi sempre ridere. Grazie Kady per essere la nostra mamma e per esserci sempre quando torno in Italia, e grazie anche al piccolo Fares. Grazie Hami e Letiz per la vostra amicizia constante dall'università ad oggi, a Luna, Alessandro, Stefano, Patti, Martina, Herta, Eleonora e tutti gli amici che quando ritorno a casa sono lì ad aspettarmi. Infine, grazie alla mia famiglia per il supporto costante e per la vicinanza. Grazie mamma per ascoltare sempre tutte le cose che ho da dire e per tutto quello che sempre fai per me. Grazie papà per i tuoi consigli saggi, per esserci sempre, farmi sempre ridere e vedere il lato profondo delle cose. Grazie ai miei fratelli per essere sempre un punto di riferimento. Grazie Samuele per sostenermi sempre, per essere sempre il fratello piccolo piú responsabile e per il tuo lato profondo e poetico. Grazie Matteo per tutto il tuo affetto dimostrato con le cose buone che cucini, per il tuo sostegno e per aver condiviso le fatiche del dottorato con me. Grazie ai miei nonni per essere sempre orgogliosi di me qualsiasi cosa io faccia, alle mie zie e a tutto il resto della mia famiglia.

Contents

Abstract iii

Acknowledgements vii

1 Introduction 1

2 Gravitational Waves 7

2.1 Introduction 7

2.2 Fundamentals of General Relativity 8

2.3 Generation of gravitational waves 14

2.3.1 Interaction of gravitational waves with test masses 18

2.3.2 Gravitational waves in linearised theory 20

2.3.3 Systematic Multipolar Expansion 24

2.3.4 Post-Newtonian expansion 27

2.4 Sources of gravitational waves 31

2.4.1 Compact binary coalescences 33

2.4.2 Eccentric binaries 37

2.5 Gravitational wave detection 41

2.5.1 Gravitational wave detectors 41

2.5.2 Matched filtering and data analysis techniques 43

2.5.3 Inferring parameters of the source 44

3 Approaches to the two-body problem in General Relativity 47

3.1 Introduction 47

3.2 Numerical Relativity 51

3.2.1 3+1 decomposition of spacetime 51

3.2.2 Constraint and evolution equations 53

3.2.3 ADM mass and momenta 56

3.2.4 Black holes initial data 58

3.2.5 Gauge conditions 60

3.3 Effective-one-body approach 61

3.3.1 Conservative dynamics 67

3.3.2 Inspiral waveform: circular 68

3.3.3 Inspiral waveform: non-circular corrections 72

3.3.4 Non-conservative dynamics 73

4 Inferring eccentricity evolution from observations of coalescing binary black holes 77

4.1 Introduction 77

4.2 Quasi-circular and eccentric waveform model 78

4.2.1 Quasi-circular model: `TEOBResumS-GIOTTO` 78

4.2.2 Eccentric model: `TEOBResumS-Dalí` 79

4.3 Methods 81

4.3.1 Gravitational Wave Parameter Estimation 81

4.3.2 Likelihood and Priors 82

4.4 Validation of the waveform model 84

4.5 Quasi-circular and eccentric initial conditions 84

4.5.1 Quasi-circular limit of the eccentric model . . . 86
4.5.2 Testing the eccentric model . . . 88
4.6 Analysis of GW150914 . . . 94
4.6.1 Quasi-circular analysis of GW150914 . . . 94
4.6.2 Eccentric analysis of GW150914 . . . 95
4.7 Model-agnostic estimate of the Eccentricity Evolution . . . 99
4.8 Discussion . . . 103

5 Mapping eccentricity evolutions between numerical relativity and effective-one-body gravitational waveforms 107

5.1 Introduction . . . 108
5.2 Numerical Simulations . . . 109
5.2.1 Overview . . . 109
5.2.2 Eccentric Initial Conditions . . . 111
5.2.3 Catalog of Simulations . . . 111
5.3 Eccentricity Estimation . . . 114
5.3.1 Introduction . . . 114
5.3.2 Methodology . . . 117
5.3.3 Assessment of Robustness . . . 123
5.4 Derivation of e_{Ψ_4} in the quasi-Keplerian parametrization . . . 129
5.5 Comparison to Analytical Models . . . 133
5.5.1 Determining Initial Conditions . . . 135
5.5.2 Robustness . . . 137
5.5.3 Extrapolation to Earlier Times . . . 142
5.5.4 Mismatches . . . 143
5.6 Conclusions . . . 144

6 Synergies between effective-one-body and numerical relativity **149**

6.1 Introduction 149

6.2 Initial conditions 150

6.2.1 Method 150

6.2.2 EOB initial conditions 151

6.3 Comparing effective-one-body and numerical relativity 153

6.3.1 Energy and angular momentum fluxes 153

6.3.2 Inclusion of eccentric corrections in the EOB dynamics 157

6.3.3 Energetics: numerical relativity simulations 163

6.3.4 Energetics: comparisons between effective-one-body and numerical relativity 169

6.4 Discussion 174

7 Conclusions **177**

A Derivatives of r, Ω, p_{r*} **181**

A.1 Second derivatives 181

A.2 Third derivatives 182

Bibliography **185**

Chapter 1

Introduction

Declaration: In this Chapter we present the astrophysical motivations and objectives underlying this work. We also provide an overview of the thesis structure. Portions of this chapter are adopted and include text from A. Bonino, R. Gamba, P. Schmidt, A. Nagar, G. Pratten, M. Breschi, P. Rettegno, S. Bernuzzi, "Inferring eccentricity evolution from observations of coalescing binary black holes" (2023) [1] and from A. Bonino, P. Schmidt, G. Pratten, "Mapping eccentricity evolutions between numerical relativity and effective-one-body gravitational waveforms" (2024) [2].

An intense experimental activity, in parallel with a vigorous theoretical effort, led to the realisation of exceptionally sensitive ground based detectors and the detection gravitational waves (GWs). Their direct detection enabled us to observe the universe in an unprecedented way and opened new avenues for research in various fields including gravitational wave astronomy, cosmology and fundamental physics. The theory of gravitational waves is very rich and bridges multiple disciplines such as General Relativity (GR), astrophysics, cosmology and field theory. Gravitational waves are produced by massive objects in the Universe warping spacetime and appear for the first time as wave-like solution of the linearised equations of GR predicted by Eistein in 1915 [3, 4]. Their first

indirect observation happened in 1974 with the discovery of a binary pulsar system by Hulse and Taylor [5]. However, their first direct evidence only occurred in 2015 when the LIGO-Virgo collaboration [6–10] observed the first coalescence of a binary black hole, GW150914 [11]. After the discovery of GW150914, many other events have been observed [12–14]. Binary systems of compact objects, such as binary black holes (BBH), binary neutron stars (BNS) or neutron star-black hole systems (NSBH) tend to circularize their orbit, as they approach merger, via emission of gravitational waves (GWs) [15–17]. Two main scenarios are considered as possible formation channels for binary black hole (BBH) systems [18–21]: (i) isolated binary evolution, which efficiently estinguish orbital eccentricity through angular momentum loss from gravitational waves emission before entering the LIGO-Virgo sensitive frequency band [16]; (ii) BBH mergers produced in dynamical formation channels which may still show a non-negligible eccentricity by the time they enter the frequency band of current ground based detectors. Isolated BBH usually present spins that are aligned with the orbital angular momentum and negligible orbital eccentricities. This motivates the analysis of gravitational-wave signals with theoretical templates that are generated by waveform models using the quasi-circular approximation. On the other hand, dynamical assembled BBH can exhibit random spin orientations and non-negligible orbital eccentricities. If the binary has a sufficiently high eccentricity, during close periapses passages it can lose sufficient energy through GW emission, which leaves a distinct imprint on the observed GW signal. Highly eccentric mergers are likely to happen as product of N-body dynamics in clusters. Even if they may form in other ways, e.g. through Lidov-Kozai mechanism (i.e. perturbed by a third body) [20], non-isolated binaries are likely to assemble dynamically in dense stellar environments. Other astrophysical systems such as Extreme-Mass-Ratio Inspirals (EMRIs) where a stellar-mass object orbits a supermassive black hole, exhibit eccentricity as a key factor in determining the astrophysical properties of the sources under study. These systems are anticipated to be

major sources of gravitational waves detectable by LISA [22–24]. Accurate eccentricity measurements therefore provide crucial astrophysical insights that can help constraining the evolution and formation pathways of compact binary systems [19, 21, 25–31]. In Ref. [21], for example, it is shown that the detection or non-detection of eccentric BBH mergers significantly constrains the contribution of certain dynamical formation channel to the BBH population. There has been a growing interest in analysing the gravitational wave events detected by LIGO and Virgo with inspiral-merger-ringdown (IMR) waveform models that include eccentricity [1, 18, 32–41]. For example, the first event that exceeded the pair-instability mass gap GW190521 [42, 43] has recently been analysed under the hypothesis that it originated from a hyperbolic capture that resulted in a highly eccentric merger [35]; other studies suggested formation through repeated merger [44, 45], claim moderate eccentricity and spin-induced precession as evidence for dynamical formation [36], a possible head-on collision [46], large eccentricity and strong spin-induced precession [32] or propose interpretations involving a high-mass black hole-disk system or intermediate mass-ratio inspirals [47, 48]. A signature of orbital eccentricity has been recently found in a neutron star-black hole system GW200105 [49].

A current limitation to extracting information on eccentricity from the current generation of ground-based gravitational wave detectors is the lack of sensitivity below 20 Hz. Recent studies suggest that eccentricities ≥ 0.05 at a gravitational wave frequency of 10 Hz will be necessary to extract eccentric information based on the current generation of detectors at design sensitivity [50]. Improving the low-frequency sensitivity of the next-generation of ground-based detectors, including Cosmic Explorer [51, 52] and the Einstein Telescope [53, 54], could lead to significant improvements and allow us to resolve eccentricities down to the $\sim 10^{-3}$ level, e.g. [55, 56]. Similarly, multiband observations between space-based and ground-based detectors may be a potential route to extracting the natal eccentricities of stellar mass black holes [57–59], though the event rates are

highly uncertain [60, 61] and they require a robust framework for tracking and modelling the evolution of eccentricity over a period of year(s). In recent years, significant effort has been invested in incorporating eccentricity into the current generation of waveform models. Within the post-Newtonian (PN) approximation [62], which assumes weak-fields and small velocities [$\epsilon \sim GM/(c^2 r) \sim (v/c)^2 \ll 1$], the conservative dynamics for generic orbits are known up to 5PN [63–73] and radiative effects up to 3PN [74–82]. This has led to the construction of numerous eccentric waveform approximants within the PN framework, e.g. [83–88]. Likewise, there have been numerous developments within the gravitational self-force (GSF) and scattering paradigms, e.g. [89–95]. However, whilst these provide an accurate description of the gravitational-wave signals throughout the inspiral, they are only valid up to moderate eccentricities ($e \sim 0.1$) and are not reliable as the binary approaches merger. To mitigate against such limitations, one can appeal to numerical relativity (NR) simulations to help model the complete inspiral-merger-ringdown (IMR) signal from eccentric binaries [96–101]. Such catalogs have enabled the construction of eccentric NR surrogates [102, 103] as well as PN-NR hybrids that blend analytical information from PN evolutions with the NR simulations [88, 96, 104–106]. Even though NR simulations cover a comparatively restricted region of the parameter space, they do provide the full non-linear solutions of the Einstein field equations and play a crucial role in accurately modelling the remnant black hole and providing an accurate representation of the gravitational wave signal through merger. As such, whilst eccentric NR surrogates and hybrid models are highly accurate, they are necessarily constrained by the poor parameter space coverage, accuracy, and finite length of available NR simulations, which often do not capture the early inspiral regime. One alternative approach is the effective-one-body (EOB) framework [107–110], a successful paradigm for modelling the complete gravitational wave signal emitted by compact binaries on arbitrarily eccentric orbits. Some of the first studies on incorporating eccentricity into the EOB framework

were outlined in [111–113]. There have been numerous subsequent technical developments that have dramatically improved the accuracy of eccentric EOB models [114–125]. Of the available models, `SEOBNRv4EHM`, [121] `TEOBResumS-Dalí` [115–117, 126–128], and `SEOBNRE` [113] are the most mature. An extension of `SEOBNRE` to eccentric binaries with precessing spins has recently been presented [129].

The main purposes of this thesis are the development of robust tools to accurately measure eccentricity from gravitational wave signals and the improvement of existing gravitational waveform models for eccentric binary systems by investigating their synergies with numerical relativity (NR). In Chapter 2 we introduce the theoretical framework of gravitational waves, with a focus on the essential features of signals emitted by compact binary systems. In Chapter 3 we discuss general relativistic treatments of the two-body problem introducing key concepts in NR and the EOB framework. We also outline the core structure of the the main building blocks of `TEOBResumS` [126, 130, 131] waveform model for coalescing binaries and its eccentric estension `TEOBResumS-Dalí`, which serves as the central waveform model studied in this thesis. In Chapter 4 we introduce a novel method for measuring the eccentricity of coalescing binary black holes from gravitational wave data. This includes results from an eccentric Bayesian inference analysis performed using `TEOBResumS-Dalí` and is based on the work presented in [1]. In Chapter 5 we present a new suite of eccentric NR simulations and assess the limitations of the estimator introduced in Chapter 4 [1]. Furthermore, we propose a new method for mapping eccentricity evolution between NR and EOB waveforms, enabling direct comparisons between these two modeling approaches. Chapter 6 is dedicated to discuss synergies between NR and EOB quantities. For these comparisons employ the mapping introduced in Chapter 5 [2]. Finally, Chapter 7 summarises the main findings of this thesis and outlines potential directions for future research.

Chapter 2

Gravitational Waves

Declaration: In this Chapter we present an overview of fundamental concepts in the study of gravitational waves. Portions of this chapter are adopted and include text from A. Bonino, R. Gamba, P. Schmidt, A. Nagar, G. Pratten, M. Breschi, P. Rettegno, S. Bernuzzi, "Inferring eccentricity evolution from observations of coalescing binary black holes" (2022) [1].

2.1 Introduction

Gravity is one of the four fundamental forces of nature, playing a central role in shaping the universe. It dictates the motion of celestial bodies, keeping planets in orbit around the Sun and guiding the paths of some of the most mysterious objects populating the Universe. Beyond keeping us anchored to Earth, gravity also plays a crucial role in the formation of large-scale cosmic structures and influences many astrophysical and cosmological phenomena. On the smallest scales, gravity connects to particle physics and is central to efforts in developing unified theories of fundamental interactions. Gravity is the weakest of the four fundamental forces yet, like the electromagnetic force, it has a long-range nature with an infinite reach, and its infinite range influences objects across

vast distances, from subatomic particles to galaxies. However, unlike electromagnetism, which is screened at large scales due to the nature of electric charge, gravity remains the dominant force at large distances. As described by General Relativity (GR), the distribution of mass in the universe bends the *spacetime*, the four-dimensional continuum of space and time. In this chapter we will briefly review the fundamentals of GR and show how gravitational waves, meaning ripples in the geometry of spacetime created by accelerating masses, arise as a solution to the linearized Einstein field equations. The chapter is organised as follows. In Sec. 2.2 we provide an overview of key concepts in GR. The section follows [132–135]. In Sec. 2.3 we explore how gravitational waves emerge from the linearised Einstein field equations and illustrate how they interact with an idealised set of test masses. We will then show that gravitational waves can be organised in a systematic expansion in multipoles and discuss the post-Newtonian (PN) approximation. In Sec. 2.4 we explore the primary sources of gravitational waves, with a particular emphasis on compact binary systems, which are the central focus of this thesis. We also discuss some of the possible formation channels for binary black holes. In Sec. 2.5 we provide an overview of data analysis techniques employed in the detection and analysis of gravitational wave signals.

2.2 Fundamentals of General Relativity

GR was published by Einstein in 1915 [136] to extend Newton's law of gravitation within the framework of Special Relativity (SR), which he had introduced in 1905. The incompatibility between SR and Newtonian mechanics stems from the fact that, in Newtonian gravity, the gravitational interaction occurs instantaneously whereas the Lorentz invariance of SR dictates that nothing, including gravity, can propagate faster than light.

Newton's equations can be expressed as follows

$$\frac{d^2x^i}{dt^2} = -\frac{\partial\Phi}{\partial x^i}, \tag{2.1}$$

$$\nabla^2\Phi = 4\pi G\rho \tag{2.2}$$

where ∇^2 is the three-dimensional flat-space Laplacian operator $\nabla^2 = \partial^2/\partial x^2 + \partial^2/\partial y^2 + \partial^2/\partial z^2$. Eq. (2.1) describes the motion of a particle in three dimensions and reveals an asymmetry between space and time which contradicts the framework of SR. The field equation (2.2) states that the Newtonian gravitational potential $\Phi(x)$ is determined by the mass density $\rho(x)$ through Poisson's equation, and responds instantaneously to changes in the density of mass at arbitrarily large distances, violating the Lorentz invariance of SR. The *principle of equivalence*, a cornerstone of GR, asserts that locally the effects of gravity can not be distinguished from those of acceleration. A fully relativistic theory of gravity must therefore uphold the equivalence principle by ensuring that space and time are treated on an equal footing, leading to a modification of Eq. (2.1) into a four-dimensional vector equation

$$\frac{d^2x^\mu}{d\tau^2} = \left(\frac{du^0}{d\tau}, \frac{du^i}{d\tau}\right) \tag{2.3}$$

where τ is the proper time, i.e. the time measured by an observer's own clock, and the 4-vectors are defined as $x^\mu = (ct, x, y, z)$ and 4-velocity $u^\mu = \frac{dx^\mu}{d\tau}$. In GR, gravity is no longer regarded as a force acting on objects but rather as an inherent property of spacetime itself. Instead of masses generating a gravitational potential Φ, they curve spacetime, thereby influencing the motion of objects within it.

GR is based on the concept of *differentiable manifold*. The geometry of spacetime is described by the pair $(\mathcal{M}, g)$ where $\mathcal{M}$ is a differentiable four-dimensional manifold and

g is a pseudo-Riemaniann, specifically Lorentzian, [1] metric measuring length of curves connecting points in $\mathcal{M}$. The points of $\mathcal{M}$ are known as *events* while physical process corresponds to a continuous sequence of events. Specifically, the motion of a point-like particle is represented by a *wordline*, which is a curve in $\mathcal{M}$ representing its trajectory through spacetime.

The metric $g_{\mu\nu}$ provides a way to map vectors to their corresponding dual vectors at every point in spacetime, enabling the raising and lowering of indices in the same manner as in SR

$$V_\mu = g_{\mu\nu} V^\mu. \tag{2.4}$$

We can define a Lorentz-invariant distance or *line element* ds^2 in terms of the metric $g_{\mu\nu}$ as

$$ds^2 = g_{\mu\nu} dx^\mu dx^\nu \tag{2.5}$$

where $dx^{\mu,\nu}$ are small displacements along the curve $x^\lambda(\lambda)$ where λ is a parameter in $\Re$. For time-like curves satisfying the condition $ds^2 < 0$, we can define the proper time τ and parametrize the curve $x^\mu \equiv x^\mu(\tau)$. The presence of the gravitational field and therefore the curvature of the manifold is fully captured by the metric tensor $g_{\mu\nu}$. It is always possible to define local inertial frames in which the effects of gravity disappear and the metric locally approximate the flat Minkowski metric $\eta_{\mu\nu}$ and objects move as if in SR. In these frames, gravity is manifested through the relative acceleration between different frames. In a curved space caution is needed when comparing vectors since the space between points is not flat. To address this, we exploit the local flatness of the manifold and compare them in a small region of the spacetime where the curvature is negligible

[1] A Lorentzian metric has signature $(-,+,+,+)$ distinguishing time-like, space-like and light-like separations, and describes spacetime with one time dimension and three spatial dimensions.

and the manifold appears flat. To define curves in a curved spacetime, we must introduce the notion of the *covariant derivative* of a vector which is defined as follows

$$\nabla_\mu V^\nu \equiv \partial_\mu V^\nu + \Gamma^\nu_{\mu\lambda} V^\lambda \tag{2.6}$$

where $\Gamma^\nu_{\mu\lambda}$ are the *Christoffel symbols* which encode the effects of the curvature and are defined in terms of the metric tensor as such in a way that the covariant derivative of the metric tensor vanishes

$$\nabla_\lambda g_{\mu\nu} = 0. \tag{2.7}$$

The covariant derivative of a tensor is defined so that the coordinate basis vectors remain unchanged, meaning that in a local inertial frame the Christoffel symbols vanish and the covariant derivative reduces to the ordinary derivative.

Curves of extremal length between two point are called *geodesics* and satisfy the geodesic equation

$$u^\mu \nabla_\mu u^\nu = \frac{du^\mu}{d\tau} + \Lambda^\mu_{\nu\rho} u^\nu u^\rho = 0 \tag{2.8}$$

where $u^\mu = \frac{dx^\mu}{d\tau}$ is the four-velocity vector and $u^\mu \frac{\partial}{\partial^\mu} = \frac{d}{d\lambda}$. Since λ is a parameter of a geodesic, i.e. Eq. (2.8) is satisfied, λ is called an *affine* parameter.

The final essential ingredient we need to describe the spacetime is the curvature. The *intrinsic* curvature of the manifold is characterized by the Riemann tensor

$$R^\sigma_{\rho\mu\nu} = \partial_\mu \Gamma^\sigma_{\nu\rho} - \partial_\nu \Gamma^\sigma_{\mu\rho} + \Gamma^\sigma_{\mu\lambda}\Gamma^\lambda_{\nu\rho} - \Gamma^\sigma_{\nu\lambda}\Gamma^\lambda_{\mu\rho}. \tag{2.9}$$

The Riemann tensor is a rank-four tensor that is asymmetric in the first and second pair of indices while remaining symmetric under the exchange of these pairs. These symmetries

reduce the number of independent components of the Riemann tensor to twenty in four dimensions. The Riemann tensor is crucial in the mathematical description of spacetime because it fully characterizes the intrinsic curvature of a manifold. For a flat manifold we have

$$R^{\sigma}_{\rho\mu\nu} = 0. \tag{2.10}$$

We will now see how the Riemann tensor is used to describe the curvature of spacetime. We can write the *geodesic deviation* equation as

$$\nabla_u \nabla_u \xi^\mu = -R^{\mu}_{\nu\sigma\rho} u^\nu u^\rho \xi^\sigma \tag{2.11}$$

where ξ^μ is the separation vector between two geodesics and the covariant derivative along a vector field $V^\mu(x)$ along the curve $x^\mu(\tau)$ is defined as

$$\nabla_V \equiv \frac{dV^\mu}{d\tau} + \Gamma^{\mu}_{\nu\rho} V^\nu \frac{dx^\rho}{d\tau}. \tag{2.12}$$

From Eq. (2.11) we observe that the second derivative of the separation vector depends on the Riemann tensor, indicating that the spacetime curvature directly influences the motion of two particles moving along nearby time-like geodesics causing them to experience tidal acceleration. We can define the Ricci tensor $R_{\sigma\rho}$ as a contraction of the Riemann tensor defined in Eq. (2.9)

$$R_{\sigma\rho} \equiv R^{\mu}_{\sigma\mu\rho} \tag{2.13}$$

and the Ricci scalar as the contraction of the Ricci tensor

$$R \equiv g^{\sigma\rho} R_{\sigma\rho}. \tag{2.14}$$

We briefly outline below how to derive the Einstein field equations from the variation of the action though they can also be derived by contracting the Bianchi identities. By varying the action $S = S_E + S_M$ with respect to the metric $g_{\mu\nu} \to g_{\mu\nu} + \delta g_{\mu\nu}$, where S_E is the Einstein-Hilbert action

$$S_{\rm EH} = -\frac{1}{16\pi}\int d^4x\sqrt{-g}R \tag{2.15}$$

and S_M is the matter action, we obtain

$$\delta S = -\frac{1}{16\pi}\int d^4x[\delta\sqrt{-g}R + \sqrt{-g}\delta R_{\mu\nu}g^{\mu\nu} + \sqrt{-g}R_{\mu\nu}\delta g^{\mu\nu}] + \delta S_M = 0. \tag{2.16}$$

where we have used $G = c = 1$. By employing $\delta\sqrt{-g} = -\frac{1}{2}\sqrt{-g}g_{\mu\nu}\delta g^{\mu\nu}$ and the *Palatini identities*[2]

$$\delta R_{\mu\nu} = \nabla_\lambda(\delta\Gamma^\lambda_{\nu\mu}) - \nabla_\nu(\delta\Gamma^\lambda_{\lambda\mu}) \tag{2.17}$$

we obtain, from the the first two terms in Eq. (2.16) the Einstein tensor $G_{\mu\nu}$

$$G_{\mu\nu} \equiv R_{\mu\nu} - \frac{1}{2}g_{\mu\nu}R \tag{2.18}$$

which is a symmetric tensor of rank two and has ten independent components. From the *Bianchi identities* $\nabla_\lambda R_{\rho\mu\nu\sigma} + \nabla_\sigma R_{\rho\mu\lambda\nu} + \nabla_\nu R_{\rho\mu\sigma\lambda} = 0$, we find that

$$\nabla_\nu G^{\mu\nu} = 0. \tag{2.19}$$

[2]By using the Palatini identities and the Gauss' theorem it is possible to demonstrate that $\sqrt{-g}\delta R_{\mu\nu}g^{\mu\nu}$ vanishes. We therefore have that the variation of the Einstein-Hilbert action is $\delta S_{\rm EH} = -\frac{1}{16\pi}\int d^4x\left(\delta\sqrt{-g}R + \sqrt{-g}R_{\mu\nu}\delta g^{\mu\nu}\right)$. By employing $\delta\sqrt{-g} = -\frac{1}{2}\sqrt{-g}g_{\mu\nu}\delta g^{\mu\nu}$ we find that $\delta S_{\rm EH} = \frac{1}{16\pi}\int d^4x\sqrt{-g}\left(\frac{1}{2}g_{\mu\nu}R - R_{\mu\nu}\right)\delta g^{\mu\nu}$ from which we can define the Einstein tensor $G_{\mu\nu} \equiv R_{\mu\nu} - \frac{1}{2}g_{\mu\nu}R$.

From the variation of the matter action we obtain the energy-momentum tensor $T^{\mu\nu}$

$$\delta S_M = \frac{1}{2}\int d^4x\sqrt{-g}\frac{1}{2}T_{\mu\nu}\delta g^{\mu\nu} \tag{2.20}$$

We can therefore define the *Einstein field equations* (EFE) as

$$G_{\mu\nu} = R_{\mu\nu} - \frac{1}{2}g_{\mu\nu}R = 8\pi T_{\mu\nu}. \tag{2.21}$$

In the weak field limit, i.e. $g_{\mu\nu} = \eta_{\mu\nu} + h_{\mu\nu}$ and $|h_{\mu\nu}| \ll 1$, we have that $h_{00} = -2\Phi$, $T_{00} = \rho$, $g_{00} = -(1+2\Phi)$ and $R_{00} = -\nabla^2\Phi$ and we therefore recover the Newtonian laws of motion in Eq. (2.2). The Einstein field equations are a set of ten non-linear differential equations that, thanks to the Bianchi identities reduce to six independent equations describing the curvature of spacetime in the presence of matter and energy. Their non-linearity makes analytical solutions challenging, ofteng necessitating numerical methods. Systems with a high degree of symmetry allow for the determination of analytical solutions. The Schwarzschild solution (1916) [137] describes the spacetime surrounding a spherically symmetric, non-rotating mass, while the Kerr solution (1963) [138] extends this solution to a rotating mass. Other notable solutions are the Kerr-Newmann [139, 140] Reissner-Nordström solution [141, 142] and the Friedmann-Lemaître-Robertson-Walker (FLRW) metric [143] describes the universe on large scales.

2.3 Generation of gravitational waves

In this section we examine how gravitational waves emerge as plane wave solutions to the linearized Einstein field equations under an appropriate gauge choice. Einstein first derived this solution in 1916 [4], soon after developing his theory of GR. The main reference for this section is the textbook [144].

Under the assumption of a weak gravitational field, Einstein found that his linearized field equations reduce to wave equations for the metric perturbation. Despite this approximation being valid in many astrophysical and cosmological situations, it breaks down in highly curved regions of spacetime such as near very dense objects where non-linear and relativistic effects become important. The solutions to these equations describe ripples that propagate in spacetime at the speed of light. This result laid the groundwork for the study of gravitational waves, ultimately leading to their detection a century later. Using standard tools of GR introduced in the previous chapter, we will show how these waves interact with detectors, modelled as an idealised set of test masses.

We expand the metric around a flat Minkowski background $\eta_{\mu\nu} = diag(-1, +1, +1, +1)$

$$g_{\mu\nu} = \eta_{\mu\nu} + h_{\mu\nu} \tag{2.22}$$

where $|h_{\mu\nu}| \ll 1$ is a small perturbation and exploit the *gauge invariance* of GR to find the transformation for $h_{\mu\nu}$. By performing an infinitesimal coordinate transformation $x'^{\mu} = x^{\mu} + \xi^{\mu}(x)$ and using the transformation law for $g_{\mu\nu}$ we have, at lowest order, the transformation of $h_{\mu\nu}$

$$h'_{\mu\nu}(x) = h_{\mu\nu}(x) - (\partial_{\nu}\xi_{\mu} + \partial_{\mu}\xi_{\nu}). \tag{2.23}$$

By inserting Eq. (2.22) in the equation for the Riemann tensor Eq. (2.9) and keeping only the terms linear in $h_{\mu\nu}$ we obtain the linearized Riemann tensor

$$R_{\mu\nu\rho\sigma} = \frac{1}{2}(\partial_{\nu}\partial_{\rho}h_{\mu\sigma} + \partial_{\mu}\partial_{\sigma}h_{\nu\rho} - \partial_{\mu}\partial_{\rho}h_{\nu\rho} - \partial_{\nu}\partial_{\sigma}h_{\mu\rho}). \tag{2.24}$$

Through algebraic manipulations and the introduction of the trace-reversed metric perturbation

$$\bar{h}_{\mu\nu} = h_{\mu\nu} - \frac{1}{2}\eta_{\mu\nu}h \tag{2.25}$$

where $h = h_{\mu\nu}\eta^{\mu\nu}$, we can write the Einstein tensor in Eq. (2.21) in its linearized form

$$\Box\bar{h}_{\mu\nu} + \eta_{\mu\nu}\partial^\rho\partial^\sigma\bar{h}_{\rho\sigma} - \partial^\rho\partial_\nu\bar{h}_{\mu\rho} - \partial^\rho\partial_\mu\bar{h}_{\nu\rho} = -\frac{16\pi G}{c^4}T_{\mu\nu}. \tag{2.26}$$

We can choose ξ_μ such that

$$\partial^\mu\bar{h}_{\mu\nu} = 0, \tag{2.27}$$

known as the *harmonic* gauge. In the harmonic gauge the Einstein field equations in Eq. (2.21) reduce to their linearized form

$$\Box\bar{h}_{\mu\nu} = -\frac{16\pi G}{c^4}T_{\mu\nu}. \tag{2.28}$$

Eq. (2.27) reduces the ten components of Eq. (2.28) to six independent components and the two equations together imply the conservation of the stress-energy tensor

$$\partial^\mu T_{\mu\nu} = 0. \tag{2.29}$$

Linearizing Einstein field equations implies that we are approximating gravitational waves sources to move in a flat space-time along trajectories detetrmined by their mutual interaction. The dynamics of self-gravitating system, such as binary neutron stars or black holes, is then described using Newtonian gravity. The response of test masses to the passage of gravitational waves is studied using $g_{\mu\nu} = \eta_{\mu\nu} + h_{\mu\nu}$ while neglecting terms $O(h^2)$. To determine the gravitational waves interaction with test masses we can analyze their propagation outside of the source ($T_{\mu\nu} = 0$) and solve the equations in vacuum. By imposing the *Transverse-Traceless* or TT gauge, i.e. setting

$$h^{0\mu} = h^i_i = \partial^j h_{ij} = 0 \tag{2.30}$$

we obtain the linearized Einstein equations in vacuum

$$\Box h_{\mu\nu} = 0 \tag{2.31}$$

which admit solutions in the form of plane waves as

$$h_{\mu\nu} = e_{\mu\nu} e^{ik_\mu x^\mu} \tag{2.32}$$

where $k_\mu = (\omega/c, \mathbf{k})$ is the wave-vector and $e_{\mu\nu}$ is a polarisation tensor. By imposing the harmonic gauge we have reduced the ten degrees of freedom of the Einstein equations to six degrees of freedom, and fixing the TT gauge (Eq. (2.30)) further reduces these to two degrees of freedom. Choosing $\hat{\mathbf{n}} = \mathbf{k}/|\mathbf{k}|$ along the z-axis we have that in the TT gauge the metric deformation $h^{TT}_{\mu\nu}$ lies in a plane perpendicular to the direction of propagation

$$h^{TT}_{\mu\nu}(t,z) = \begin{pmatrix} 0 & 0 & 0 & 0 \\ 0 & h_+ & h_\times & 0 \\ 0 & h_\times & -h_+ & 0 \\ 0 & 0 & 0 & 0 \end{pmatrix}_{\mu\nu} e^{i(\omega t - kz)} \tag{2.33}$$

where h_+ and $h_\times$ are called *plus* and *cross* polarisations. The local gauge invariance of GR, meaning its invariance under coordinate transformations, initially led to the belief that gravitational waves were not physical phenomena but merely artifacts of the gauge freedom, implying they could be eliminated through a suitable coordinate transformation. However, although an adequate gauge choice can simplify the Einstein equations by imposing conditions on the metric perturbation, the physical effects of gravitational waves remains unchanged. In the next section we will show how gravitational waves interact with a set of test masses assuming no external gravitational field as a useful idealized

setting to understand the fundamental principles underlying gravitational wave detection.

2.3.1 Interaction of gravitational waves with test masses

To properly understand the effects of gravitational waves, we need to carefully choose the reference frame, i.e. the observer. We can start from the equation of the geodesic deviation in the TT gauge

$$\left.\frac{d^2\xi^i}{d\tau^2}\right|_{\tau=0} = -\left[\dot{h}_{ij}\frac{d\xi^i}{d\tau}\right]_{\tau=0}, \tag{2.34}$$

where ξ^i is the separation between two test masses. In we set $\tau = 0$ in Eq. (2.34), we have that $\frac{d\xi^i}{d\tau} = 0$ and therefore $\frac{d^2\xi^i}{d\tau^2} = 0$. This shows that, at least at leading order, in the TT gauge masses that are initially at rest remain at rest at all times. Although gravitational waves have a very simple form in this frame, this is not the most suitable choice for detection experiments, as the positions are not defined by free-falling particles. If we consider a region of space such that the characteristic linear size of the detector $L \ll \lambda$ where λ is the typical scale over which variations of the gravitational field are non-negligible, we can write the equation for the geodesic deviation in the proper detector frame neglecting all effects of the background, as

$$\frac{d^2\xi^i}{d\tau^2} = -c^2 R^i_{0j0}\xi^j = -\frac{1}{2}\ddot{h}^{TT}_{ij}\xi^j \tag{2.35}$$

where ξ^i is the separation of masses and for the last equivalence we have used the fact that the linearised Riemann tensor is invariant under gauge transformations and we can choose the frame that we prefer to compute it. The TT gauge is the optimal choice since in this frame gravitational waves take the simplest form. Note that the condition $L \ll \lambda$ where λ is not satisfied for example by the LISA detector [22–24] which is sensitive to gravitational waves whose wavelength is larger or comparable to L. Eq. (2.35) is a

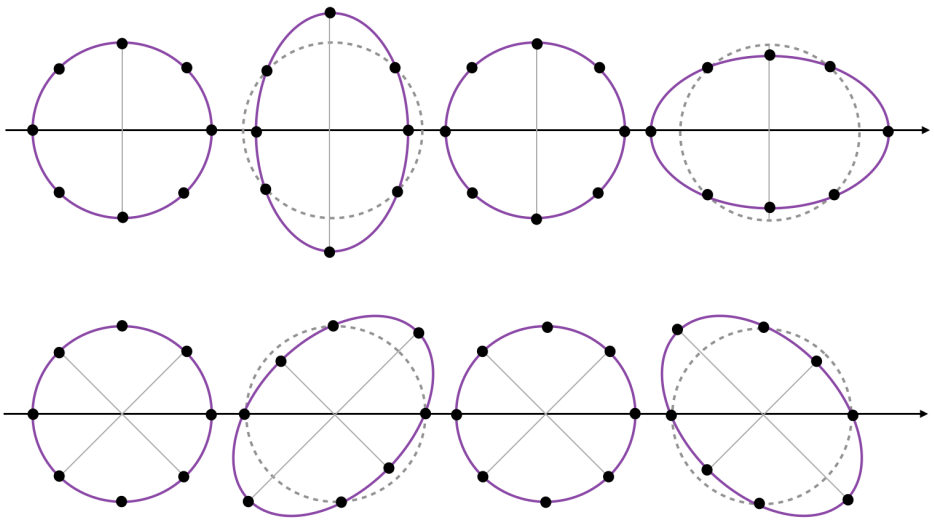


Figure 2.1: Effect of gravitational waves on a ring of test masses. We can see the *plus* and *cross* polarisations respectively in the upper and bottom panel.

Newton-like equations and therefore shows that in the proper detector frame the effect of gravitational waves can be described in terms of Newtonian force and the interaction of gravitational waves with detectors can be analysed without requiring GR. Two nearby test particles in a gravitational background undergo a relative acceleration due to the passage of gravitational waves, governed by the spacetime curvature encoded in the Riemann tensor. By considering the motion of a test particle in the (x, y)-plane and setting $z = 0$, we find that the displacement induced by the passage of gravitational waves remains confined to the (x, y)-plane. By writing the separation between two point particles as $\xi_i(t) = (x_0 + \delta x(t), y_0 + \delta y(t))$ where x_0, y_0 are the initial unperturbed positions and $\delta x(t)$ and $\delta y(t)$ are the displacements induced by the gravitational waves and integrating Eq. (2.35), to linear order in h we obtain the displacements for the plus polarization

$$\delta x(t) = \frac{h_+}{2} x_0 \sin(\omega t), \;\; \delta y(t) = -\frac{h_+}{2} y_0 \sin(\omega t) \tag{2.36}$$

and for the cross polarization

$$\delta x(t) = \frac{h_\times}{2} y_0 \sin(\omega t), \ \delta y(t) = -\frac{h_\times}{2} x_0 \sin(\omega t). \tag{2.37}$$

As gravitational waves pass through, a ring of test masses in the (x, y)-plane is *stretched* and *squeezed*, as illustrated in Fig. 2.1, demostrating the transverse nature of gravitational waves.

2.3.2 Gravitational waves in linearised theory

In the previous section, we derived solutions to the equation outside the source but a more general solution can be found for $T_{\mu\nu} \neq 0$. In linearised theory we assume that the gravitational field generated by the source is weak, so that the background spacetime can be taken as flat and the metric $g_{\mu\nu}$ is written as $g_{\mu\nu} = \eta_{\mu\nu} + h_{\mu\nu}$. We recall that we choose the harmonic gauge and the energy-momentum tensor satisfies the conservation law in Eq. (2.29). The formula that we derive is exact in v/c and can be expanded in powers of v/c to produce a multipole expansion whose leading order contribution corresponds to the *quadrupole radiation*. A general solution of Eq. (2.28) is

$$\bar{h}_{\mu\nu} = -\frac{16\pi G}{c^4} \int d^4x' G(x - x') T_{\mu\nu}(x') \tag{2.38}$$

where $G(x - x')$ is the retarded Green's function defined as

$$G(x - x') = -\frac{\delta(x^0_{\text{ret}} - x'^0)}{4\pi|\mathbf{x} - \mathbf{x}'|} \tag{2.39}$$

with $x'^0 = ct'$ and $x^0_{\rm ret} = ct_{\rm ret}$ and $t_{\rm ret} = t - \frac{|\mathbf{x}-\mathbf{x}'|}{c}$. Outside the source and in a generic direction $\hat{\mathbf{n}}$ we have

$$h^{TT}_{ij}(t,\mathbf{x}) = \frac{4G}{c^4}\Lambda_{ij,kl}(\hat{\mathbf{n}})\int d^3x' \frac{1}{|\mathbf{x}-\mathbf{x}'|}T_{kl}(t - \frac{|\mathbf{x}-\mathbf{x}'|}{c}, \mathbf{x}') \tag{2.40}$$

where $\Lambda_{ij,kl}$ is the Lambda tensor defined as $h^{TT}_{ij} = \Lambda_{ij,kl}h_{kl}$. We are interested in h^{TT}_{ij} at large distances from the source, where the detector is located. At $r \gg \mathbf{x}'$, where $\mathbf{x}'$ indicates a point inside the source, we can expand $|\mathbf{x}-\mathbf{x}'| = r - \mathbf{x}'\hat{\mathbf{x}} + O(d^2/r)$ with $r \equiv |\mathbf{x}|$ and d the typical radius of the source. At large distances and neglecting $O(d^2/r)$ terms we obtain

$$h^{TT}_{ij}(t,\mathbf{x}) = \frac{1}{r}\frac{4G}{c^4}\Lambda_{ij,kl}(\hat{\mathbf{n}})\int d^3x' T_{kl}(t - \frac{r}{c} + \frac{\mathbf{x}'\cdot\hat{\mathbf{n}}}{c}, \hat{\mathbf{x}}'). \tag{2.41}$$

If the typical velocities v inside the source are small compared to the speed of light, i.e. $v \sim \omega_s d \sim \omega d \ll c$ with ω_s typical frequency of the motion inside the source and ω frequency of the gravitational radiation, we have that $\frac{\omega}{c}\mathbf{x}'\cdot\hat{\mathbf{n}} \simeq \frac{\omega_s d}{c} \ll 1$ and we can therefore expand $T_{kl}(t - \frac{r}{c} + \frac{\hat{\mathbf{x}}'\cdot\hat{\mathbf{n}}}{c}, \mathbf{x}')$ around $(t - \frac{r}{c}, \mathbf{x}')$ obtaining

$$T_{kl}(t - \frac{r}{c} + \frac{\hat{\mathbf{x}}'\cdot\hat{\mathbf{n}}}{c}, \mathbf{x}') \simeq \underbrace{T_{kl}(t - \frac{r}{c}, \mathbf{x}')}_{\rm N} + \frac{1}{c}x'^i n^i \partial_t T_{kl}(t - \frac{r}{c}, \mathbf{x}') + \frac{1}{2c^2}\partial_t^2 T_{kl}(t - \frac{r}{c}, \mathbf{x}')x'^i x'^j n^i n^j + ... \tag{2.42}$$

where the Newtonian term is indicated by N and the other terms are high order corrections. We define the momenta of T^{ij} as

$$\begin{aligned} S^{ij}(t) &= \int d^3x T^{ij}(t,\mathbf{x}), \\ S^{ij,k}(t) &= \int d^3x T^{ij}(t,\mathbf{x})x^k, \end{aligned} \tag{2.43}$$

$$S^{ij,kl}(t) = \int d^3x T^{ij}(t,\mathbf{x}) x^k x^l$$

and similarly for higher order momenta. These momenta are symmetric in the first set of indices and in the second set but not necessarily under the exchange of indices of different type. Inserting Eq. (2.42) in Eq. (2.40) we obtain

$$h_{ij}^{TT}(t,\mathbf{x}) = \frac{1}{r}\frac{4G}{c^4}\Lambda_{ij,kl}(\hat{\mathbf{n}})[S^{kl} + \frac{1}{c}n_m \dot{S}^{kl,m} + \frac{1}{2c^2}\ddot{S}^{kl,mp} n_m n_p + ...]. \tag{2.44}$$

We can define the momenta S^{ij} and derivatives in terms of two sets of momenta that have a more immediate physical interpretation called the *mass moments* $\{M, M^i, M^{ij}, ...\}$ and the *current moments* $\{P^i, P^{i,j}, ...\}$. Using the conservation of the stress energy tensor we define the momenta of the energy density T^{00}/c^2 as

$$\begin{aligned} M &= \int d^3x T^{00}(t,\mathbf{x}), \\ M^i &= \frac{1}{c^2}\int d^3x T^{0i}(t,\mathbf{x}) \\ M^{ij} &= \frac{1}{c^2}\int d^3x T^{00}(t,\mathbf{x}) x^i x^j \end{aligned} \tag{2.45}$$

and so on, while the momenta of the momentum density T^{0i}/c are defined as

$$\begin{aligned} P^i &= \int d^3x T^{0i}(t,\mathbf{x}), \\ P^{i,j} &= \int d^3x T^{0i}(t,\mathbf{x}) x^j \end{aligned} \tag{2.46}$$

and so on. We can define

$$S^{ij} = \frac{1}{2}\ddot{M}^{ij} \tag{2.47}$$

and by inserting in Eq. (2.44) we obtain, at leading order

$$h_{ij}^{TT}(t,\mathbf{x}) = \frac{1}{r}\frac{4G}{c^4}\Lambda_{ij,kl}(\hat{\mathbf{n}})\frac{\partial^2}{\partial_t^2}\int T^{00}x^k x^l d^3x' = \frac{1}{r}\frac{2}{G}c^4\Lambda_{ij,kl}(\hat{\mathbf{n}})\ddot{M}^{kl}(t-\frac{r}{c}). \tag{2.48}$$

The physical components are given by the traceless terms and we can define, by removing the trace from M^{ij}, the *quadrupole moment*

$$Q^{ij} = M^{ij} - \frac{1}{3}\delta^{ij}M^{kk} = \int d^3x\rho(t,\mathbf{x})(x^i x^j - \frac{1}{3}\delta^{ij}r^2) \tag{2.49}$$

where $\rho(t,\mathbf{x})$ is the mass density of the source. By defining

$$\ddot{Q}_{ij}^{TT}(t-\frac{r}{c}) = \Lambda_{ij,kl}(\hat{\mathbf{n}})\ddot{Q}_{kl}(t-\frac{r}{c}) \tag{2.50}$$

Eq. (2.48) becomes

$$[h_{ij}^{TT}(t,\mathbf{x})]_{\text{quad}} = \frac{1}{r}\frac{2G}{c^4}\ddot{Q}_{ij}^{TT}(t-\frac{r}{c}) \tag{2.51}$$

which is known as the *quadrupole formula* and states that any accelerated mass generates gravitational waves and the emission of gravitational radiation is primarily governed by the lowest multipole moments that is the mass quadrupole. Additionally, subleading contributions to the metric perturbation can be calculated by including more terms in the expansion above, such as the next-to-leading order terms given by the current octupole term, mass octupole, etc. In linearized theory M and P^i are conserved and the *monopole* and *dipole* terms depending on these quantities do not appear. However, the absence of monopole and dipole radiation holds also in the full non-linearized theory (see for example [144] for more details). The absence of monopole and dipole radiation reflects the fact that the graviton is a massless particle with spin 2. The two polarizations h_+ and $h_\times$ can

be expressed in terms of M^{ij} as

$$h_+ = \frac{1}{r}\frac{G}{c^4}(\ddot{M}_{11} - \ddot{M}_{22}), \qquad (2.52)$$
$$h_\times = \frac{2}{r}\frac{G}{c^4}\ddot{M}_{12}$$

and will in general depend on the polar angles (θ, ϕ) in a generic direction $\hat{\mathbf{n}}$. In the quadrupole approximation we have that the total radiated power is given by

$$P_{\rm quad} = \frac{G}{5c^5}\langle \dddot{Q}_{ij}\dddot{Q}^{ij}\rangle \qquad (2.53)$$

where $\dddot{Q}_{ij}$ is evaluated at the retarded time $t - r/c$. The rates of energy and agular momentum carried away by the gravitational waves are given by

$$\frac{dE}{dt} = \frac{c^3 r^2}{32\pi G}\int d\Omega \langle \dot{h}^{TT}_{ij}\dot{h}^{TT}_{ij}\rangle = \frac{G}{5c^5}\langle \dddot{Q}_{ij}\ddot{Q}_{ij}\rangle, \qquad (2.54)$$
$$\frac{dJ^i}{dt} = \frac{c^3}{32\pi G}\int r^2 d\Omega \langle -\epsilon^{ikl}\dot{h}^{TT}_{ab}x^k\partial^l h^{TT}_{ab} + 2\epsilon^{ikl}\dot{h}^{TT}_{al}h^{TT}_{ak}\rangle = \frac{2G}{5c^5}\epsilon^{ikl}\langle \ddot{Q}_{ka}\dddot{Q}_{la}\rangle.$$

2.3.3 Systematic Multipolar Expansion

It is possible to construct a systematic multipole expansion for the gravitational waveform [145]. Using the spin-weighted spherical harmonics ${}^sY_{\ell m}(\iota, \varphi)$ of spin-weight $s = -2$, it is possible to write

$$h_+ - ih_\times = \frac{1}{D_L}\sum_{\ell=2}^{+\infty}\sum_{m=-\ell}^{\ell} h_{\ell m}\,{}^{-2}Y_{\ell m}(\iota, \varphi) \qquad (2.55)$$

where D_L is the luminostity distance, (ι, φ) are the polar angles corresponding to spherical coordinates in a unit sphere $h_{\ell m}$ are the waveform multipoles and $Y_{\ell m}(\iota, \varphi)$ are the

spherical harmonics defined in terms of Wigner d-matrices [146] as

$$ {}^{-2}Y_{\ell m}(\iota,\varphi) = (-1)^s \sqrt{\frac{(2\ell+1)}{4\pi}} d^{\ell}_{ms}(\iota) e^{im\varphi} \tag{2.56} $$

where the Wigner d-matrices are defined as

$$ d^{\ell}_{ms}(\iota) = \sqrt{(\ell+s)!(\ell-s)!(\ell+m)!(\ell-m)!} \sum_{k=k_{\min}}^{k_{\max}} \frac{(-1)^{k-s+m} (\sin\frac{\iota}{2})^{2k-s+m} (\cos\frac{\iota}{2})^{2\ell-2k+s-m}}{k!(\ell+s-k)!(\ell-k-m)!(k-s+m)!} \tag{2.57} $$

where $k_{min} = \max(0, s-m)$ and $k_{max} = \min(\ell+s, \ell-m)$.

In the multipole expansion there are two types of spherical harmonics, the ones that remain unchanged under parity transformations, i.e. they pick a factor $\pi_\ell = (-1)^\ell$ called of *electric type* (*even*) and the ones that pick a factor $\pi_\ell = (-1)^{\ell+1}$ under parity transformations and are called of *magnetic type* (*odd*). The first ones are associated to the mass multipoles while the second ones to the current multipoles. In order to get Eq. (2.55) it is possible to write h^{TT}_{ij} in Eq. (2.44) using a decomposition of $\dot{S}^{kl,m}$ into irreducible representations of the rotation group SO(3). The reason to introduce this *symmetric and trace-free tensor decomposition* is to separate the contributions corresponding to the mass and current multipoles and write them in a systematic expansion so that there is no interference between the two types of multipoles at all orders. The most general expansion for h^{TT}_{ij} in the wave zone is written as

$$ h^{TT}_{ij} = \frac{1}{r}\frac{G}{c^4} \sum_{\ell=2}^{\infty} \sum_{m=-\ell}^{\ell} \left[u_{\ell m}(T^{E2}_{\ell m})_{ij}(\iota,\varphi) + v_{\ell m}(T^{B2}_{\ell m})_{ij}(\iota,\varphi) \right] \tag{2.58} $$

where $u_{\ell m}$ and $v_{\ell m}$ are functions of $t - r/c$ while $(T^{E2}_{\ell m})_{ij}$ and $(T^{B2}_{\ell m})_{ij}$ are tensors of the

electric and magnetic type that can be decomposed as [145]

$$(T^{E2}_{\ell m}) = c_\ell \, r^2 \Lambda_{ij,i'j'}(\hat{\mathbf{n}}) \partial_{i'} \partial_{j'} Y_{\ell m}(\iota, \varphi) \tag{2.59}$$

and similarly for $(T^{B2}_{\ell m})_{ij}$. The index 2 indicates the helicity states of the gravitational waves and c_ℓ is a coefficient indicating the parity. The coefficients $u_{\ell m}$ and $v_{\ell m}$ are determined by the source multipole moments. A detailed derivation of the coefficients can be found in [144, 145] while we provide here the final expression. The coefficients are given by

$$u_{\ell m} = \frac{d^\ell}{dt^\ell} I_{\ell m} \tag{2.60}$$

where, to leading order in v/c we obtain the spherical component of the tensor $M^{i_1 \dots i_\ell}$

$$I_{\ell m} = \frac{1}{c^{\ell-2}} \frac{16\pi}{(2\ell+1)!!} \left[\frac{(\ell+1)(\ell+2)}{2\ell(\ell-1)} \right]^{1/2} Y^{\ell m *}_{i i_1 \dots i_{\ell-1}} M^{i_1 \dots i_\ell} \tag{2.61}$$

and similarly

$$v_{\ell m} = \frac{d^\ell}{dt^\ell} S_{\ell m} \tag{2.62}$$

defining the spherical component of the tensor $P^{j,k i_1 \dots i_{\ell-1}}$

$$S_{\ell m} = \frac{1}{c^{\ell-1}} \frac{32\pi}{(2\ell+1)!!} \left[\frac{\ell(\ell+2)}{2(\ell-1)(\ell+1)} \right]^{1/2} Y^{\ell m *}_{i i_1 \dots i_{\ell-1}} \epsilon_{ijk} P^{j,k i_1 \dots i_{\ell-1}}. \tag{2.63}$$

We remember that $M^{i_1 \dots i_\ell}$ and $\epsilon_{ijk} P^{j,k i_1 \dots i_{\ell-1}}$ represent, respectively, the moments of the mass and the the angular momentum density for a non-relativistic source with negligible

self-gravity. By substituting

$$h_{\ell m} = \frac{1}{r}\left[\frac{1}{\sqrt{2}}u_{\ell m} - \frac{i}{\sqrt{2}}v_{\ell m}\right] \tag{2.64}$$

into Eq. (2.58) we obtain the multipolar expansion in Eq. (2.55). We can write the radiated energy and angular momentum to all orders in terms of multipole expansion as

$$\frac{dE}{dt} = \frac{1}{16\pi}\sum_{\ell=2}^{\infty}\sum_{m=-\ell}^{\ell}|\dot{h}_{\ell m}|^2, \tag{2.65}$$

$$\frac{dJ}{dt} = -\frac{1}{16\pi}\sum_{\ell=2}^{\infty}\sum_{m=-\ell}^{\ell} m\,\Im\left(\dot{h}_{\ell m}h^*_{\ell m}\right). \tag{2.66}$$

The waveform multipoles $h_{\ell m}$ can in general be written, in the time domain, as

$$h_{\ell m} \equiv h_{\ell m}(\boldsymbol{\theta}, t) = A_{\ell m}(\boldsymbol{\theta}, t)e^{-im\,\phi_{\ell m}(\boldsymbol{\theta},t)} \tag{2.67}$$

where $\boldsymbol{\theta}$ are the intrinsic parameters of the source and $A_{\ell m}(\boldsymbol{\theta}, t)$, $\phi_{\ell m}(\boldsymbol{\theta}, t)$ are the amplitude and phase relative to the waveform multipoles. The strain is expressed as a sum over all waveform multipoles with the main contribution given by the $(2, 2)$-mode and it will in general be written as

$$h(\boldsymbol{\theta}, t) = h_\times(\boldsymbol{\theta}, t) - ih_+(\boldsymbol{\theta}, t) = A(\boldsymbol{\theta}, t)e^{-i\phi(\boldsymbol{\theta},t)} \tag{2.68}$$

where $A(\boldsymbol{\theta}, t)$ and $\phi(\boldsymbol{\theta}, t)$ are the amplitude and phase of $h(\boldsymbol{\theta}, t)$.

2.3.4 Post-Newtonian expansion

In the previous sections we have explored how gravitational waves arise as a solution to the linearised Einstein field equations by assuming flat spacetime. In this approximation we are assuming that the sources generating gravitational waves in the *far-field* or

radiation region contribute negligibly to the spacetime curvature in the *near-field* region. We computed h_{ij} as an expansion in v/c with the leading order given by the quadrupole formula and saw that higher order corrections can then be structured in a multipole expansion [145]. In linearised gravity we assumed that the spacetime curvature and the velocity of the source are independent parameters. This assumption breaks down for self-gravitating systems where $(v/c)^2 \sim R_{\rm S} d$ with $R_{\rm S} = 2GM/c^2$ Schwarzschild radius and d typical size of the system that, for a binary system, is the orbital distance. For these systems, post-Newtonian (PN) corrections are crucial in the inspiral phase and break down in the strong-field regime.

The PN approximation [62, 147] was introduced by Lorentz and Droste [148] and subsequently by Einstein, Infeld and Hoffmann [149]. In the PN approximation we consider slowly moving, weakly self gravitationg sources such that the parameter

$$\epsilon \sim (v/c) \sim (R_S d)^{1/2} \ll 1. \tag{2.69}$$

We also require a smooth matter distribution inside the source such that the components of the energy-momentum tensor satisfy $|\frac{T^{0i}}{T^{00}}| \ll 1$ and $|\frac{T^{0i}}{T^{00}}|^{1/2} \ll 1$ [62]. For non-relativistic sources it is convenient to distinguish between near zone where $d < r \ll \lambda$ and the far or wave zone where $r \gg \lambda$. Retardation effects or *tails* due to the back-reaction of gravitational waves are negligible in the near zone and in that region the potentials can be considered static. However, they are crucial in the wave zone, necessitating a different approach. The key idea is to employ distinct techniques for the near zone and the wave zone and match the two solutions in an intermediate region where $r \sim \lambda$. In practice this means using the PN expansion in the near zone and the post-Minkowskian (PM) formalism [62], i.e. an expansion in the gravitational constant G, in the wave zone. Nevertheless, having a formalism that computes systematically the generation of gravitational waves at all orders in v/c is very complicated. The source emits gravitational waves which carry

energy away and, beyond a certain order, gravitational waves back-react on the matter sources, influencing their dynamics. This is due to the non-linearity of GR that leads the gravitational field itself to become a source of gravitational waves. Difficulties in the PN expansion lie in the fact that when trying to solve the Einstein equations iteratively, divergences appear beyond a certain order. As the PN order increases, so does the order of the multipoles that contribute. The field associated to a multipole of order ℓ includes a factor $(\mathbf{x}\mathbf{x}')^\ell$ which arises from the expansion $1/|\mathbf{x}-\mathbf{x}'|$. When this field is used as a source for the next iteration, sufficiently large values of ℓ lead to divergences at large $\mathbf{x}'$ in the retarded integral. The solution to this challenging problem is to use of the PN expansion only in the near region and employ a different expansion in the far region. The two expansions are then matched in an intermediate region where both remain valid. This procedure is called *matched asymptotic expansion* [150–153]. The spacetime metric of a PN source is expanded as follows, where under time reversal g_{00} and g_{ij} are even while g_{0i} is odd

$$\begin{aligned} g_{00} &= -1 + {}^{(2)}g_{00} + {}^{(4)}g_{00} + {}^{(6)}g_{00} + ... \\ g_{0i} &= {}^{(3)}g_{0i} + {}^{(5)}g_{0i} + ... \\ g_{ij} &= \delta_{ij} + {}^{(2)}g_{ij} + {}^{(4)}g_{ij} + ... \end{aligned} \tag{2.70}$$

and the energy-momentum tensor

$$\begin{aligned} T^{00} &= {}^{0}T^{00} + {}^{(2)}T^{00} + ... \\ T^{0i} &= {}^{(1)}T^{0i} + {}^{(3)}T^{0i} + ... \\ T^{ij} &= {}^{(2)}T^{ij} + {}^{(4)}T^{ij} + ... \end{aligned} \tag{2.71}$$

The 1PN correction can be computed by conveniently choosing the de Donder or harmonic

gauge condition in Eq. (2.27). The Einstein field equations in harmonic coordinates can be written as

$$\Box h^{\alpha\beta} = \frac{16\pi G}{c^4}\tau^{\alpha\beta} \tag{2.72}$$

where $\tau^{\alpha\beta}$ is

$$\tau^{\alpha\beta} = |g|T^{\alpha\beta} + \frac{c^4}{16\pi G}\Lambda^{\alpha\beta} \tag{2.73}$$

where $T^{\alpha\beta}$ is the stress-energy tensor of the matter and the gravitational field given by $\Lambda^{\alpha\beta}$. The most general solution to Eq. (2.72) in the vacuum region outside the source is given in terms of a *multipolar post-Minkowskian* (MPM) expansion which is given in terms of non-linear functionals of the source multipoles. The asymptotic gravitational waveform is then computed in terms of *radiative* moments at infinity, whose relationship with the source moments is given explicitly in [62]. By matching the MPM solution with the PN solution in the matching region it is then possible to understand how a specific choice of physical system describing the matter stress energy tensor selects a specific set of source multipole moments [62].

The waveform polarisations can be written as an expansion in the parameter $x = (\frac{GM\Omega}{c^3})^{2/3}$

$$h_{+,\times} = \frac{2G\mu x}{c^2 R}\sum_{n=0}^{+\infty} x^{n/2} H_{+,\times}^{(n/2)} + \mathcal{O}\left(\frac{1}{R^2}\right) \tag{2.74}$$

where M is the mass of the binary, Ω is the orbital frequency, n is the PN order, μ is the reduced mass, R is the orbital radius and the coefficients $H_{+,\times}$ are given at 3.5PN order and for non-spinning binaries for example in Ref. [62]. Extension that account for eccentricity, spin and memory contribution effects can be found, for example, in Refs. [76,

80, 124].

2.4 Sources of gravitational waves

Gravitational waves are produced by the acceleration of mass distributions and are generated by a variety of astrophysical sources. However, the masses and accelerations of objects on Earth are far too small to be detected by gravitational wave detectors. Instead, gravitational wave signals observable by detectors are produced by very massive objects located far outside our solar system. Gravitational waves can generally be classified into four main categories: *continuous* gravitational waves, gravitational waves produced by *compact binary coalescences* (CBCs), *stochastic* gravitational waves, and *burst* gravitational waves. Continuous gravitational waves are produced by single spinning massive objects like neutron stars and their signal is quasi-monochromatic, i.e. characterized by a constant frequency. In contrast, gravitational waves emitted by compact binary systems are characterised by a frequency that evolves in time and will be discussed in details in this sections since they are the main subject of this thesis. Burst gravitational waves are emitted by short-lived, transient astrophysical events and are very challenging to detect due to the nature of their sources that is hard to predict. This section provides an overview of some of the most significant sources of gravitational waves [154, 155].

- *Compact binary coalescences* [14]: these systems consist of two black holes (BBH), neutron stars (BNS), or a black hole and a neutron star (NSBH) that are close enough to each other that they will eventually merge within the age of the universe. Over time, the system evolves losing energy via gravitational wave emission, gradually spiraling inward (*inspiral* phase) until they merge (*merger* phase). After the merger, the remnant object will go through a *postmerger* phase that is called *ringdown* if the remnant object is a black hole. At sufficiently late times, the black

hole remnant vibrates in a discrete set of damped oscillation frequencies known as quasinormal modes. If one or both objects are neutron stars, the merger can be followed by an electromagnetic signal, such as a gamma-ray burst or a kilonova.

- *Explosion of massive stars*: these violent explosions occur when the core of a massive star rapidly collapses at the end of its lifetime. Throughout their existence stars progress through the first stages of their lives by converting hydrogen into helium. As the hydrogen is depleted, fusion reactions slow down resulting in the release of less energy and gravity causes the core to contract. This raises the temperature of the core again causing the helium fusion to begin. Once helium has been used up, the core contracts again. The star undergoes a series of processes where light elements are fused into heavier ones. Fusion of heavy elements produces no enery output so no further fusion can take place, leaving a compacted mass of inert core. If the mass of this inert core exceed the Chandrasekhar limit ($1.4M_{\odot}$), the electron degeneracy is no longer sufficient to counter the gravitational compression. As a result, the outer layers of the core rapidly fall inward before being violently expelled in a supernova explosion. If the collapsing core of a massive star exhibits a significant asymmetry due to either rapid rotation or the presence of a strong magnetic field, it can emit gravitational waves.

- *Spinning neutron stars*: these are rapidly rotating neutron stars with strong magnetic fielsd and an asymmetric mass distribution known as *pulsars*. Any imperfection or non-uniformity on the star will generate gravitational waves as it spins. Pulsars emit twin beams of radiation from their magnetic poles. If these poles are misaligned with the star's rotational axis, these beams sweep across they sky as the star spins, creating periodic signals. Pulsars act as a very precise cosmic clock and the gravitational wave can be detected by the change in the time of arrival of the pulses [156, 157].

- *Stochastic background*: low-frequency gravitational wave signals from a stochastic background can contain a superposition of signals from many sources that are either too weak or too numerous to be individually detected. Sources detectable by current generation detectors are mainly stellar mass BBH and BNS mergers which produce typical signals from approximately 10 Hz up to a few kHz [158]. An alternatove way of detecting the stochastic background is using pulsar timing arrays (PTAs) that are sensitive to gravitational waves in the nHz frequency range. A stochastic gravitational wave signal has been detected independently by different consortia: NANOGrav [159], EPTA [160], CPTA [161].

- *Exotic sources*: hypothetical gravitational waves sources include coalescence of exotic compact objects (ECOs), e.g. boson stars, dark matter stars, gravastars, among others [162, 163].

2.4.1 Compact binary coalescences

A binary system of compact objects such as neutron stars or black holes of mass m_1, m_2 and positions $\mathbf{r}_1$ and $\mathbf{r}_2$, can be treated as a one-body problem by transforming to the center-of-mass frame. For a more detailed discussion we refer for example to [144, 164]. In this frame, the system's reduced mass is given by

$$\mu = \frac{m_1 m_2}{M} \tag{2.75}$$

where $M = m_1 + m_2$ total mass of the system. We describe here the case of circular orbit, while the eccentric case will be discussed in the next chapter. In the case of a circular orbit the orbital frequency Ω is related to the orbital radius R by Kepler's law

$$\Omega = \sqrt{\frac{GM}{R^3}}. \tag{2.76}$$

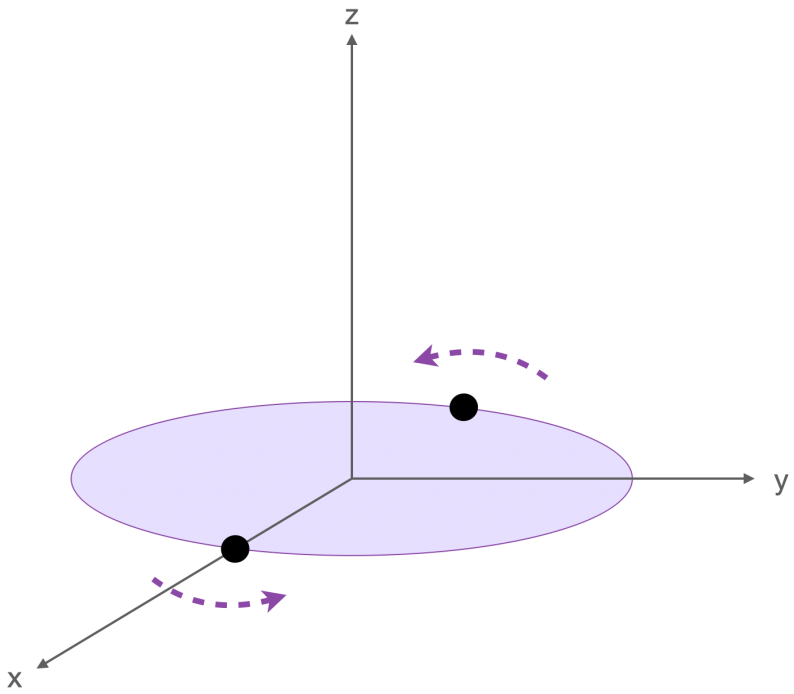


Figure 2.2: Non-spinning binary system in a circular orbit in the xy-plane.

We define the chirp mass as

$$M_c = \mu^{3/5} M^{2/5} = \frac{(m_1 m_2)^{3/5}}{(m_1 + m_2)^{1/5}}. \tag{2.77}$$

The chirp mass determines the frequency evolution of the gravitational wave signal and is one of the most important parameters in gravitational wave astronomy used to identify and analyse the source of gravitational wave signals. The plus and cross polarizations can be written at lowest order as

$$h_+ = \frac{4}{r}\left(\frac{GM_c}{c^2}\right)^{5/3}\left(\frac{\pi f_{\rm gw}}{c}\right)^{2/3}\frac{1+\cos^2\iota}{2}\cos(2\pi f_{\rm gw}(t-r/c)), \tag{2.78}$$

$$h_\times = \frac{4}{r}\left(\frac{GM_c}{c^2}\right)^{5/3}\left(\frac{\pi f_{\rm gw}}{c}\right)^{2/3}\cos\iota\sin(2\pi f_{\rm gw}(t-r/c)) \tag{2.79}$$

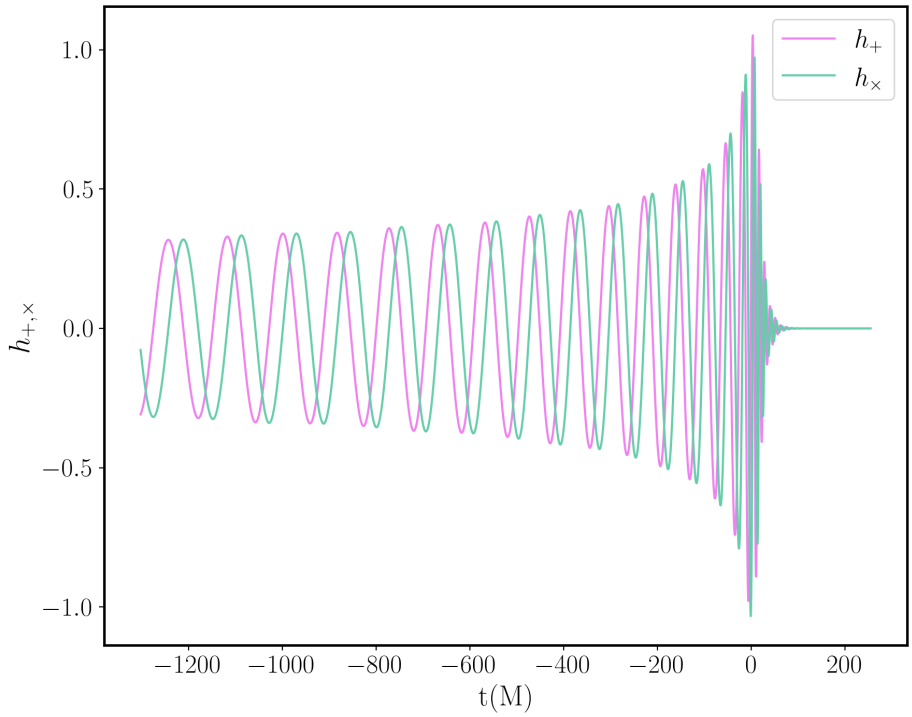


Figure 2.3: Gravitational wave polarisations h_+ and $h_\times$. The figure illustrate the three phases of the gravitational wave signal: the *inspiral*, *merger* and *ring-down*. The time of merger is indicated by $t = 0$.

where the frequency of the gravitational wave is $f_{\rm gw} = f_{\rm orb}/2$, the inclination angle ι is the angle between the line of sight and the orbital angular momentum of the binary system. The frequency of the gravitational wave increases as the binary system loses energy and the two objects spiral towards each other. The rate of change of the frequency is given by

$$\dot{f}_{\rm gw} = \frac{96}{5}\pi^{8/3}\left(\frac{GM_c}{c^3}\right)^{5/3} f_{\rm gw}^{11/3}. \tag{2.80}$$

The frequency $f_{\rm gw}$ can be computed from Eq. (2.80) and written in terms of the time to merger $t_{\rm merger}$ as

$$f_{\rm gw}(t_{\rm merger}-t)=\frac{1}{\pi}\left(\frac{5}{256}\frac{1}{(t_{\rm merger}-t)}\right)^{3/8}\left(\frac{GM_c}{c^3}\right)^{-5/8}. \tag{2.81}$$

For a binary system with primary masses of approximately $36M_\odot$ and $29M_\odot$, such as GW150914 [11], the system merges around 150 Hz and the duration of its gravitational wave signal from the moment it enters the detector's sensitivity at around 30 Hz is ~ 200 milliseconds [165]. An illustration of the two polarisations h_+ and $h_\times$ is shown in Fig. 2.3. As the binary loses energy via emission of graviational waves, the orbital radius shrinks and the frequency increases. The two object inspiral one around each other until the reach the minimum value or radial distance allowed, meaning the *last stable circular orbit* (ISCO) and then merge. For Schwarzschild metric we have that $r_{\rm ISCO}$ is given by

$$r_{\rm ISCO}=\frac{6GM}{c^2}. \tag{2.82}$$

When the ISCO is reached, the dynamics is dominated by the strong field regime and the two objects plunge towards each other. The number of cycles $\mathcal{N}_{\rm cyc}$ spent by the signal in the detector bandwith $f\in[f_{\rm min},f_{\rm max}]$, where $f_{\rm max}$ is a maximum frequency $f_{\rm max}$ beyond which the inspiral phase ends, is given by

$$\mathcal{N}_{\rm cyc}=\int_{f_{\rm min}}^{f_{\rm max}}\frac{f_{\rm gw}}{\dot{f}_{\rm gw}}df=\frac{5}{256}\left(\frac{GM_c}{c^3}\right)^{-5/8}\left(\frac{f_{\rm max}^{5/3}-f_{\rm min}^{5/3}}{f_{\rm gw}^{5/3}}\right) \tag{2.83}$$

while the total energy emitted can be calculated by integrating

$$\frac{dE}{df}=\frac{\pi^{2/3}}{3G}\left(GM_c^{5/3}\right)f^{-1/3}. \tag{2.84}$$

which is derived from Eq. (2.65) by rewriting in terms of h_+ and $h_\times$ as it can be found for example in [144].

2.4.2 Eccentric binaries

As we have discussed, CBCs lose energy and angular momentum through the emission of gravitational waves, leading their orbits to shrink and progressively circularise [15–17] and for this reason templates based on quasi-circular waveform models are employed in the analysis of gravitational wave signals. However, as extensively discussed in Chapter 1, many studies highlight that precise measurements of eccentricity can offer crucial astrophysical insights and help to distinguish between binary formation channels. The discovery of the Hulse-Taylor pulsar in 1974 provided the first indirect evidence of gravitational waves and demostrated how the average rate at which the system radiates energy depends on the eccentricity. In the case of Newtonian orbits the energy and angular momentum are conserved and the orbit can be described in terms of mean motion and eccentricity. The pericenter occurs at the same value of angular coordinate at each orbit and the periastron precession does not occur. There is no close-form solution of the form $r(t)$ for the orbital radius. However, in polar coordinates and in the center-of-mass frame, the eccentric motion can be parametrised as [66, 166]

$$\begin{aligned} r &= a(1 - e\cos u), \\ \phi_{\rm orb} - \phi_{0,\rm orb} &= v \equiv 2\arctan\left[\left(\frac{1+e}{1-e}\right)^{1/2}\tan\frac{u}{2}\right] \end{aligned} \tag{2.85}$$

where r and $\phi_{\rm orb}$ are the components of the relative separation vector $\mathbf{r} = r(\cos\phi_{\rm orb}, \sin\phi_{\rm orb}, 0)$, $\phi_{0,\rm orb}$ is a constant initial phase, a is the semi-major axis, e is the eccentricity and v, u are auxiliary angles shown in Fig. 2.4 called respectively *true anomaly* and *eccentric anomaly*. In this parametrisation, the Kepler law reads

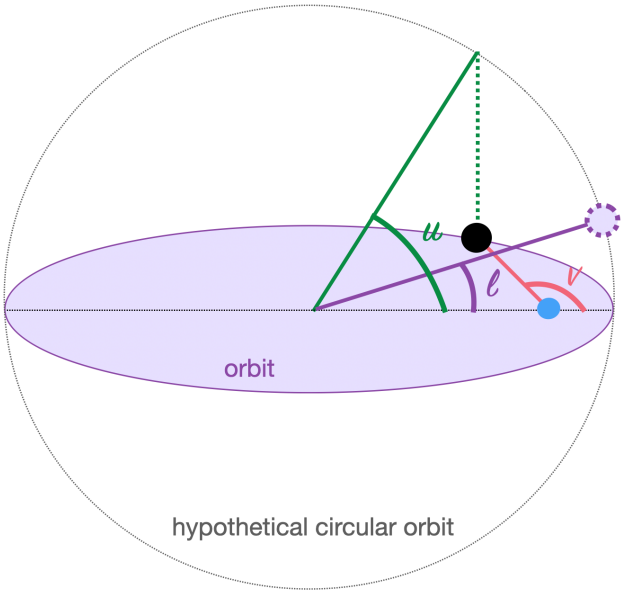


Figure 2.4: Representation of the eccentric anomalies. The true anomaly v is the angle between the position of the body measured from the focus and the direction of periapsis, the eccentric anomaly u is the angle between the projection of the body on an hypothetical circular orbit (with the same semi-major axis) and the center of the ellipse, the mean anomaly l is the angle representing the position the body would have on the circular orbit if it moved at a constant angular speed and it increases uniformly with time.

$$l = n(t - t_0) = u - e \sin u \tag{2.86}$$

where l is called *mean anomaly*, t_0 is an initial constant time and n is the *mean motion*. The latter satisfies $n = 2\pi/P$ where P is the orbital period. Eq. (2.85) can be also written in terms of v and p as

$$r = \frac{p}{1 + e \cos v} \tag{2.87}$$

where $p = a(1 - e^2)$ is the semilatus rectum. The apocenters and pericenters are respectively given by

$$r_a = \frac{p}{1 - e} \qquad r_p = \frac{p}{1 + e}. \tag{2.88}$$

At the leading order the mean loss of eccentricity is given by Ref. [16]

$$\left\langle \frac{de}{dt} \right\rangle = -\frac{304}{15} e \frac{G^3 m_1 m_2 (m_1 + m_2)}{c^5 a^4 (1 - e^2)^{5/2}} \left(1 + \frac{121}{304 e^2} \right). \tag{2.89}$$

This result, first derived by Peters and Mathews, was used to model the variation of the period of the Hulse-Taylor binary pulsar and shows how the eccentricity of the orbit is gradually shrunk by emission of gravitational waves. The average rate at which the system radiates energy is, over one period of the elliptical motion

$$P = \frac{32}{5} \frac{G^4}{c^5} \frac{m_1^2 m_2^2 (m_1 + m_2)}{a^5 (1 - e^2)^{7/2}} \left(1 + \frac{73}{24} e^2 + \frac{37}{96} e^4 \right). \tag{2.90}$$

where e is the eccentricity of the orbit and a is the semi-major axis. The bodies radiate most at their closest approach and the radiated power has a strong dependence on the eccentricity, enhanced with respect to the circular case, to a factor $\frac{\left(1+\frac{73}{24}e^2+\frac{37}{96}e^4\right)}{(1-e^2)^{7/2}}$ [15–17]. In the next section, we provide a brief introduction to the extension of the classical Keplerian solution to account for relativistic corrections.

Quasi-Keplerian parametrisation

The Newtonian equations for r, ϕ and l given by Eq. (2.85) and Eq. (2.86) can be generalised to the PN case by the addition of higher order terms [63, 66, 167–169]. The quasi-Keplerian (QK) parametrisation was introduced by Damour and Deruelle [63] as a 1PN generalisation of the Newtonian binary dynamics. The generalisation to 2PN is given by [167–169], while the 3PN is given by [66]. At 1PN we have a Kepler-like parametrisation

$$\begin{aligned} r &= a(1 - e_r \cos u), \\ l &= n(t - t_0) = u - e_t \sin u, \end{aligned} \tag{2.91}$$

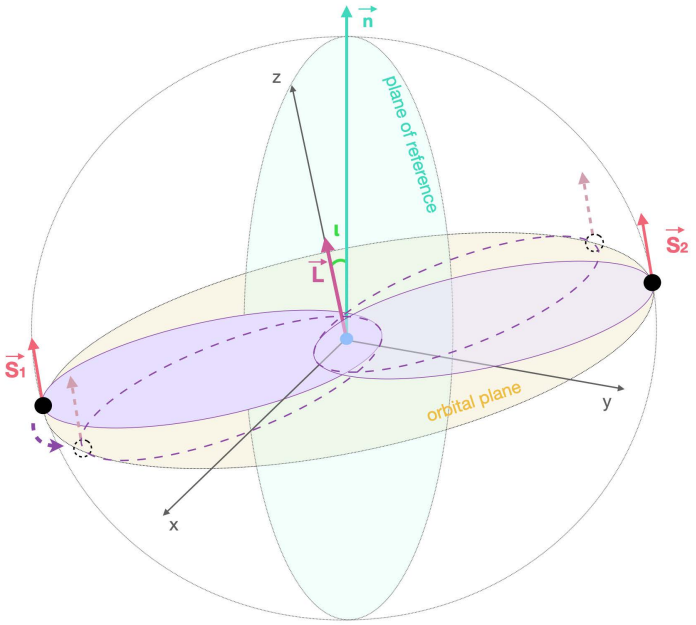


Figure 2.5: The figure depicts the motion of two black holes following an eccentric orbit. The angle between the normal to the orbit and the line-of-sight **n** is the inclination angle ι. The black holes have spins $\mathbf{S}_1$ and $\mathbf{S}_2$ aligned with the orbital angular momentum **L**. The solid lines represent the initial elliptic orbits while the dashed lines represent the orbits after the first periastron passage. The figure does not show the shrinking of the orbit due to the emission of gravitational waves.

$$\frac{\phi_{\rm orb} - \phi_{0,\rm orb}}{K} = v = 2 \arctan \left[\left(\frac{1+e_\phi}{1-e_\phi} \right) \tan \frac{u}{2} \right]$$

where the three eccentricities e_r, e_t and e_ϕ are eccentric parameters including PN corrections which are introduced to ensure the parametrisation closely resembles the Keplerian form and a is a 1PN semi-major axis whose PN expansion can be found for example in Ref. [86]. At 1PN we have the orbit precesses by an angle $K = \Delta\phi_{\rm orb} - 2\pi$ per orbital revolution. K is called *periastron advance* and is the difference between the angle $\Delta\phi_{\rm orb}$ swept during a full orbit, meaning from one periastron passage to the next, and 2π which is the angle swept by a Keplerian orbit. Fig. 2.5 illustrates a binary system on eccentric orbits. The black holes, indicated by black filled circles, are located at the first periastron

with their spins $\mathbf{S_1}, \mathbf{S_2}$ aligned with the orbital angular momentum $\mathbf{L}$. Due to periastron precession, the second periastron occurs at a shifted location with respect the first one.

2.5 Gravitational wave detection

2.5.1 Gravitational wave detectors

The first gravitational wave detectors were developed in the 1960s and were *resonant mass detectors* [170, 171]. The detectors operated on the principle that gravitational waves transfer energy to a resonant bar, causing it to oscillate. Current gravitational wave detectors such as the Laser Interferometer Gravitational Wave Observatory (LIGO) [6–8], Virgo [9, 10] and the Kamioka Gravitational Wave Detector (KAGRA) [172, 173] are *beam detectors* that function similarly to a Michelson interferometer [174]. In these detectors, a laser beam is split and sent along two perpendicular arms before recombining to produce an interference pattern. The laser ligh is used to measure variations in the relative lengths of the two arms. As discussed in Sec. 2.3.1, the TT gauge provides the most convenient framework for analysing the interaction between gravitational waves and test masses, as it allows physical effects to be directly interpreted in terms of *proper distances* and *proper times*. If we consider two events at $(t, x_1, 0, 0)$ and $(t, x_2, 0, 0)$ respectively, their coordinate distance $x_2 - x_1 = L$, meaning the distance between the beam-splitter and the end mirror, remains the same. We can compute the proper distance for a flat metric as

$$ds^2 = g_{\mu\nu} dx^\mu dx^\nu = -c^2 dt^2 + (1 - h_+) dx^2 + (1 + h_\times) dy^2 + dz^2. \tag{2.92}$$

In the x direction we have

$$L_x = \int_{x_1}^{x_2} \sqrt{g_{xx}} dx = \int_{x_1}^{x_2} \sqrt{1 + h_{xx}(t, 0)} dx \simeq L(1 + \frac{1}{2} h_{xx}(t, 0)) \tag{2.93}$$

If we compute the relative change in the coordinate distance we obtain

$$\frac{\delta L}{L} \simeq \frac{1}{2} h_{xx}(t,0) \equiv \frac{1}{2} h_{+} \tag{2.94}$$

and similarly for the y direction. Gravitational wave detectors observe fractional variations in length of the order $h \sim O(10^{-21})$ and measuring such small displacements requires extremely advanced technology. To enhance sensitivity, test masses are used to increase the optical path length. In general the input of the detector will have the form

$$h(t) = \frac{\delta L(t)}{L} = \sum_{A=+,\times} D^{ij} e^{A}_{ij}(\hat{\mathbf{n}}) h_A(t) \tag{2.95}$$

where D^{ij} is the detector tensor depending on the geometry of the detector and e^{A}_{ij} are the polarisation tensors. The detector pattern functions are defined as

$$\begin{aligned} F_{+}(\Theta, \Phi, \psi) &= D^{ij} e^{+}_{ij}, \\ F_{\times}(\Theta, \Phi, \psi) &= D^{ij} e^{\times}_{ij}. \end{aligned} \tag{2.96}$$

The detector response to a gravitational wave signal is given in terms of the location of the source in the sky and its orientation relative to the detector described by the polar and azimuthal angles (Θ, Φ) commonly referred to as declination δ and right ascension α, and the polarisation angle ψ. The gravitational wave strain can be therefore written as

$$h(t) = h_{+}(t) F_{+}(\Theta, \Phi) + h_{\times}(t) F_{\times}(\Theta, \Phi). \tag{2.97}$$

When observing the orbit edge-on $\iota = \pi/2$, the $h_{\times}$ polarisation vanishes, resulting in linearly polarised gravitational waves. For $\iota = 0$, h_{+} and $h_{\times}$ having the same amplitude, the radiation describes a circle parametrised by t and the radiation is circularly polarised.

Elliptic polarisation occurs for intermediate values of ι where the amplitudes of h_+ and $h_\times$ are different.

2.5.2 Matched filtering and data analysis techniques

The output of a gravitational wave detector is a time series that typically consists of both the true gravitational wave signal and background noise. The various noise within the detector can be conveniently treated in the frequency domain by introducing a *noise power spectral density* which has units of $1/\sqrt{Hz}$ and defines the *sensitivity* of the detector [175]. The detector output data $d(t)$ can be written as

$$d(t) = h(t) + n(t) \tag{2.98}$$

where $h(t)$ is the gravitational wave signal and $n(t)$ is the background noise. The analysis of the detector output and *matched filtering* techniques are therefore performed in the frequency domain. We assume stationary noise [176] with zero mean ($\langle n(t) \rangle = 0$) such that the different Fourier components are uncorrelated. We can therefore define [177]

$$\langle \tilde{n}^*(f)\tilde{n}(f') \rangle = \delta(f - f')\frac{1}{2}S_n(f) \tag{2.99}$$

where $\langle \tilde{n}^*(f)\tilde{n}(f') \rangle$ denotes the average of an ensemble of noise realisations and $S_n(f)$ is the *single-sided power spectral density* (PSD) that is obtained by integrating over the physical range of frequencies $0 \leq f < \infty$ such that

$$\langle n(t)^2 \rangle = \int_0^\infty df\, S_n(f). \tag{2.100}$$

We define the *noise-weigthted inner product* as

$$\langle h_1|h_2\rangle = 4\Re\int_0^\infty df\frac{\tilde{h}_1(f)\tilde{h}_2^*(f)}{S_n(f)}. \tag{2.101}$$

where $\tilde{h}_1(f)$ and $\tilde{h}_2(f)$ are the Fourier transforms of time domain signals. The *signal-to-noise ratio* (SNR) between the data and the waveform template is defined as

$$\rho = \sqrt{\langle d|h\rangle}. \tag{2.102}$$

The agreement between two signals can be quantified in terms of *mismatch* or *unfaithfulness* defined as

$$\bar{\mathcal{M}} = \bar{F} = 1 - F = 1 - \max_{t_0,\phi_0}\frac{\langle h_1|h_2\rangle}{\sqrt{\langle h_1|h_1\rangle\langle h_2|h_2\rangle}} \tag{2.103}$$

where (t_0, ϕ_0) are the initial time and phase of coalescence and $\langle h_{\rm GW}|h_{\rm GW}\rangle$ is the noise weigthed inner product between two waveforms. By identifying with $h_1 = h_{\rm GW}$ the gravitational wave signal and with $h_2 = h_{\rm model}$ the model template, we obtain the mismatch between a gravitational wave signal and a template.

2.5.3 Inferring parameters of the source

The measurement of the parameters that describe the gravitational wave emitting binary is carried out within the framework of Bayesian inference, which relies on Bayes' theorem [178]

$$p(\boldsymbol{\theta}|d,H) = \frac{p(d|\boldsymbol{\theta},H)\,p(\boldsymbol{\theta}|H)}{p(d|H)}, \tag{2.104}$$

where $p(\boldsymbol{\theta}|d,H)$ is the posterior probability of a set of parameters $\boldsymbol{\theta}$ given the data d assuming a specific model H, $p(\boldsymbol{\theta}|H)$ is the prior, $p(d|\boldsymbol{\theta},H)$ is the likelihood and $p(d|H)$

is the evidence or marginalized likelihood. The evidence can be expressed as:

$$Z \equiv p(d|H) = \int p(d|\boldsymbol{\theta}, H)\, p(\boldsymbol{\theta}|H) d\boldsymbol{\theta}, \tag{2.105}$$

where the integral extends over the entire parameters space. The evidence assumes the role of an overall normalization constant but plays an important role in Bayesian model selection. Given two competing hypotheses H_A and H_B, the Bayes' factor is defined as the ratio of evidences

$$\mathcal{B}^B_A = \frac{p(\mathbf{d}|H_B)}{p(\mathbf{d}|H_A)}\,, \tag{2.106}$$

where the hypothesis H_B is favoured by the data over H_A if $\mathcal{B}^B_A > 1$. Under the assumption of Gaussian, stationary noise that is uncorrelated between each detector, and assuming a time domain signal model $h \equiv h(t, \boldsymbol{\theta})$ and data set $d \equiv d(t)$, the likelihood $p(d|\boldsymbol{\theta}, H) \equiv \mathcal{L}(d|\boldsymbol{\theta})$ is

$$\mathcal{L}(d|\boldsymbol{\theta}) \propto e^{-\frac{1}{2}\sum_{i=1}^{N} \langle h - d_i | h - d_i \rangle}. \tag{2.107}$$

The gravitational wave signal emitted by an eccentric coalescing binary black hole system is fully described by 17 parameters:

$$\boldsymbol{\theta}_{\mathrm{CBC}} = \{m_1, m_2, \boldsymbol{\chi_1}, \boldsymbol{\chi_2}, D_L, \iota, \alpha, \delta, \psi, t_0, \phi_0, e_0, f_0\}, \tag{2.108}$$

where $m_{1,2}$ denotes the (detector-frame) masses of the two black holes such that $m_1 \geq m_2$, $\boldsymbol{\chi}_{1,2}$ are the dimensionless spin angular momenta vectors with three spatial components, D_L is the luminosity distance to the source, ι is the inclination angle, $\{\alpha, \delta\}$ are the right ascension and declination and define the sky location of the source, ψ is the polarisation angle, $\{t_0, \phi_0\}$ are the reference time and phase, and $\{e_0, f_0\}$ are two parameters describing the eccentricity of the system. An important caveat is that the observed gravitational wave signal is redshifted with respect to the source frame. For the component masses,

the redshifted masses are related to the source frame masses by

$$m_{1,2}^{\text{detector}} = (1+z)m_{1,2}^{\text{source}} \tag{2.109}$$

where z is the redshift of the source. This relationship holds also for the other masses.

If we want to estimate the posterior distribution of a single specific parameter, we marginalise over the remaining parameters obtaining the marginalised posterior

$$p(\theta_i|d) = \int \left(\prod_{k\neq i} d\theta_k\right) p(\boldsymbol{\theta}|d) = \frac{\mathcal{L}(d|\theta_i)\pi(\theta_i)}{\int d\boldsymbol{\theta}\mathcal{L}(d|\boldsymbol{\theta})\pi(\boldsymbol{\theta})} \tag{2.110}$$

where we have defined the prior distribution $p(d|\boldsymbol{\theta}, H) \equiv \pi(\boldsymbol{\theta})$ and $\int d\boldsymbol{\theta}\mathcal{L}(d|\boldsymbol{\theta})$ is the marginalised likelihood defined as

$$\mathcal{L}(d|\theta_i) = \int \left(\prod_{k\neq i} d\theta_k\right) \pi(\theta_k)\mathcal{L}(d|\boldsymbol{\theta}). \tag{2.111}$$

Note that we have assumed that the prior distributions are uncorrelated, meaning that the prior distribution for a given set of parameters $\pi(\boldsymbol{\theta})$ can be written as a product for the prior distributions for each single parameter $\pi(\theta_i)$. With this assumption we do not impose *a priori* any astrophysical constraints on the parameters, allowing model-agnostic analyses. Constructing the posterior distribution of the parameters of the source is a very challenging task due to the high dimensionality of the parameter space. What is typically done to solve this problem is use Markov Chain Monte Carlo (MCMC) [179, 180] and nested sampling [181] methods. For the analyses presented in Chapter 4 we employ the `bajes` package for Bayesian inference [182] and the nested sampling algorithm `dynesty` [183] to extract samples of the posterior distributions.

Chapter 3

Approaches to the two-body problem in General Relativity

3.1 Introduction

In this chapter we discuss different approaches to dealing with the two-body problem in GR, studying the dynamics of coalescencing binary objects and their resulting gravitational wave emission. This Chapter primarily serves as a literature review and aims to introduce fundamentals of Numerical Relativity (NR) and effective-one-body approach (EOB), which will be central themes of the subsequent chapters. The NR sections closely follow [184, 185] while the EOB sections follow [107, 108, 115, 126, 127, 186–189]. Other relevant papers will be cited thoughout the Chapter. In Sec. 2.4.2 we have seen how a Newtonian system can be parametrised in terms of an eccentric and an anomaly parameters. Within the QK framework, briefly discussed in Sec. 2.4.2, the orbit is characterised by three eccentric parameters which introduce small perturbations into the equations of motion and, along with the mean anomaly parameter, colletively capture deviations from the circular motion. This leads to difficulties in defining eccentricity in GR. In recent years,

considerable effort has been devoted to developing precise definitions of eccentricity [1, 2, 98, 190–193]. One of the main objectives of this thesis is to develop tools to accurately measure eccentricity from gravitational wave datasets and employ the method to compare simulations of binary black hole mergers with gravitational waveform models. The EFE in Eq. (2.21) are very complicated and comprise ten coupled, non-linear, second-order partial differential equations in a four dimensional spacetime. For this reason, closed-form analytical solutions, including for example the Schwarzschild [137], Kerr [138], Kerr-Newmann [139], Tolman–Oppenheimer–Volkoff [194] or the Friedmann-Lemaître-Robertson-Walker solutions [143, 195], are only known for highly symmetric systems, such as those with spherical or axial symmetry, static or stationary configurations, homogeneous or isotropic structures. However, when investigating realistic astrophysical scenarios involving strong and dynamical gravitational fields with minimal or no symmetry, exact solutions to the Einstein field equations are unattainable. The EFE can be solved numerically within the framework of NR which will be discussed in Sec. 3.2. The numerical evolution of black hole systems solves the complete EFE without approximations, resulting in highly accurate and reliable gravitational waveforms, provided that sufficient resolution is used and numerical errors are well controlled. However, these simulations are highly computationally demanding. The first analytical approach that tried to solve the two-body problem in GR was PN theory [196], that we have discussed in Sec. 2.3.4. As mentioned, the PN approximation is a perturbative approach that finds approximate solutions to the EFE as an expansion in terms of v/c. Despite the PN expansion being very accurate in the weak field regime, and therefore valid for the inspiral phase of the coalescence, it breaks down in the strong field regime, where the gravitational field is strong and the velocities are relativistic. A complementary approach is the PM approximation [196] which, as mentioned in Sec. 2.3.4, is an expansion in powers of G and is valid in the weak field regime, without assuming small velocities. This framework is particularly well-suited for describing unbound orbits

and has experienced significant development in recent years [197–201]. Similarly to the PN expansion, the PM expansion also becomes unrealiable when the gravitational field is strong. The PN expansion is valid in the near zone while the PM expansion can be used in the far zone where we want to compute the waveforms. These approaches are therefore complementary and a multipolar PM expansion (MPM) can be matched with PN results in an intermediate region. This enables a complete description of the waveform within the weak-field approximation and for arbitrarily high velocities, covering both bound and unbound systems. The phases of the coalescence of a binary system can be therefore studied using different techniques. As discussed, the PN and PM approximations are useful to describe the inspiral phase, while the merger phase requires the use of NR simulations. Approximate solutions in the strong field regime can be derived using Wordline Effective Field Theory (WEFT) [202–206], Quantum Field Theory (QFT) [207–210] or Wordline Quantum Field Theory (WQFT) [211–213] techniques. Nonetheless, these computations are technically highly demanding and only a limited number of higher-order results have been achieved to date. Other perturbative techniques involve the gravitational self-force approach (GSF) [214], where the expansion is carried out in terms of the mass ratio of the binary [215, 216]. This method is reliable for binaries with intermediate and extreme mass ratios, where one black hole is significantly more massive than the other. This area of research has made considerable progresses over the past several years, especially in the study of EMRIs, with computations now extended to second order in the mass ratio [217, 218]. The ringdown stage of the coalescence can be studied with black hole perturbation theory. This perturbative method provides a way to calculate the quasi normal modes associated with the remnant black hole, whose oscillations depend on the black hole's final parameters and their amplitudes [219, 220]. One of the most promising approaches towards modelling the full gravitational wave signal emitted by compact binaries is the effective-one-body framework (EOB) [107–110]. The EOB framework is a semi-analytical

approach that blends both analytical and numerical techniques to model the waveforms and dynamics of binary systems. It efficiently incorporates PN results using specific resummation techniques. Additionally, EOB models can be enhanced by integrating PM and GSF results and they are calibrated against NR simulations to ensure accuracy in the strong-field regime. Finally, these models are completed with a ringdown waveform, making them suitable for modelling the full gravitational wave signal. The EOB approach is discussed in details in Sec. 3.3. Two of the most developed families among the existing EOB models are `TEOBResumS` [126, 130, 131] and `SEOBNR` [221–224]. NR surrogate models, including eccentric NR surrogates, are developed by numerically interpolating available numerical data [102, 103, 225, 226]. Finally, inspiral-merger-ringdown (IMR) phenomenological models [227–234] are a class of waveform models designed to be computationally efficient, making them suitable for data analysis, where a large number of waveforms must to be generated for a comprehensive Bayesian analysis. These models have been developed both in the frequency and time domain and employ PN approximants with the addition of free parameters that are fitted to NR simulations [235–239], EOB models and test mass data in the merger regime. All of these waveform models can incorporate precession, see for example [223, 224, 229, 240–246], and noncircularised dynamics [114–125]. Recently, a new inspiral model has been developed that incorporates both eccentricity and spin precession effects [38]. An overview of waveform models that include eccentricity was already provided in Chapter 1 and will not be repeated here. In this thesis, we focus on improving `TEOBResumS-Dalí` [115–117, 126–128] for coalescing binaries along generic orbits and compare it with a set of NR simulations of eccentric binary black hole mergers that we carried out by employing the open source code `Einstein Toolkit` [247, 248]. In Sec. 3.2 we introduce key concepts in NR and Sec. 3.3 we give an overview of the EOB framework.

3.2 Numerical Relativity

Key contributions in NR include Yvonne Choquet-Bruhat's formulation of the initial value problem in 1952 [249] and the development of the Arnowitt-Deser-Misner (ADM) formalism in 1962 [250]. Breakthroughs in NR occurred with the first successful full numerical simulations of binary black hole mergers. In 2005 Pretorius [251] presented an inspiral-merger-ringdown evolution based on a generalization of harmonic coordinates where the black hole singularity is completely removed via black hole excision. Shortly after, Campanelli et al. achieved the same result by employing the Baumgarte-Shapiro-Shibata-Nakamura (BSSN) formulation of the Einstein filed equations alongside the moving punctures method [252]. The Einstein field equations admit several reformulations and a variety of methods have been proposed to define initial conditions and evolution of the gravitational field. The so called *3+1 decomposition* of spacetime is a very common approach which splits the spacetime into a three-dimensional space and time reformulating the EFE as an *initial value problem*. In the 3+1 decomposition the four-dimensional spacetime is foliated into a series of three-dimensional spacelike hypersurfaces identified by a *universal time function* [184]. Alternative approaches include the *characteristic formalism* and the *conformal formalism* which are discussed for example in [184, 185].

3.2.1 3+1 decomposition of spacetime

In the 3+1 decomposition of spacetime, the dynamics of a physical system is recast as an *inital value* or *Cauchy* problem which allows a reformulation of the EFE as a well-posed system of partial differential equations (PDE) [184]. This framework requires that, given appropriate initial data, the equations determine both the future and past evolution of the system [185]. A spacetime $(\mathcal{M}, g_{\mu\nu})$ where $g_{\mu\nu}$ is a metric on the manifold $\mathcal{M}$, is called *globally hyperbolic* if it admits a Cauchy surface Σ such that all points on the surface

happen simultaneously or in other words, each causal (meaning timelike or null) curve intersects Σ only once. A globally hyperbolic spacetime can then be foliated into a family of 3-dimensional spacelike hypersurfaces Σ_t, each associated with a smooth scalar field t on $\mathcal{M}$ which is regular and therefore it has a non-vanishing gradient. We can then write

$$\mathcal{M} = \bigcup_{t\epsilon\mathbb{R}} \Sigma_t. \tag{3.1}$$

This foliation of spacetime is also called *synchronization* and each Σ_t is called *slice* of the foliation. We can define a *lapse* function α [134, 185]

$$\alpha = (-\nabla t \cdot \nabla t)^{-1/2}, \; n^\mu = -\alpha \nabla^\mu t \tag{3.2}$$

where n^μ is the normal vector to the hypersurface Σ_t. With the normal vector n^μ we can also define the spatial 3-dimensional metric $\gamma_{\mu\nu}$[2] induced by $g_{\mu\nu}$ on the 3-dimensional hypersurfaces Σ_t

$$\gamma_{\mu\nu} = g_{\mu\nu} + n_\mu n_\nu \tag{3.3}$$

which is a projection tensor with the role of projecting out all objects along n^μ and intuitively serves to measure distances within the hypersurfaces. When considering the foliation of spacetime we need to distinguish between *intrinsic* and *extrinsic* curvature. The intrinsic curvature is given by the 3-dimensional Riemann tensor written in terms of $\gamma_{\mu\nu}$. The extrinsic curvature describes how hypersurfaces are embedded in the 4-dimensional spacetime or, in other words, measures the change in direction of n^μ under parallel transport along the hypersurface Σ_t. We can define a projection operator $P^\alpha_\beta =$

[2]Where $\gamma_{\mu\nu}$ is 4-dimensional. The time component will vanish when choosing adapted coordinates as discussed afterwards.

$\delta^\alpha_\beta + n^\alpha n_\beta$ and utilising it to define an extrinsic curvature tensor $K_{\mu\nu}$

$$K_{\mu\nu} = -P^\alpha_\mu \Delta_\alpha n_\nu. \tag{3.4}$$

Using some algebra it is possible to show that

$$K_{\mu\nu} = -\frac{1}{2}\mathcal{L}_n \gamma_{\mu\nu} \tag{3.5}$$

where $\mathcal{L}_n$ is the Lie derivative by the normal vector n^μ. Intuitively this means that the vector $\delta t\, n^\mu$ carries the hypersurface Σ_t into the neighboring hypersurface $\Sigma_{t+\delta t}$ [185].

3.2.2 Constraint and evolution equations

The metric $\gamma_{\mu\nu}$ and the extrinsic curvature $K_{\mu\nu}$ can not be chosen arbitrarily. We need to relate the 4-dimensional Riemann tensor defined on the manifold $\mathcal{M}$ and the 3-dimensional one defined on Σ_t. By performing a complete spatial projection of the 4-dimensional Riemann tensor $\gamma^\mu_\alpha \gamma^\nu_\beta \gamma^\rho_\gamma \gamma^\sigma_\delta \, {}^{(4)}R_{\mu\nu\rho\sigma}$ and a 3+1-normal projection $\gamma^\mu_\alpha \gamma^\nu_\beta \gamma^\rho_\gamma n^\sigma \, {}^{(4)}R_{\mu\nu\rho\sigma}$ it is possible to find the so called *Gauss-Codazzi* relations that can be employed on the $n^\mu n^\nu$ contraction of the EFE to find the *Hamiltonian* and *momentum constraints* [184]. The constraint equations take the form

$$\begin{aligned} R + K^2 - K_{\alpha\beta}K^{\alpha\beta} &= 16\pi\rho, \\ D_\alpha K^\alpha_\mu - D_\mu K &= 8\pi j_\mu \end{aligned} \tag{3.6}$$

where D_α is the covariant derivative associated to the 3-metric $\gamma_{\mu\nu}$ and $\rho = n^\mu n^\nu T_{\mu\nu}$, $j_\mu = -\gamma^\alpha_\mu n^\beta T_{\alpha\beta}$ are respectively the total energy and momentum density measured by a normal observer. The constraint equations only involve $\gamma_{\mu\nu}$, $K_{\mu\nu}$ and their spatial derivatives. They represent four of the ten independent EFE and must be satisfied at all times on

Σ_t. Their existences implies that the 12 dynamical quantities $\gamma_{\mu\nu}, K_{\mu\nu}$ cannot be specified arbitrarily. The constraint equations can be transformed into a system of partial differential equations by introducing coordinates on the manifold $\mathcal{M}$. We can choose coordinates *adapted* to the foliation $x^\mu = (t, x^i)$ with $i = 1, 2, 3$ such that the spatial coordinates x^i on Σ_t vary smoothly between neighboring hypersurfaces and define a *shift* function β^μ so that $\beta_\mu n^\mu = 0$ (β^μ is tangent to Σ_t) and

$$(\partial t)^\mu = \alpha n^\mu + \beta^\mu. \tag{3.7}$$

The metric of the spacetime can be expressed in adapted coordinates as a function of $\alpha, \beta^\mu, \gamma_{ij}$ in the following way

$$ds^2 = (-\alpha^2 + \beta_i\beta^i)dt^2 + 2\beta_i dt dx^i + \gamma_{ij}dx^i dx^j \tag{3.8}$$

and the normal vector in adapted coordinates takes the form $n^\mu = (1/\alpha, -1/\alpha\beta^i)$, $n_\mu = (-\alpha, 0, 0, 0)$. The constraint equations contain no time derivatives and are entirely independent of the gauge functions α and β^i. This highlights that the constraints are relations referring solely to a given hypersurface. The lapse and the shift can be freely specified and encode information about the coordinate system used. As a result, the foliation of the spacetime is not unique. By using adapted coordinates we have that the Lie derivative along $(\partial t)^\mu$ reduces to the partial derivative with respect to t and we obtain the evolution equations

$$\begin{aligned} &\partial_t\gamma_{ij} = -2\alpha K_{ij} + D_i\beta_j + D_j\beta_i, \\ &\partial_t K_{ij} = -D_iD_j\alpha + \alpha\left(R_{ij} + KK_{ij} - 2K_{ik}K^k_j + 4\pi\left[\,(S-\rho)\gamma_{ij} - 2S_{ij}\,\right]\right) \\ &+ \beta^k D_k K_{ij} + K_{ik}D_j\beta^k + K_{kj}D_i\beta^k. \end{aligned} \tag{3.9}$$

These are known as ADM equations written in York form [253]. These equations are mathematically well posed, in contrast to the original ADM formulation. It is important to note that the 3+1 evolution equations are not unique. It is indeed possible to add arbitrary multiples of the constraint equations to derive alternative forms of the evolution equations. Even in the York formulation, the ADM equations are only weakly hyperbolic, which results in insufficient stability for long-term evolutions. An alternative formulation of the ADM equations that enhances stability and yields a strongly hyperbolic system of evolution equations has been presented by Baumgarte, Shapiro, Shibata and Nakamura [254, 255]. Their formulation, known as the BSSN formulation, is based on a conformal transformation of the spatial metric defined by

$$\tilde{\gamma}_{ij} = \psi^{-4}\gamma_{ij} \tag{3.10}$$

where ψ is a conformal factor that can be conveniently chosen. We can choose $\psi = \gamma^{1/12}$ such that $\det(\tilde{\gamma}_{ij}) = 1$ and introduce the traceless extrinsic curvature A_{ij} as

$$K = \gamma^{ij}K_{ij},\ A_{ij} = K_{ij} - \frac{1}{3}\gamma_{ij}K,\ \tilde{A}_{ij} = \psi^{-4}A_{ij} = e^{-4\phi}A_{ij}. \tag{3.11}$$

We therefore have the following evolution variables

$$\phi = \ln\psi = \frac{1}{12}\ln\gamma,\ K = \gamma_{ij}K^{ij},\ \tilde{A}_{ij} = e^{-4\phi}A_{ij},\ \tilde{\gamma}_{ij} = e^{-4\phi}\gamma_{ij}. \tag{3.12}$$

A convenient choice is to use the W-variant [256] defined as

$$W = e^{-2\phi}. \tag{3.13}$$

The BSSN formulation also introduces *conformal connection functions* $\tilde{\Gamma}^i$ defined as

$$\tilde{\Gamma}^i = \tilde{\gamma}^{jk}\tilde{\Gamma}^i_{jk} = -\partial_j\tilde{\gamma}^{ij} \tag{3.14}$$

where $\tilde{\Gamma}^i_{jk}$ are the Christoffel symbols of the conformal metric and the second equality follows from $\det\tilde{\gamma} = 1$. In this formulation we have that instead of the 12 ADM variables γ_{ij} and K_{ij}, 17 variables $\phi, K, \tilde{\gamma}_{ij}, \tilde{A}_{ij}, \tilde{\Gamma}^i$ are used. The change of variable introduced above is advantageous for the following motivations. First, the conformal transformation and the separation of the trace of the extrinsic curvature are performed to gain better control over the slicing conditions which are related to the trace of K_{ij}. Second, the introduction of the conformal connection variables $\tilde{\Gamma}^i$ has a significant consequence. When treated as independent variables, the second derivatives of the conformal metric that appear in the evolution equations reduce to the simple scalar Laplace operator.

3.2.3 ADM mass and momenta

In GR the conservation of the stress-energy tensor $\nabla_\mu T^{\mu\nu} = 0$ does not imply a global conservation of energy and the reason is that $T^{\mu\nu}$ takes into account only the contribution of matter and not of the gravitational field. However, it is still possible to define the total energy of a system in a meaningful way. An approach is to consider weak gravitational fields in the region $r \to \infty$ also called *spatial infinity* i_0. The spacetime is assumed to be asymptotically flat such that on each slice Σ_t exists a background metric

$$\gamma_{ij} = f_{ij} + O(r^{-1}),\ \partial_k\gamma_{ij} = O(r^{-2}),\ K_{ij} = O(r^{-2}),\ \partial_k K_{ij} = O(r^{-3}) \tag{3.15}$$

and the coordinates (x^i) can be chosen such that they are of the Cartesian-type ($f_{ij} = \delta_{ij}$ for $r \to \infty$). We can define the total energy and angular momentum densities as

$$M = \int \rho dV, \;\; P_i = \int j_i dV \tag{3.16}$$

and using the Hamiltonian and momentum constraints it is possible to define the ADM mass and momentum as integrals on the boundary of the hypersurface $\partial\Sigma_t = \partial\mathcal{M} \cap \Sigma_t$ [1]

$$M^{\mathrm{ADM}} = -\frac{1}{2\pi} \lim_{r\to\infty} \oint_{\partial\Sigma_t} \left(\bar{\mathcal{D}}^j \gamma_{ij} - \bar{\mathcal{D}}_i (f^{kl}\gamma_{kl})\right) s^i \sqrt{q}, \tag{3.17}$$

$$P_i^{\mathrm{ADM}} = \frac{1}{8\pi} \lim_{r\to\infty} \oint_{\partial\Sigma_t} \left(K_{jk} - K\gamma_{jk}\right) (\partial_i)^j s^k \sqrt{q} \tag{3.18}$$

where $\bar{\mathcal{D}}^j$ is the covariant derivative associated to the metric f^{ij}, s^i is the unit outward-pointing normal vector to the surface $\partial\Sigma_t$, q is the determinant of the induced metric on $\partial\Sigma_t$. Using the same procedure is also possible to define an ADM total angular momentum angular momentum with the invariance of the action under rotations.

$$J_i^{\mathrm{ADM}} = \frac{1}{8\pi} \lim_{r\to\infty} \oint_{\partial\Sigma_t} \left(K_{jk} - K\gamma_{jk}\right) (\phi_i)^j s^k \sqrt{q} \tag{3.19}$$

where (ϕ_i) are the Killing vectors [2] of f^{ij} associated with rotations with respect the cartesian axes. An important property of the ADM mass and momentum is the fact that since they are defined at spatial infinity i_0 while the gravitational waves taking energy and angular momentum away will reach null infinity $\mathscr{I}^+$, the ADM mass and angular

[1] In Eq. (3.17) we have set $\alpha = 0$ and $\beta^i = 0$ while in Eq. (3.18) we have set $\alpha = 0$ and $\beta^i = (\partial_j)^i$ with $(\partial_i)_{i\in\{1,2,3\}}$. The ADM mass is associated with time translations at infinity, the linear momentum with the invariance of the action under time translations and the angular momentum with the invariance of the action under rotations.

[2] A Killing vector is defined as the vector vector field ξ which, given a metric $g_{\mu\nu}$ satisfies the equation $\xi^\mu \partial_\mu g_{\alpha\beta} + g_{\mu\alpha}\partial_\beta \xi^\mu + g_{\mu\beta}\partial_\alpha \xi^\mu = 0$. The existence of a Killing field implies a symmetry of the manifold. If the coordinate x^1 is adapted to the integral curves of ξ the equation above becomes $\partial_1 g_{\alpha\beta} = 0$ and the components of the metric tensor are independent of the coordinate x^1.

mometum stay constant during the evolution.

3.2.4 Black holes initial data

In order to find suitable initial data, we have to solve the constraint equations which constitute a system of elliptic partial differential equations that must be satisfied at all times for every hypersurface Σ_t. The 12 independent components of γ_{ij}, K_{ij} cannot be freely chosen as initial data because they have to satisfy the constraint equations. There is no natural way to identify which components represent the true dynamical components and which ones must satisfy the constraint equations. Among these 12 components, 4 are associated with choordinate choices or *gauge* freedom, 4 represent the true dynamical degrees of freedom, and the remaining 4 must satisfy the constraint equations. There are several ways of solving constraint equations, but in this thesis we focus on the Bowen-York initial data [257]. The first step is to specify conformally and asymptotically flat initial data on the initial time slice Σ_0 such that

$$K = 0, \tag{3.20}$$

$$\tilde{\gamma}_{ij} = \eta_{ij}. \tag{3.21}$$

The first condition is called *maximal slicing* and implies that they hypersurface Σ_t has maximum volume. It is possible to write the constraint equations in terms of the conformal factor ψ and a vector potential $\mathbf{V}$ that is a function of the linear and angular momenta of the *puntures* and contains a finite number of poles at the location of the latters. The punctures are defined as the asymptotically flat ends of the black holes which are compactified and identified with the points r_i in $\Re^3$ that are called *punctures*. This topology enforces the presence of Einstein–Rosen bridges or *throats*. Ref. [258] has pointed out that a specific solution of the Hamiltonian constraint is possible for the extrinsic curva-

ture such that the conformal factor is written as a sum of a singular piece and a finite correction u,

$$\psi = \psi_{\rm BL} + u, \quad \psi_{\rm BL} = 1 + \sum_{i=1}^{N} \frac{m_i}{2r_i} \tag{3.22}$$

with $u \to 0$ for $r_i = |\mathbf{r} - \mathbf{r}_i| \to 0$ and $\psi_{\rm BL}$ known as the Brill-Lindquist conformal factor [258, 259]. The parameters m_i are the *bare masses* of each black hole and in terms of ADM mass we have $M_{\rm ADM} = \sum_i m_i$. In the case of a single black hole the bare mass corresponds to the individual mass of the black hole, while in the case of multiple black holes the situation is more complicated. A possible definition of mass is obtained by computing the ADM mass at the punctures. In this case the ADM mass of each black hole can be written as

$$M_i = m_i \left(1 + u_i \sum_{i \neq j} \frac{m_i}{2r_{ij}} \right). \tag{3.23}$$

An alternative method for defining the mass of each black hole involves locating the individual apparent horizons and applying the Schwarzschild relation between mass and horizon area

$$M_i^2 = \frac{A_{H,i}}{16\pi} + \frac{4\pi S_{H,i}^2}{A_{H,i}} \tag{3.24}$$

where $A_{H,i}$ is the apparent horizon area for a sphere of radius $r = 2M_{AH,i}$ and $S_{H,i}$ is the angular momentum of the sphere at the horizon. Eq. (3.24) is known as Christodoulou formula [260]. After specifying linear and angular momenta $(\mathbf{P}_i, \mathbf{S}_i)$ the Hamiltonian constraint can be solved using spectral methods [261]. In the puncture method, also known as *moving punctures* [258] the conformal factor is evolved and contains a constant logarithmic singularity. The key point of this approach is that all evolved variables remain sufficiently

regular at the punctures during the evolution. Because the method assumes conformal flatness while binary black hole spacetimes are not truly conformally flat, the simulation begins with an unphysical burst of gravitational radiation known as *junk radiation*.

3.2.5 Gauge conditions

In order to solve the evolution equations we need to fix a gauge by specifying the lapse function α and the shift vector β^i. A straightforward choice is the so called *geodesic slicing* corresponding to $\alpha = 1$ and $\beta^i = 0$. However, a major drawback of the geodesic slicing is that it does not avoid the singularity, causing the simulation to crash after short time. A condition that avoids the singularity is the *maximal slicing*. By employing maximal slicing condition the lapse experience an exponential *collapse* when approaching the singularity. The collapse of the lapse is used as an indicator that a black hole has formed through gravitational collapse. However, the maximal slicing condition does not solve the problem of the distortion and stretching of the spatial slices. The rapid growth of the radial metric components leads to the development of large gradients, causing numerical codes to eventually crash. In addition, maximal slicing is very expensive since it requires to solve elliptic equations in three dimensions. In 1994 Bona et al. [262] generalised the *harmonic slicing condition* for which the lapse has to satisfy

$$\frac{d}{dt}\alpha = -\alpha^2 f(\alpha) K \tag{3.25}$$

with $f(\alpha)$ positive arbitrary function of α. The solution $f = 2/\alpha$ corresponding to $\alpha = 1 + \log\gamma$ [263] has been found to be particularly robust and well behaved. We also need to choose the shift vector such that the coordinates are only minimally distorted.

The *hyperbolic Gamma driver condition* suggested by Alcubierre et al. [264]

$$\partial_t \beta^i = \frac{3}{4} B^i, \partial_t B^i = \partial_t \bar{\Gamma}^i - \eta B^i \tag{3.26}$$

provides a shift condition that controls the coordinate distortion. In NR codes, the 1+log slicing and the hyperbolic Gamma driver conditions are typical choices to evolve binary black hole spacetimes using the puncture method.

3.3 Effective-one-body approach

The effective-one-body (EOB) formalism was first introduced in 1999 by Buonanno and Damour [107–110] and is built upon a canonical transformation that recasts the 2PN Lagrangian originally formulated in harmonic coordinates $L^{\rm harm}(\boldsymbol{z}, \boldsymbol{v}, \boldsymbol{a})$ where $(\boldsymbol{z}, \boldsymbol{v}, \boldsymbol{a})$ are the harmonic coordinates, velocities and accelerations, into a Lagrangian $L^{\rm ADM}(\boldsymbol{q}, \dot{\boldsymbol{q}})$ in ADM coordinates $\boldsymbol{q}$ [250] that does not contain any acceleration dependence. A detailed derivation of this transformation can be found in [265]. A Legendre transformation is then applied to derive the corresponding Hamiltonian $H^{\rm ADM}(\boldsymbol{q}, \dot{\boldsymbol{q}})$ [265–267] (the esplicit expression for this Hamiltonian can be found in [265]). The Hamiltonian is then expressed in the *reduced center of mass frame* [107] by defining the coordinates

$$\boldsymbol{q} \equiv \frac{\boldsymbol{Q}}{GM}, \ \boldsymbol{p} \equiv \frac{\boldsymbol{P}}{\mu}, \tag{3.27}$$

$$\hat{t} \equiv \frac{t}{GM}, \hat{H} = \frac{H^{\rm NR}}{\mu} \equiv \frac{H^{\rm R} - Mc^2}{\mu} \tag{3.28}$$

where $\boldsymbol{Q} = \boldsymbol{q}_1 - \boldsymbol{q}_2$, $\boldsymbol{P}$ is the canonical momentum associated to $\boldsymbol{Q}$, $M = m_1 + m_2$ is the total mass of the system, $\mu = m_1 m_2 / M$ is the reduced mass and the superscripts NR and R mean respectively *non-relativistic* and *relativistic*. Starting from the 2PN Hamiltonian

in ADM coordinates

$$\widehat{H}(\boldsymbol{q},\boldsymbol{p}) = \widehat{H}_0(\boldsymbol{q},\boldsymbol{p}) + \frac{1}{c^2}\widehat{H}_2(\boldsymbol{q},\boldsymbol{p}) + \frac{1}{c^4}\widehat{H}_4(\boldsymbol{q},\boldsymbol{p}), \tag{3.29}$$

(where $\widehat{H}_0(\boldsymbol{q},\boldsymbol{p})$, $\widehat{H}_2(\boldsymbol{q},\boldsymbol{p})$, $\widehat{H}_4(\boldsymbol{q},\boldsymbol{p})$ can be found in [107]), it is possible to solve the Hamilton-Jacobi equation for the action S

$$\frac{\partial S}{\partial t} + H\left(q_i, \frac{\partial S}{\partial q_i}\right) = 0 \tag{3.30}$$

and use the fact that the Hamiltonian is invariant under time translations and rotations and that the non-relativistic energy $\hat{E}^{\mathrm{NR}}$ and the angular momentum $\boldsymbol{j}$ defined as

$$\widehat{H}(\boldsymbol{q},\boldsymbol{p}) = \hat{E}^{\mathrm{NR}}, \tag{3.31}$$

$$\boldsymbol{q}\times\boldsymbol{p} = \boldsymbol{j} \equiv \frac{\mathcal{J}}{G\mu M} \tag{3.32}$$

are conserved, to find an expression for $\hat{E}^{\mathrm{NR}} = \mathcal{E}(\mathcal{N},\mathcal{J})$ as a function of the rescaled angular momentum $\mathcal{J}$ and $\mathcal{N} = I_R + \mathcal{J}$ where I_R is the radial action of the system. This classical problem can be reinterpreted from a quantum perspective by treating it as a Coulomb problem where $\mathcal{J}$ and $\mathcal{N}$ are quantised in units of $\hbar$, taking the form $\mathcal{J}/\hbar$ and $\mathcal{N}/\hbar$ respectively. It is possible to build an energy map [107] that recasts the motion of the two masses m_1 and m_2 orbiting around their center-of-mass into the motion of a test particle of mass μ moving in an effective external metric that is a symmetric deformation of the Schwarzschild (for non-spinning bodies) or Kerr (for spinning bodies) metric. The deformation parameter is the symmetric mass ratio $\nu = \mu/M$. In order to build the EOB map we can start from the action of a test particle

$$S_{\mathrm{EOB}} = -\mu c \int ds_{\mathrm{eff}} \tag{3.33}$$

where for a static and spherically symmetric metric with effective coordinates $x^{\mu}_{\rm eff} = (t, R, \theta, \phi)$ we have

$$ds^2_{\rm eff} = g^{\rm eff}_{\mu\nu} dx^{\mu}_{\rm eff} dx^{\nu}_{\rm eff} = -A(R)c^2 dt^2 + \frac{B(R)}{A(R)} dR^2 + R^2(d\theta^2 + \sin^2\theta d\varphi^2). \tag{3.34}$$

The functions $A(R)$ and $B(R)$ need to be determined so that the dynamics of the test particle moving along the geodesics of the effective metric is equivalent to the dynamics of the real two-body problem. They take the generic form

$$A(R) = 1 + \frac{a_1}{c^2 R} + \frac{a_2}{c^4 R^2} + \frac{a_3}{c^6 R^3} + O\left(\frac{1}{R^4}\right), \tag{3.35}$$

$$B(R) = 1 + \frac{b_1}{c^2 R} + \frac{b_2}{c^4 R^2} + O\left(\frac{1}{R^3}\right) \tag{3.36}$$

The coefficient a_1 determines the dynamics of the particle at 0PN, a_2 and b_1 enter at 1PN, a_3 and b_2 enter at 2PN and so on with the addition of higher-order coefficients. Requiring that the Schwarzschild metric is recovered at lowest order immediately fixes a_1 to be -2. Buonanno and Damour employed the Hamilton-Jacobi equations for a test particle of mass μ with coordinates $x^{\mu}_{\rm eff}$ and moving in an effective metric $g^{\rm eff}_{\mu}$

$$g^{\mu\nu}_{\rm eff} \frac{\partial S}{\partial x^{\mu}_{\rm eff}} \frac{\partial S}{\partial x^{\nu}_{\rm eff}} + \mu^2 c^2 = 0 \tag{3.37}$$

and found an expression for the non relativistic energy $\mathcal{E}_0(\mathcal{N}_0, \mathcal{J}_0)$ of an effective system as a function of $\mathcal{N} = \mathcal{N}_0$ and $\mathcal{J} = \mathcal{J}_0$. Requiring that at 2PN the motion of the two-body problem with masses m_1, m_2 and described by an energy $\mathcal{E}(\mathcal{N}, \mathcal{J})$ can be mapped into the one of an effective one body problem with energy $\mathcal{E}_0(\mathcal{N}_0, \mathcal{J}_0)$ for a particle of mass μ satisfying Eq. (3.37) determines the metric coefficients to take the form

$$A(R) = 1 - \frac{2GM}{c^2 R} + 2\nu \left(\frac{GM}{c^2 R}\right)^3, \tag{3.38}$$

$$B(R) = 1 + \frac{2GM}{c^2 R} + (4 - 6\nu)\left(\frac{GM}{c^2 R}\right)^2 . \tag{3.39}$$

The energy map between the real two body problem and the effective one found by Buonanno and Damour [107] is given by

$$\frac{\mathcal{E}_{\rm eff}}{\mu c^2} = \frac{\mathcal{E}_{\rm real}^2 - m_1^2 c^4 - m_2^2 c^4}{2 m_1 m_2 c^4} \tag{3.40}$$

where the energy of the real problem is $\mathcal{E}_{\rm real} \equiv \mathcal{E}(\mathcal{N}, \mathcal{J})$ and the energy of the effective one is $\mathcal{E}_{\rm eff}$. This mapping simplifies the complex 2PN dynamics of the two-body system to a simple result. By employing this map the EOB Hamiltonian of the real two-body system can be written in terms of the effective Hamiltonian $H_{\rm eff}$ as

$$\hat{H}_{\rm EOB} \equiv \frac{H_{\rm EOB}}{\mu} = \frac{1}{\nu}\sqrt{1 + 2\nu\left(\hat{H}_{\rm eff} - 1\right)} \tag{3.41}$$

where $\hat{H}_{\rm eff} = H_{\rm eff}/\mu$. It has been shown [197] that this map is valid also at higher PN orders and for spinning binaries. At higher PN orders however, the action must be modified by including additional higher-order terms to ensure the energy mapping Eq. (3.41) remains valid. The action can then be written as

$$S_{\rm EOB} = -\mu c \int ds_{\rm eff}\left[1 + Q_{\mu\nu\rho\sigma} u^\mu u^\nu u^\rho u^\sigma\right], \tag{3.42}$$

where $u^\mu = dx^\mu/ds_{\rm eff}$ and $Q_{\mu\nu\rho\sigma} u^\mu u^\nu u^\rho u^\sigma$ is a non-geodesic term introduced to ensure that the energy map in Eq. (3.41) remains valid at PN orders higher than 2PN. In this regime, the motion is no longer geodesic and the mass-shell condition in Eq. (3.37) is modified by introducing a function Q that depends on the coordinates x^μ and the momenta

$p_\mu^{\rm eff} = \partial S/\partial x_{\rm eff}^\mu$ to keep the mapping valid. We therefore have that Eq. (3.37) becomes

$$g_{\rm eff}^{\mu\nu}\frac{\partial S}{\partial x_{\rm eff}^\mu}\frac{\partial S}{\partial x_{\rm eff}^\nu} + \mu^2 c^2 + \mu^2 Q = 0. \tag{3.43}$$

The EOB motion is described by a conservative Hamiltonian and a radiation reaction force accounting for energy losses due to the emission of gravitational waves. The EOB Hamiltonian is a deformation of the Hamiltonian of a test particle in a Schwarzschild or, for the spinning case, Kerr background. The ν dependent corrections appear in the functions $A(r,\nu)$ and $B(r,\nu)$ as well as the non geodesic term $Q(r,\nu,p_r)$ and make the potential more repulsive than the Schwarzschild case. The system therefore plunges at higher frequencies with respect the test particle limit. The dynamics of the system can be evaluated by solving the Hamilton's equations

$$\begin{aligned}
\dot{\varphi} &= \Omega = \frac{\partial \hat{H}_{\rm EOB}}{\partial p_\varphi}, \\
\dot{r} &= \sqrt{\frac{A}{B}}\frac{\partial \hat{H}_{\rm EOB}}{\partial p_{r*}}, \\
\dot{p}_\varphi &= \hat{\mathcal{F}}_\varphi, \\
\dot{p}_{r_*} &= \sqrt{\frac{A}{B}}\left(-\frac{\partial \hat{H}_{\rm EOB}}{\partial r} + \hat{\mathcal{F}}_r\right)
\end{aligned} \tag{3.44}$$

where the phase-space coordinates are defined as $t = T_{\rm eff}/M, r = R_{\rm eff}/M, p_r = P_{R,\rm eff}/\mu, p_\varphi = P_{\varphi,\rm eff}/(\mu M)$, and $p_{r_*} = (A/B)^{1/2} p_r$, (A,B) are the EOB metric potentials, Ω is the orbital frequency and $\hat{\mathcal{F}}_{\varphi,r} = \mathcal{F}_{\varphi,r}/\nu$ the angular and radial components of the radiation reaction forces. The ODE system described above by Eq. (3.44) is computed by using a standard numerical solver. Particular resummation techiniques are used to resum the metric potentials A, B, Q, the radiation reaction forces and the waveform to extend their reliability in the strong-field regime. Finally EOB models are calibrated in the strong-field regime against NR simulations and test mass data, and completed with a prescription for the

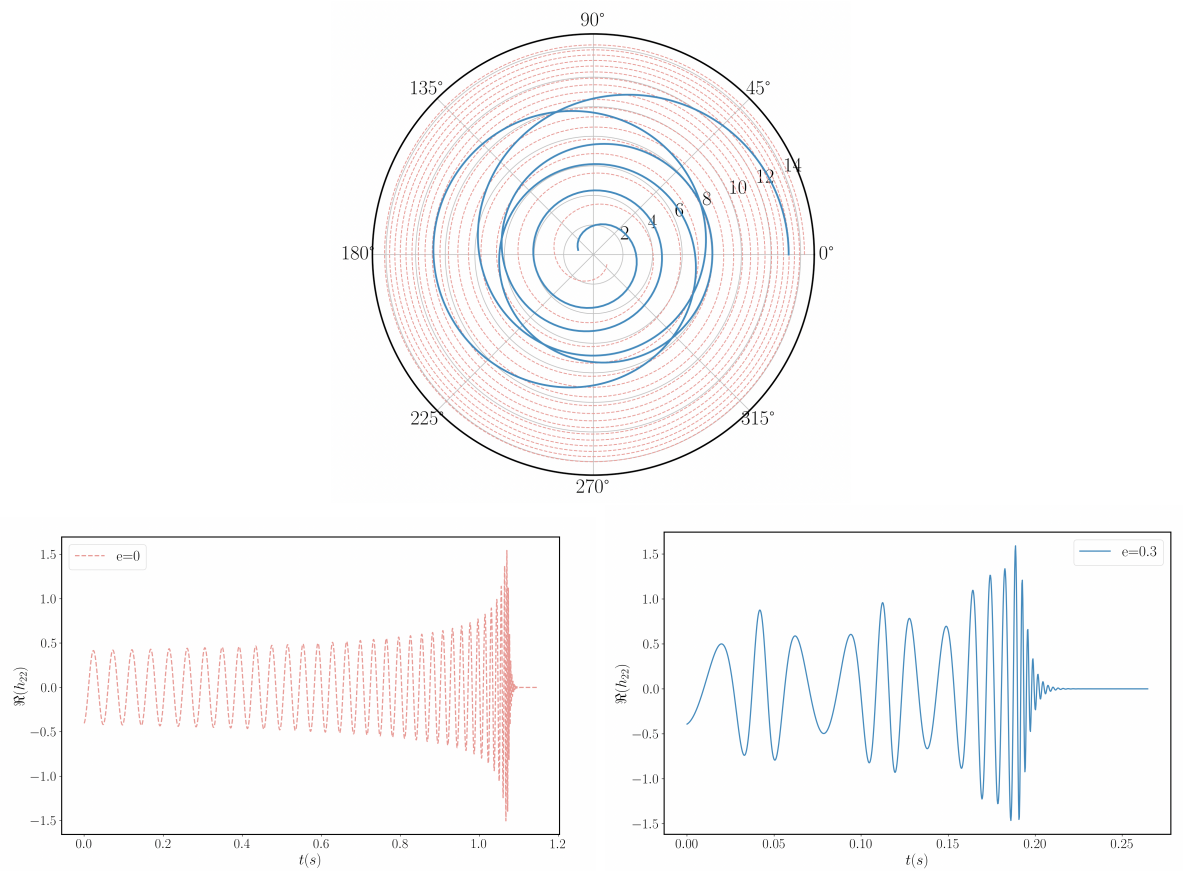


Figure 3.1: Orbits and real part of h_{22} for a circular (pink) and an eccentric (blue) system of aligned-spin binary black holes with initial eccentricities $e = 0$ and $e = 0.3$ starting at the same initial frequency $f_0 = 20$ Hz.

ringdown phase. EOB models are usually referred to as semi-analytical models. In the following sections we will describe the main building blocks of the EOB formalism which are (i) an Hamiltonian describing the conservative part of the system, (ii) a radiation reaction force accounting for the back reaction onto the system due to gravitational losses of energy and angular momentum and (iii) a prescription for the waveform. In this thesis we focus on `TEOBResumS` gravitational waveform model coalescing binaries [126, 130, 131], in particular our work is dedicated to improving the eccentric extension `TEOBResumS-Dalí` [115, 116]. Fig. 3.1 illustrates the orbits and the real part of the h_{22} mode for a circular and an eccentric system of aligned-spin binary black holes computed with `TEOBResumS-Dalí`.

3.3.1 Conservative dynamics

The conservative sector of the EOB dynamics is described by the effective Hamiltonian $H_{\rm eff}$. The most important functions entering the Hamiltonian are the potentials A, B and Q which characterise the attraction between the bodies. These potentials represent a deformation of the Schwarzschild or Kerr metrics and depend on the simmetric mass ratio ν. Spin-orbit and spin-spin couplings are incorporated in the EOB Hamiltonian. We consider a system with masses $m_1 > m_2$ and spins $S_{i=1,2}$. We also defined the following quantities: $\chi_i \equiv S_i/m_i^2$, $\tilde{a}_i \equiv S_i/(m_i M)$, $\tilde{a}_0 \equiv \tilde{a}_1 + \tilde{a}_2$. The general effective Hamiltonian for a spinning system takes the form

$$\hat{H}_{\rm eff} = \frac{H_{\rm eff}}{\mu} = \hat{H}_{\rm eff}^{\rm orb} + \hat{H}_{\rm eff}^{\rm SO} \tag{3.45}$$

where the orbital Hamiltonian is defined as

$$\hat{H}_{\rm eff}^{\rm orb} = \sqrt{p_{r_*}^2 + A\left(1 + p_\varphi^2 u_c^2 + Q\right)} \tag{3.46}$$

and depends on the momenta p_φ and $p_{r*} = (A/B)^{1/2} p_r$, p_{r*} being the conjugate momenta of the tortoise coordinate $r_* = \int dr (A/B)^{-1/2}$. The potentials A and $B \equiv A/D$ that enter the Hamiltonian are given by

$$A = \frac{1+2u_c}{1+2u} A_{\rm orb}\,(u_c), \tag{3.47}$$

$$D = \frac{r^2}{r_c^2} D_{\rm orb}\,(u_c) \tag{3.48}$$

where $u = r^{-1}$, $r_c = u_c^{-1}$ is the centrifugal radius and the esplicit form of the 5PN potentials $A_{\rm orb}$ and $D_{\rm orb}$ as well as the Q function can be found in [126]. The Q function is kept in its Taylor expanded form, without any resummation and only the local-in-time

part is retained. The A potential includes an unknown coefficient $a_6^c(\nu)$ which is kept as free parameter and is fitted to NR simulations. The resummation procedure for the A and D potentials is described in [188] and is based on the use of Padé approximants. The even-in-spin contributions are incorporated in the centrifugal radius r_c which is defined as [189]

$$r_c^2 = \left(r_c^{\rm LO}\right)^2 \hat{r}_c^2 = \left[r^2 + \tilde{a}_0^2\left(1+\frac{2}{r}\right)\right]\left(1+\frac{\delta a^2_{\rm NLO}}{r\left(r_c^{\rm LO}\right)^2}\right) \tag{3.49}$$

where $(r_c^{\rm LO})^2 = r^2 + \tilde{a}_0^2\left(1+\frac{2}{r}\right)$ and the next-to-leading order correction $\delta a^2_{\rm NLO} = -\frac{9}{8}\tilde{a}_0^2 - \frac{1}{8}(1-4\nu)\tilde{a}_{12} + \frac{5}{4}\tilde{a}_0\tilde{a}_{12}$ is given by [268]. The spin-orbit contribution (odd-in-spin) is given by

$$\hat{H}^{\rm SO}_{\rm eff} = \left(G_S\hat{S} + G_{S_*}\hat{S}_*\right)p_\varphi = \tilde{G}p_\varphi \tag{3.50}$$

where $S = S_1 + S_2, S_* = \frac{m_2}{m_1}S_2 + \frac{m_1}{m_2}S_2, \hat{S} \equiv S/M^2, \hat{S}_* \equiv S_*/M^2$ and G_S, G_{S_*} are the gyro-gravitomagnetic functions that enter the spin-orbit sector and are used at next-to-next-to-leading order (NNLO) with the addition of the next-to-next-to-next-to-leading order (N^{3}LO) parameter $c_3(\nu, \chi_{1,2})$ determined through NR calibration [188, 189]. The gyro-gravitomagnetic functions are chosen following Ref. [189] and fixing the Damour-Jaranowski-Schäfer gauge (DJS) [109, 269] such that they are only functions of (r, p_{r*}) and not of p_φ.

3.3.2 Inspiral waveform: circular

In general, a PN waveform is expressed as a sum of various contributions as $h_{\ell m} = 1 + h_1 x + h_{1.5}x^{3/2} + \ldots$ where $x = (M\Omega)^{2/3}$ is the PN parameter for $G = c = 1$. In contrast, the approach introduced in Ref. [187] employs a multiplicative approach where

relativistic corrections are factorised. The EOB waveform is decomposed as Eq. (2.55) where each multipolar mode is factorised with the following ansatz

$$h_{\ell m} = h^N_{\ell m} \hat{h}^{(\epsilon)}_{\ell m} \hat{h}^{\rm NQC}_{\ell m} \tag{3.51}$$

where $h^N_{\ell m}$ is the Newtonian prefactor and is computed from the derivatives of mass and current source multipoles $I^{(\ell)}_{\ell m}$ and $S^{(\ell)}_{\ell m}$ in Eq. (2.61) and Eq. (2.63). This factorisation generalises a resummation method of PN results introduced in [187, 270, 271] and is based on a multiplication of several physically motivated factors: (i) a Newtonian waveform ($h^N_{\ell m}$), (ii) a relativistic correction including various factors separately resummed that are an effective source, a term accounting for tail effects, and two terms accounting for residual tail dephasing and residual amplitude corrections ($\hat{h}^{(\epsilon)}_{\ell m}$) and (iii) a term that accounts for corrections to the EOB waveform that depend on the radial momentum and are relevant during the plunge up to merger ($\hat{h}^{\rm NQC}_{\ell m}$) [130, 270]. Explicitly, $h^N_{\ell m}$ is proportional to the ℓ-th time derivative of the mass or current multipole, depending on the parity of $\ell + m$

$$h^N_{\ell m} \propto \begin{cases} I^{(\ell)}_{\ell m} & \text{if} \quad \ell + m \text{ is even} \\ S^{(\ell)}_{\ell m} & \text{if} \quad \ell + m \text{ is odd.} \end{cases} \tag{3.52}$$

For circular orbits we have that the derivatives of the radius and orbital frequency vanish ($\dot{r} = 0, \dot{\Omega} = 0, ...$) and $\hat{h}^{(N,\epsilon)c}_{\ell m}$ is given in a closed-form by

$$\hat{h}^{(N,\epsilon)c}_{\ell m} = M\nu n^{(\epsilon)}_{\ell m} c_{\ell+\epsilon}(\nu) x^{\frac{(\ell+\epsilon)}{2}} Y^{\ell-\epsilon,-m}\left(\frac{\pi}{2}, \varphi\right), \tag{3.53}$$

where ϵ is the parity of $\ell + m$ ($\epsilon = 0$ if $\ell + m$ is even, $\epsilon = 1$ otherwise), $x = \Omega^{2/3}$ and the coefficients are given by [187]

$$
\begin{aligned}
n^{(0)}_{\ell m} &= (\mathrm{i}m)^{\ell} \frac{8\pi}{(2\ell+1)!!} \sqrt{\frac{(\ell+1)(\ell+2)}{\ell(\ell-1)}}, \\
n^{(1)}_{\ell m} &= -(\mathrm{i}m)^{\ell} \frac{16\pi \mathrm{i}}{(2\ell+1)!!} \sqrt{\frac{(2\ell+1)(\ell+2)\,(\ell^2-m^2)}{(2\ell-1)(\ell+1)\ell(\ell-1)}}, \\
c_{\ell+\epsilon} &= \left(\frac{m_2}{M}\right)^{\ell+\epsilon-1} + (-1)^{\ell+\epsilon} \left(\frac{m_1}{M}\right)^{\ell+\epsilon-1}.
\end{aligned}
\tag{3.54}
$$

The relativistic correction $\hat{h}_{\ell m}$ incorporates higher-order PN terms through a process of factorization and resummation and is explicitly expressed as product of factors

$$
\hat{h}_{\ell m} = \hat{S}_{\mathrm{eff}} T_{\ell m} e^{i\delta_{\ell m}} \left(\rho_{\ell m}\right)^{\ell}, \tag{3.55}
$$

- The $\hat{S}_{\mathrm{eff}}$ is the effective source term given by

$$
\hat{S}_{\mathrm{eff}} = \begin{cases} \hat{H}_{\mathrm{eff}}(x) & \text{if} \quad \ell + m \text{ is even} \\ \frac{p_\varphi}{r_\Omega v_\varphi} & \text{if} \quad \ell + m \text{ is odd} \end{cases} \tag{3.56}
$$

with $\hat{H}_{\mathrm{eff}}(x)$ being the effective energy and $p_\varphi/(r_\Omega v_\varphi)$ the normalized angular momentum. To enhance the behaviour of the Newtonian factor it is possible to replace x with $v_\varphi^2 = (r_\Omega \Omega)^2$ where $\Omega = \dot{\varphi}$ is the orbital frequency, v_φ is a non-Keplerian azimutal velocity and r_Ω reads explicitly as [189]

$$
r_\Omega \equiv \left\{ \frac{\left(r_c^3 \psi_c\right)^{-1/2} + \tilde{G}}{\hat{H}_{\mathrm{EOB}}} \right\}^{-2/3}_{p_{r_*}=0} \tag{3.57}
$$

$$
\psi_c = -\frac{2}{A'} \left(u_c' + \frac{\tilde{G}'}{u_c A} \sqrt{\frac{A}{p_\varphi^2 + u_c^2 A}} \right) \tag{3.58}
$$

where the prime indicates the derivative with respect to r. Eq. (3.57) is valid during the adiabatic quasi-circular inspiral such that a Kepler-like law $r_\Omega^3\Omega^2 = 1$ holds.

- The tail factor reads

$$T_{\ell m} = \frac{\Gamma(\ell + 1 - 2\mathrm{i}\hat{\hat{k}})}{\Gamma(\ell+1)} e^{\pi\hat{\hat{k}}} e^{2\mathrm{i}\hat{\hat{k}}\log(2kr_0)} \tag{3.59}$$

where $\hat{\hat{k}} = mH_{\rm EOB}\Omega, k = m\Omega, r_0 = 2M/\sqrt{e}$ and $\Gamma(z)$ is the Euler Gamma function [272] and is a resummed version of leading logarithms entering the tail effects, which arise from the backscattering of gravitational waves off the curved spacetime.

- The $\rho_{\ell m}$ are residual amplitude and phase corrections obtained in the circular limit as functions of $x = \Omega^{2/3}$ and $y = E\Omega$ where E is the energy along circular orbits. The residual phase $\delta_{\ell m}$ is accounts for fact that $T_{\ell m}$ includes only the leading-order contributions. It serves to correct the phase effects that are not captured by the complex tail factor. The residual relativistic amplitude corrections $\rho_{\ell m}$ are amplitude corrections given at certain PN order and their structure is described in [268]. The amplitude and phase corrections are resummed using Padé approximants as described in [188, 268, 273, 274].

The waveform is then completed including next-to-quasi-circular (NQC) corrections $\hat{h}^{\rm NQC}_{\ell m}$ that are NR-informed functions aimed at improving the behavior of the analytical waveform during the plunge and ensure a smooth transition to the post-merger signal. Their structure can be found in [188, 270, 275]. The complete waveform describing the full inspiral-merger-ringdown (IMR) signal is written as

$$h^{\rm IMR}_{\ell m} = \theta(t^{\rm match}_{\ell m} - t) h^{\rm insp}_{\ell m} \hat{h}^{\rm NQC}_{\ell m} + \theta(t - t^{\rm match}_{\ell m}) h^{\rm rng}_{\ell m} \tag{3.60}$$

where $\theta(t)$ is a Heaviside step function and $t^{\rm match}_{\ell m}$ is the matching time, i.e. the time where

the ringdown is attached to the inspiral-merger waveform.

3.3.3 Inspiral waveform: non-circular corrections

To extend beyond the quasi-circular regime, the standard quasi-circular Newtonian prefactor $h_{\ell m}^{(N,\epsilon)}$ is generalised to apply to generic orbits, i.e. without neglecting the time derivatives of r and Ω that vanish in the quasi-circular case. In the eccentric case, the inspiral waveform takes the form

$$h_{\ell m} = h_{\ell m}^{(N,\epsilon)_{\rm c}} \hat{h}_{\ell m}^{(N,\epsilon)_{\rm nc}} \hat{S}_{\rm eff}^{(\epsilon)} T_{\ell m} e^{i\delta_{\ell m}} \left(\rho_{\ell m}\right)^{\ell} \tag{3.61}$$

where $h_{\ell m}^{(N,\epsilon)_{\rm nc}}$ is a *non-circular* Newtonian prefactor that is obtained from the derivatives of the symmetric-trace-free mass and current multipoles in Eq. (2.65) and Eq. (2.66) [115]. In practice we have

$$\hat{h}_{\ell m}^{(N,0)_{\rm nc}} = \left(h_{\ell m}^{(N,0)_{\rm c}}\right)^{-1} I_{\ell m}^{(\ell)}, \tag{3.62}$$

$$\hat{h}_{\ell m}^{(N,1)_{\rm nc}} = \left(h_{\ell m}^{(N,1)_{\rm c}}\right)^{-1} S_{\ell m}^{(\ell)} \tag{3.63}$$

$$\tag{3.64}$$

The corrections for the $(2,2)$ and $(2,1)$ modes read

$$\begin{aligned} \hat{h}_{22}^{(N,0)_{\rm nc}} &= 1 - \frac{\ddot{r}}{2r\Omega^2} - \frac{\dot{r}^2}{2r^2\Omega^2} + \frac{2\mathrm{i}\dot{r}}{r\Omega} + \frac{\mathrm{i}\dot{\Omega}}{2\Omega^2}, \\ \hat{h}_{21}^{(N,1)_{\rm nc}} &= 1 - \frac{6\dot{r}^2}{r^2\Omega^2} - \frac{3\ddot{r}}{r\Omega^2} - \frac{6\dot{r}\dot{\Omega}}{r\Omega^3} - \frac{\ddot{\Omega}}{\Omega^3} + i\left(\frac{6\dot{r}}{r\Omega} + \frac{3\dot{\Omega}}{\Omega^2}\right) \end{aligned} \tag{3.65}$$

while corrections for the other modes can be found in [127]. In Chapter 6 we will give an explicit expression for the first, second and third derivatives of r and Ω.

3.3.4 Non-conservative dynamics

The leading order contribution to the radiation reaction forces appears at 2.5 PN. Once the radiation reaction forces $(\mathcal{F}_r, \mathcal{F}_\varphi)$ are specified, the dynamics of the system can be determined by solving the Hamilton's equations in Eq. (3.44). The requirement we impose is that the energy and angular momentum lost by the system equal the energy and angular momentum fluxes $(\dot{E}, \dot{J})$ carried away by gravitational waves. We have that the balance equations [111] are

$$\dot{r}\mathcal{F}_r + \Omega\mathcal{F}_\varphi + \Omega_H\mathcal{F}_\varphi^H + \dot{E} + \dot{E}_{\rm Schott} = 0, \tag{3.66}$$

$$\mathcal{F}_\varphi + \mathcal{F}_\varphi^H + \dot{J} = 0 \tag{3.67}$$

where $\dot{E} = \nu\dot{\hat{H}}_{\rm EOB}$ and $\dot{E}_{\rm Schott}$ represents the contribution of the Schott energy [111] which is related to the interaction of the source with the local field. The Schott term is factorized as described in [115] and it vanishes along circular orbits. The angular component of the radiation reaction includes leading order horizon flux contributions $\mathcal{F}_\varphi^H$, which is the small fraction of radiation absorbed by the black holes [189, 276, 277] while $\mathcal{F}_\varphi \equiv \mathcal{F}_\varphi^\infty$ and $\mathcal{F}_r \equiv \mathcal{F}_r^\infty$ are the angular and radial component of the radiation reaction forces. The expression for the horizon flux at leading order reads as [189]

$$\mathcal{F}_\varphi^H = -\frac{32}{5}\nu^2\Omega^5 r_\Omega^4\left(\hat{J}_1^H + \hat{J}_2^H\right) \tag{3.68}$$

with

$$\hat{J}_{1,2}^H = \frac{v_\varphi^5}{4}X_{1,2}^3\left(1+3\chi_{1,2}^2\right)\left[-\chi_{1,2} + 2\left(1+\sqrt{1-\chi_{1,2}^2}\right)X_{1,2}v_\varphi^3\right] \tag{3.69}$$

where $X_{1,2} = \frac{1}{2}(1 + \sqrt{1-4\nu})$. The expression for the Schott energy can be found in Ref. [115]. In the quasi-circular case, gravitational wave loss occurs primarily along the angular component and the radial componet of the radiation reaction $\mathcal{F}_r$ is neglected and. However, in the eccentric case, a dissipative contribution along the radial direction needs to be taken into account. The prescription for the radiation reaction forces follows [115, 116, 126, 188]. Specifically, the radiation reaction along the angular component is obtained by factorising a circular prefactor as suggested in [115]

$$\hat{\mathcal{F}}_\varphi \equiv \mathcal{F}_\varphi/\nu = -\frac{32}{5}\nu r_\Omega^4 \Omega^5 \hat{f}(x) \tag{3.70}$$

where the factor $\hat{f}(x)$ is given by

$$\hat{f}(x) = \sum_{\ell=2}^{8}\sum_{m=-\ell}^{\ell} \hat{f}_{\ell m}\hat{f}^{\rm Nnc}_{\ell m} \tag{3.71}$$

$$\hat{f}_{\ell m} = \frac{\hat{F}^{\rm Newt}_{\ell m}}{\hat{F}^{\rm Newt}_{22}}\left|\hat{h}_{\ell m}\right|^2 \tag{3.72}$$

where the $\hat{h}_{\ell m}$ are expressed as in Eq. (3.55), $\hat{F}^{\rm Newt}_{\ell m}$ is

$$\hat{F}^{\rm Newt}_{\ell m} = \frac{1}{8\pi} m^2\Omega^2 \tag{3.73}$$

and $\hat{f}^{\rm Nnc}_{\ell m}$ are non-circular Newtonian corrections obtained directly from the derivatives of the waveform multipoles using Eq. (2.65) and Eq. (2.66). The Newtonian flux is $\hat{F}^{\rm Newt}_{22} = 32/5x^5$ and by using the generalised third Kepler law $r_\Omega^3\Omega^2 = 1$ we obtain Eq. (3.70). The non-circular correction factor $\hat{f}^{\rm Nnc}_{\varphi,22}$ reads as

$$\hat{f}^{\rm N_{nc}}_{\varphi,22} = 1 + \frac{3}{4}\frac{\ddot{r}^2}{r^2\Omega^4} - \frac{\ddot{\Omega}}{4\Omega^3} + \frac{3\dot{r}\dot{\Omega}}{r\Omega^3} + \frac{4\dot{r}^2}{r^2\Omega^2} + \frac{\ddot{\Omega}\dot{r}^2}{8r^2\Omega^5} + \frac{3}{4}\frac{\dot{r}^3\dot{\Omega}}{r^3\Omega^5} + \frac{3}{4}\frac{\dot{r}^4}{r^4\Omega^4} + \frac{3}{4}\frac{\dot{\Omega}^2}{\Omega^4} \tag{3.74}$$

In this work we have incorporated an additional correction factor associated with the $(2,1)$ mode into `TEOBResumS-Dalí` which takes the form

$$\begin{aligned}\hat{f}^{\rm Nnc}_{\varphi,21} = 1 &+ \frac{72\dot{r}^4}{r^4\Omega^4} + \frac{144\dot{r}^3\dot{\Omega}}{r^3\Omega^5} + \frac{27\dot{r}^2}{r^2\Omega^4} + \frac{27\ddot{r}\dot{r}\dot{\Omega}}{r^2\Omega^5} - \frac{18r^{(3)}\dot{r}}{r^2\Omega^4} + \frac{126\dot{r}^2\dot{\Omega}^2}{r^2\Omega^6} - \frac{12\dot{r}^2\ddot{\Omega}}{r^2\Omega^5} \\ &+ \frac{30\dot{r}^2}{r^2\Omega^2} - \frac{18\ddot{r}\dot{\Omega}^2}{r\Omega^6} + \frac{21\ddot{r}\ddot{\Omega}}{r\Omega^5} - \frac{12\ddot{r}}{r\Omega^2} - \frac{9r^{(3)}\dot{\Omega}}{r\Omega^5} + \frac{18\dot{r}\dot{\Omega}^3}{r\Omega^7} + \frac{24\dot{r}\dot{\Omega}\ddot{\Omega}}{r\Omega^6} - \frac{6\dot{r}\Omega^{(3)}}{r\Omega^5} \\ &+ \frac{30\dot{r}\Omega}{r\Omega^3} + \frac{3\ddot{\Omega}\dot{\Omega}^2}{\Omega^7} + \frac{4\ddot{\Omega}^2}{\Omega^6} - \frac{3\Omega^{(3)}\dot{\Omega}}{\Omega^6} + \frac{15\dot{\Omega}^2}{\Omega^4} - \frac{5\ddot{\Omega}}{\Omega^3}.\end{aligned} \tag{3.75}$$

The various prefactors associated with higher-order modes were already computed in [127]. However, the third derivatives of the orbital quantities have been calculated here and the implementation of this correction in `TEOBResumS-Dalí` code has been carried out in this work. These expressions will be presented in Chapter 6 where where we also assess the impact of including the correction in the model through comparisons with NR simulations. The radial component of the radiation reaction force is given by

$$\hat{\mathcal{F}}_r = -\frac{5\,p_{r_*}}{3\,p_\varphi}\hat{\mathcal{F}}_\varphi \hat{f}_{p_{r_*}} \tag{3.76}$$

where the polynomial function $\hat{f}_{p_{r*}}$ is specified in [131, 188] and reads as

$$\hat{f}_{p_{r_*}} = 1 + \left(\frac{5317}{1680} - \frac{227}{140}\nu\right) u + \left(\frac{1296935}{1016064} - \frac{274793}{70560}\nu + \frac{753}{560}\nu^2\right) u^2 \tag{3.77}$$

which is resummed using a Padé approximant. The initial prescription for the radial component of the radiation reaction followed Ref. [111, 115, 116] but it was later found that an alternative prescription yields better agreement with the data.

Chapter 4

Inferring eccentricity evolution from observations of coalescing binary black holes

Declaration: This chapter is a reformatted version of A. Bonino, R. Gamba, P. Schmidt, A. Nagar, G. Pratten, M. Breschi, P. Rettegno, S. Bernuzzi, "Inferring eccentricity evolution from observations of coalescing binary black holes" (2023) [1]. A. Bonino carried out all the parameter estimation runs, developed the routine to measure the eccentricity evolution, generated almost all figures and contributed to the writing.

4.1 Introduction

In this Chapter we focus on `TEOBResumS` [130, 278, 279] and study the performance of its circular and eccentric versions [115, 116, 126] when applied to GW parameter estimation. We do so with the aim of validating the model and gauging possible biases due to eccentricity (or lack thereof). We dedicate special attention to the study of the quasi

circular limit of `TEOBResumS-Dalí`, and investigate how its structural differences with respect to `TEOBResumS-GIOTTO` – quantified in terms of unfaithfulness against numerical relativity waveforms – reflect on GW data analysis of synthetic signals and GW150914. We then introduce a method to estimate the eccentricity directly from GW observations and determine its evolution as a function of frequency. This procedure is efficient and suitable to be applied to any eccentric waveform model in post-processing. Furthermore it is advantageous for comparing different eccentric analysis of GW events. The chapter is organized as follows: In Sec. 4.2 we summarize the main elements of the EOB waveform model used here. In Sec. 4.3 we present a brief review of the elements of Bayesian inference needed for our analysis. Section 4.4 is devoted to the validation of the waveform model via specific injection and recovery analyses. The model is then used to analyze GW150914 data in Sec. 4.6 and Sec. 4.7 is dedicated to presenting our method to estimate the eccentricity evolution of a coalescing BBHs system in post-processing. Concluding remarks are reported in Sec. 4.8. Throughout we use $G = c = 1$ unless stated otherwise.

4.2 Quasi-circular and eccentric waveform model

All analyses presented in this paper are performed with `TEOBResumS`, either in its native quasi-circular version, `TEOBResumS-GIOTTO` [279], or in its eccentric version, `TEOBResumS-Dalí` [116]. In this section we describe in some detail the features of the two models, highlighting their structural differences and quantifying their (dis-)agreement as measured by the unfaithfulness (or mismatch) defined as in Eq. (2.103).

4.2.1 Quasi-circular model: `TEOBResumS-GIOTTO`

`TEOBResumS-GIOTTO` is a semi-analytical state-of-the-art EOB model for spinning coalescing compact binaries [130, 189, 278–281]. The conservative sector of the model

includes analytical Post-Newtonian (PN) information, resummed via Padé approximants. Spin-orbit effects are included in the EOB Hamiltonian via two gyro-gravitomagnetic terms [189], while even-in-spin effects are accounted for through the centrifugal radius [189]. Numerical Relativity (NR) data is used to inform the model through an effective 5PN orbital parameter, a_6^c, and a next-to-next-to-next-to leading order (NNNLO) spin-orbit parameter, c_3 [130]. In the dissipative sector, waveform multipoles up to $\ell = 8$ are factorized and resummed according to the prescription of [278]. Next-to-quasicircular (NQC) corrections ensure a robust transition from plunge to merger, and a phenomenological NR-informed ringdown model completes the model for multipoles up to $\ell \leq 5$. Although we focus here on BBH systems, we note that `TEOBResumS-GIOTTO` can also generate waveforms for binary neutron star coalescences, see [130] and references therein.

Waveforms built from `TEOBResumS-GIOTTO` employing only the dominant multipole $\ell = |m| = 2$ have been tested against the entire catalog of spin-aligned waveforms from the Simulating-eXtreme-Spacetimes (SXS) collaboration [282], and were shown to be consistently more than 99% faithful to NR [279]. When higher modes are included in the dissipative sector of the model, the EOB/NR unfaithfulness always lies below the 0.3% threshold when considering waveforms constructed only with the $\ell = |m| = 2$ mode, and below 3% for waveforms with modes up to $\ell = 4$ if the system has total mass smaller than $120 M_\odot$ [278].

4.2.2 Eccentric model: `TEOBResumS-Dalí`

The eccentric generalization of `TEOBResumS`, `TEOBResumS-Dalí` [115, 116], builds on the features of the quasi-circular model detailed above but differs in few key aspects. First, the quasi-circular Newtonian prefactor that enters the factorized waveform multipoles is replaced by a general expression obtained by computing the time-derivatives of the Newtonian mass and current multipoles [116], as described in Sec. 3.3. The same

approach is implemented for the azimuthal radiation reaction force. Second, for eccentric binaries, the radial radiation reaction force $\mathcal{F}_r$ that contributes to the time evolution of the radial EOB momentum can no longer be neglected [115]. Third, the initial conditions must be specified in a different manner with respect to the quasi-circular case: instead of employing the post-adiabatic procedure of [283], `TEOBResumS-Dalí` computes adiabatic initial conditions and always starts the evolution of the system at the apastron, see Appendix 4.5 for further details. These conservative eccentric initial conditions, however, do not reduce to the quasi-circular initial conditions in the limit of small eccentricity. To partially correct for this issue, the quasi-circular initial conditions are switched on for $e_0 < 10^{-3}$. Finally, the values of a_6 and c_3 were modified in order to ensure that the model remains faithful to its quasi-circular limit [116].

Quasi-circular limit of `TEOBResumS-Dalí`

All of the modifications above allow `TEOBResumS-Dalí` to provide waveforms and dynamics that are faithful to mildly eccentric SXS simulations [115, 116], scattering angle calculations [116] and highly eccentric test-mass waveforms [127]. At the same time, however, because of these structural differences, the quasi-circular limit of the eccentric model `TEOBResumS-Dalí` does not exactly reduce to the `TEOBResumS-GIOTTO` model. In order to quantify the agreement of `TEOBResumS-Dalí` with NR simulations and `TEOBResumS-GIOTTO`, respectively, we calculate the unfaithfulness defined in Eq. (2.103).

In Fig. 4.1 we show the unfaithfulness of `TEOBResumS-Dalí` against almost all[1] non-eccentric, spin-aligned NR simulations in the version 2 of the SXS catalogue [284] using the designed power spectral density (PSD) of Advanced LIGO [285]. This figure complements, with many more simulations, Fig. 3 of [116]. Let us remind the reader that the corresponding plot for `TEOBResumS-GIOTTO` is centered around 10^{-3} with $\max(\bar{F}_{\rm EOBNR}) \leq 9 \times 10^{-3}$

[1] We exclude the following simulations due to large numerical errors: SXS:BBH:0002, SXS:BBH:1110, SXS:BBH:1141, SXS:BBH:1142

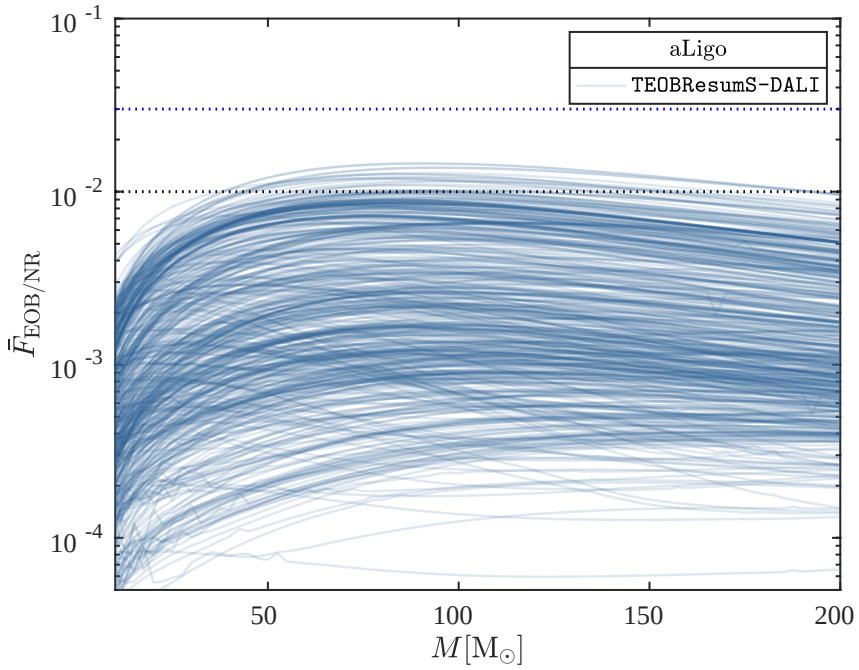


Figure 4.1: EOB/NR unfaithfulness using `TEOBResumS-Dalí` with $e_0^{\rm inj} = 10^{-8}$ over the non-precessing and non-eccentric SXS catalog. See text for more details.

with only a few outliers above 3×10^{-3} (see Fig. 4 of [279]). We thus see here that `TEOBResumS-Dalí` and `TEOBResumS-GIOTTO` are two EOB models, similarly informed by NR simulations, that perform differently with respect to quasi-circular NR simulations, though both are clearly below the usual threshold of 3% unfaithfulness. It is therefore interesting to understand how this difference translates in terms of biases on parameters. This will be discussed in Sec. 4.4.

4.3 Methods

4.3.1 Gravitational Wave Parameter Estimation

The measurement of the parameters that describe the GW emitting binary is carried out within the framework of Bayesian inference, which relies on Bayes' theorem [178]

in Eq. (2.104). In this work we utilize the `bajes` package for Bayesian inference [182] employing the nested sampling [181] algorithm `dynesty` [183] in order to extract the posterior probability density functions (PDFs) and to estimate the evidence. In the following sections we will described the likelihood and the prior distributions used in our analyses.

4.3.2 Likelihood and Priors

We are interested in the joint likelihood between N detectors in a GW detector network

$$p(\mathbf{d}|\boldsymbol{\theta}, H_S) = \prod_{i=1}^{N} p(\mathbf{d}_i|\boldsymbol{\theta}, H_S), \tag{4.1}$$

where H_S denotes the hypothesis that the data contains a GW signal. For the analyses presented in Sec. 4.4 we adopt priors that broadly follow [12, 182] and are given as follows:

- The prior distribution for the masses is chosen to be flat in the components masses $\{m_1, m_2\}$ and can be written in terms of the chirp mass $M_c = (m_1 m_2)^{3/5}/(m_1 + m_2)^{1/5}$ and the mass ratio $q = m_1/m_2 \geq 1$ as

$$p(M_c, q|H_S) = \frac{M_c}{\Pi_{M_c}\Pi_q}\left(\frac{1+q}{q^3}\right)^{2/5}, \tag{4.2}$$

  where Π_{M_c} and Π_q are the prior volumes, as defined in Sec.V B of [182] delimited by the prior bounds of M_c and q.

- To aid the comparison with results from analyses that allow for precessing spins, we assume priors that correspond to the projection of a uniform and isotropic spin distribution along the $\hat{z}$-direction as proposed by Veitch [182, 286]:

$$p(\chi_i|H_S) = \frac{1}{2\chi_{\rm max}} \ln\left|\frac{\chi_{\rm max}}{\chi_i}\right|, \tag{4.3}$$

where χ_i is the magnitude of each black hole spin and $\chi_{\rm max}$ is the maximum spin magnitude.

- The prior distribution for the luminosity distance D_L is specified by a lower and an upper bound and its analytic form is defined by a uniform distribution over the sphere centred around the detectors:

$$p(D_L|H_S) = \frac{3D_L^2}{D_{\rm max}^3 - D_{\rm min}^3} \tag{4.4}$$

- The prior distributions for α and δ, defining the sky location, are taken to be isotropic over the sky with $\alpha \in [0, 2\pi]$, $\delta \in [-\pi/2, +\pi/2]$ and

$$p(\alpha, \delta|H_S) = \frac{\cos\delta}{4\pi}. \tag{4.5}$$

- Analogously, for the inclination we have

$$p(\iota, H_S) = \frac{\sin\iota}{2}, \tag{4.6}$$

where $\iota \in [0, \pi]$.

- For $\{\psi, t_0, \phi_0\}$, the prior distributions are taken to be uniform within the given bounds.

- The prior on $\{e_0, f_0\}$ are taken to be uniform or logarithmic-uniform within the provided bounds that are [0.001, 0.2] and [18, 20.5], respectively. The routine for the specification of these initial conditions in `TEOBResumS-Dalí` is detailed in Sec. 4.5.

4.4 Validation of the waveform model

In this section, we test the consistency of `TEOBResumS-Dalí` with `TEOBResumS-GIOTTO` (and vice-versa) by performing Bayesian inference on simulated GW signals referred to as *injections*. The aim of this section is to give a more quantitative meaning to the standard EOB/NR unfaithfulness figures of merit discussed above. To do so, we inject mock signals into a zero noise realization with a signal-to-noise ratio (SNR) of ~ 42 in the Advanced LIGO and Advanced Virgo network. We employ the Advanced LIGO and Advanced Virgo design sensitivity PSDs [9, 175, 285]. All injections are performed at the same GPS time, $t_{\rm GPS} = 1126259462.4$s and inclination $\iota = \pi/2$. We analyze segments of 8s in duration with a sampling rate of 4096Hz. We use `dynesty` to sample the posterior distributions, using the following setting: 3000 live points to initialise the MCMC chains, 5 MCMC sub-chains, a maximum of 10^4 MCMC steps, a stopping criterion on the evidence of $\Delta \ln Z = 0.1$, and we require five autocorrelation times before accepting a point. For all our analyses, we restrict the waveform model to only the $(2, |2|)$-mode, allowing us to analytically marginalize over the phase.

4.5 Quasi-circular and eccentric initial conditions

For quasi-circular binaries, `TEOBResumS` applies Kepler's law to the initial frequency of the orbit to compute the initial separation r. Then, the initial values of the EOB angular and radial momenta p_φ, p_{r_*} are estimated via an iterative process (known as post-adiabatic expansion, "PA" henceforth) in which the right-hand side of the Hamilton equations is solved analytically under the assumption that $p_{r_*} \sim 0$ [283, 287]. At zeroth PA order, one assumes that $p_{r_*} = 0$ exactly. Then, by evaluating $\partial_r \hat{H}_{\rm EOB} = 0$ one can analytically find the circular angular momentum $j_0(r)$ at the requested initial separation. Neglecting

terms of $O(p_{r_*}^2)$, one can then use $dp_\varphi/dr = \hat{\mathcal{F}}_\varphi \dot{r}^{-1}$ to compute p_{r_*} at the first PA order. This procedure can then be repeated any number of times, with even (odd) PA orders providing corrections to p_φ (p_{r_*}). Correctly computing the initial conditions of the systems and having p_{r_*} different from zero at the initial separation is crucial to avoid effects due to spurious eccentricity. For eccentric binaries, initial conditions necessarily need to be specified in a different manner. Let us denote with e the eccentricity of the ellipse that the system would orbit along assuming no GW emission. Similarly, let us denote with p its semilatus rectum and with ξ its anomaly. A generic point on the ellipse has radial coordinate $r = p/(1 + e\cos\xi)$. To find adiabatic initial conditions for our EOB dynamics we need to find a way to map (f_0, e, ξ) into $(r_0, p^0_\varphi, p^0_{r_*})$. In practice, for convenience, the initial orbital frequency Ω_0 is always assumed to correspond either to the apastron ($r_0 = p_0/(1-e)$), periastron ($r_0 = p_0/(1+e)$) or to the average frequency between the two points. We then solve numerically

$$\partial_{p_\varphi} H(r_0(p_0), j_0(p_0), p_{r_*} = 0) = \Omega_0 \tag{4.7}$$

where j_0 is the adiabatic angular momentum computed using energy conservation

$$\hat{H}^0_{\rm eff}(p_0, j_0, \xi = 0) = \hat{H}^0_{\rm eff}(p_0, j_0, \xi = \pi), \tag{4.8}$$

and estimate the semilatus rectum of the obit p_0. The evolution of the system is then always started at the apastron, so that

$$r_0 = \frac{p_0}{(1-e)}, \tag{4.9}$$

$$p^0_\varphi = j_0, \tag{4.10}$$

$$p^0_{r_*} = 0. \tag{4.11}$$

This adiabatic procedure can be generalized to higher PA orders[2]. We leave a discussion of such initial conditions to future work.

4.5.1 Quasi-circular limit of the eccentric model

As mentioned above, `TEOBResumS-Dalí` is structurally different to the quasi-circular `TEOBResumS-GIOTTO` model. Moreover, despite having been informed by the same NR simulations, its unfaithfulness to NR is *larger* than that of `TEOBResumS-GIOTTO`. To better understand how this difference in the unfaithfulness translates into parameter biases, we perform an unequal mass injection in the quasi-circular limit, as detailed in Table 4.2. More precisely, the injected waveform is generated with `TEOBResumS-GIOTTO` from a fixed initial frequency of 20 Hz, and it is recovered with either the same model (Prior 1) or with `TEOBResumS-Dalí` assuming a fixed initial eccentricity of $e_0 = 10^{-8}$ at 20 Hz (Prior 2). In Fig. 4.2 we show the one-dimensional and joint posterior distributions for M_c[3], q and the effective spin

$$\chi_{\rm eff} = \frac{m_1\chi_{1z} + m_2\chi_{2z}}{m_1 + m_2}, \tag{4.12}$$

where the two spins are taken to be aligned along the $\hat{z}$-direction: $\chi_{1z} = \chi_1$ and $\chi_{2z} = \chi_2$. The median values of M_c, $\chi_{\rm eff}$ and q recovered with `TEOBResumS-GIOTTO` and `TEOBResumS-Dalí` are shown, with their 90% credibility interval, respectively in the first and second column of Table 4.1. Comparing the results, we notice that the median values of the parameters recovered with `TEOBResumS-GIOTTO` are in good agreement with the injected ones, while those recovered with the quasi-circular limit of `TEOBResumS-Dalí` are slightly biased towards higher values. This is not surprising given the different analytical structures (dissipative sectors and NR-informed parameters) of the two models and the fact that `TEOBResumS-Dalí` is less NR-faithful than `TEOBResumS-GIOTTO` by, on average, one order

[2] 1PA eccentric initial conditions have been implemented in the public `TEOBResumS` code in commit `eb5208a`

[3] We note that we quote the detector-frame chirp mass throughout the chapter.

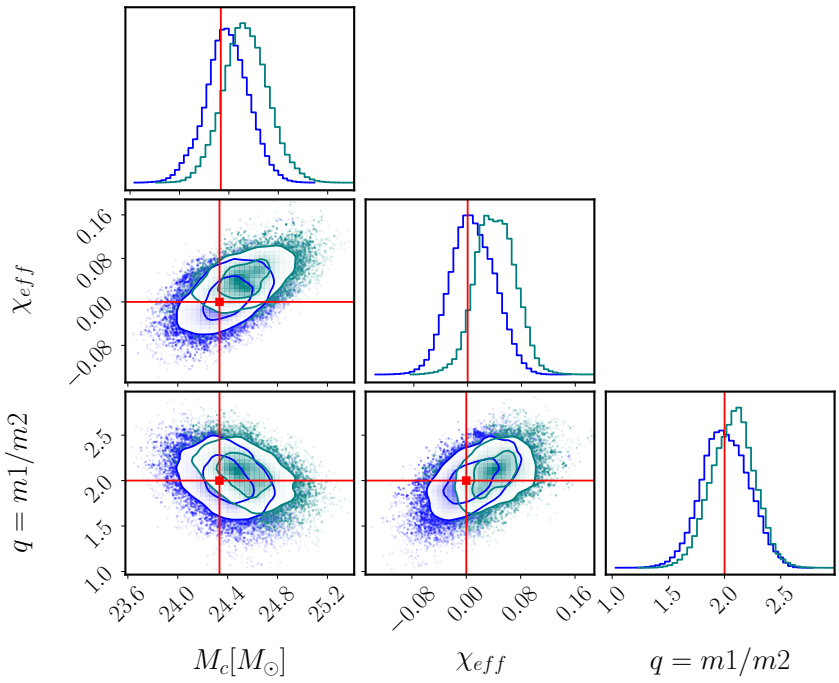


Figure 4.2: Testing the quasi-circular limit of `TEOBResumS-Dalí`. We inject a quasi-circular waveform generated with `TEOBResumS-GIOTTO` and recover it with either `TEOBResumS-GIOTTO` (blue) or with `TEOBResumS-Dalí` with fixed initial eccentricity at $e_0 = 10^{-8}$ (teal). The injected values are indicated by the solid lines. We find that the parameters recovered with `TEOBResumS-Dalí` are slightly biased. See text for discussion.

of magnitude ($\sim 10^{-2}$ vs. 10^{-3}) (see Fig. 4.1 and Fig. 4 of [279]). Moreover, when comparing the two models with each other, we also find an average unfaithfulness of $2-3\%$, which increases slightly with the total mass of the binary.

	Circular injection				
Model	`TEOBResumS-GIOTTO`	`TEOBResumS-Dalí`	`TEOBResumS-Dalí`	`TEOBResumS-Dalí`	`TEOBResumS-Dalí`
e_0-prior	$e_0 = 0$ (fixed)	$e_0 = 10^{-8}$ (fixed)	$\mathcal{U}(0.001,0.2)$	$\mathcal{U}(0.001,0.2)$	Log-uniform(0.001, 0.2)
f_0-prior	$f_0 = 20$ Hz (fixed)	$f_0 = 20$ Hz (fixed)	$\mathcal{U}(18, 20.5)$	$f_0 = 20$ Hz	$\mathcal{U}(18, 20.5)$
$M_c(M_\odot)$	$24.38^{+0.17}_{-0.16}$	$24.53^{+0.18}_{-0.17}$	$24.32^{+0.18}_{-0.19}$	$24.33^{+0.18}_{-0.21}$	$24.35^{+0.17}_{-0.16}$
$\chi_{\rm eff}$	$0.01^{0.03}_{-0.03}$	$0.04^{+0.03}_{-0.03}$	$0.00^{+0.03}_{-0.03}$	$0.00^{+0.03}_{-0.03}$	$0.00^{+0.02}_{-0.02}$
q	$2.00^{+0.22}_{-0.19}$	$2.08^{+0.18}_{-0.20}$	$2.00^{+0.14}_{-0.19}$	$2.02^{+0.17}_{-0.18}$	$1.97^{+0.17}_{-0.20}$
e_0	–	–	$0.01^{+0.01}_{-0.01}$	$0.01^{+0.01}_{-0.01}$	$0.00^{+0.01}_{-0.01}$

Table 4.1: Posterior distribution functions for M_c, $\chi_{\rm eff}$ and q for a circular injection ($e^{\rm inj}_\omega = 0$ and $f_0 = 20$Hz) with different recoveries using `TEOBResumS-GIOTTO` and `TEOBResumS-Dalí`.

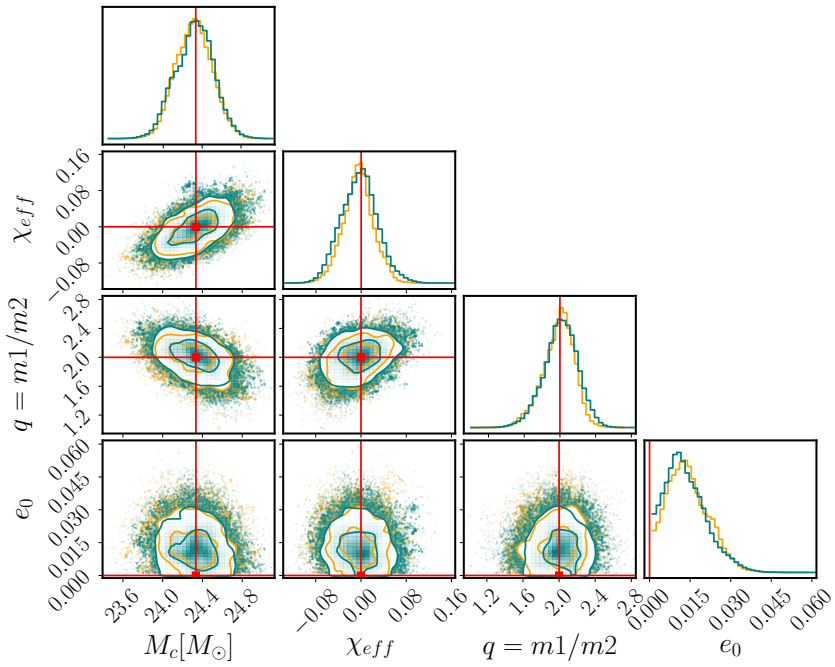


Figure 4.3: Injection with `TEOBResumS-GIOTTO` and recovery with `TEOBResumS-Dalí`. The posterior distributions are obtained by sampling in (e_0, f_0) (orange) or by sampling only in e_0 while keeping f_0 fixed (teal). The injected values are represented by the solid lines. We do not find appreciable biases in the reconstructed parameters when sampling only in e_0.

4.5.2 Testing the eccentric model

In the EOB framework, the dynamics of a system of coalescing binaries is evolved from initial conditions. For the `TEOBResumS-Dalí` model, this is done by defining an initial eccentricity e_0 and an initial frequency f_0 and, through Eq. (4.7)-(4.11), determining (r_0, p^0_φ, p^0_{r*}). The degree to which the initial frequency f_0 has an impact on Bayesian inference and our ability to constrain this parameter from the observations is poorly understood. In previous similar analyses, comparable quantities, such as the argument of the periapsis or mean anomaly, have typically been ignored. However, recent studies [33, 102] suggest that the mismatches can degrade as we vary these parameters for a given eccentricity. It is therefore useful to quantify the impact of f_0 on Bayesian inference. To do so we perform

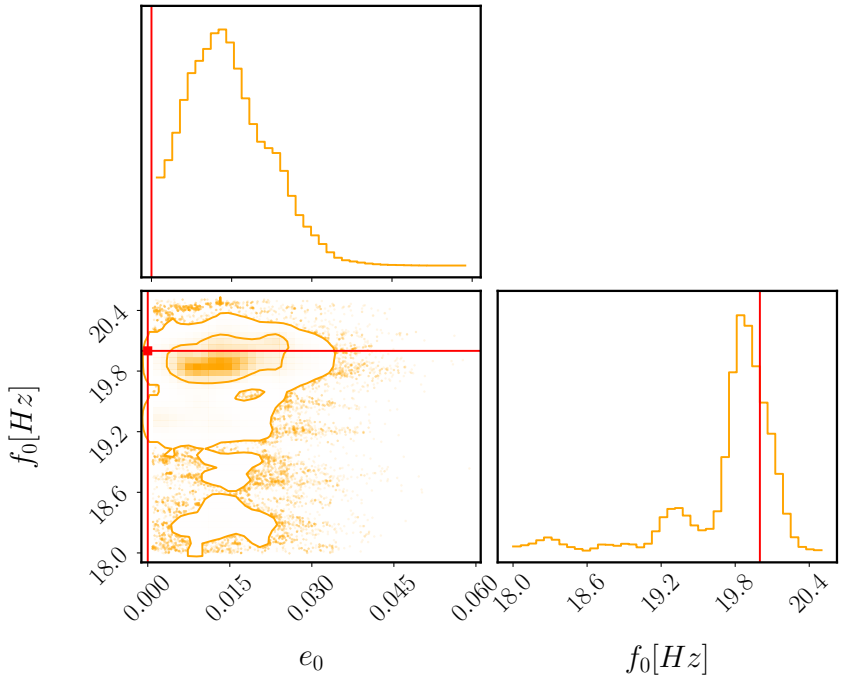


Figure 4.4: Two-dimensional eccentricity and frequency posterior distributions for the same `TEOBResumS-GIOTTO` injection and recovery with `TEOBResumS-Dalí` as in Fig. 4.3. We do not observe any significant correlation between e_0 and f_0.

a non-eccentric injection with $e_0 = 0$ and $f_0 = 20$ Hz and recover with `TEOBResumS-Dalí` either sampling on e_0 and f_0 (Prior 1) or only on e_0 (Prior 2). The details of the injection and the priors are listed in Table 4.4. For the other parameters, the injected values and prior ranges are the same as in Table 4.2.

Figures 4.3 and 4.4 show the one-dimensional and joint posterior distributions obtained with the two different priors. In Fig. 4.3, we show the posterior distributions for M_c, $\chi_{\rm eff}$, q and e_0 obtained using the first prior choice (orange) and the second prior choice (teal). The median values, at 90% credibility, are shown in the third (Prior 1) and fourth (Prior 2) columns of Tab. 4.1. We do not observe any significant differences between the two analyses and we find that the posterior on f_0 is weakly correlated with e_0 about its true value as can be seen from Fig. 4.4. This is in broad agreement with the conclusions of [34], who found that the argument of periapsis is only likely to be resolvable for the

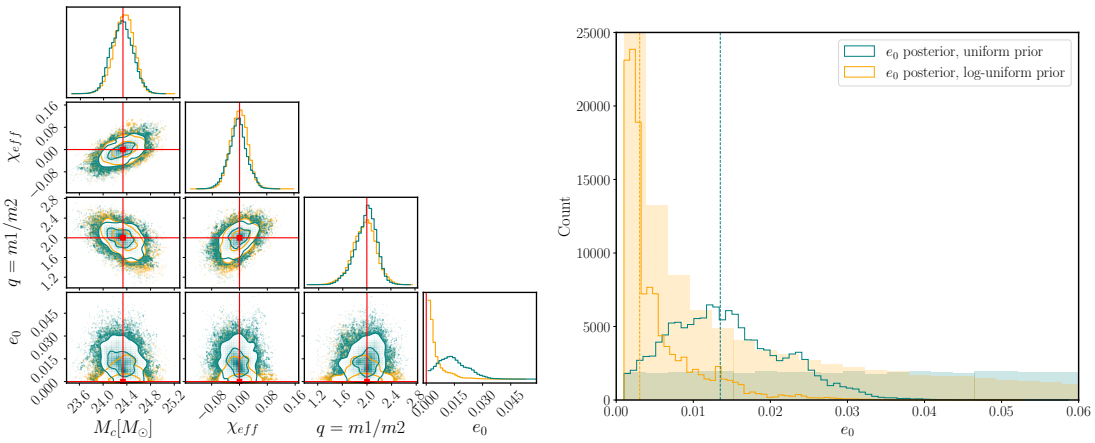


Figure 4.5: Injection with `TEOBResumS-GIOTTO` and recovery with `TEOBResumS-Dalí`. Left: the posterior distribution for the $(M_c, q, \chi_{\rm eff})$. Right: the posterior distribution for the initial eccentricity using two different choices of priors: uniform (teal) and logarithmic-uniform (orange). The corresponding prior distributions are also displayed (filled colours)

.

loudest events. However, as also discussed in Refs. [18, 34, 288], we could potentially see biases if we fix f_0 to a frequency that effectively corresponds to the argument of the periapsis being out of phase with the true value. In the $e_0 \to 0$ limit, however, one may expect f_0 to become increasingly degenerate with the coalescence phase.

We note that although the injected value for e_0 is not contained within the priors, we do not see evidence that this impacts the inferred results. But we find a prior- dependence in the posterior of e_0 (see Fig. 4.5 and the discussion below), in addition to the systematic differences between the two models in the circular limit already highlighted in Fig. 4.2.

We next inject mock signals with two different values of e_0 and recover them using `TEOBResumS-GIOTTO` and `TEOBResumS-Dalí` respectively. The details of the injected values for e_0 and f_0 and their priors are described in Tab. 4.5. The injected values and priors for the other parameters are the same as before as given in Tab. 4.2. Fig. 4.5 shows the one- and two-dimensional posterior distributions for M_c, $\chi_{\rm eff}$ and q (left) and the one-dimensional posterior distribution for e_0 (right) for a non-eccentric injection recov-

Parameter	Injected value	Prior 1	Prior 2
$M_c(\mathrm{M}_\odot)$	24.33	$[18, 45]$	$[18, 45]$
q	2	$[1, 3]$	$[1, 3]$
χ_1	0	$[-0.8, 0.8]$	$[-0.8, 0.8]$
χ_2	0	$[-0.8, 0.8]$	$[-0.8, 0.8]$
$D_L(\mathrm{Mpc})$	800	$[50, 2000]$	$[50, 2000]$
$\cos\iota$	0	$[-1, 1]$	$[-1, 1]$
$\alpha(\mathrm{rad})$	0.37	$[0, 2\pi]$	$[0, 2\pi]$
$\delta(\mathrm{rad})$	0.81	$[-\pi/2, \pi/2]$	$[-\pi/2, \pi/2]$
$\psi(\mathrm{rad})$	0	$\mathcal{U}(0, \pi)$	$\mathcal{U}(0, \pi)$
$t_0(\mathrm{s})$	0	$\mathcal{U}(-1, 1)$	$\mathcal{U}(-1, 1)$
$\phi_0(\mathrm{rad})$	0	–	–
e_0	0	0	10^{-8}
$f_0(\mathrm{Hz})$	20	20	20
Model	`GIOTTO`	`GIOTTO`	`DALI`

Table 4.2: Parameters of the circular injection and two different priors. The prior distributions are described in Sec. 4.3.2. The sky location corresponds to the maximum sensitivity for the Advanced LIGO Hanford detector.

	Eccentric injection	
Model	`TEOBResumS-GIOTTO`	`TEOBResumS-Dalí`
e_0-prior	$e_0 = 0$ (fixed)	$\mathcal{U}(0.001,0.2)$
f_0-prior	$f_0 = 20$ Hz (fixed)	$\mathcal{U}(18, 20.5)$
$M_c(M_\odot)$	$24.34^{+0.17}_{-0.17}$	$24.43^{+0.19}_{-0.24}$
$\chi_{\rm eff}$	$-0.03^{+0.03}_{-0.03}$	$-0.03^{+0.03}_{-0.03}$
q	$1.84^{+0.19}_{-0.21}$	$1.97^{+0.17}_{-0.20}$
e_0	–	$0.05^{+0.01}_{-0.01}$

Table 4.3: Posterior distribution functions for M_c, $\chi_{\rm eff}$ and q for an eccentric injection ($e^{\rm inj}_\omega = 0.05$ and $f_0 = 20$Hz) with different recoveries using `TEOBResumS-GIOTTO` and `TEOBResumS-Dalí`.

ered with `TEOBResumS-Dalí` with two different choices of prior distributions: logarithmic-uniform (teal), uniform (orange). The recovered median values corresponding to the Prior 1 (orange) are shown in the third column while the one corresponding to the Prior 2 (teal) are shown in the fifth column of Tab. 4.1. We observe that for eccentricities comparable to zero, the mass and spin measurements are robust and independent of the choice of eccentricity prior. In the right panel of Fig. 4.5, we observe that when using a logarithmic-

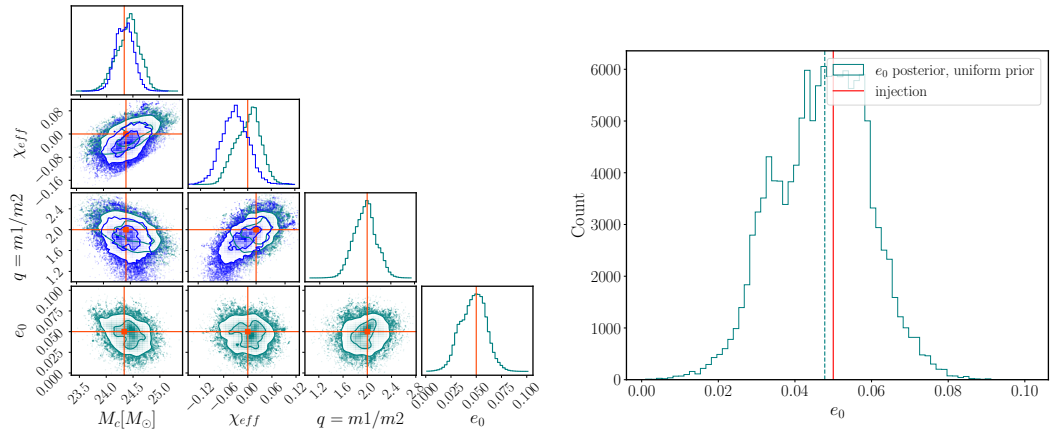


Figure 4.6: Injection with `TEOBResumS-Dalí` with fixed EOB eccentricity $e_0 = 0.05$ at 20 Hz and recovery with `TEOBResumS-GIOTTO` (blue) or `TEOBResumS-Dalí` (teal). When the analysis is performed with the latter, all recovered parameters look consistent with the injected ones. Conversely, neglecting eccentricity leads to biases in the mass ratio and effective spin posterior distributions.

uniform prior for the eccentricity, the recovered median value of the eccentricity is pushed to smaller values as a result of the priors.

In Fig. 4.6, instead, we show the posterior distributions for an injection with $e_0 = 0.05$ (`TEOBResumS-Dalí`) and recovered with both the models, `TEOBResumS-GIOTTO` and `TEOBResumS-Dalí`. The median values of the parameters recovered with `TEOBResumS-GIOTTO` (orange) are indicated in the first column of Tab. 4.3, while the ones recovered with `TEOBResumS-Dalí` (teal) are indicated in the second column of the same Table. In the left figure, we observe a stronger correlation between mass and spin parameters when we recover with `TEOBResumS-GIOTTO`. Previous studies have pointed out correlations between the chirp mass, the effective inspiral spin and the eccentricity [18, 96, 288]. As our recovery model neglects eccentricity, biases in the mass and spin parameters are anticipated to compensate for this. Lastly, we draw our attention on the right figure of the bottom panel, where it is shown how excellently the recovery of the eccentricity is accomplished, pointing out the robustness and accuracy of the model.

In terms of model selection, we find that for the non-eccentric injection, the recovery

Parameter	Injected value	Prior 1	Prior 2
e_0	0	$\mathcal{U}(0.001, 0.2)$	$\mathcal{U}(0.001, 0.2)$
f_0(Hz)	20	$\mathcal{U}(18, 20.5)$	20 (fixed)
Model	–	`DALI`	`DALI`

Table 4.4: Injected values for e_0 and f_0 and their priors. Two choices of recovery are made to perform this first testing analysis of `TEOBResumS-Dalí`. We choose to sample in both parameters in one case (Prior 1) and only in e_0 in the other case (Prior 2).

Parameter	Injection 1	Prior 1	Prior 2	Injection 2	Prior 1	Prior 2
e_0	0	$\mathcal{U}(0.001, 0.2)$	Log-uniform$(0.001, 0.2)$	0.05	$\mathcal{U}(0.001, 0.2)$	0 (fixed)
$f_0(Hz)$	20	$\mathcal{U}(18, 20.5)$	$\mathcal{U}(18, 20.5)$	20	$\mathcal{U}(18, 20.5)$	20 (fixed)
Model	–	`DALI`	`DALI`	`DALI`	`DALI`	`GIOTTO`

Table 4.5: Second test of `TEOBResumS-Dalí` with an eccentric recovery. First column: injected values for e_0 and f_0 and their prior limits for an injection with $e_0 = 0$ injection recovered with `TEOBResumS-Dalí` with two different prior choices. Second column: injected values for e_0 and f_0 and their prior limits for an injection with $e_0 = 0.05$ recovered with `TEOBResumS-Dalí` and `TEOBResumS-GIOTTO`.

with `TEOBResumS-GIOTTO` is preferred with respect to the one with `TEOBResumS-Dalí` with an estimated logarithmic Bayes' factor of $\ln \mathcal{B}^{\rm circ}_{\rm ecc} \sim 9$. Similarly, for the eccentric injection, the eccentric model `TEOBResumS-Dalí` is preferred with respect to the quasi-circular model `TEOBResumS-GIOTTO` with an estimated logarithmic Bayes' factor of $\ln \mathcal{B}^{\rm ecc}_{\rm circ} \sim 5$ in the case of the uniform eccentricity prior, and $\ln \mathcal{B}^{\rm ecc}_{\rm circ} \sim 10$ when using the log-uniform prior. The difference in Bayes' factor between the two priors can be attributed to the $1/e_0$-scaling for the log-uniform prior, which *a priori* favours smaller values of eccentricity. The investigations presented in this section demonstrate that `TEOBResumS-Dalí` is a reliable waveform model to analyze spin-aligned, eccentric binaries. However, since our injection studies assume $\chi_{\rm eff} = 0$, further tests are needed to confirm the accuracy of the model for spinning binaries.

4.6 Analysis of GW150914

In this section, we reanalyse GW150914 with the `TEOBResumS-Dalí` and `TEOBResumS-GIOTTO` waveform models. The strain data and PSDs are obtained from the GW Open Science Center [289]. We analyse an $8s$-long data stretch centered around the GPS time of the event $t_{\rm GPS} = 1126259462.4\,$s sampled at a sampling rate of 4096 Hz. For the inference, we use `dynesty` choosing the same settings discussed in Sec. 4.4.

4.6.1 Quasi-circular analysis of GW150914

First, we analyse GW150914 under the assumption of a quasi-circular binary black holes system. To do so, we perform two analyses, either using `TEOBResumS-GIOTTO` or `TEOBResumS-Dalí`, fixing initial EOB eccentricity to $e_0 = 10^{-8}$, as described in Tab. 4.6. In both cases we recover a maximum likelihood SNR of ~ 26 corresponding to ~ 20 in LIGO-Hanford and ~ 18 in LIGO-Livingston. In Fig. 4.7 we show the marginalized one-dimensional and two-dimensional posterior distributions for $(M_c, \chi_{\rm eff}, q)$ obtained with `TEOBResumS-Dalí` (teal) and `TEOBResumS-GIOTTO` (blue). The recovered median values are reported in the second and third column of Tab. 4.7. We observe that the values recovered with `TEOBResumS-GIOTTO` are consistent with the values for GW150914 reported in GWTC-1 [12], while the median values for the chirp mass and effective inspiral spin found with `TEOBResumS-Dalí` with fixed $e_0 = 10^{-8}$ are slightly higher in comparison to GWTC-1, but still consistent at the 90% credible level. In terms of Bayes' factors we find that the analysis with `TEOBResumS-GIOTTO` is favored with a $\ln \mathcal{B}^{\rm circ}_{{\rm ecc},10^{-8}} \sim 1$. Based on the results for mock signals presented in Sec. 4.2.2, this is not surprising because of the structural difference between the two models and the influence of initial conditions on the quasi-circular limit as discussed extensively in Sec. 4.2.2.

Parameter	Prior	
$M_c(\mathrm{M}_\odot)$	$[12, 45]$	$[12, 45]$
q	$[1, 3]$	$[1, 3]$
χ_{1z}	$[-0.8, 0.8]$	$[-0.8, 0.8]$
χ_{2z}	$[-0.8, 0.8]$	$[-0.8, 0.8]$
$D_L(\mathrm{Mpc})$	$[50, 2000]$	$[50, 2000]$
$\cos\iota$	$[-1, 1]$	$[-1, 1]$
$\alpha(\mathrm{rad})$	$[0, 2\pi]$	$[0, 2\pi]$
$\delta(\mathrm{rad})$	$[-\pi/2, \pi/2]$	$[-\pi/2, \pi/2]$
$\psi(\mathrm{rad})$	$\mathcal{U}(0, \pi)$	$\mathcal{U}(0, \pi)$
$t_0(s)$	$\mathcal{U}(-1, 1)$	$\mathcal{U}(-1, 1)$
$\phi_0(\mathrm{rad})$	–	–
e_0	0 (fixed)	10^{-8} (fixed)
$f_0(\mathrm{Hz})$	20 (fixed)	20 (fixed)
Model	`TEOBResumS-GIOTTO`	`TEOBResumS-Dalí`

Table 4.6: Choice of priors for the analysis of GW150914 to test the quasi-circular limit of `TEOBResumS-Dalí`. The prior distributions are described in detail in Sec. 4.3.2.

	GW150914 Analysis				
Model	`TEOBResumS-GIOTTO`	`TEOBResumS-Dalí`	`TEOBResumS-Dalí`	`TEOBResumS-Dalí`	GWTC-1
e_0-prior	$e_0 = 0$(fixed)	$e_0 = 10^{-8}$ (fixed)	$\mathcal{U}$(0.001,0.2)	Log-uniform(0.001, 0.2)	–
f_0-prior	$f_0 = 20$ Hz (fixed)	$f_0 = 20$ Hz (fixed)	$\mathcal{U}$(18, 20.5)	$\mathcal{U}$(18, 20.5)	–
$M_c(M_\odot)$	$31.33^{+0.75}_{-0.52}$	$32.53^{+0.84}_{-1.08}$	$31.54^{+0.92}_{-1.19}$	$31.79^{+1.12}_{-0.94}$	$31.23^{+1.08}_{-0.96}$
$\chi_{\rm eff}$	$0.01^{+0.05}_{-0.03}$	$0.13^{+0.06}_{-0.08}$	$0.06^{+0.06}_{-0.10}$	$0.08^{+0.08}_{-0.07}$	$-0.01^{+0.12}_{-0.11}$
q	$1.14^{+0.14}_{-0.10}$	$1.15^{+0.15}_{-0.10}$	$1.18^{+0.17}_{-0.11}$	$1.21^{+0.19}_{-0.14}$	$1.16^{+0.19}_{-0.11}$
e_0	–	–	$0.05^{+0.03}_{-0.02}$	$0.02^{+0.03}_{-0.01}$	–

Table 4.7: Results for the different analysis of GW150914 with `TEOBResumS-GIOTTO` or `TEOBResumS-Dalí`. The prior ranges for e_0 and f_0 for each analysis are indicated. We give the median values and symmetric 90% credible interval for M_c, $\chi_{\rm eff}$ and q. Our results are contrasted by the values obtained from the non-eccentric, precessing analysis presented in GWTC-1 [12] shown in the last column.

4.6.2 Eccentric analysis of GW150914

Finally, we reanalyse GW150914 with the eccentric model `TEOBResumS-Dalí` sampling in both the initial eccentricity e_0 and f_0 (see Tab. 4.7 for prior details). For the eccentricity we use two different priors: one uniform in e_0 and the other one logarithmic-uniform

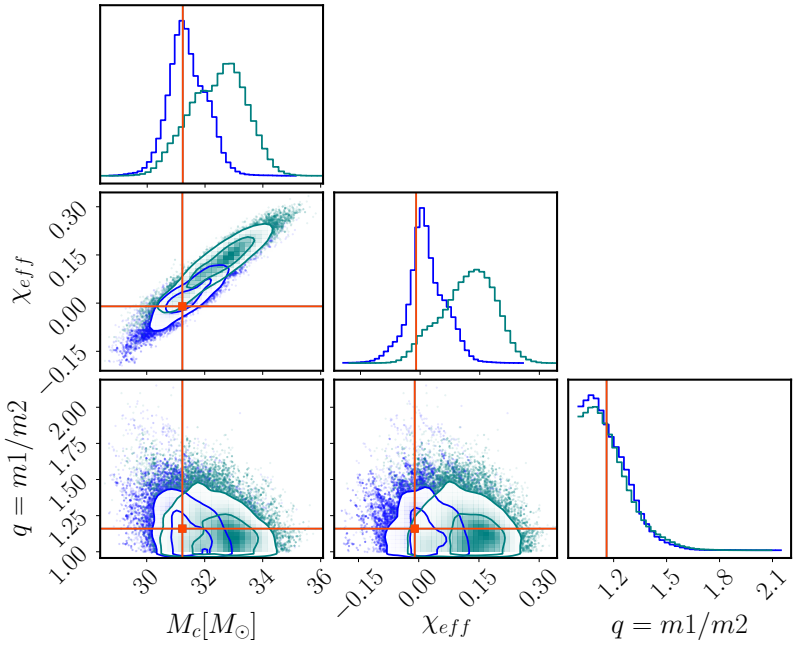


Figure 4.7: One-dimensional and two-dimensional posterior distributions for M_c, q and $\chi_{\rm eff}$ obtained with the quasi-circular model `TEOBResumS-GIOTTO` (blue) and the eccentric `TEOBResumS-Dalí` in the quasi-circular limit (i.e. e_0 fixed to 10^{-8} (teal)). The solid lines indicate the values from the quasi-circular analysis presented in GWTC-1 [12].

which occupies a larger prior volume at low eccentricities. All other priors and settings are identical to the quasi-circular analysis of Sec. 4.6.1. Consistently with this, we estimate a network SNR of ~ 26 with ~ 20 in LIGO-Hanford and ~ 18 in LIGO-Livingston for the maximum likelihood parameters. In Fig. 4.8 we show the one-dimensional and joint posterior distributions together with the median values reported in GWTC-1 [12] or calculated from [290] (solid lines). The median values for $(M_c, \chi_{\rm eff}, q)$ are given in Table 4.7. The two eccentric analyses give consistent results for the mass and spin parameters, i.e. we do not find any appreciable difference between the results for the two different choices of the eccentricity prior. We do, however, find differences in the e_0 posterior under the two different prior assumptions as shown in the bottom panel of Fig. 4.8. While both posteriors are consistent with small values of initial eccentricity, we find that the e_0-posterior peaks

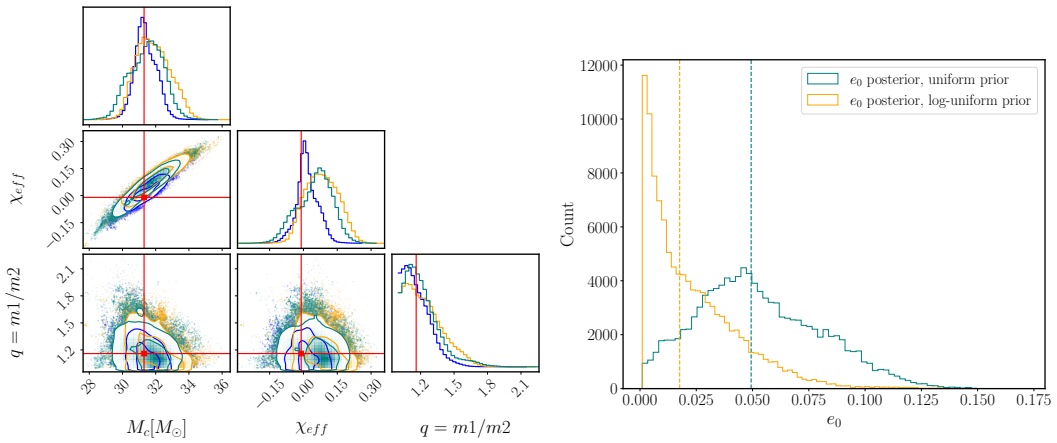


Figure 4.8: Analyses of GW150914 with `TEOBResumS-GIOTTO` (blue) and `TEOBResumS-Dalí` with a uniform e_0-prior (teal) and a logarithmic-uniform e_0-prior (orange). Upper panel: Joint posterior distributions with 90% and 50% credibility interval and median values reported in GWTC-1 [12] (solid lines). Bottom panel: Marginalised one-dimensional posterior distributions and median values of e_0 (dashed lines) for the two eccentric analyses.

at ~ 0.05 for the uniform e_0-prior, which is in mild tension with other results [291, 292]. However, we note that this may be due to the uniform prior, which may not sufficiently explore low values of eccentricity. By contrast, when choosing the logarithmic-uniform prior, lower values of e_0 are preferred in full agreement with other analyses. We find that the maximum 90% upper limit is $e_0 \lesssim 0.08$, which is consistent with the results based on NR simulations presented in [293], where it was shown that the log-likelihood drops sharply as the eccentricity grows beyond ~ 0.05 at about 20 Hz. For the other parameters, see Figs. 4.9 and 4.10, we find broad agreement with the exception of the right ascension, where a different mode is preferred. In comparison to the quasi-circular analysis, the eccentric analyses give slightly higher median values for M_c and $\chi_{\rm eff}$ in agreement with [291, 292]. In terms of model selection we find that `TEOBResumS-GIOTTO` is favoured over `TEOBResumS-Dalí` with an estimated Bayes' factor of $\ln \mathcal{B}^{\rm circ}_{\rm ecc} \sim 2$ irrespective of the prior. This is in agreement with the results reported in [291], but differs from the ones in [292]. However we note that Ref. [292] uses higher order modes while in our analysis

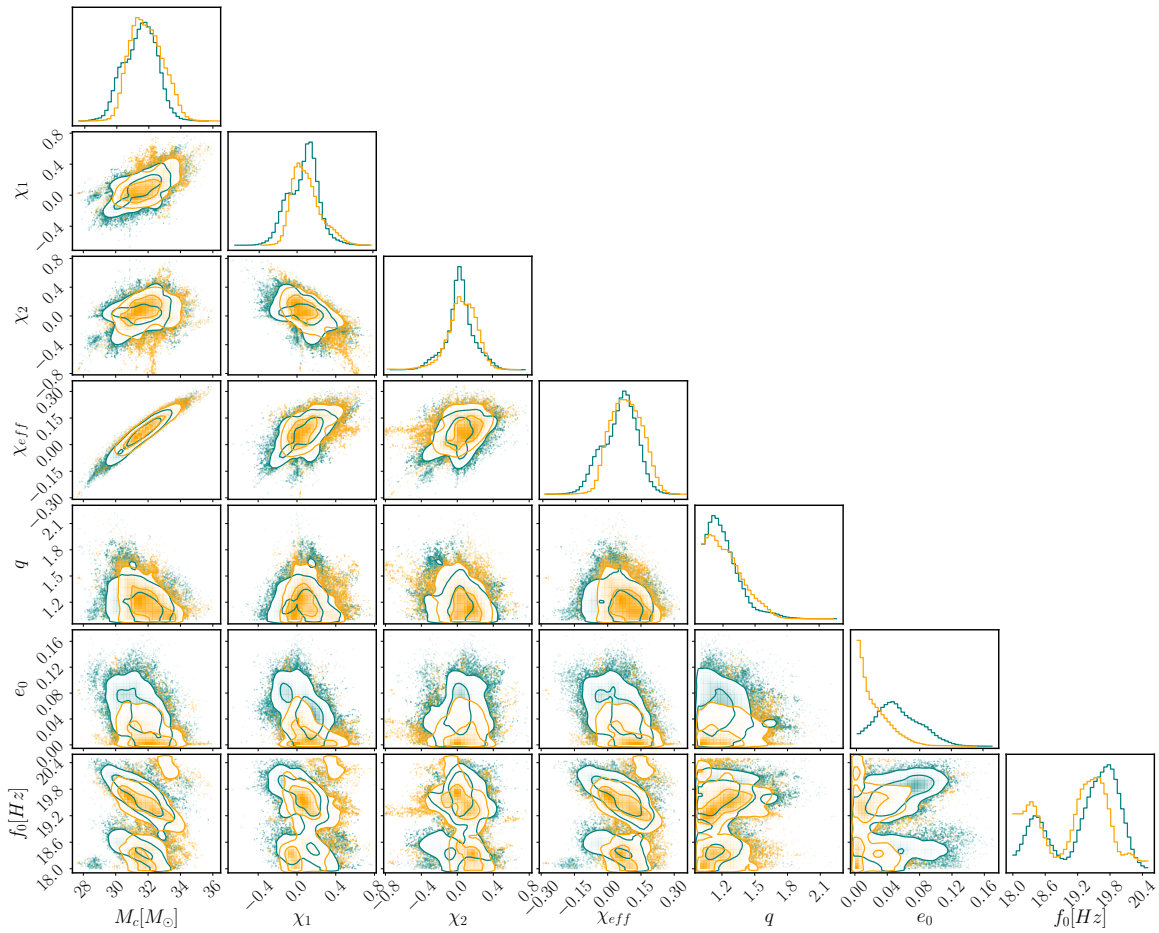


Figure 4.9: One dimensional and join posterior distributions for the intrinsic parameters in addition with e_0 and f_0 recovered with the two eccentric analyses of GW150914. The analysis using a uniform eccentricity prior is represented in teal, the one utilizing a logarithmic-uniform prior for the eccentricity is shown in orange.

we only employ the dominant multipole $\ell = |m| = 2$ in the waveform. We conclude that, while the hypothesis of a quasi-circular BBH merger is preferred for GW150914, we cannot exclude a small value of eccentricity at 20 Hz. All three analyses, however, give consistent results for the intrinsic parameters at 90% confidence. Our results are in agreement with previous analyses [12, 18, 291].

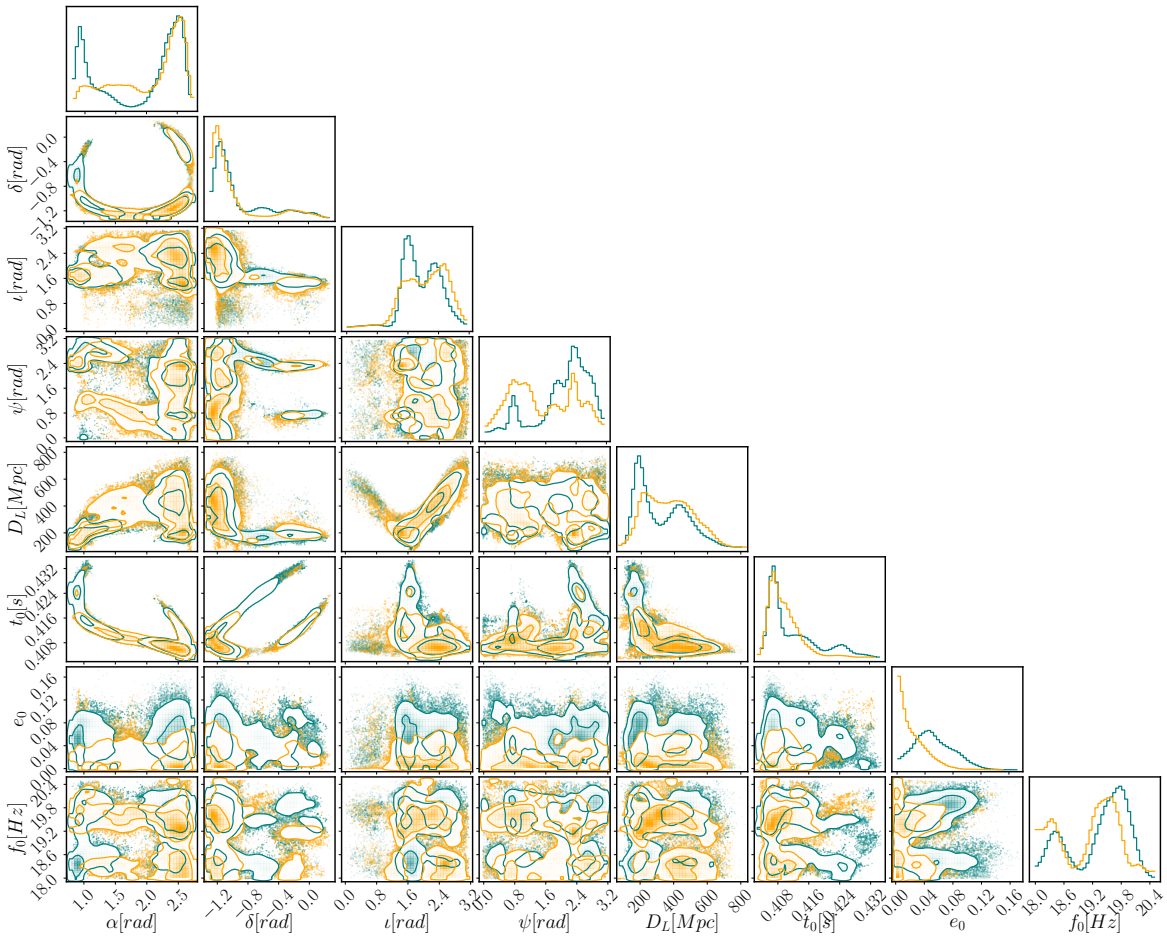


Figure 4.10: One dimensional and join posterior distributions for the extrinsic parameters in addition with e_0 and f_0 recovered with the two eccentric analyses of GW150914. The analysis using a uniform eccentricity prior is represented in teal, the one utilizing a logarithmic-uniform prior for the eccentricity is shown in orange.

4.7 Model-agnostic estimate of the Eccentricity Evolution

Bayesian inference allows us to determine the posterior distributions of binary parameters at a certain reference frequency. Certain parameters are, however, frequency dependent and hence change over time. One of these parameters is the eccentricity of

the orbit, which decays due to the emission of GWs. In Sec. 4.6.2 we determined the posterior distribution of the initial eccentricity e_0 of the EOB model measured at a (varying) reference average frequency f_0. We now devise a scheme to determine the evolution of the eccentricity as a function of frequency using a previously introduced eccentricity estimator [190]. Gravitational radiation at future null infinity is expected to be manifestly gauge invariant, motivating the use of an estimator based on the relative oscillations in the gravitational-wave frequency. This mitigates against the contamination of eccentricity measurements through the use of gauge dependent quantities [294]. This has the additional advantage of allowing for the direct comparison between different eccentric analyses, which often use different definitions of eccentricity [295][4]. Our scheme is computationally efficient and applicable to any eccentric waveform model in post-processing. An advantage of estimating the eccentricity in post-processing is that it can be calculated directly from the GW signal, rather than being inferred from the underlying dynamics [5]. In addition, it also reduces to the Newtonian definition of eccentricity, even in the high eccentricity limit [96, 190].

To calculate the eccentricity evolution, we employ the eccentricity estimator first introduced by Mora et al. [190]:

$$e_\omega(t) = \frac{\omega_p(t)^{1/2} - \omega_a(t)^{1/2}}{\omega_p(t)^{1/2} + \omega_a(t)^{1/2}}, \tag{4.13}$$

where $\omega_p(t)$ and $\omega_a(t)$ are fits to the GW frequency of the $(2,2)$-mode at the periastron and the apastron, respectively. We note that this eccentricity estimator is also used in other works, e.g. either based on the orbital [96, 102, 297] or the GW frequency [115,

[4] We remind the reader that in general relativity one does not have a unique, Newtonian-like definition of orbital eccentricity: due to periastron precession elliptic orbits do not generally close, even in the absence of dissipation caused by GW. Moreover, and most importantly, eccentricity is not a gauge invariant quantity, but rather it depends on the specific choice of coordinates. A detailed discussion on this topic can be found in e.g. [296].

[5] Nonethless, we note that since we also have at hand the EOB dynamics, the same approach could be applied to the EOB orbital frequency.

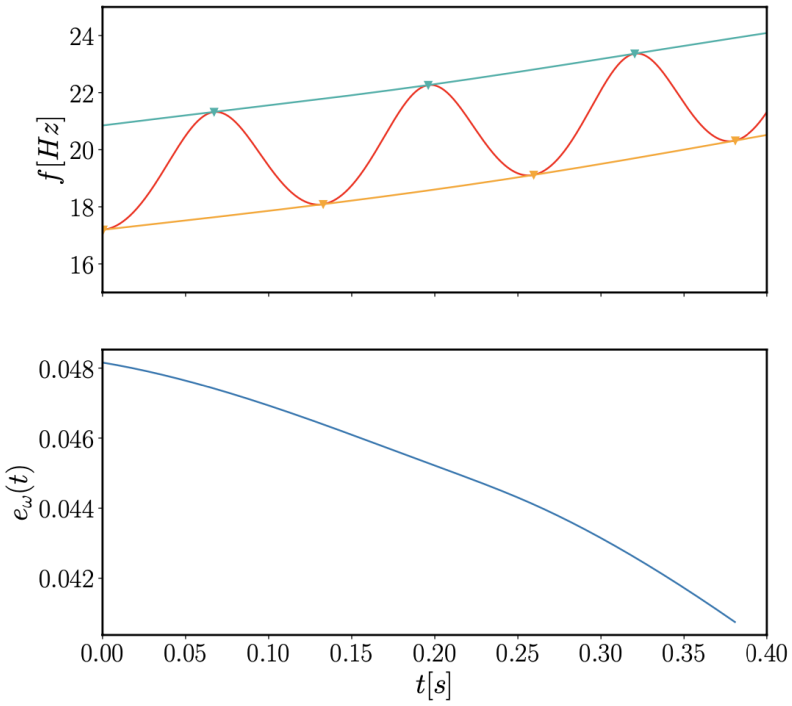


Figure 4.11: Upper panel: Illustration of the fitting procedure to determine the maxima (teal) and minima (orange) of the GW frequency (red). Bottom panel: Evolution of the eccentricity $e_\omega(t)$ calculated using the method described in the text for a BBH with $M_c = 24.74$, $\chi_{\rm eff} = 0$ and $q = 1.5$.

116]. To calculate $\omega_p(t)$ and $\omega_a(t)$, we first generate the `TEOBResumS-Dalí` waveform for each posterior sample and compute the GW frequency as $\omega(t) = \dot{\phi}(t)$, where $\phi(t)$ is the phase of the $(2,2)$-mode defined as $h_{22} = A(t)e^{-i\phi(t)}$ with $A(t)$ being the amplitude of the waveform. We then identify the maxima (periastron) and the minima (apastron) of the *second time-derivative* of the GW frequency. We use the second derivative in order to amplify the peaks such that the identification of the maxima and minima is more robust for small eccentricities.

Once the minima and maxima are identified, we fit $f(t) = \omega(t)/(2\pi)$ using cubic spline interpolation. An example of this is shown in the upper panel of Fig. 4.11, where the red curve shows the GW frequency with clearly visible eccentricity-induced oscillations and

the green and orange curves show the fits to the maxima and minima respectively. From Eq. (4.13) we calculate $e_\omega(t)$ for each posterior sample to find the corresponding eccentricity evolution, as shown in the bottom panel of Fig. 4.11. We note that the eccentricity estimated at the initial time $e_\omega(t=0)$ can differ from the initial EOB eccentricity e_0 defined by the EOB dynamics as the eccentricity at the average frequency between apastron and periastron, as explained by Eq. (4.9).

Since we are interested in determining how the eccentricity decays as the GW frequency increases towards merger, we need to map $t \to f$. Due to the non-monotonic behavior of the GW frequency, such a mapping is not unique and hence we introduce the average GW frequency $\bar{f}(t)$ instead:

$$\bar{f}(t) = \frac{1}{2}\left(f_p(t) + f_a(t)\right), \tag{4.14}$$

where $f_p(t) = \omega_p(t)/(2\pi)$ and $f_a(t) = \omega_a(t)/(2\pi)$, and use linear interpolation to infer the eccentricity as a function of $\bar{f}$ throughout the inspiral.

As we mentioned before, this method benefits of the fact that it allows the eccentricity to be calculated directly from the GW signal and it reduces to the Newtonian definition of eccentricity, even in the high eccentricity limit, however, the method also has some limitations. A caveat to the correct calculation of $e_\omega(t)$ is, in fact, that it requires the inspiral to be sufficiently long such that many periastron and apastron peaks can be resolved. In particular, for short waveforms where we only have one or two maxima and minima available, this method is expected to become inefficient and inaccurate [96]. A way to circumvent this situation is to generate the EOB waveforms from a lower starting frequency but at the cost of increasing the waveform generation time and hence the time taken for a Bayesian inference run to complete. Similarly, in the low-eccentricity limit, we may also expect peak-finding algorithms to become numerically unstable. While strategies to amplify the peaks, such as the use of the second derivative of the frequency,

help to isolate the stationary points, in practice we found that the peaks can still be poorly resolved for a small subset of the samples. However, by cutting the frequencies at sufficiently small times ($t = 0.4$ s), we found the eccentricity estimator to be numerically robust with only a small percentage of samples ($\lesssim 0.03\%$) potentially suffering from pathologies. For those samples, we can adjust the cutoff time/frequency to produce an estimate of the eccentricity. In Fig. 4.12 we show the 90% upper limit of the eccentricity evolution $e_\omega(\bar{f})$ as a function of the average frequency for the simulated eccentric signal with $e_0 = 0.05$ and $f_0 = 20$Hz, as discussed in Sec. 4.5.2. In addition, we also show the eccentricity evolution for the injected waveform itself (black triangles). We see that it is always contained within the 90% upper limit. Finally, we apply the same method to calculate the eccentricity evolution for GW150914 from the posterior samples obtained using the eccentric `TEOBResumS-Dalí` model as outlined in Sec. 4.6.2. Fig. 4.13 shows the 90% upper limit of $e_\omega(\bar{f})$ obtained for the uniform e_0-prior distribution (blue) as well as for the log-uniform e_0-prior distribution (orange). We obtain an upper limit of $e_\omega(\bar{f})$ at ~ 20 Hz of ~ 0.075 for the analysis with the uniform e_0-prior and ~ 0.055 for the analysis with the logarithmic-uniform e_0-prior. This is comparable with Fig. 7 of [293] where it was found that GW150914 is unlikely to have an eccentricity higher than ~ 0.05 at about 20 Hz at 90% credibility. We also see that while we cannot exclude small values of eccentricities at low frequencies, once an average frequency of ~ 30 Hz is reached, any residual eccentricity $e_\omega(\bar{f})$ can no longer be distinguished from zero.

4.8 Discussion

In this chapter we presented a Bayesian validation of the `TEOBResumS-Dalí` waveform model [116] for eccentric coalescing binary black holes with aligned spins, a fully Bayesian reanalysis of GW150914 and a systematic method to estimate the eccentric-

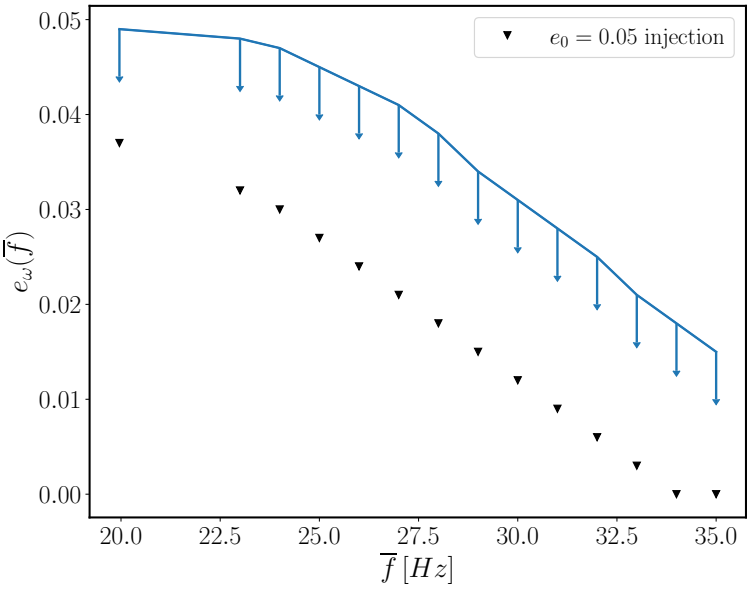


Figure 4.12: Upper limit of the 90% credibility interval for the estimated eccentricity evolution $e_\omega(\bar{f})$ for an injection with $e_0 = 0.05$. The upper limit is calculated estimating $e_\omega(\bar{f})$ for all the posterior samples, interpolating it at different values of $\bar{f}$ and then taking the 90 % credibility interval of the of the data. The black triangles represent the injection. We note that the estimated initial eccentricity is slightly lower than $e_0 = 0.05$, where e_0 is defined from the EOB dynamics.

ity in post-processing. Our study explores the potential of `TEOBResumS-Dalí` and allows us to test its reliability. Our work is an extension of our previous study [116] and demonstrates the efficacy of the model in distinguishing between circular and eccentric GW signals. In particular, we find that the differences between the quasi-circular limit of `TEOBResumS-Dalí` and its quasi-circular companion `TEOBResumS-GIOTTO` are relevant, and lead to clear (though small) biases in the recovered parameters. We attribute these biases to differences between the two models in both the dynamics (and especially in the radiative sector) and the waveform itself. When performing parameter estimation

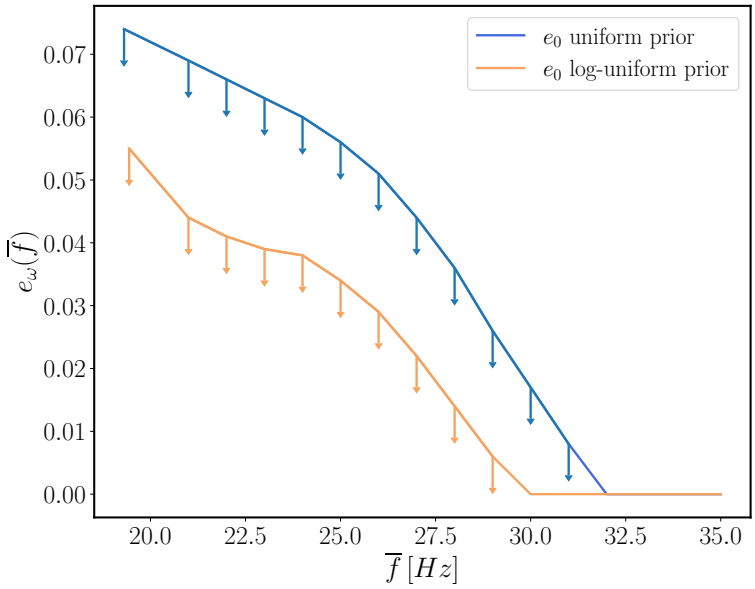


Figure 4.13: Upper limit of the 90% credibility interval for the estimated eccentricity evolution $e_\omega(\bar{f})$ for the two eccentric analyses of GW150914 with `TEOBResumS-Dalí`. The upper limit is calculated estimating $e_\omega(\bar{f})$ for all the posterior samples, interpolating it at different values of $\bar{f}$ and then taking the 90 % credible interval of the data. This result is agreement with previous results [293].

with small fixed eccentricity[6] this results in appreciable differences in the posteriors of numerous parameters. This indicates that the original `TEOBResumS-Dalí` model needs improvements, notably to recover a quasi-circular limit that is as accurate as the one of `TEOBResumS-GIOTTO`. Some work in this direction has been done [126] (see in particular Fig. 8 therein) but more investigations are needed to improve the model in the nearly equal-mass regime[7].

After testing `TEOBResumS-Dalí` for quasi-circular binaries, we validate the model on

[6] We note that if the initial eccentricity is sufficiently small the setup of the initial data is identical in both models.

[7] We also note that the `TEOBResumS` strategy is rather different from the one followed by the `SEOBNRv4EHM` model [121] that substantially limits itself at changing initial conditions, without touching the structural elements of the dynamics. Although this choice guarantees, by construction, an excellent quasi-circular limit, it introduces inaccuracies for eccentric dynamics, as highlighted in Ref. [119]

injections with nonzero initial eccentricity. In particular we find that `TEOBResumS-Dalí` excellently recovers the injected value of eccentricity. In addition, we quantify the impact of eccentricity on the estimation of the intrinsic parameters of the binary: notably, we observe that the correlations between parameters became less strong when introducing eccentricity. If neglecting eccentricity, however, we see biases in the mass and spin parameters to compensate for it.

We then perform Bayesian inference with `TEOBResumS-Dalí` on the first GW event, GW150914. We find that the circular analysis is preferred with respect to the eccentric ones with $\ln \mathcal{B}^{\rm circ}_{\rm ecc} \sim 2$. However, we also find that we cannot exclude small values of eccentricities at low frequencies, and that once an average frequency of ~ 30 Hz is reached, any residual eccentricity becomes indistinguishable from zero.

Lastly we perform the calculation of the eccentricity evolution using an eccentricity estimator deduced from the instantaneous GW frequency. After testing the calculation on mock signals, we apply the method to the data of GW150914 finding that, at about 20 Hz, the maximum eccentricity allows for the system is ~ 0.075 for a uniform prior and ~ 0.055 for a logarithmic-uniform prior on the initial eccentricity. This is quantitatively comparable with the findings of [293]. In the late stages of the preparation of this manuscript we became aware of related but independent work on eccentricity definitions [192].

Given current BBH merger rate estimates [298] and the sensitivity of the LIGO-Virgo-KAGRA detector network [299], future detections of eccentric binaries will significantly constrain the lower limit of mergers that result from clusters and other dynamical channels [21]. The possibility of several eccentric BBH candidates [33, 292] makes it crucial to have a reliable method to infer the eccentricity directly from observations. For the first time we present a systematic method to infer the eccentricity evolution directly from observations of GWs from coalescing BBHs that can be used in the future to robustly measure the eccentricity and make meaningful comparisons between different models.

Chapter 5

Mapping eccentricity evolutions between numerical relativity and effective-one-body gravitational waveforms

Declaration: This chapter is a reformatted version of A. Bonino, P. Schmidt, G. Pratten, "Mapping eccentricity evolutions between numerical relativity and effective-one-body gravitational waveforms" (2024) [2]. A. Bonino conducted NR simulations in collaboration with G. Pratten and P. Schmidt, carried out all analyses including the post-processing of the NR data, led the development of the routine to determine the map between initial conditions, generated almost all figures and contributed to the writing.

5.1 Introduction

As discussed in the previous chapter, a key limitation in comparing eccentric waveform models is that eccentricity itself is not gauge invariant in GR. This means that we need to exercise due caution if we are to ensure that we are comparing equivalent binary configurations. A number of different estimators for eccentricity have been introduced with [98] having recently identified an estimator that can be applied directly to the GW signal and has the correct Newtonian limit. If we are able to construct a map between models that allows us to set up self-consistent initial conditions (ICs), we can start to meaningfully compare the physics content of each model and the subsequent evolution of the eccentricity. This also has implications for understanding astrophysical formation scenarios, in which recent work has highlighted the need for self-consistent definitions of eccentricity between gravitational-wave data analysis and astrophysical population simulations [300]. The aim of this work is to (i) extend the parameter space coverage in available catalogs of NR simulations for eccentric binary black holes; (ii) to build a robust pipeline for measuring the eccentricity evolution from numerical relativity waveforms that is applicable even for short-duration signals that span at least $\gtrsim 7$ orbits; and (iii) to identify a map between the measured eccentricity evolution and initial conditions. We revisit the framework introduced in [1] and demonstrate its robustness against our suite of new aligned-spin eccentric NR simulations and `TEOBResumS-Dalí`. The chapter is organised as follows. Sec. 5.2 provides an extensive overview of the new suite of NR simulations we have performed. Sec. 5.3 furnishes the methodology we use to measure the eccentricity from the numerical data and assesses the impact of numerical errors on the procedure. Sec. 5.4 illustrates the derivation of the eccentricity estimator for the Newman-Penrose scalar Ψ_4 in the quasi-Keplerian parametrization. This formulation can be useful for estimating the eccentricity directly from Ψ_4 rather than h. Sec. 5.5 provides a detailed description

and assessment of the mapping between initial conditions from numerical simulations and one particular EOB waveform model, `TEOBResumS-Dalí`. In Sec. 5.6 we discuss and summarize the main results of this work. Throughout the paper, we use $G = c = 1$ unless otherwise stated.

5.2 Numerical Simulations

5.2.1 Overview

In this chapter, we present a catalog of 28 eccentric NR simulations performed with the open-source Einstein Toolkit [247, 248] within the moving punctures framework [252, 301]. We use conformally flat Bowen-York initial data [257, 258] as computed using the `TwoPunctures` thorn[1] [261]. Evolution is performed using the W-variant [256] of the Baumgarte-Shapiro-Shibata-Nakamura (BSSN) formulation of the Einstein field equations [254, 255] as implemented by the `McLachlan` thorn. The black holes are evolved using the moving punctures gauge conditions [252, 301]. The lapse is evolved using a $1 + \log$ slicing condition [263] and the shift is evolved using the hyperbolic $\tilde{\Gamma}$-driver equation [264]. Spatial derivatives are computed using an 8th order accurate finite differencing scheme together with Kreiss-Oliger dissipation [304]. The apparent horizons (AH) are computed using the `AHFinderDirect` [305]. The black hole spins are estimated through a dynamical horizon formalism as implemented in `QuasiLocalMeasures` where [306–308]

$$S = \frac{1}{8\pi} \oint_{\rm AH} n^a \varphi^b K_{ab} \, d^2A, \tag{5.1}$$

[1] A thorn is a module aimed at implementing a particular feature in the code. The Einstein Toolkit is built on Cactus [302], which is a modular infrastructure used for building numerical simulations. Cactus components are called thorns and their complete list with documentation is available at [303].

where φ^a denotes an (approximate) axial Killing vector field, n^a a spacelike unit normal to the horizon, and K_{ab} the extrinsic curvature. Adaptive mesh refinement is provided by `Carpet` [309], with the near-zone being covered by high-resolution Cartesian grids. The wave extraction zone is computed using the Llama infrastructure [310, 311], whose grids are adapted to the spherical topology of the zone and allow for high-resolution extraction out to comparatively large radii relative to standard Cartesian grids. Gravitational waves are extracted from the simulations using the Newman-Penrose Weyl scalar Ψ_4, as provided by the `WeylScal4` thorn [312]. As is conventional, Ψ_4 is decomposed into spin-weighted spherical harmonics of spin weight $s = -2$, such that

$$r\Psi_{4,\ell m} = \int_0^{2\pi} \int_0^{\pi} {}^{-2}Y^*_{\ell m}(\theta,\phi)\Psi_4(\theta,\phi)\sin\theta\, d\theta\, d\phi, \tag{5.2}$$

where ${}^{-2}Y^*_{\ell m}$ denotes the complex conjugate of the spin-weighted spherical harmonics and (θ,ϕ) the spherical coordinates on the unit sphere. The gravitational-wave strain h can then be derived from $\Psi_4 \equiv -\ddot{h}$ through fixed frequency integration (FFI) [313].

To help mitigate against near-field gauge effects, we calculate the asymptotic waveform at future null infinity $\mathscr{I}^+$ using extrapolation, e.g. [314, 315]. In this framework, we extract a quantity $\mathcal{Q}$ on a series of spheres of increasing radii and perform a least-squares fit to find the asymptotic behaviour of the non-oscillatory function $\mathcal{Q}$

$$\mathcal{Q}(u_i, r) = \sum_{n=0}^{N} \frac{\mathcal{Q}_n}{r^n}, \tag{5.3}$$

such that the leading order coefficient $\mathcal{Q}_0$ represents the asymptotic value at $\mathscr{I}^+$ at an order N. For a subset of simulations, we also use the perturbative framework introduced in [316] to extrapolate $r\Psi_4$, finding good agreement between the two methods.

5.2.2 Eccentric Initial Conditions

In order to produce eccentric initial data, we use a PN approximation to estimate the momenta of the black holes given a specific eccentricity at some reference separation. We follow the approach outlined in [317] in which the tangential momentum is perturbed away from the quasi-circular value by a correction factor that is derived within a quasi-Keplerian parametrization [77]. This procedure was used in [317] to iteratively construct low-eccentricity initial data, and in [96] to construct initial data with a prescribed eccentricity. As detailed in [96, 317], the correction factor for the tangential momenta λ_t in the low eccentricity limit is given by

$$\lambda_t(D, e_0, \nu, \text{sign}) = 1 + \frac{e_0}{2} \times \text{sign} \times \left[1 - \frac{1}{D}(\nu + 2)\right], \tag{5.4}$$

where $\nu = m_1 m_2/M^2$ is the symmetric mass ratio, $M = m_1 + m_2$ the total mass, D the initial orbital separation, e_0 is the initial eccentricity, and sign $= \pm 1$ depends on the initial phase. However, as discussed in [96], the correction factor that we apply to the tangential momentum is taken to be the average between the inverse of λ_t with a plus sign and λ_t with a minus sign, i.e.

$$\bar{\lambda}_t^0(D, e_0, \nu) = \frac{1}{2}\left[\lambda_t(D, e_0, \nu, +1)^{-1} + \lambda_t(D, e_0, \nu, -1)\right]. \tag{5.5}$$

5.2.3 Catalog of Simulations

The suite of eccentric aligned-spin NR simulations presented here spans a range of parameters. The mass ratio $q = m_1/m_2 \geq 1$ of the binaries' components ranges from $q = 1$ to $q = 6$ with initial eccentricities e_0 up to moderate values of 0.3. The largest dimensionless black hole spin that we consider for the i-th black hole is $|\chi_i| \simeq 0.5$. The simulations cover between 3 and 15 complete orbits before merger, depending on the

binary parameters, typically starting at an initial separation of $D \sim 12.5M$.

The Cartesian grids are implemented using the Carpet thorn, which provides a multi-block scheme that implements Berger-Oliger adaptive mesh refinement. The grids are nested, such that there are L^k levels of increasing resolution, i.e., $\Delta x^k = \Delta x^{k-1}/2$. The innermost Cartesian grids are initialized such that their radii are $\sim 1.2\, r_{\rm AH}$, where $r_{\rm AH}$ is the radius of the coordinate apparent horizon. Likewise, the outermost Cartesian grid, L^0, spans a domain that covers both black holes with a resolution set by the transition to the spherical grids managed by the Llama thorn. The resolution of the radial grids when extracting the gravitational waves is guided by the expected wavelength of higher multipole moments in the ringdown, typically resulting in a resolution $\Delta x < 1.0M$.

In Tab. 5.1, we provide a summary of the simulation properties for the catalog presented here, including the number of complete GW cycles up to merger $N_{\rm cycles}$ computed from Ψ_4, where we define the merger time as the time of the maximum rms amplitude of the $(\ell, m) = (2, \pm 2)$ modes and remove all data before junk radiation plus $50M$ when computing the number of GW cycles. We also give the Christodolou mass of the remnant black hole, M_f as well as its dimensionless spin $\chi_f = S_f/M_f^2$, with the Christodolou mass given by [260]

$$M_f = \sqrt{M_{\rm irr}^2 + \frac{S_f^2}{4M_{\rm irr}^2}}, \quad M_{\rm irr} = \sqrt{\frac{A}{16\pi}}, \tag{5.6}$$

where $M_{\rm irr}$ is the irreducible mass and is related to the area A of the BH horizon. The last column in Tab. 5.1 is the angular frequency measured at the first periastron $M\omega_0^p$, see Sec. 5.3 for further details. The $\{q, \chi_{\rm eff}, e_0\}$ parameter space covered by our simulations is shown in Fig. 5.1.

In addition to the final mass and spin of the remnant, we also compute the Christodoulou mass and spin associated with each black hole horizon after equilibrium is reached at a

simulation time of $t = 100M$. This allows us to evaluate the remnant spin fit of Ref. [318] for quasi-circular non-precessing BBHs and compare it to our measurements. We find that for all our simulations the absolute difference between the quasi-circular prediction and our eccentric mergers is on the order of $\mathcal{O}(10^{-3})$, consistent with previous findings for equal-mass, moderately eccentric systems [102].

We also compute the peak luminosity taking into account all multipoles of Ψ_4 up to $\ell = 6$ [319]

$$\mathcal{L}_{\rm peak} = \max_t \frac{1}{16\pi} \sum_{\ell=2}^{6} \sum_{m=-\ell}^{\ell} |\dot{h}^{\infty}_{\ell m}(t)|^2, \tag{5.7}$$

where $h^{\infty}_{\ell m}$ denotes the strain modes obtained via FFI and extrapolated to infinity. We note that we exclude the $(m = 0)-$modes from our calculation since they are significantly affected by numerical noise. The obtained peak luminosity for each simulation is given in the final column of Tab. 5.1. Comparing to the fit for quasi-circular simulations from Ref. [320], we find small differences of the order of 10^{-3}, suggesting that the binaries have circularised sufficiently before the peak emission is reached. Finally, we compute the fractional periastron advance per orbit following Eq. (29) of [321]

$$\frac{\Omega^p_{\rm orb}}{\Omega^p_r} = \frac{\phi_{\rm orb}(t^p_{i+1}) - \phi_{\rm orb}(t^p_i)}{2\pi}, \tag{5.8}$$

where t^p_i and t^p_{i+1} indicate two consecutive periastra passages, $\Omega^p_{\rm orb}$ and Ω^p_r are respectively the orbital and the radial frequencies at periastron passages, and $\phi_{\rm orb}$ is the orbital phase of the binary. We define the periastron advance per orbit as

$$K \equiv \frac{\Omega^p_{\rm orb}}{\Omega^p_r} - 1. \tag{5.9}$$

Figure 5.2 shows the periastron advance for all simulations that have at least 16 complete GW cycles. The periastron precession K across all simulations spans $\sim 0.2 - 0.63$, in

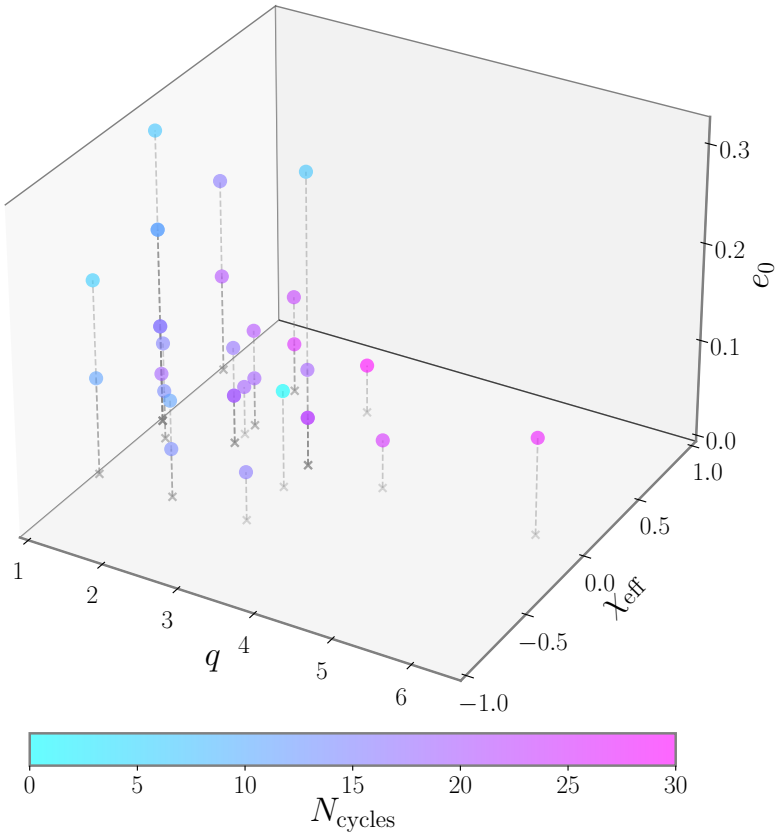


Figure 5.1: Parameter space coverage of our NR simulations listed in Tab 5.1. We show the mass ratio q, the effective aligned-spin $\chi_{\rm eff}$, and the initial PN eccentricity e_0. The colour represents the number of complete GW cycles.

agreement with Fig. (7) of [321].

5.3 Eccentricity Estimation

5.3.1 Introduction

As has been extensively discussed in the literature, e.g. see [190, 192, 294, 296], eccentricity is not a uniquely defined quantity in GR and gauge ambiguities make comparisons between measurements difficult. A number of estimators have been proposed in the liter-

ID	q	$\chi_{1,z}$	$\chi_{2,z}$	$\chi_{\rm eff}$	e_0	$D\,[M]$	$N_{\rm cycles}$	M_f	χ_f	$M\omega_{22}^p$	$\mathcal{L}_{\rm peak}$
0001	1	0	0	0	0.05	12.5	19	0.9515	0.6861	0.052	0.00105
0002	1	0	0	0	0.1	12.5	16	0.9513	0.6864	0.062	0.00106
0003	1	0.5	−0.5	0	0.1	12.5	16	0.9511	0.6855	0.060	0.00107
0004	1	−0.5	−0.5	−0.5	0.1	12.5	11	0.9620	0.5261	0.068	0.00086
0005	1	0.5	0.5	0.5	0.1	12.5	21	0.9327	0.8312	0.058	0.00137
0006	1	0	0	0	0.2	12.5	11	0.9516	0.6839	0.080	0.00103
0007	1	0.5	−0.5	0	0.2	12.5	11	0.9514	0.6830	0.070	0.00104
0008	1	−0.5	−0.5	−0.5	0.2	12.5	6	0.9622	0.5323	0.060	0.00090
0009	1	0.5	0.5	0.5	0.2	12.5	16	0.9330	0.8299	0.060	0.00135
0010	1	0	0	0	0.3	12.5	7	–	–	0.060	0.00109
0011	1.24	0.31	−0.46	−0.1163	0.05	11.05	14	0.9527	0.6869	0.060	0.00102
0012	1.24	0.31	−0.46	−0.1163	0.1	11.05	15	0.9524	0.6879	0.062	0.00104
0013	2	0	0	0	0.05	12.5	20	0.9613	0.6236	0.050	0.00080
0014	2	0	0	0	0.05	12.1579	18	0.9611	0.6235	0.054	0.00080
0015	2	−0.5	−0.5	−0.5	0.05	12.5	14	0.9700	0.4273	0.054	0.00064
0016	2	0.5	0.5	0.5	0.05	12.5	26	0.9448	0.8045	0.050	0.00107
0017	2	0	0	0	0.1	12.5	17	0.9614	0.6226	0.060	0.00079
0018	2	−0.5	−0.5	−0.5	0.1	12.5	11	0.9699	0.4264	0.068	0.00064
0019	2	0.5	0.5	0.5	0.1	12.5	23	0.9445	0.8048	0.060	0.00108
0020	3	0	0	0	0.05	12.5	22	0.9713	0.5402	0.052	0.00054
0021	3	0	0	0	0.05	12.379	22	0.9712	0.5399	0.052	0.00054
0022	3	−0.5	−0.5	−0.5	0.05	12.379	16	0.9780	0.2991	0.054	0.00043
0023	3	0.5	0.5	0.5	0.05	12.379	30	0.9582	0.7685	0.050	–
0024	3	0	0	0	0.1	12.5	19	–	–	0.062	0.00054
0025	3	0.1	−0.3	−0.2	0.1	12.5	19	0.9703	0.5747	0.064	0.00056
0026	3	0	0	0	0.3	12.5	7	–	–	0.100	0.00056
0027	4	0	0	0	0.05	12.379	25	0.9778	0.4715	0.052	0.00038
0028	6	0	0	0	0.1	12.83	28	0.9854	0.3727	0.060	0.00022

Table 5.1: Summary of the eccentric NR simulations presented in this work. The first column gives the identifier of the simulation. The following columns indicate the mass ratio q , the z-components of the dimensionless spins $\chi_{1,z}$ and $\chi_{2,z}$, the effective spin $\chi_{\rm eff}$, the initial PN eccentricity e_0, the initial separation D/M, the number of complete GW cycles up to the rms peak of the $(2,\pm2)$-modes $N_{\rm cycles}$ as well as the mass M_f and spin χ_f of the final black hole, the angular frequency at the first periastron $M\omega_{22}^p$ measured from the $(2,2)$-mode of Ψ_4 and the peak luminosity.

ature, including a more recent definition of eccentricity that resolves some of these gauge ambiguities [96]. We are particularly interested in inferring the evolution of the eccentricity directly from the gravitational-wave signal, be it on real data, (semi-)analytical waveform models, or numerical relativity simulations. This requires a number of key in-

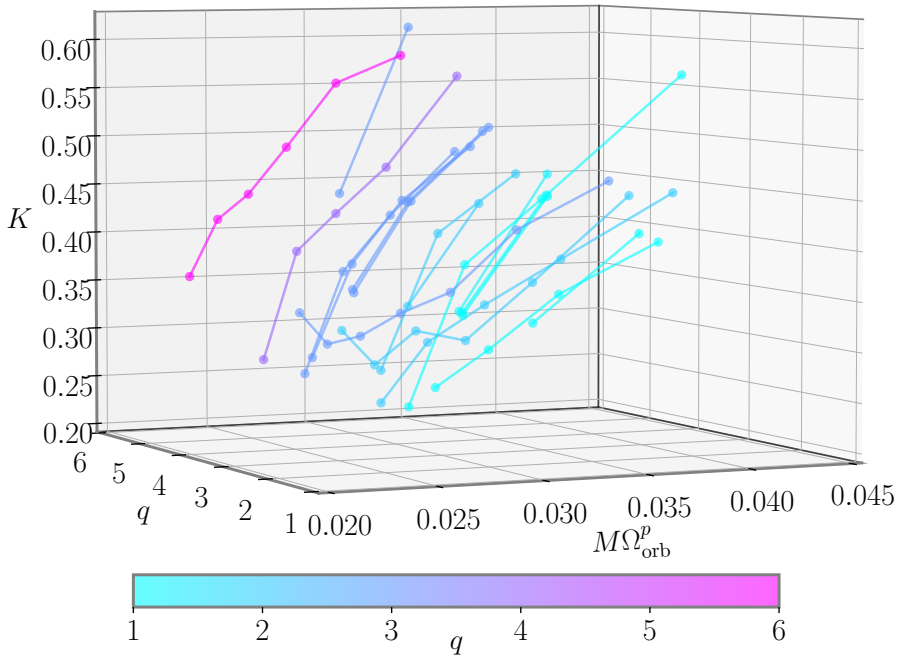


Figure 5.2: Periastron advance per orbit K as a function of orbital frequency at periastra passages (marked by the dots) for our NR simulations that span at least 16 complete GW cycles, coloured by mass ratio q.

gredients: i) a robust estimator for the eccentricity, ii) a parameter that describes the position of the compact objects on the orbit, iii) a parameter that characterizes the size of the orbit, and iv) a mapping between the time and some appropriately averaged frequency. In tackling this challenge, two highly complementary approaches have recently been presented in [1] and [192]. The framework outlined in [192] provides a very thorough and detailed discussion on the challenges of inferring eccentricity and the robustness of the implementation. To fully characterize an eccentric orbit, [192] adopts the eccentricity

estimator introduced in [98] $e_{\rm gw}(t)$ together with a generalization of the Newtonian mean anomaly $l_{\rm gw}(t)$ over an interval between two consecutive periastron passages t^p_i and t^p_{i+1} defined as

$$l_{\rm gw}(t) = 2\pi \frac{t - t^p_i}{t^p_{i+1} - t^p_i}. \tag{5.10}$$

In order to estimate the reference frequency, [192] uses an orbit-averaged frequency $\hat{\omega}_{22}$ that is again defined between two consecutive periastron passages [98, 322]. The framework presented in [1] also adopts the eccentricity estimator defined in [98] but uses the value of the eccentricity at an initial frequency such that the system always starts at the apastron. In this instance, the joint specification of the initial eccentricity and initial frequency replaces the eccentricity and mean anomaly. The final ingredient introduced in [1] is to use the mean of the frequencies between the periastra $\omega^p_{22}(t)$ and apastra $\omega^a_{22}(t)$ to estimate a monotonically increasing mean frequency $\bar{\omega}(t)$. Here we build on the methodology introduced in [1]. We note that the choice of using the mean frequency $\bar{\omega}(t)$ rather than $\hat{\omega}_{22}$ is motivated by the comparison of our numerical simulations against the EOB model `TEOBResumS-Dalí` in Sec. 5.5. However, the framework that will be presented below can also be applied to $\hat{\omega}_{22}$.

5.3.2 Methodology

The starting point for our discussion is the choice of the eccentricity estimator. Whilst this issue has previously been outlined in the literature, e.g. [1, 35, 96, 98, 116, 167, 190, 192, 296, 323], we include some discussion here for completeness. In the Newtonian limit, the eccentricity is uniquely defined by the separation of the binary at its periastron r^p

and apastron r^a

$$e_{\rm Newt.}(t) = \frac{r^a - r^p}{r^a + r^p}. \tag{5.11}$$

However, the Newtonian expression rapidly breaks down as PN corrections are included with additional parameters being required to fully characterize the eccentricity. Moreover, an eccentricity defined through the trajectories of the binary is gauge dependent, see [98, 192, 321, 324]. The second key drawback is that the estimator defined in Eq. (5.11) depends on quantities that are not directly observable through GWs, which impedes the applicability of the estimator to GW observations.

To mitigate against some of these issues, an estimator defined from the *orbital* frequencies at the periastron $\Omega^p_{\rm orb}$ and apastron passages $\Omega^a_{\rm orb}$ was introduced in [190] and is given by

$$e_{\Omega_{\rm orb}}(t) = \frac{\sqrt{\Omega^p_{\rm orb}(t)} - \sqrt{\Omega^a_{\rm orb}(t)}}{\sqrt{\Omega^p_{\rm orb}(t)} + \sqrt{\Omega^a_{\rm orb}(t)}}. \tag{5.12}$$

This estimator has the correct Newtonian limit Eq. (5.11) but is also estimated from orbital trajectories, leading to the same caveats as before. An estimator based on the GW frequency of the $(2,2)$-mode, $\omega_{22} = d\phi_{22}/dt$, was introduced in Ref. [191] and is given by

$$e_{\omega_{22}}(t) = \frac{\sqrt{\omega^p_{22}(t)} - \sqrt{\omega^a_{22}(t)}}{\sqrt{\omega^p_{22}(t)} + \sqrt{\omega^a_{22}(t)}}. \tag{5.13}$$

This estimator has the joint benefit of being gauge-independent and directly observable from the GW signal alone. However, it was noted in [98] that Eq. (5.13) does not obey the Newtonian limit, see also the discussion in [192]. To correct for this, [98] proposed a

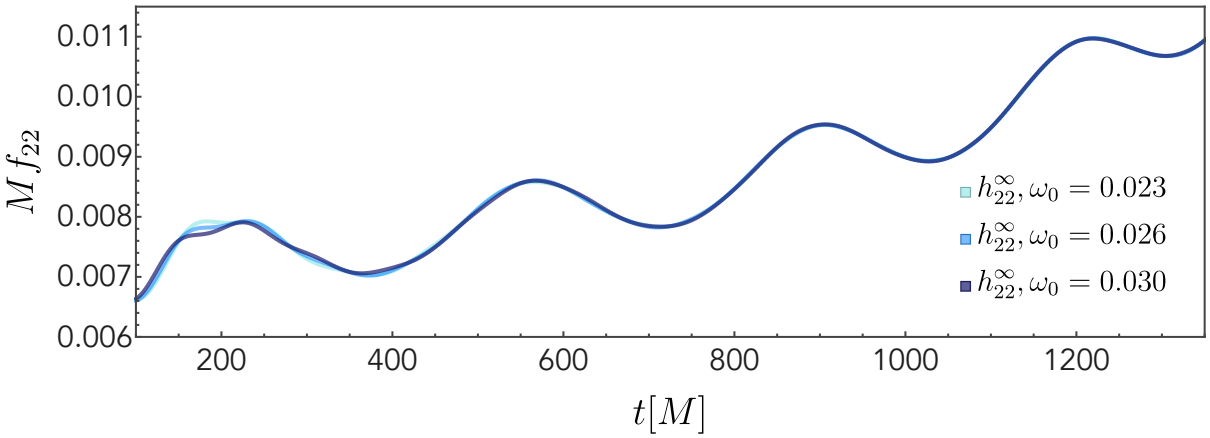


Figure 5.3: Gravitational-wave frequency $f_{22} = \omega_{22}/(2\pi)$ obtained from h^{∞}_{22} using different values of ω_0 for the simulation with `ID:0001`. Depending on the choice of ω_0 that is used to carry out the FFI, the location of the first peak varies.

modified estimator defined by

$$e_{\rm gw}(t) = \cos\left(\frac{\Psi(t)}{3}\right) - \sqrt{3}\sin\left(\frac{\Psi(t)}{3}\right), \tag{5.14}$$

where

$$\Psi(t) = \arctan\left(\frac{1 - e^2_{\omega_{22}}(t)}{2e_{\omega_{22}}(t)}\right). \tag{5.15}$$

Unless otherwise stated, we will adopt the eccentricity estimator $e_{\rm gw}(t)$ given in Eq. (5.14) for the remained of this work.

In order to measure the eccentricity from the NR data, we first need to determine $\omega_{22}(t)$. For each simulation in Tab. 5.1, we follow the steps described in Sec. 5.2 to obtain the extrapolated multipole moments $\Psi_{4,\ell m}$, from which we calculate the extrapolated strain modes $h^{\infty}_{\ell m}$. This requires us to choose a physically motivated low-frequency cutoff ω_0 for the FFI that suppresses spurious non-linear drifts arising from the numerical integration and the amplification of unphysical frequencies resulting from spectral leakage [313]. The choice of ω_0 can impact the location of the first peak in the GW frequency,

which in turn will impact the measured eccentricity. An example of this is shown in Fig. 5.3 for three different values of ω_0. As a consistency check on the above procedure, we compare against the strain h that is directly calculated from the metric perturbations via the Regge-Wheeler-Zerilli equations [325–327], as provided in the SXS waveform catalog [284]. Using `SXS:BBH:1360`, we find good agreement between the two methods for estimating h, with small variations in ω_0 having a subdominant impact on the h inferred using the FFI (see Fig. 5.7). For our analyses, we choose $\omega_0 = \omega_{22}^p/2$, where ω_{22}^p is the frequency of $\Psi_{4,22}$ at the time of the first periastron. After performing the time integration, we remove the junk radiation in all the simulations being mindful of preserving the first peak of $\omega_{22}(t)$. We have checked that this procedure is robust across all of our simulations and adopt $t_{\rm min} \equiv 100M$.

Next we need an algorithm to identify the peaks in the GW frequency, which correspond to the periastron and apastron passages. Rather than fitting the first and second derivatives to identify the peaks, as was done in [1], we instead opt to use a rational function to calculate the residual between the frequency and its secular trend. We find this to be more robust than using derivatives due to the presence of numerical noise. After isolating the peaks, we fit the maxima and the minima of the frequency using a linear fit if only two peaks are available and a nonlinear rational fit of the form $(a + bx)/(1 + cx)$ when more peaks are available. We typically find rational functions to be more robust than an equivalent high-order polynomial. In order for the procedure to work, we require at least two peaks to be present, though we caution against the accuracy of the estimated eccentricity in this limit, see the discussion below in Sec. 5.3.3.

As discussed in [1], it is convenient to define the eccentricity as a function of a monotonically increasing frequency, providing a bijective correspondence between the eccentricity and the frequency. There are two possible choices for defining such a frequency that have been adopted in the literature: The first is to define a *mean* GW frequency from the

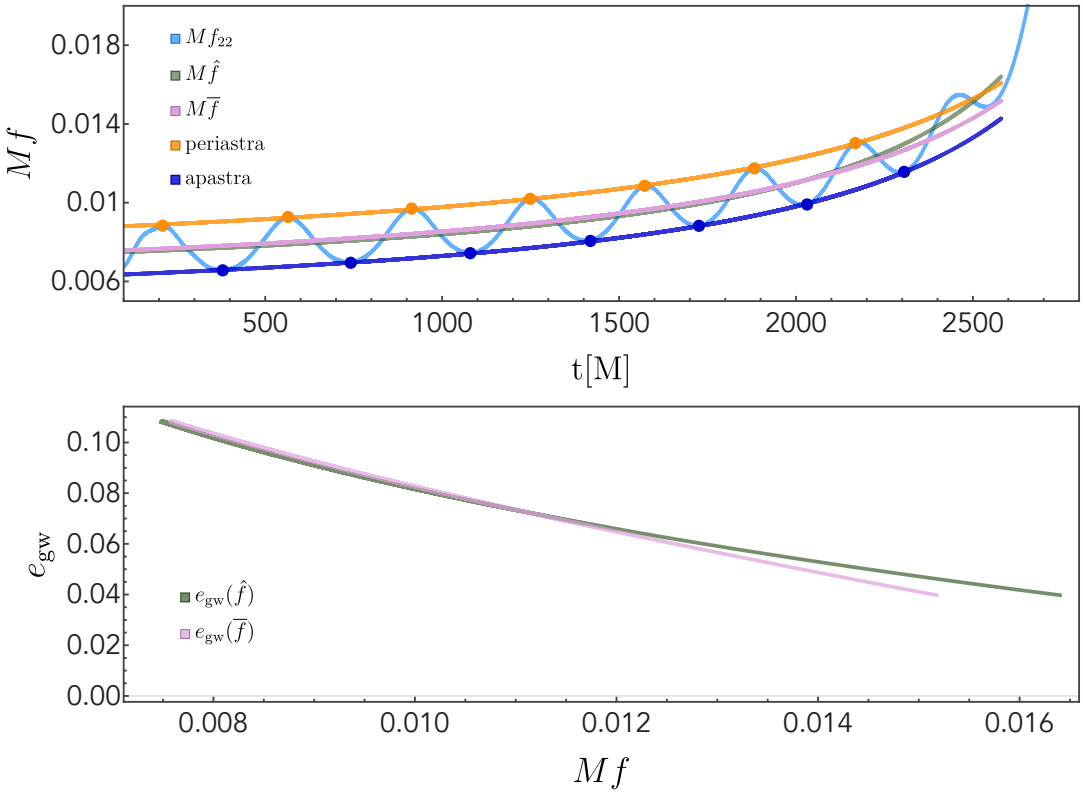


Figure 5.4: Illustration of the end-to-end procedure to measure the eccentricity from a GW signal for our $q = 6$ simulation (`ID:0028`). The top panel shows the GW frequency (light blue), the fits of the apastra (orange) and periastra (blue) following the procedure described in the main text. We also show the two monotonic frequencies $\bar{f}$ (pink) and $\hat{f}$ (green). The bottom panel shows the measured evolution of the eccentricity as a function of either $\hat{f}$ (green) or $\bar{f}$ (pink).

$(2,2)$-mode [1], as

$$\bar{f} \equiv \frac{1}{2}\left(f_{22}^{p} + f_{22}^{a}\right), \tag{5.16}$$

where $f_{22}^{X} = \omega_{22}^{X}/(2\pi)$ and X denotes the periastron (p) or apastron (a) respectively.

The second choice is to introduce an *average* GW frequency $\hat{f}$ that provides an orbit average between any two consecutive periastra or apastra [98, 192] enumerated by the

index i

$$\begin{aligned}\hat{f}^X_{22,i}(t) &= \frac{1}{t^X_{i+1} - t^X_i} \int_{t^X_i}^{t^X_{i+1}} f_{22}(t) dt, \\ &= \frac{\phi_{22}(t^X_{i+1}) - \phi_{22}(t^X_i)}{t^X_{i+1} - t^X_i}.\end{aligned} \tag{5.17}$$

The average frequency can then be defined as

$$\hat{f}_i(t) \equiv \hat{f}^p_{22,i}(t) + \hat{f}^a_{22,i}(t), \tag{5.18}$$

over the interval $t_i \leq t < t_{i+1}$. We refer the reader to [98, 121, 192, 322] for a detailed discussion on the orbit-averaging procedure. We interpolate $\hat{f}(t)$ with either a rational function or a linear fit. As also discussed in [98, 192], we observe that the average frequency $\hat{f}$ and the mean frequency $\bar{f}$ start to diverge on their approach to merger but agree in the early stages of the inspiral. This suggests that the impact of the explicit choice of the frequency parameter is subdominant in the determination of the eccentricity for simulations that have at least $3-4$ complete orbits prior to the plunge.

The end-to-end procedure to calculate the eccentricity evolution $e_{\rm gw}$ is illustrated for our $q = 6$ simulation (`ID:0028`) in Fig. 5.4: In the upper panel, we show the highly oscillatory GW frequency (light blue), the periastra (orange dots) and apastra (blue dots), as well as the nonlinear rational fits, and the mean (pink) and average frequency (green). The bottom panel shows the resulting eccentricity measurement as a function of the mean frequency (pink) and the average frequency (green). In the next section, we will discuss the robustness of this method to measure the eccentricity from NR simulations and possible sources of error.

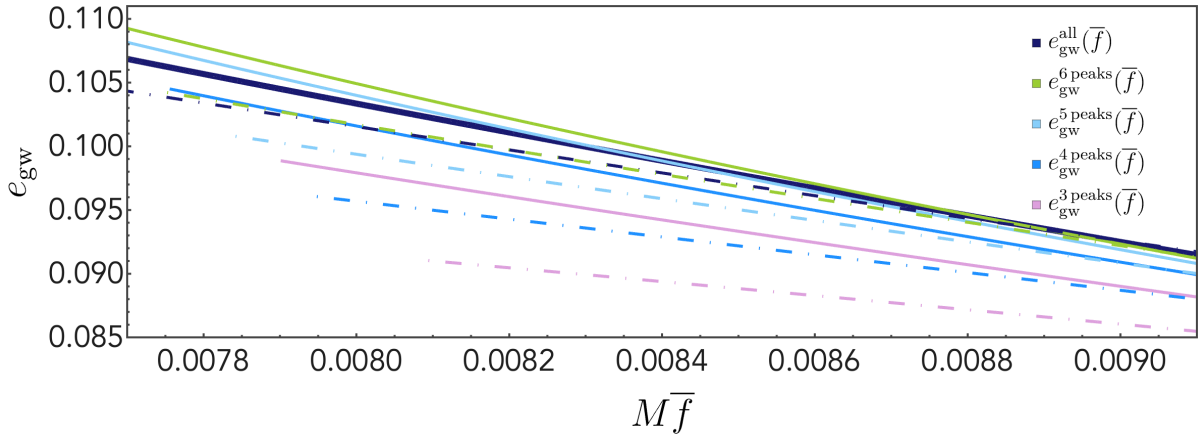


Figure 5.5: Eccentricity evolution for `ID:0028` as a function of mean frequency for different numbers of peaks. The dot-dashed lines show the evolution obtained retaining the last peak, the solid lines the evolution obtained when removing the last peak. The solid dark blue line is the reference baseline which includes all peaks except the last one. We observe that retaining the last peak (dot-dashed) usually leads to lower values of the inferred eccentricity reflecting the uncertainty in determining the eccentricity.

5.3.3 Assessment of Robustness

Filtering of Ψ_4 and choice of ω_0

In Fig. 5.6, we illustrate our filtering of Ψ_4, noting that due care needs to be taken not to introduce unphysical features into the data. Figure 5.7 shows how the eccentricity evolution depends on the choice of cutoff frequency ω_0 for `ID:0001`. The evolution is strongly dependent on the choice of ω_0 and this can introduce large numerical errors. As stated in Sec. 5.3.2, taking $\omega_0 = \omega_{22}^p/2$ was found to be a robust choice for the cutoff frequency entering the FFI.

We also checked the agreement between the strain extracted from the multipole moments $\Psi_{4,\ell m}$ and the one directly calculated from the metric perturbations via the Regge-Wheeler-Zerilli equations (as discussed in Sec.5.3.2) finding that small variations in ω_0 only have a small impact on h constructed using FFI as shown in Fig. 5.8.

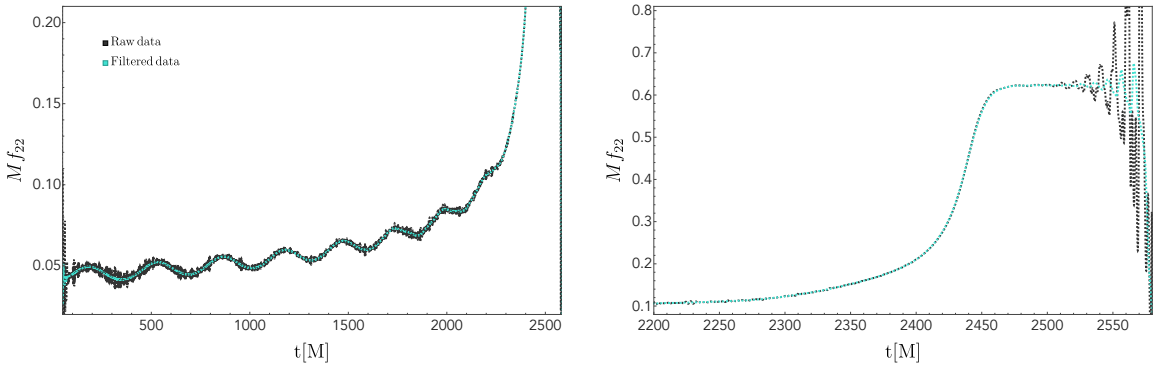


Figure 5.6: Noise filtering of Ψ_4. When filtering the data, we need to be careful to not introduce unphysical features or behaviour.

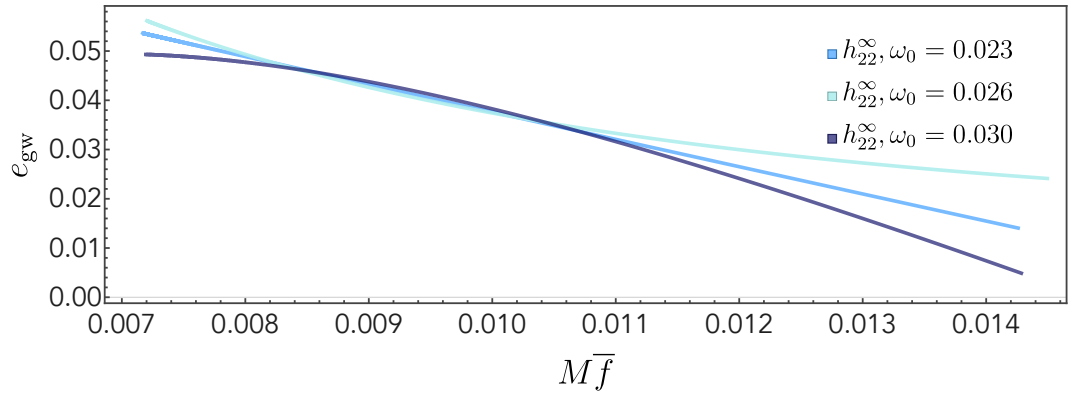


Figure 5.7: Eccentricity curves for `ID:0001` obtained by varying the FFI cutoff ω_0. We note how the eccentricity evolution is dependent on the choice of the parameter.

Simulation Length

A crucial part of the eccentricity estimation are the fits to the apastra and periastra. However, the outcome depends on the choice of the domain that the fits are performed over. To obtain a robust measurement, and to safeguard against using the eccentricity estimator in a regime where it is no longer valid, we need to truncate the data before merger. We opt to remove the last $\sim$ 4 GW cycles before merger from the data in agreement with [192], which allows us to remove all spurious peaks close to merger whilst retaining as much information as possible.

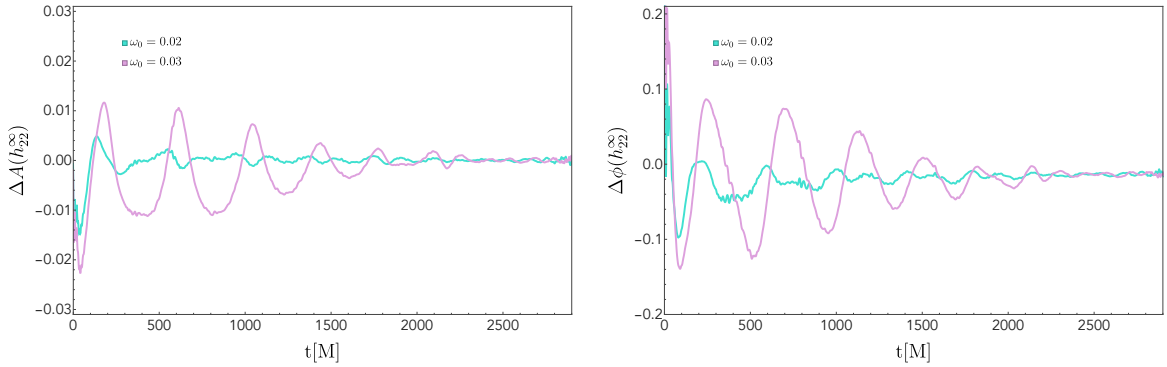


Figure 5.8: Test of consistency between the strain extracted from the multipoles of the Newman-Penrose scalar, $\Psi_{4,\ell m}$, and the one calculated from the metric perturbations via the Regge-Wheeler-Zerilli equations (as discussed in Sec. 5.3.2), using `SXS:BBH:1360`. The left (right) panel shows the differences $\Delta A(h_{22}^{\infty}) = A_{22}^{\rm RWZ} - A_{22}^{\rm FFI}$ ($\Delta\phi(h_{22}^{\infty}) = \phi_{22}^{\rm RWZ} - \phi_{22}^{\rm FFI}$) between the amplitudes (phases) calculated using the RWZ formalism and the ones extracted from $\Psi_{4,\ell m}$ for different values of ω_0. Different values of ω_0 have a small impact on the h_{22}^{∞} inferred using the FFI, leading to a maximum difference after junk radiation of ~ -0.02 for the amplitudes and ~ -0.15 rad for the phases. We note that the waveform data were also extrapolated.

We assess the impact of the number of peaks included to infer the eccentricity evolution, which we find to be non-trivial. For the vast majority of our simulations, we found it beneficial to remove the last periastron and apastron. This is demonstrated in Fig. 5.5, where we show the eccentricity evolution, $e_{\rm gw}(\bar{f})$, inferred with a varying number of peaks. Using our longest simulation with 28 GW cycles (`ID:0028`), we initially include all frequency peaks and sequentially omit peaks starting from the beginning. The solid (dot-dashed) lines represent the inferred eccentricity evolution when the last peak has been removed (retained). By comparing to the eccentricity curve that uses the most information (black line), we note that removing the last peak typically leads to a smaller spread in the estimated eccentricity relative to the evolution inferred when retaining the last peak . This is particularly prominent for short simulations that span fewer than ~ 15 GW cycles as the peaks closest to merger correspond to the regime where the GW frequency changes rapidly and can therefore shift the inferred eccentricity to higher or

lower values, introducing inaccuracies in the inferred quantities. As we do not trust the estimator close to merger, and given the observed lack of robustness, we always remove the last peak when estimating the eccentricity.

Extrapolation vs. finite radius

Numerical relativity simulations often extract the GW signal at a series of finite radii, which are then extrapolated to future null infinity. This procedure can introduce errors, which can impact the eccentricity measurement. In Fig. 5.9 we compare the eccentricity curves $e_{gw}(\bar{f})$ obtained from different extraction radii against those inferred using the extrapolated waveforms. We find very good agreement throughout the inspiral phase but see more differences during the later stages close to merger, as shown in the bottom panel. Our results suggest that one can use either finite radius waveforms or extrapolated waveforms to reliably compute the eccentricity evolution up to ~ 4 orbits before merger.

h vs. ψ_4

Until now, we have investigated the eccentricity estimated only from the $(2, 2)$-mode of the gravitational-wave strain h. In this section, we use Ψ_4 to estimate the eccentricity, as this is often a directly computed quantity in NR data.

To estimate the eccentricity evolution from Ψ_4, we use the same procedure as for h, described in Sec. 5.3.2. However, when using Ψ_4, we apply a *trimmed mean* function of Mathematica [328] filter to the data to mitigate against numerical noise when calculating the derivative of the phase, which can induce errors in determining the positions of the apastra and periastra. Care needs to be taken when filtering the data to ensure that we do not introduce unphysical features, e.g. artificially shifting the time of the merger (see Fig. 5.3).

An important subtlety is that the eccentricity measured from Ψ_4 differs from the

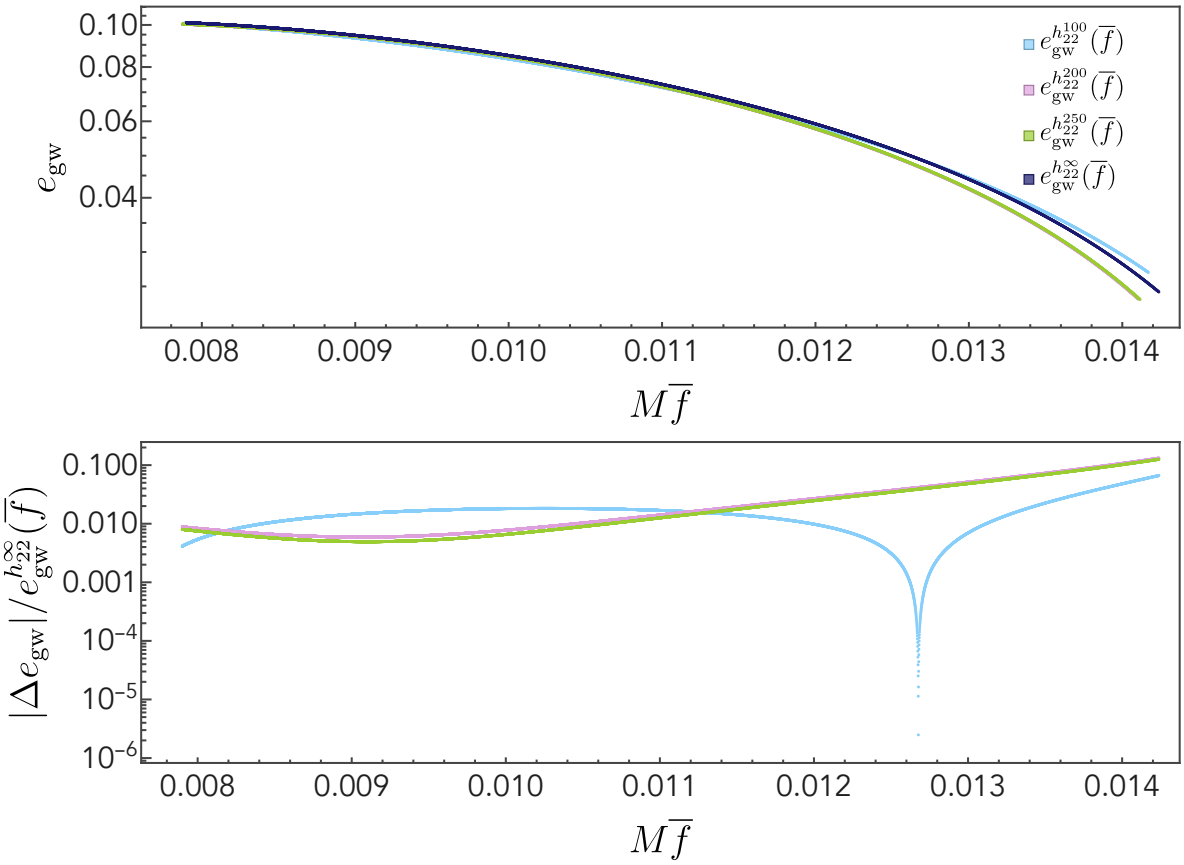


Figure 5.9: Top panel: Eccentricity evolution computed for simulation `ID:0002` for a series of finite extraction radii compared to the extrapolated waveform (dark blue). Bottom panel: The relative error, where $\Delta e_{\rm gw} = e^{X}_{\rm gw} - e^{h^{\infty}_{22}}_{\rm gw}$, between the eccentricity inferred from the extrapolated waveform and the finite-radii waveforms. The curves agree for most of the inspiral phase up to around 4 orbits before merger, where we cut the data.

eccentricity measured from h, e.g., see [324]. The eccentricity derived from the GW frequency of Ψ_4 and h can be analytically estimated to leading order in terms of an eccentric parameter e_t defined in the quasi-Keplerian parametrization [66]. To preserve a smooth flow of the discussion, the derivation of the eccentricity estimator e_{Ψ_4} will be presented in the next section. At 1PN, we have

$$e_{\Psi_4} = \frac{7}{4} e_t - \epsilon\, x \left(\frac{125 + 52\nu}{168}\right) e_t, \tag{5.19}$$

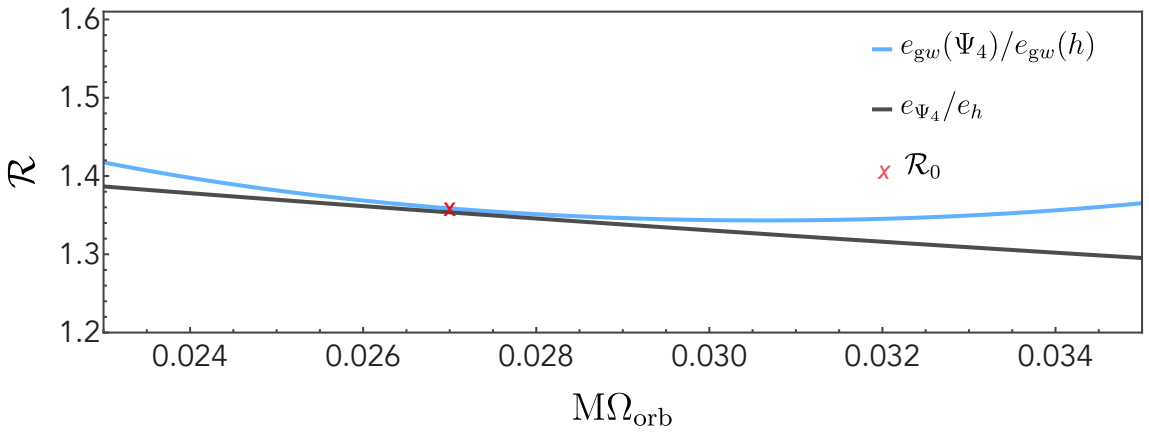


Figure 5.10: Ratio $\mathcal{R}$ between the eccentricity evolution computed employing Ψ_4 and eccentricity evolution computed employing h. The blue curve shows the ratio $e_{\rm gw}(\Psi_4)/e_{\rm gw}(h)$ as estimated from the numerical data. The black curve shows the ratio calculated from Eq. (5.19) and Eq. (5.20).

$$e_h = e_t + \epsilon\, x \left(\frac{115 - 16\nu}{42}\right) e_t, \tag{5.20}$$

where e_{Ψ_4} is derived in the quasi-Keplerian parametrization and e_h is derived using Eq. (19) and (23) of [98], expanded for small eccentricities. In Eq. (5.19) and Eq. (5.20) $x = (M\Omega_{\rm orb})^{2/3}$, and $\epsilon^2 = c^{-2}$ tracks the PN order. We can calculate the ratio between the two as a consistency check on the agreement between the eccentricity inferred from h and Ψ_4,

$$\mathcal{R} \equiv \frac{e_{\Psi_4}}{e_h} \tag{5.21}$$

and we see how this agrees at Newtonian order, with Eq. (C25) of [324]. In Fig. 5.10, we calculate the eccentricity evolution of `ID:0016` using Ψ_4 and h and numerically calculate the ratio (blue curve). The black curve shows the analytical ratio in Eq. (5.21) derived from Eq. (5.19) and Eq. (5.20). The red cross indicates the value $\{M\Omega_{\rm orb} = 0.027, \mathcal{R}_0 = 1.36\}$ calculated in [324], see Sec. II and Fig.(20) therein. We see how the value agrees with our computed ratios. The numerically and analytically estimated ratios agree

reasonably well within a range of frequencies spanning $0.025 \lesssim M\Omega_{\rm orb} \lesssim 0.029$. The disagreement at low- and high-frequencies is likely driven by a number of factors including numerical noise and the comparatively low PN order used for the estimators.

5.4 Derivation of e_{Ψ_4} in the quasi-Keplerian parametrization

In this section we derive the eccentricity estimator from the Newman-Penrose Weyl scalar Ψ_4 in Eq. (5.19) following the procedure to derive the eccentricity estimator from the waveform in the quasi-Keplerian parametrization described in Appendix C of [98]. We emphasize that this derivation is original. We start from the expression for the $(2,2)$-mode of the waveform $h_{22}^{\rm QK}$ given by Eq. (C26-C28) of [98] and compute $\Psi_4 \equiv -\ddot{h}$. The time derivatives of x, e_t, the mean anomaly l and the phase of the $(2,2)$-mode of the waveform $\phi \equiv \phi_{22}$ at 1PN are found in [67, 329] and the Kepler equation for the eccentric anomaly u at Newtonian order is obtained by deriving Eq. (2.86) [98]

$$\dot{u} = \frac{\dot{l} + \dot{e}_t \sin u}{1 - e_t \cos u}, \tag{5.22}$$

with higher-order corrections entering at 2PN.

The time derivatives of $h_{22}^{\rm QK}(x, e_t, u, l, \phi)$ are expressed as

$$\dot{h}_{22}^{\rm 1PN} \equiv \frac{dh_{22}^{\rm QK}}{dt} = \frac{\partial h_{22}^{\rm QK}}{\partial x}\dot{x} + \frac{\partial h_{22}^{\rm QK}}{\partial e_t}\dot{e}_t + \frac{\partial h_{22}^{\rm QK}}{\partial u}\dot{u} + \frac{\partial h_{22}^{\rm QK}}{\partial l}\dot{l} + \frac{\partial h_{22}^{\rm QK}}{\partial \phi}\dot{\phi}, \tag{5.23}$$

$$\ddot{h}_{22}^{\rm 1PN} \equiv \frac{d\dot{h}_{22}^{\rm 1PN}}{dt} = \frac{\partial \dot{h}_{22}^{\rm 1PN}}{\partial x}\dot{x} + \frac{\partial \dot{h}_{22}^{\rm 1PN}}{\partial e_t}\dot{e}_t + \frac{\partial \dot{h}_{22}^{\rm 1PN}}{\partial u}\dot{u} + \frac{\partial \dot{h}_{22}^{\rm 1PN}}{\partial l}\dot{l} + \frac{\partial \dot{h}_{22}^{\rm 1PN}}{\partial \phi}\dot{\phi}. \tag{5.24}$$

The 1PN expressions for $\Psi^{\rm QK}_{4,22}$ can be written as

$$\Psi^{\rm QK}_{4,22} = 4\nu x^4 \sqrt{\frac{\pi}{5}} \left[\hat{\Psi}^{\rm 0PN}_{4,22} + \epsilon \hat{\Psi}^{\rm 1PN}_{4,22}\right] e^{-2i\phi}, \tag{5.25}$$

$$\hat{\Psi}^{\rm 0PN}_{4,22} = \frac{-8 + e_t \cos(u) + e_t^2(6+\cos(2u)) + i10e_t\sqrt{1-e_t^2}\sin(u)}{(e_t\cos(u)-1)^{\,5}}, \tag{5.26}$$

$$\begin{aligned}
\hat{\Psi}^{\rm 1PN}_{4,22} = \frac{x}{168\left(1-e_t^2\right)^{3/2}(e_t\cos(u)-1)^{\,7}}\Bigg\{ & \nu\left(e_t^2-1\right)\Bigg[\sqrt{1-e_t^2}\,\big(\,e_t^4(-338\cos(2u)+17\cos(4u)+149) \\
& - e_t^3(485\cos(u)\,+87\cos(3u)) + 4e_t^2(424\cos(2u)+431) - 4436e_t\cos(u) + 1760\big) \\
& - 14ie_t\left(e_t\left[e_t\left(81-191e_t^2\right)\sin(u) + 5e_t\left(5e_t^2+1\right)\sin(3u) + 8\left(16e_t^2-31\right)\sin(2u)\right] + 260\sin(u)\right)\Bigg] \\
& + 14ie_t\left(e_t^2-1\right)\big[\,e_t\left(e_t\left(845-423e_t^2\right)\sin(u) + 45e_t\left(e_t^2+5\right)\sin(3u) + 4\left(17e_t^2-287\right)\sin(2u)\right) \\
& + 928\sin(u)\,\big] + e_t\sqrt{1-e_t^2}\,\big[\,e_t^3\,(\,-57e_t^2(\cos(4u)+45) + 1107e_t\cos(3u) + 6\left(515e_t^2-2227\right)\cos(2u) \\
& - 279\cos(4u) - 5999\,)\;+ e_t\,(-99e_t\cos(3u) + 10944\cos(2u) + 10180) + (\,6737e_t^4 + 3851e_t^2 \\
& - 16972\,)\cos(u)\,\big] + 3424\sqrt{1-e_t^2}\Bigg\}.
\end{aligned} \tag{5.27}$$

The phase of Eq. (5.25) can be written as

$$\phi^{\rm 1PN}_{22} = \hat{\phi}^{\rm 0PN}(\Psi^{\rm QK}_{4,22}) + \epsilon\hat{\phi}^{\rm 1PN}(\Psi^{\rm QK}_{4,22}), \tag{5.28}$$

$\hat{\phi}^{\rm 0PN}(\Psi^{\rm QK}_{4,22}) =$

$$\text{Arctan}\left[\frac{20e_t\left(e_t^2-1\right)\sin(u)\cos(2\phi)+2\sqrt{1-e_t^2}\sin(2\phi)\left(6e_t^2+e_t(e_t\cos(2u)+\cos(u))-8\right)}{20e_t\left(e_t^2-1\right)\sin(u)\sin(2\phi)-2\sqrt{1-e_t^2}\cos(2\phi)\left(6e_t^2+e_t(e_t\cos(2u)+\cos(u))-8\right)}\right], \tag{5.29}$$

$$\hat{\phi}^{\text{1PN}}(\Psi^{\text{QK}}_{4,22}) = \frac{A}{B}, \tag{5.30}$$

where

$$\begin{aligned}A = xe_t\Big[&2\sin(u)\left((18339-4428\nu)e_t^6+(5745\nu-30328)e_t^4+(93\nu-3965)e_t^2-2880\nu+17424\right)\\&+e_t\Big[2\sin(2u)\left(e_t^2\left((2895\nu-7804)e_t^2-3594\nu+19202\right)+1854\nu-12553\right)\\&+e_t\Big(15e_t^2\sin(5u)\left((3\nu-1)e_t^2+4\nu-6\right)+e_t\sin(4u)\left((753\nu-3163)e_t^2-1068\nu+3478\right)\\&+\sin(3u)\left(e_t^2\left(3(423\nu-2759)e_t^2-5586\nu+22582\right)+4002\nu-13990\right)\Big)\Big]\Big],\end{aligned} \tag{5.31}$$

$$\begin{aligned}B = 42\sqrt{1-e_t^2}\,(e_t\cos(u)-1)^{\,2}\Big[&e_t\Big[\left(26e_t^2-32\right)\cos(u)+e_t\left(e_t\left(e_t\cos(4u)+2\cos(3u)\right)\right.\\&\left.+\left(124e_t^2-131\right)\cos(2u)\right)\Big]-27e_t^4-91e_t^2+128\Big].\end{aligned} \tag{5.32}$$

The frequency of $\Psi^{\text{QK}}_{4,22}$ can be expressed as the derivative of the Eq. (5.28) as

$$\omega^{\text{1PN}}_{22} \equiv \frac{d\phi^{\text{1PN}}_{22}}{dt} = \frac{\partial\phi^{\text{1PN}}_{22}}{\partial x}\dot{x}+\frac{\partial\phi^{\text{1PN}}_{22}}{\partial e_t}\dot{e}_t+\frac{\partial\phi^{\text{1PN}}_{22}}{\partial u}\dot{u}+\frac{\partial\phi^{\text{1PN}}_{22}}{\partial l}\dot{l}+\frac{\partial\phi^{\text{1PN}}_{22}}{\partial\phi}\dot{\phi}. \tag{5.33}$$

At the turning points, periastron ($u = 0$) and apastron ($u = \pi$), the $(2, 2)$-waveform

frequency at 1PN can be written as

$$\omega_{22,p}^{\rm 1PN} = \frac{8(e_t+1)(2+3e_t)}{\sqrt{1-e_t^2}\left(7e_t^2+e_t-8\right)}x^{3/2} + \epsilon\, e_t\, x^{5/2}\frac{\left(9(134\nu-327)e_t^3+(2028\nu-6094)e_t^2+(2238\nu-823)e_t+24(52\nu+125)\right)}{21\sqrt{1-e_t^2}\left(7e_t^2+e_t-8\right)^2}, \tag{5.34}$$

and

$$\omega_{22,a}^{\rm 1PN} = \frac{8(2-3e_t)\sqrt{1-e_t}}{(1+e_t)^{3/2}(7e_t-8)}x^{3/2} + \epsilon\, e_t\, x^{5/2}\frac{\sqrt{1-e_t^2}\left(-9(134\nu-327)e_t^3+(2028\nu-6094)e_t^2+(823-2238\nu)e_t+24(52\nu+125)\right)}{21\,(8-7e_t)^{\,2}\,(e_t-1)\,(e_t+1)^{\,3}}. \tag{5.35}$$

Substituting Eq. (5.35) and Eq. (5.36) into Eq. (5.13), and expanding up to 1PN, we find

$$e_{\omega_{22}}(\Psi_4) = \frac{21e_t^4-(C+15)\,e_t^2+C-16}{32e_t^3-42e_t} - \frac{x\left(e_t\left(30(54\nu+269)e_t^4+(13194\nu+1615)e_t^2-192(52\nu+125)\right)\right)}{84\left(C\left(21e_t^4+(C-15)\,e_t^2-C-16\right)\right)}. \tag{5.36}$$

with

$$C = \sqrt{441e_t^4-772e_t^2+256} \tag{5.37}$$

Substituting in Eq. (5.14) and Eq. (5.15) and expanding for small eccentricities we obtain Eq. (5.19)

$$e_{\Psi_4} = \frac{7}{4} e_t - \epsilon\, x\, e_t \left(\frac{52\nu + 125}{168} \right). \tag{5.38}$$

5.5 Comparison to Analytical Models

In this section, we compare our suite of NR simulations to `TEOBResumS-Dalí` [115–117, 126–128]. In this model, eccentricity is incorporated by dressing the circular azimuthal radiation reaction term with the Newtonian (leading-order) non-circular correction [115]. This modelling of eccentricity has been improved by incorporating higher order post-Newtonian information in a factorized and resummed form [117, 119, 120], building on the 2PN results presented in [81] as explained in Chapter 3.

In the previous section we introduced a robust method for identifying pairs of mean frequency and eccentricity, $\{M\bar{f}, e_{\rm gw}\}_{\rm NR}$ at the first apastron from NR simulations. In this section we will now use the eccentricity evolution as a function of mean frequency to develop a robust procedure for directly compare eccentric NR simulations with other waveform models that may use a different definition of eccentricity, which can obfuscate comparisons between different waveform models. The advantage of this is that we can perform these direct comparisons without the need for numerical optimisations over the eccentricity as was done in previous works, e.g [116, 117, 120, 121, 330]. We will demonstrate the efficacy of our procedure for the new simulations listed in Tab. 5.1 as well as for a selected number of simulations from the `SXS` catalog [284] to compare against `TEOBResumS-Dalí`.

Numerical Relativity			TEOBResumS-Dalí		$\Delta\phi$ [rad]	$\Delta t\,[M]$
ID	$M\bar{f}_{\rm NR}$	$e_{\rm NR}$	$M\bar{f}_{\rm DALI}$	$e_{\rm DALI}$		
0001	0.0076203	0.0510486	0.00762334	0.0510313	0.439	1.64
0002	0.00853042	0.0980399	0.00852527	0.0980725	0.346	−1.78
0003	0.00853016	0.0993008	0.00853787	0.0992382	0.383	2.59
0004	0.00949267	0.116386	0.00937463	0.119877	0.319	−16.92
0005	0.00807595	0.0876158	0.00811259	0.0873528	−0.012	18.17
0006	0.0113294	0.186742	0.0111475	0.192453	0.053	−13.96
0007	0.0113196	0.1871	0.0111526	0.192687	0.098	−12.70
0008	–	–	–	–	–	–
0009	0.00987994	0.170253	0.00998654	0.16836	−0.426	24.35
0010	–	–	–	–	–	–
0011	0.00914328	0.0398909	0.00910584	0.0405297	0.195	−8.14
0012	0.00862177	0.0869213	0.00863143	0.0868591	0.490	3.17
0013	–	–	–	–	–	–
0014	0.00791276	0.053303	0.00793832	0.0531359	0.463	12.90
0015	0.00799565	0.0613589	0.00794926	0.0622875	0.211	−16.89
0016	0.00736959	0.0457956	0.0073548	0.0458236	−0.345	−16.40
0017	0.00845326	0.101092	0.00844698	0.101141	0.306	2.29
0018	0.00936701	0.11873	0.00925574	0.121864	0.018	−18.90
0019	0.00801989	0.0871244	0.00803822	0.087002	−0.40	11.03
0020	0.0074702	0.0533001	0.00747325	0.0532801	0.654	2.31
0021	0.00757658	0.0547304	0.00756598	0.0548007	0.725	−7.71
0022	0.00800259	0.0617299	0.00797527	0.0619813	0.452	−14.36
0023	0.00741632	0.0477771	0.00738662	0.0479505	−0.459	−30.35
0024	0.00834383	0.102726	0.00835499	0.102646	0.586	5.60
0025	0.00834383	0.102726	0.00835499	0.102646	0.586	5.60
0026	–	–	–	–	–	–
0027	0.00751769	0.0542868	0.00751769	0.0542868	0.499	−15.40
0028	0.00781405	0.105506	0.00777383	0.105979	1.326	−0.60
SXS:BBH:1358	0.00592098	0.152821	0.00595224	0.152033	0.509	52.10
SXS:BBH:1360	0.0065153	0.207213	0.00664508	0.202663	0.605	136.59

Table 5.2: Summary of the eccentric initial conditions calculated for our set of NR simulations (were applicable) and for two SXS simulations. The first column indicates the simulation ID, the second and third columns give the eccentric initial conditions at first apastron in the NR data. The fourth and fifth columns give the values of the eccentric initial conditions calculated following our procedure. In last two columns we give the phase differences at merger as well as the time difference Δt. Simulations without values are too short to reliably determine the eccentricity evolution.

5.5.1 Determining Initial Conditions

We start by calculating the mean frequency and eccentricity evolution of the NR simulations that have at least two clear peaks in the waveform frequency using the method described in Sec. 5.3.2. We use the first apastron to set a reference time, $t^a_{\rm NR}$, and denote the values of the mean frequency and the eccentricity at the first apastron as $\{M\bar{f}, e\}_{\rm NR}$. We then initialise `TEOBResumS-Dalí` with these values to generate the waveform to which we apply a time shift such that the merger occurs at the same time as in the corresponding NR waveform. Note that we choose $M\bar{f}$ for consistency with the definition of the monotonic frequency in `TEOBResumS-Dalí`, which is defined as $\bar{f}_{\rm TEOB} = (f^a + f^p)/2$. However, the same procedure can be applied utilizing $M\hat{f}$.

After generating the `TEOBResumS-Dalí` waveform, we find that the time of its first apastron does not exactly correspond to $t^a_{\rm NR}$. This offset is due to the following: 1) `TEOBResumS-Dalí` uses a different definition of the eccentricity, which is based on orbital quantities, while the gauge invariant estimator in Eq. (5.14) only depends on the waveform; 2) the eccentric initial conditions in `TEOBResumS-Dalí` are estimated using a post-adiabatic expansion [287] (see also Appendix A of [1]), which makes the model sensitive to changes in the frequency and eccentricities at the $\sim \mathcal{O}(10^{-6})$ level [116]. We determine the difference in the time of the apastra as

$$\Delta t = t^a_{\rm NR} - t^a_{\rm TEOB}, \tag{5.39}$$

and calculate a *new* pair of initial conditions defined at the time $t^a_{\rm NR} + \Delta t$ such that $t^a_{\rm TEOB} \simeq t^a_{\rm NR}$. The procedure can be schematically written as:

1. Calculate $\{M\bar{f}, e_{\rm gw}\}_{\rm NR}$ at the time of the first apastron $t^a_{\rm NR}$ using the methodology described in Sec. 5.3.2.

2. Use $\{M\bar{f}, e_{\rm gw}\}_{\rm NR}$ to initialise `TEOBResumS-Dalí` and perform a time shift such that the `TEOBResumS-Dalí` merger time corresponds to the NR merger time.

3. Identify the time difference Δt between the first apastron in NR vs. `TEOBResumS-Dalí`.

4. Read off from the NR data a new pair values at $t^a_{\rm NR}+\Delta t$ and denote these $\{M\bar{f}, e_{\rm gw}\}_{\rm DALI}$.

5. Use $\{M\bar{f}, e_{\rm gw}\}_{\rm DALI}$ to initialise `TEOBResumS-Dalí`.

6. Perform an overall phase shift to align the phases at $t_{\rm TEOB} = 0$.

We note that by specifying the initial conditions at the time of the first apastron for a given frequency, we are effectively fixing the mean anomaly. This provides a geometrically motivated picture for generating a set of self-consistent initial conditions. Other approaches, such as [116], numerically optimize over the eccentricity and frequency, making it difficult to meaningfully compare the dynamics in a transparent manner. The significance of this novel approach lies in its ability to enable direct comparisons between GW models and NR simulations, as well as between different models[2]. Since waveform models adopt different definitions for the orbital eccentricity, establishing such mappings is crucial to ensure consistent and reliable analyses of GW events in the future. This procedure can also be applied to construct hybrid waveforms and enhance existing waveform models. In the last chapter of this thesis, we apply this method to compare `TEOBResumS-Dalí` with our suite of NR simulations, with the goal of further improving this model in future work. It is worth noting that this method has some limitations. In particular, the procedure to determine the mapping is performed for each simulation and we could not establish a universal map valid for all configurations. Establishing a general mapping is deferred to future investigations. In addition, in our procedure for finding the EOB initial conditions we assumed that the true *first apastron* is the one closer to NR, meaning the one with the

[2]However, the mapping procedure has not yet been tested for other waveform models; this is left to future work.

smallest $|\Delta t|$. Nevertheless, it is possible that the actual first apastron may correspond to another point farther away.

To validate our procedure for determining self-consistent initial conditions we apply it to a `TEOBResumS-Dalí` waveform with $\{q = 6, \chi_{1,z} = \chi_{2,z} = 0\}$ as shown in Fig. 5.11. In the upper panel, we see that the eccentricity evolution generated using the initial conditions calculated through our procedure (blue) closely matches the original evolution (purple) with phase differences smaller than 0.2 rad (bottom panel).

The result of applying this procedure to the suite of NR simulations is summarised in Tab. 5.2. The initial conditions used to start the EOB dynamics closely resemble the initial conditions originally computed, with differences ranging from 10^{-6} to 10^{-4} for the frequency and 10^{-4} to 10^{-3} for the eccentricity. In Tab. 5.2 we also indicate the dephasing $\Delta\phi = \phi_{\rm NR} - \phi_{\rm TEOB}$ at the time of merger, which acts as a measure of the accumulated error.

A comparison between a subset of the NR simulations across the parameter space and `TEOBResumS-Dalí` waveforms is shown in Fig. 5.12. For each configuration the top panel shows the real part of h_{22}^{∞} of the NR waveform (purple, dashed) and the corresponding `TEOBResumS-Dalí` waveform (blue, solid); the bottom panel shows the dephasing $\Delta\phi$ with the maximum dephasing on the order of ~ 1.326 rad.

5.5.2 Robustness

We verify the reliability of the described procedure by testing a range of different assumptions, including: i) accounting for the last peak, ii) employing Ψ_4 instead of the strain h, iii) determining the initial conditions using the second apastron, and iv) considering finite extraction radii. The obtained initial conditions are summarised in Tab. 5.3. Figure 5.13 illustrates the impact of the inclusion (exclusion) of the last peak, as well as the inclusion (exclusion) of the first peak for `ID:0028`. The two upper panels (5.13a

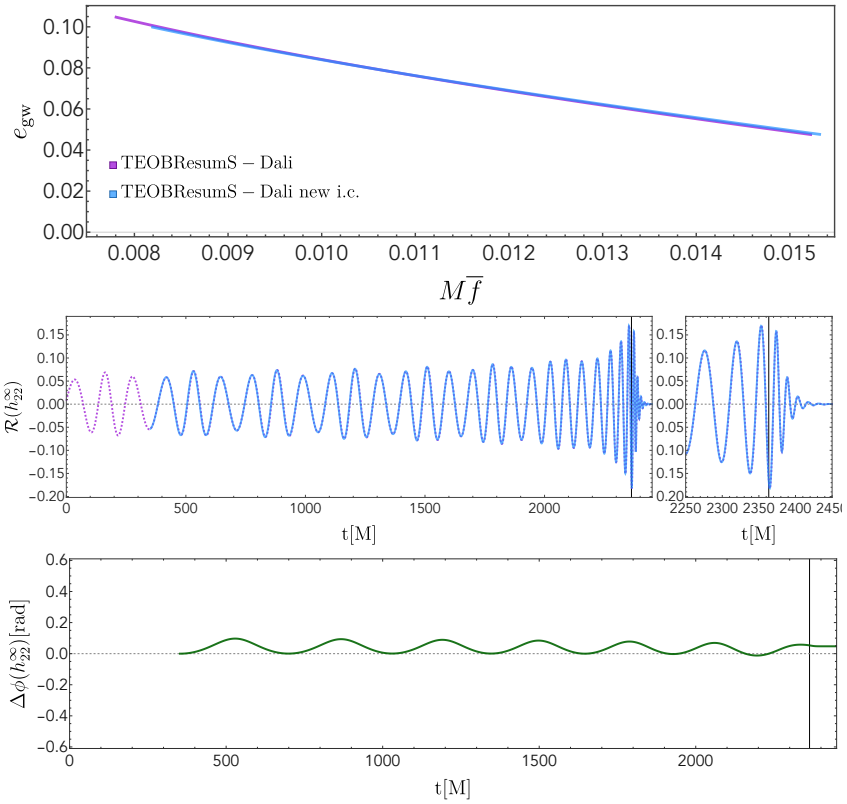


Figure 5.11: Comparison between two `TEOBResumS-Dalí` waveforms to verify the proposed procedure to determine the initial conditions. The upper panel shows the eccentricity curves $e_{\rm gw}$, the middle panel the waveforms and the bottom panel the phase differences. We find almost identical waveforms and oscillatory phase difference smaller than 0.2 rad.

and 5.13b) show the waveforms and phases obtained by retaining the first peak, the two bottom panels (5.13c and 5.13d) show the waveforms and phases obtained by removing the first peak. As expected from the study in Sec. 5.3.3, in both cases oscillatory phase differences are more pronounced and a larger phase shift is needed (see Tab. 5.3) when including the last peak (right panels) than when removing it (left panels). On the other hand, it can sometimes be advantageous to start the EOB dynamics at the second peak as the first peak can be affected by numerical noise, making the eccentricity estimation more prone to errors. We demonstrate that our procedure is capable of handling such noise artifacts by applying it starting from the second apastron instead. As expected, we

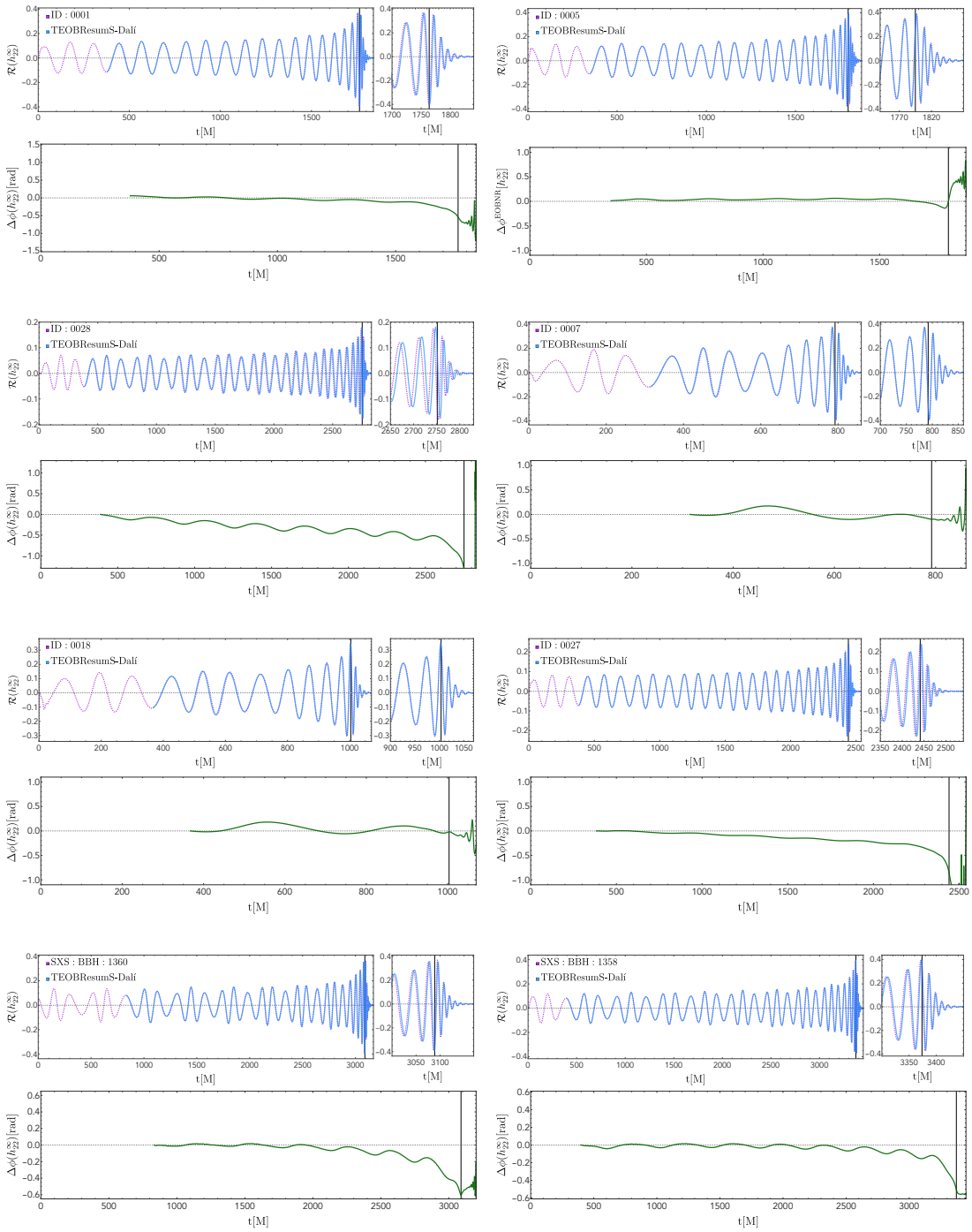


Figure 5.12: Illustration of the ICs-finding procedure for a selection of NR simulations. For each simulation we show the NR (purple, dashed) and `TEOBResumS-Dalí` (blue, solid) waveforms in the top panel with a zoom-in of the merger part on the right. The bottom panel shows the phase difference. We see that the EOB waveforms generated with the initial conditions as determined by the procedure described in Sec. 5.5.1 closely match the NR waveforms; the phase differences are less than ~ 1 rad at merger.

Numerical Relativity			TEOBResumS-Dalí		$\Delta\phi$ [rad]	$\Delta t\,[M]$
ID	$M\bar{f}_{\rm NR}$	$e_{\rm NR}$	$M\bar{f}_{\rm DALI}$	$e_{\rm DALI}$		
0001	0.0076203	0.0510486	0.00762334	0.0510313	0.439	1.64
0001 (incl. last peak)	0.00765019	0.048717	0.00762572	0.0487785	0.461	−14.86
0002	0.00853042	0.0980399	0.00852527	0.0980725	0.346	−1.78
0002 ($r_0 = 100$ M)	0.00851419	0.0970785	0.0085116	0.0970969	0.636	−0.87
0002 ($r_0 = 200$ M)	0.00851574	0.0974921	0.00851574	0.0974921	0.511	1.56
0002 ($r_0 = 250$ M)	0.00851735	0.0975702	0.00852125	0.0975467	0.403	1.31
0016	0.00736959	0.0457956	0.0073548	0.0458236	−0.345	−16.40
0016 (Ψ_4)	0.00738382	0.046704	0.00734072	0.0468821	−0.483	−38.83
0028	0.00781405	0.105506	0.00777383	0.105979	1.326	−44.02
0028 (incl. last peak)	0.00827036	0.0990475	0.00820059	0.0997272	1.285	−70.19
0028 ($2^{\rm nd}$ apastron)	0.00822478	0.101856	0.00818341	0.102409	1.285	−36.69
0028 ($2^{\rm nd}$ apastron, incl. last peak)	0.0078723	0.102723	0.00779677	0.103425	1.504	−96.02
SXS:BBH:1360 (earlier time)	0.00598258	0.228105	0.00597789	0.228307	0.645	−8.28

Table 5.3: Summary of initial conditions calculated under different assumptions: Varying number of peaks, using Ψ_4 instead of h and different finite extraction radii. The last row gives the initial conditions inferred when extrapolating to earlier times.

obtain slightly different initial conditions but find a very similar maximal dephasing at merger. As before, the largest phase error is seen when also including the last peak.

As shown previously in Fig. 5.9 for ID:0002, waveforms extracted at a finite radius rather than extrapolated to infinity yield a slightly different eccentricity evolution, resulting in a small change in initial conditions. We find that the smallest extraction radii lead to the largest dephasing at merger, while the extrapolated waveforms give the best agreement with TEOBResumS-Dalí.

Finally, we also test the procedure using Ψ_4 instead of the strain. This can be useful when the waveform extraction procedure is particularly challenging or affected by numerical noise. This approach allows indeed to compute the eccentricity evolution directly from Ψ_4 by simply using the ratio Eq. (5.21). Employing the latter we calculate the ratio $\mathcal{R}(\bar{\omega}_{\rm NR}/2)$ where $\bar{\omega}_{\rm NR} = 2\pi\bar{f}_{\rm NR}$ for ID:0016 at the frequency of first apastron to be 1.385.

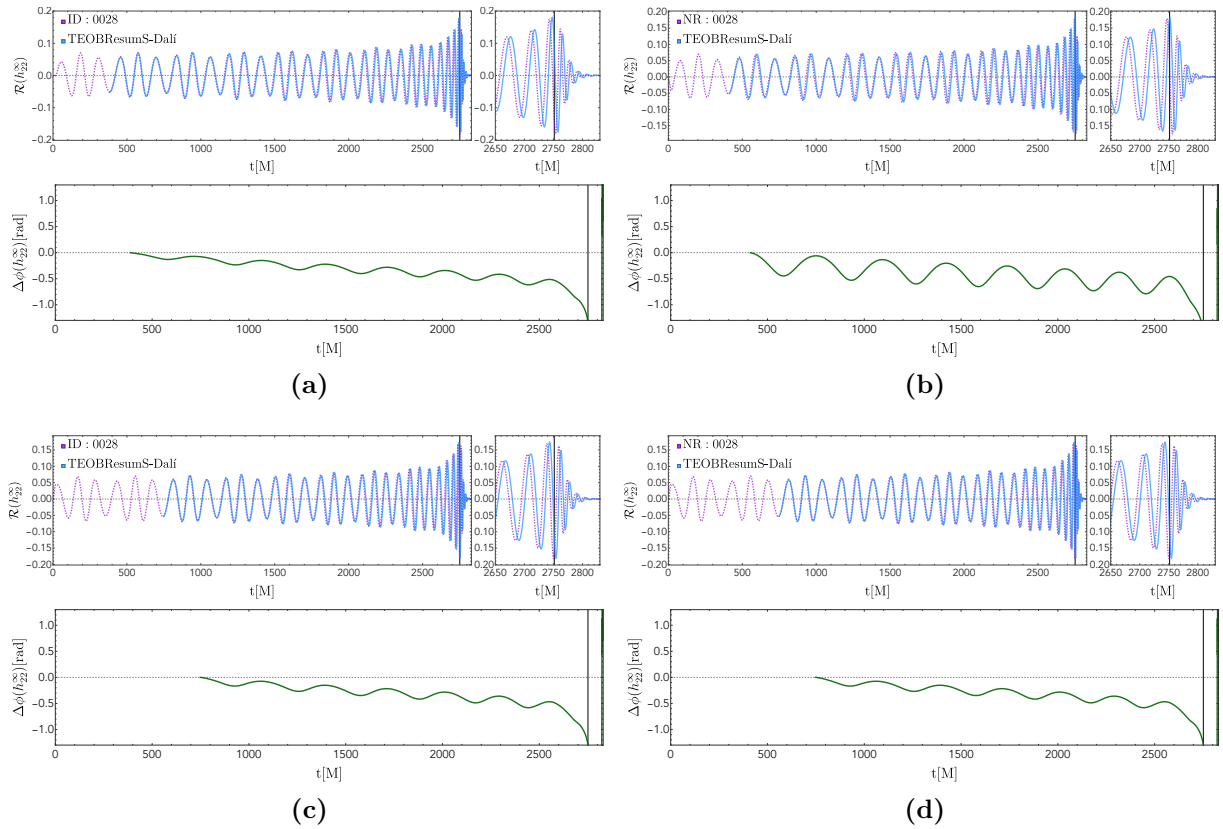


Figure 5.13: Here we explore the impact of including the last peak using simulation `ID:0028`. The two upper panels (a and b) show the waveforms and phases differences obtained when retaining the *first* peak. The bottom two panels (c and d) are when we exclude the *first* peak from the estimation. The left panels (a and c) are obtained by *removing* the last peak, whereas the right panels (b and d) are obtained by *including* the last peak. We generally observe larger oscillatory phase differences when we include the last peak, i.e., the right panels.

The initial eccentricity is then calculated as

$$e_{\rm NR} = \frac{e_{\rm gw}(\Psi_4)}{\mathcal{R}}. \tag{5.40}$$

The phase differences obtained using Ψ_4 are very similar to the ones obtained from h, see Tab. 5.3. This suggests that the procedure is equally applicable to Ψ_4 and h.

Overall, we find that our procedure is robust and gives self-consistent results for the

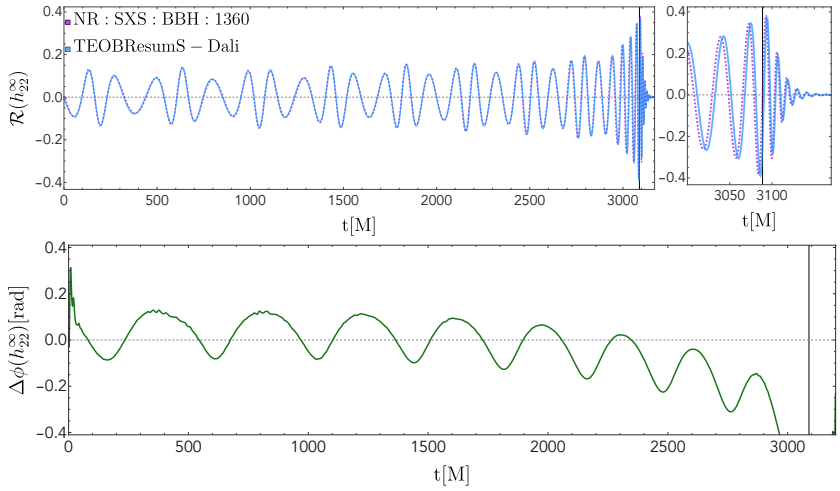


Figure 5.14: Comparison of `SXS:BBH:1360` (purple) and `TEOBResumS-Dalí` (blue) using the end-to-end pipeline to calculate the initial conditions at earlier times, as described in Sec. 5.5.3, together with the phase difference (lower panel).

various assumptions made.

5.5.3 Extrapolation to Earlier Times

A limitation of this procedure is that we define a reference time based on the first apastron in the data. When using NR simulations, for example, this results in a loss of $\sim 300-400M$ at the start of the simulation. We could start the evolution from an earlier time using, e.g., a backwards PN evolution or, alternatively, we could try to extrapolate the initial conditions. In this section we test the extrapolation of the initial conditions, demonstrating that we can robustly generate a waveform from earlier times.

Using `SXS:BBH:1360`, we want our waveform to start at $t_{\rm NR} = 0$. However, this requires determining initial conditions for an apastron that occurs before $t_{\rm NR} = 0$. As we do not know the exact location of the apastron at earlier times, we empirically estimate it using the periastron advance as a guide, e.g., we find $t^a_{\rm NR} \sim -63M$ for `SXS:BBH:1360`. The procedure laid out in Sec. 5.5.1 is then slightly modified:

1. Read off the NR initial conditions at $t^a_{\rm NR} + \Delta t$, taking Δt to be the time difference

already found and listed in Tab. 5.2. This constitutes our original initial conditions, as listed in columns two and three of Tab. 5.3.

2. We then iterate the procedure to find new initial conditions based on the original values identified in 1) to help mitigate against the fact that the apastron was only estimated empirically, therefore allowing for a more precise measurement of the initial conditions.

The initial conditions, phase difference and the final Δt are listed in the last row of Tab. 5.3. The total time difference between the NR and the EOB evolution is given by the sum of the time differences listed in Tab. 5.2 and Tab. 5.3. The resulting waveforms and dephasing are shown in Fig. 5.14. We see that the phases differences are larger compared to Fig. 5.12 but the dephasing is still quite small, with a maximum of 0.645 rad at merger. Whilst this procedure is promising, the robustness of extrapolating to earlier times needs to be carefully checked across the parameter space.

5.5.4 Mismatches

In order to quantify the (dis)agreement between the NR simulations and the `TEOBResumS-Dalí` waveforms, we use the match $\mathcal{M}$, defined in the usual way as

$$\mathcal{M}(h_{\rm NR}, h_{\rm TEOB}) = \max_{t_c,\phi_c} \frac{\langle h_{\rm NR}|h_{\rm TEOB}\rangle}{\sqrt{\langle h_{\rm NR}|h_{\rm NR}\rangle\langle h_{\rm TEOB}|h_{\rm TEOB}\rangle}}, \tag{5.41}$$

where t_c and ϕ_c denote the time and phase of coalescence respectively, and $\langle h_{\rm NR}|h_{\rm TEOB}\rangle$ denotes a noise-weighted inner product

$$\langle h_{\rm NR}|h_{\rm TEOB}\rangle = 4\Re \int_{f_{\rm min}}^{f_{\rm max}} \frac{\tilde{h}_{\rm NR}(f)\tilde{h}^*_{\rm TEOB}(f)}{S_n(|f|)} df, \tag{5.42}$$

where $S_n(|f|)$ is the one-sided power spectral density (PSD) of the strain noise, $\tilde{h}$ the Fourier transform of h and * denotes the complex conjugate. In practice, we will use the mismatch, which is defined as

$$\overline{\mathcal{M}}(h_{\rm NR}, h_{\rm TEOB}) = 1 - \mathcal{M}(h_{\rm NR}, h_{\rm TEOB}) \tag{5.43}$$

where $h_{\rm NR} \equiv h_{22}^{\infty}$ from the numerical data. The mismatches are computed assuming $f_{\rm min} = 20$ Hz and a total mass M in the range $[50, 200]M_{\odot}$. We use a PSD that corresponds to the approximate sensitivity of the Advanced LIGO detector in the fourth observing run (O4) [331, 332]. The resulting mismatches are shown in Fig. 5.15. We find good agreement between the NR and EOB waveforms across the parameter space spanned by our simulations, with a typical mismatch on the order of $\sim \mathcal{O}(10^{-3})$. We do not find any strong correlations with q, e_0 and $\chi_{\rm eff}$ but note that the worst mismatches between our NR data and `TEOBResumS-Dalí` waveforms are found for unequal masses and large eccentricities. Our result is in broad agreement with [116] but it is crucial to note that, as opposed to other works, we have not performed any optimisations over eccentricity parameters as this is not necessary due to the identified mapping between initial conditions. This allows us to treat the orbital eccentricity as a meaningful physical parameter that characterises the binary rather than as a nuisance parameter that is numerically optimised over.

5.6 Conclusions

The primary goal of this chapter was to establish and validate a robust framework for defining a map between the eccentricity evolution as measured directly from a GW signal and eccentric initial conditions to allow for a direct comparison between different eccentric waveform models. Our framework builds on [1] in terms of the eccentricity

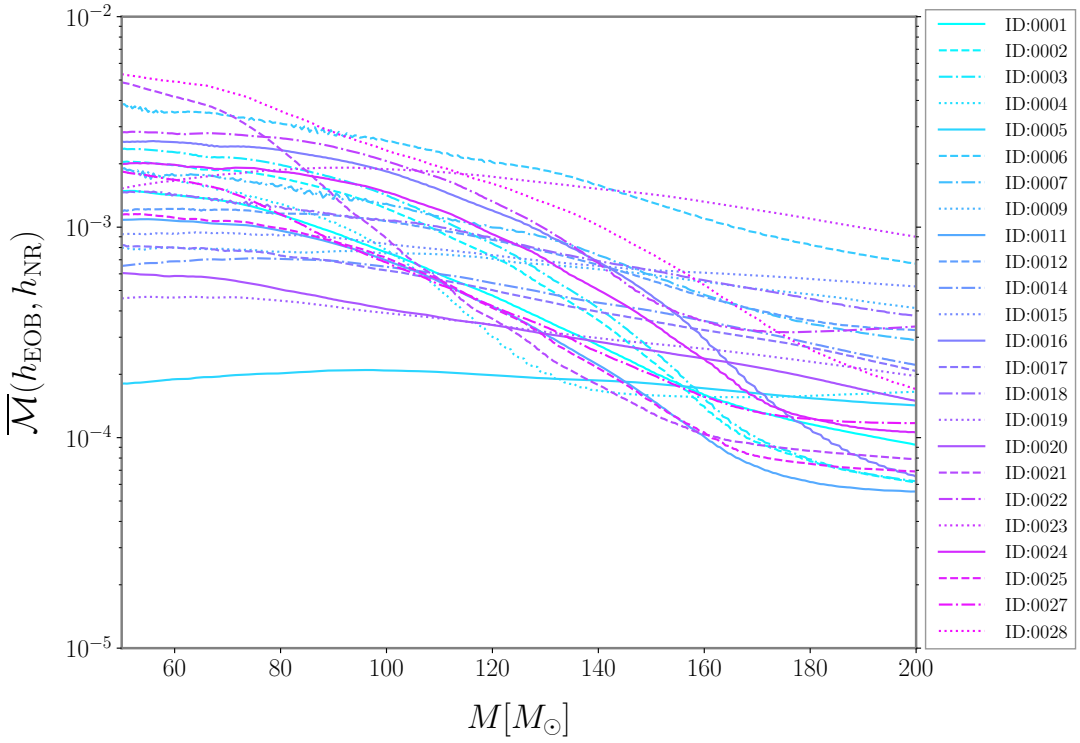


Figure 5.15: Mismatches between our suite of numerical simulations and `TEOBResumS-Dalí` across a range of total masses. The mismatches vary between a few times 10^{-3} to just below 10^{-4}. For binaries with a total mass of $65M_\odot$ the mean mismatch across our simulations is 0.0015.

estimator $e_{\rm gw}$ recently introduced in [98], which has the correct Newtonian limit and is defined purely in terms of observables from the GW signal. The pipeline can be applied to any generic waveform data, including NR simulations and semi-analytic waveform models. In support of the analysis, we introduced a suite of 28 aligned-spin, eccentric NR simulations for binary black hole mergers, designed to help us understand the dynamics of eccentric binaries. We validated our pipeline against this catalog of NR simulations, as well as publicly available SXS simulations.

A crucial ingredient is the measurement of the eccentricity evolution. To assess its robustness, we systematically tested a number of possible limitations. In particular, we investigated how the number of peaks in the GW signal, the data quality, extrapolation to

future null infinity, and the use of Ψ_4 versus the strain h impacted our ability to infer the eccentricity evolution from the NR simulations. As a result, we found that the minimum length of an NR simulation required to accurately measure the eccentricity evolution is ~ 15 GW cycles (~ 7 orbits). Similarly, we found that the procedure breaks down as the binary approaches merger and is unreliable ~ 4 GW cycles (~ 2 orbits) before merger, see also the discussion in [192]. In testing the pipeline, we also found that dropping the last peak from the fitting procedure results in a more reliable determination of the eccentricity, as discussed in Sec. 5.3.2, see also Fig. 5.13. Furthermore, our procedure can be defined using various definitions of (monotonic) frequency, including the mean frequency and the average frequency, also in agreement with [192].

With a reliable procedure for determining $e_{\rm gw}$ in place, we presented a simple framework for mapping eccentric initial conditions between NR simulations and EOB models in Sec. 5.5.1. When performing comparisons between NR simulations against `TEOBResumS-Dalí`, we found that we needed to account for a time shift between the NR and EOB waveforms before we could construct a map between the initial conditions. Nevertheless, after accounting for this time shift, we found excellent agreement between the NR and EOB initial conditions, resulting in waveforms with typical mismatches on the order of $\sim 10^{-3}$, as shown in Fig. 5.15. We also verified that the determination of the initial conditions is robust under different options for the input data such as waveform extrapolation, finite extraction radii or the use of Ψ_4, finding that the least dephasing is achieved when determining the eccentricity evolution from the extrapolated strain and excluding the last apastron peak in the fitting procedure. Utilising the periastron advance as an empirical estimator, we were also able to extrapolate our procedure to earlier times, allowing us to retain more of the NR data.

A key advantage of our framework is that we no longer need to perform any numerical optimisation over eccentric parameters but it instead appeals to geometrically meaningful

initial conditions. A key practical application of this approach is towards calibrating an EOB model, in which the eccentricity evolution is matched to that of a corresponding NR simulation in terms of the same $\{M\bar{f}, e_{\rm gw}\}$ pair. We will leave this for future work.

Chapter 6

Synergies between effective-one-body and numerical relativity

Declaration: This Chapter is based on a work in progress that A. Bonino is carrying out in collaboration with G. Pratten and P. Schmidt at the University of Birmingham. A. Bonino carried out all the analytical calculations and implemented them in the `TEOBResumS` *code. A. Bonino carried out all comparisons to NR, generated all figures and wrote the text.*

6.1 Introduction

Deviations from circular motion introduce perturbations in both the dynamical quantities and the emitted gravitational radiation, leading to complications in the analysis of gravitational wave signals. As discussed in the previous chapters, a further difficulty arises due to the gauge-dependent nature of orbital eccentricity, which is inherently tied to the dynamics of the system. To enable comparisons of eccentric signals across different datasets, Ref. [2] introduced a mapping between a gauge-invariant measure of eccentricity built on the estimator [98] and the eccentricity used in `TEOBResumS-Dalí` which depends

on the dynamics of the EOB system. In this chapter, we employ this mapping to perform a comparison between the `TEOBResumS-Dalí` and the suite of non-precessing numerical relativity simulations introduced in Ref. [2]. The primary objectives are to gain a deeper understanding of the key quantities that characterise non-circular effects within the EOB framework and identify where these effects are predominant in the conservative dynamics, emitted radiation and waveform.

6.2 Initial conditions

6.2.1 Method

In our analysis we utilize the set of eccentric, aligned-spin binary black holes with mass ratio ranging from 1 to 6 presented in Tab. 5.1 and Ref. [2]. Simulations `ID:0008`, `ID:0013`, and `ID:0026` are excluded due to the inability to compute their initial conditions caused by an insufficient number of identifiable peaks in the gravitational wave frequency. The initial conditions for the NR and EOB systems are listed in Tab. 6.1 and include updates relative to those in Tab. 5.2 reflecting the use of a newer version of the model available in [333]. Additionally, two errors identified in simulations `ID:0011` and `ID:0025` have been corrected. In Ref. [2] we generated the $(2, 2)$-mode of the gravitational wave strain h using `TEOBResumS-Dalí` and compared the resulting waveforms to those obtained from the NR simulations. The waveforms, along with their corresponding phase differences, are presented in Fig. 5.12. In Sec. 6.2.2 we discuss initial conditions while in Sec. 6.3.1 we show the energy and angular momentum fluxes, identifying regions where discrepancies between the EOB model and NR simulations arise. In Sec. 6.3.3 and Sec. 6.3.4 we assess the agreement between EOB and NR using gauge-invariant relations between the binding energy and total angular momentum of the system. The procedure we present here is intended not only to showcase our results, but also as a useful guideline for future studies

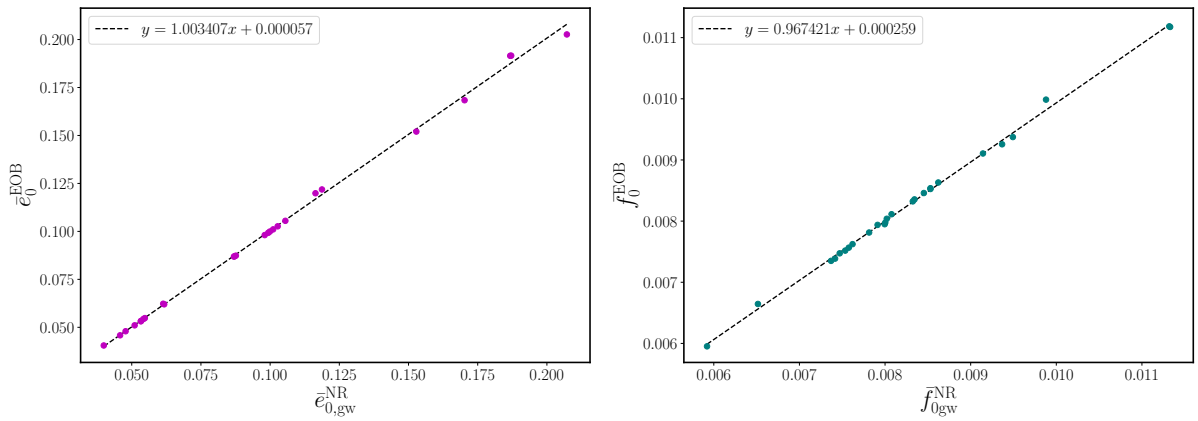


Figure 6.1: `TEOBResumS-Dalí` initial conditions as computed in Tab. 6.1. We observe an overall linear trend indicated by the dashed lines in the panels, however variations in initial frequency and eccentricity can lead to significant phase differences and it is not possible to obtain a reliable fit of the data that can be used to determine the initial conditions.

and baseline for improving eccentric EOB models in the comparable-mass regime.

6.2.2 EOB initial conditions

Fig. 6.1 displays the EOB initial conditions used to generate the gravitational waveform strain with `TEOBResumS-Dalí` and align its $(2,2)$-mode to the one extracted from NR simulations. The waveform multipoles $h_{\ell m}$ are extracted from the Newman-Penrose Weyl scalar Ψ_4 [312] as described in Eq. (5.2) and extrapolated to future null infinity $\mathscr{I}^+$ using Richardson extrapolation [314, 315] using the `ReadRadiallyExtrapolatedStrain` function from the `SimulationTools` [334] package in Mathematica [328]. The two panels of the figure show that the relations linking the initial eccentricities $e_0^{\rm EOB}$, $e_{0,\rm gw}^{\rm NR}$ and frequencies $f_0^{\rm EOB}$, $f_{0,\rm gw}^{\rm NR}$ exhibit an overall linear trend. However, the system exhibit a strong sensitivity to variations as small as $\sim 10^{-5}$ in eccentricity and $\sim 10^{-6}$ in frequency and even minor changes in the initial conditions can induce significant oscillations in the phase differences, as observed in Fig. 5.12. As a result, attempts to derive a robust fitting formula to predict EOB initial conditions have proven unreliable, and the method intro-

Numerical Relativity			TEOBResumS-Dalí		$\Delta\phi$ [rad]	$\Delta t\,[M]$
ID	$M\bar{f}_{\rm NR}$	$e_{\rm NR}$	$M\bar{f}_{\rm DALI}$	$e_{\rm DALI}$		
0001	0.0076203	0.0510486	0.00762334	0.0510313	0.459	1.64
0002	0.00853042	0.0980399	0.00852527	0.0980725	0.530	−1.78
0003	0.00853016	0.0993008	0.00853787	0.0992382	0.411	2.59
0004	0.00949267	0.116386	0.009392074	0.1193554	0.395	−14.42
0005	0.00807595	0.0876158	0.00811259	0.0873528	−0.012	18.17
0006	0.0113294	0.186742	0.0111475	0.192453	0.053	−13.96
0007	0.0113196	0.1871	0.0111526	0.192687	0.098	−12.70
0009	0.00987994	0.170253	0.00998654	0.16836	−0.426	24.35
0011	0.00914328	0.0398909	0.00910584	0.0405297	0.289	−8.14
0012	0.00862177	0.0869213	0.00863143	0.0868591	0.490	3.17
0014	0.00791276	0.053303	0.00793832	0.0531359	0.463	12.90
0015	0.00799565	0.0613589	0.00794926	0.0622875	0.211	−16.89
0016	0.00736959	0.0457956	0.0073548	0.0458236	−0.345	−16.40
0017	0.00845326	0.101092	0.00844698	0.101141	0.306	2.29
0018	0.00936701	0.11873	0.00925574	0.121864	0.018	−18.90
0019	0.00801989	0.0871244	0.00803822	0.087002	−0.40	11.03
0020	0.0074702	0.0533001	0.00747325	0.0532801	0.654	2.31
0021	0.00757658	0.0547304	0.00756598	0.0548007	0.725	−7.71
0022	0.00800259	0.0617299	0.00797527	0.0619813	0.452	−14.36
0023	0.00741632	0.0477771	0.00738662	0.0479505	−0.459	−30.35
0024	0.00834383	0.102726	0.00835499	0.102646	0.586	5.60
0025	0.00832376	0.0999094	0.00832258	0.0999178	0.591	−0.60
0027	0.00751769	0.0542868	0.00751769	0.0542868	0.499	−15.40
0028	0.00781405	0.105506	0.00777383	0.105979	1.330	−0.60

Table 6.1: Summary of the updated (computed using the version of the model available in [333]) eccentric initial conditions calculated for our set of NR simulations presented in [2]. As the previous Table, the first column lists the simulation ID. The second and third columns show the eccentric initial conditions at the first apastron based on the NR data. The fourth and fifth columns present the corresponding values computed using our method. The final two columns provide the phase difference at merger and the time difference Δt.

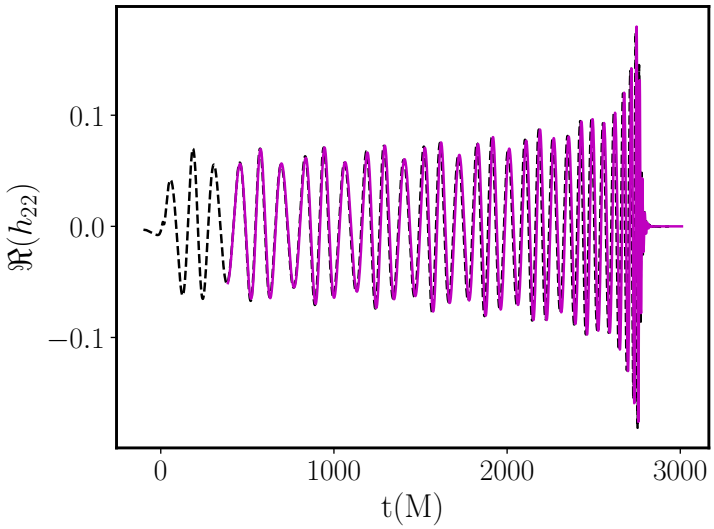


Figure 6.2: Alignment of the $(2,2)$-mode for `ID:0028`. The waveforms are aligned following the procedure outlined in [2].

duced in [2] remains the most robust approach to compute initial conditions. Fig. 6.2 shows the $(2,2)$-mode of the NR (black) and EOB (magenta) waveforms for `ID:0028` while Fig. 6.3 illustrates that higher-order multipoles, specifically the $(2,1)$, $(3,2)$, $(3,3)$ and $(4,4)$ modes, also exhibit a good alignment, despite the alignment procedure being applied only to the fundamental mode.

6.3 Comparing effective-one-body and numerical relativity

6.3.1 Energy and angular momentum fluxes

In Fig. 6.4 we show comparisons between the energy and angular momentum fluxes $\dot{E}$ and $\dot{J}$ for `ID:0001` and `ID:0028` computed from the EOB waveform and dynamics and from the waveforms extracted from the NR simulations. The relative differences are

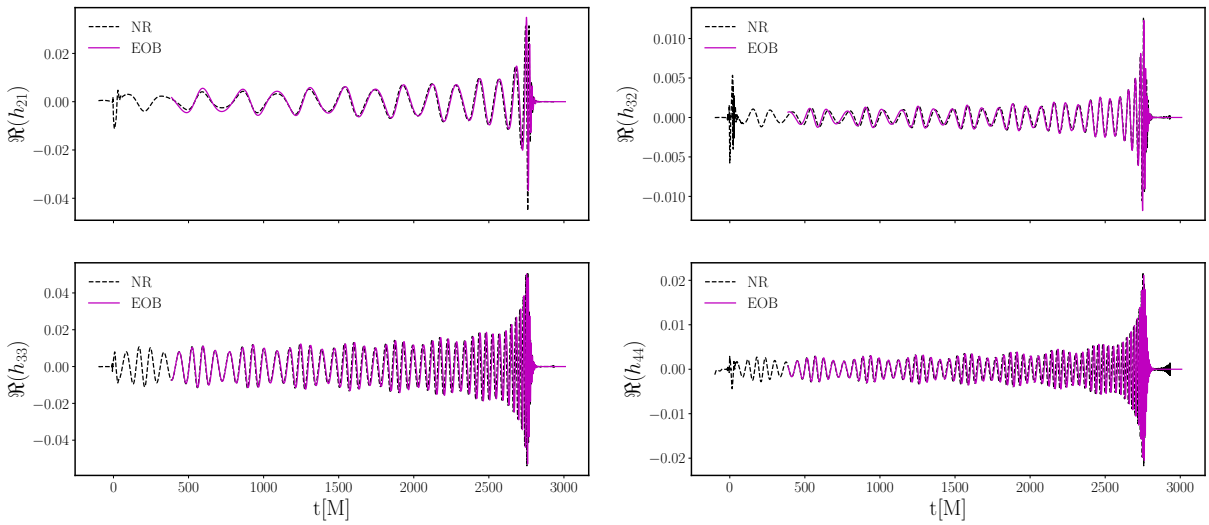


Figure 6.3: Alignment of the higher-order multipoles of the gravitational waveform strain h for `ID:0028`. Although the alignment procedure is applied only to the $(2,2)$-mode, it is sufficient to ensure that the higher-order modes are also aligned.

defined as

$$\frac{|\Delta \dot{E}|}{\dot{E}} = \frac{|\dot{E}^{\rm NR} - \dot{E}^{\rm EOB}|}{E^{\dot{\rm NR}}}, \quad \frac{|\Delta \dot{J}|}{\dot{J}} = \frac{|\dot{J}^{\rm NR} - \dot{J}^{\rm EOB}|}{J^{\dot{\rm NR}}} \tag{6.1}$$

and the NR and EOB energy and angular momentum fluxes are computed from the waveform multipoles $h_{\ell m}$ using Eq. (2.65) and Eq. (2.66) so that

$$\dot{E}^{\rm EOB}_{h_{\ell m}} = \frac{1}{16\pi} \sum_{\ell=2}^{\infty} \sum_{m=-\ell}^{\ell} |\dot{h}^{\rm EOB}_{\ell m}|^2, \tag{6.2}$$

$$\dot{J}^{\rm EOB}_{h_{\ell m}} = -\frac{1}{16\pi} \sum_{\ell=2}^{\infty} \sum_{m=-\ell}^{\ell} m\, \Im \left(\dot{h}^{\rm EOB}_{\ell m} h^{\rm EOB*}_{\ell m} \right)$$

and

$$\dot{E}^{\rm NR}_{h_{\ell m}} = \frac{1}{16\pi} \sum_{\ell=2}^{\infty} \sum_{m=-\ell}^{\ell} |\dot{h}^{\rm NR}_{\ell m}|^2, \tag{6.3}$$

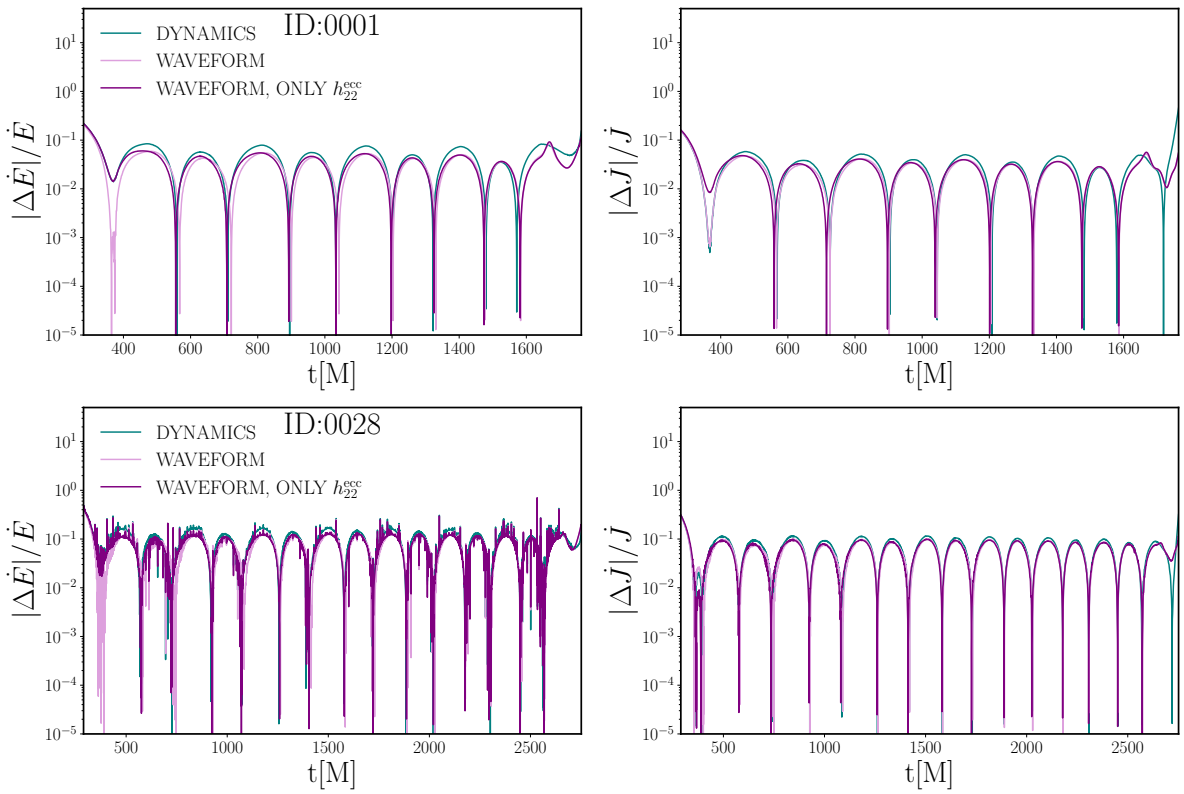


Figure 6.4: Energy and angular momentum fluxes differences computed from $\hat{\mathcal{F}}_\varphi$ (dynamics, teal) and from the waveform multipoles including either all multipoles up to $\ell = 8$ (light plum) or only the $(2,2)$-mode (violet) for `TEOBResumS-Dalí` waveforms with the same physical parameters as `ID:0001` and `ID:0028` (see Tab. 2 of [2]) and initial conditions in Tab. 6.1. The panels display the relative differences between the $\dot{E}$ and $\dot{J}$ and the NR fluxes. Fluxes computed directly from the waveform multipoles exhibit better agreement with the NR fluxes.

$$\dot{J}^{\rm NR}_{h_{\ell m}} = -\frac{1}{16\pi}\sum_{\ell=2}^{\infty}\sum_{m=-\ell}^{\ell} m\,\Im\left(\dot{h}^{\rm NR}_{\ell m} h^{\rm NR*}_{\ell m}\right).$$

In the figure, we show the fluxes differences computed from the waveform multipoles including all available modes up to $\ell = 8$ (light plum) and those computed using only the $(2,2)$-mode (violet) as well as the fluxes computed from the dynamics (teal). To test the procedure and minimise addional sources of noise, we only include the (2,2)-mode in the computation of the fluxes employed for the comparisons we carry out in this chapter.

However, we plan to apply the same procedure including higher-order multipoles. The fluxes relative to the EOB dynamics are computed from the radiation reaction forces employing the energy balance equation in Eq. (3.66) and Eq. (3.67). In practice we have

$$\begin{aligned} \dot{J}^{\rm EOB}_{\rm dyn} &= -\mathcal{F}_\varphi - \mathcal{F}^H_\varphi \\ \dot{E}^{\rm EOB}_{\rm dyn} &= -\dot{r}\mathcal{F}_r - \Omega\mathcal{F}_\varphi \end{aligned} \tag{6.4}$$

where we have ignored the Schott energy contribution and the horizon flux contribution in the energy flux. Future investigations will include assessments of the contribution of the Schott term. This comparisons reveal that the relative differences are more pronounced in the dynamics (teal), suggesting that non-circular contributions may be missing from the dynamical sector. We observe no significant differences between the results obtained using only the $(2,2)$-mode (violet) and those including higher-order modes, i.e. including all available modes up to $\ell = 8$ (light plum), aside from an increase in numerical noise in the energy flux. Given this discrepancy between the dynamical and the waveform sectors is observed, we aim to better understand what elements might be missing in the dynamical sector. A natural first step would be to consider adding higher-order corrections. On that basis, we undertook the derivation and implementation of an eccentric correction within the dynamics, with the aim of investigating its impact. The significance of this computation lies not only in demonstrating the impact of this particular correction, but also in providing a systematic method for comparing eccentric contributions and establishing a foundation for future studies. In previous works, see for example [115, 118, 127, 187, 335], comparisons aimed at testing eccentric contributions within the EOB framework were conducted by performing fluxes comparisons in the test-mass limit. These analysis are essential as they enable direct comparisons between the analytical EOB fluxes and the exact ones derived from perturbation theory [187, 336]. The urgent demand for templates

based on eccentric waveforms has motivated recent studies such as [1, 2, 98, 192, 193, 323] to propose eccentricity definitions derived from waveform quantities, thereby preserving their gauge-invariance. In Ref. [2] we established a mapping between eccentricity evolutions in `TEOBResumS-Dalí` and NR simulations thus enabling subsequent direct comparisons in the comparable-mass regime. With accurate initial conditions now available, conducting such comparisons becomes a crucial next step. We perform two types of comparisons. In Sec. 6.3.2 we incorporate an eccentric correction into the EOB dynamics and compare the resulting waveforms with those obtained without the correction employing in both cases `TEOBResumS-Dalí` to generate waveforms. The aim is to assess the relevance of this correction and identify regimes where its impact becomes significant. A similar strategy could be extended in the future to incorporate corrections for the other higher-order modes. Lastly, in Sec. 6.3.3 and Sec. 6.3.4 we carry out comparisons between gauge-invariant relations between the binding energy and total angular momentum of the system. The importance of parametrising eccentric systems in terms of energy and total angular momentum was hightlited in [323] and similar comparisons were performed, for the circular case, in [280, 337]. In particular, [280] highlighted the importance of computing such relations to assess the quality and performance of the analytical components of model, such as the the radiation reaction.

6.3.2 Inclusion of eccentric corrections in the EOB dynamics

As previously discussed in Sec. 3.3.3 and Sec. 3.3.4, eccentric contributions are factorised and enter Eq. (3.70) as Newtonian prefactors. The non-circular correction relative to the $(2,2)$ and $(2,1)$ modes are given in Eq. (3.74) and Eq. (3.75) respectively. In general, eccentric contributions are factorised and have the form

$$\hat{f}^{\rm Nnc}_{\ell m} = f(r, \Omega, \dot{r}, \dot{\Omega}, \ddot{r}, \ddot{\Omega}, \ldots), \tag{6.5}$$

where f is a function of the radial coordinate r, the orbital frequency Ω, and their time derivatives and is computed from Eq. (2.66) and from

$$\dot{J}^{\infty} \equiv -\mathcal{F}_{\varphi} = \frac{32}{5}\nu r_{\Omega}^{4}\Omega^{5}\hat{f}(x) \tag{6.6}$$

as in Eq. (3.70). In this work we implement the non-circular correction in Eq. (3.75) in the [333] version of the `TEOBResumS-Dalí` model. The time derivatives that we compute to obtain this non-circular correction are provided in the [338] `Mathematica` notebook. The non-circular correction in Eq. (3.75) is obtained by computing time derivatives of the dynamical quantities and employing the Hamilton's equations in Eq. (3.44). The procedure of computing derivatives can be quite convoluted, so we demonstrate here only the computation of the first derivatives. Expressions for higher order derivatives can be found in the `Mathematica` notebook and in App. A. Some of these expressions can also be found in Appendix A of Ref. [188].

For the radial coordinate we have

$$\dot{r} = \sqrt{\frac{A}{B}}\frac{\partial \hat{H}_{\rm EOB}}{\partial p_{r*}} = \sqrt{\frac{A}{B}}\left[\frac{1}{\nu \hat{H}_{\rm EOB}}\frac{\partial \tilde{G}}{\partial p_{r*}}p_{\varphi} + \frac{1}{\nu \hat{H}_{\rm EOB}\hat{H}_{\rm eff}^{\rm orb}}\left(\frac{A}{2}\frac{\partial Q}{\partial p_{r*}} + p_{r*}\right)\right] \tag{6.7}$$

where the EOB hamiltonian $\hat{H}_{\rm EOB}$ is given by Eq. (3.41) which we recall here for convenience

$$\hat{H}_{\rm EOB} \equiv \frac{H_{\rm EOB}}{\mu} = \frac{1}{\nu}\sqrt{1 + 2\nu\left(\hat{H}_{\rm eff} - 1\right)} \tag{6.8}$$

with

$$\begin{aligned} \hat{H}_{\rm eff} &= \frac{H_{\rm eff}}{\mu} = \hat{H}_{\rm eff}^{\rm orb} + \hat{H}_{\rm eff}^{\rm SO}, \\ \hat{H}_{\rm eff}^{\rm orb} &= \sqrt{p_{r_*}^2 + A\left(1 + p_{\varphi}^2 u_c^2 + Q\right)}, \end{aligned} \tag{6.9}$$

$$\hat{H}^{\rm SO}_{\rm eff} = \left(G_S \hat{S} + G_{S_*} \hat{S}_*\right) p_\varphi = \tilde{G} p_\varphi$$

where the metric potentials $A \equiv A(u)$ and $B \equiv B(u)$ and the non geodesic term $Q \equiv Q(u, p_{r*})$ are functions of $u = 1/r$ and p_{r*}. Their explicit expressions can be found in [126]. The gyro-gravitomagnetic functions entering the spin-orbit sector $G_S \equiv G_S(r_c, p^2_{r_*}), G_{S_*} \equiv G_{S_*}(r_c, p^2_{r_*})$ can be found in [189] and depend on the centrifugal radius r_c (see Eq. (3.49)) and $p_{r_*} = \sqrt{A/B}\, p_r$. The derivatives of Q, G_S and G_{S_*}[1] are easily obtained from their functional forms and can be found in the `Mathematica` notebook. The orbital frequency is given by the Hamilton's equation

$$\Omega = \dot{\varphi} = \frac{\partial \hat{H}_{\rm EOB}}{\partial p_\varphi} = \frac{p_\varphi A u_c^2}{\nu \hat{H}_{\rm EOB} \hat{H}^{\rm orb}_{\rm eff}} + \frac{\tilde{G}}{\nu \hat{H}_{\rm EOB}}. \tag{6.10}$$

To obtain its time derivative $\dot{\Omega}$ we differentiate Eq. (6.10) with respect to time obtaining (see also Appendix A of [188])

$$\begin{aligned} \dot{\Omega} = &\frac{1}{\nu \hat{H}_{\rm EOB} \hat{H}^{\rm orb}_{\rm eff}} \left[\left(A u_c^2\right)' p_\varphi \dot{r} + A u_c^2 \left(\dot{p}_\varphi - p_\varphi \frac{1}{\nu \hat{H}_{\rm EOB} \hat{H}^{\rm orb}_{\rm eff}} \frac{d}{dt} \left(\nu \hat{H}_{\rm EOB} \hat{H}^{\rm orb}_{\rm eff} \right) \right) \right] \\ &+ \frac{1}{\nu \hat{H}_{\rm EOB}} \left[\tilde{G}' \dot{r} + \frac{\partial \tilde{G}}{\partial p_{r_*}} \dot{p}_{r_*} - \tilde{G} \frac{\dot{\hat{H}}_{\rm EOB}}{\hat{H}_{\rm EOB}} \right], \end{aligned} \tag{6.11}$$

where the prime denote the derivative with respect to the radial coordinate r, and we have used the chain rule, e.g. $\frac{d\tilde{G}}{dt} = \dot{r}\tilde{G} + \dot{p}_{r*} \frac{\partial \tilde{G}}{\partial p_{r*}}$. The derivative with respect to r of $(A u_c^2)$, is given by

$$(A u_c^2)' = A' u_c^2 - 2A (r_c)' u_c^3 \tag{6.12}$$

[1] Derivatives of $\tilde{G}$ are computed in terms of derivatives of G_S and G_{S_*}, e.g. $\dot{\tilde{G}} = \dot{G}_S \hat{S} + \dot{G}_{S_*} \hat{S}_* = (\dot{r} \frac{\partial G_S}{\partial r} + \dot{p}_{r*} \frac{\partial G_S}{\partial p_{r*}}) \hat{S} + (\dot{r} \frac{\partial G_S}{\partial r} + \dot{p}_{r*} \frac{\partial G_{S_*}}{\partial p_{r*}}) \hat{S}_*$

where we have used $u_c = 1/r_c$ and the fact that $A \equiv A(r(t)), u_c \equiv u_c(r(t))$ and $r_c \equiv r_c(r(t))$ depend on the time through the radial coordinate $r(t)$. The derivative $A' \equiv \frac{\partial A}{\partial r}$ is computed from the functional form of the A potential. The derivatives of $\hat{H}_{\rm EOB}$ and $\hat{H}_{\rm orb}$ are computed by introducing the quantities E and H which simplify the notation

$$E \equiv \nu \hat{H}_{\rm EOB},\ H \equiv E \hat{H}_{\rm orb}. \tag{6.13}$$

With this notation Eq. (6.10) becomes

$$\dot{\Omega} = \frac{1}{H}\left[\left(A u_c^2\right)' p_\varphi \dot{r} + A u_c^2 \left(\dot{p}_\varphi - p_\varphi \frac{\dot{H}}{H}\right)\right] + \frac{1}{E}\left[\tilde{G}' \dot{r} + \frac{\partial \tilde{G}}{\partial p_{r_*}} \dot{p}_{r_*} - \tilde{G}\frac{\dot{E}}{E}\right]. \tag{6.14}$$

The derivatives of $\hat{H}_{\rm EOB}$ and p_φ are computed using the energy balance equations Eq. (3.67)

$$\begin{aligned} \dot{p}_\varphi &= \hat{\mathcal{F}}_\varphi, \\ \dot{\hat{H}}_{\rm EOB} &= \dot{r}\hat{\mathcal{F}}_r + \Omega \hat{\mathcal{F}}_\varphi \end{aligned} \tag{6.15}$$

where the contribution of the horizon flux and of the Schott energy are neglected. In terms of E and H we therefore have

$$\dot{E} = \nu \dot{\hat{H}}_{\rm EOB},\ \dot{H} = \dot{E}\hat{H}_{\rm orb} + E\dot{\hat{H}}_{\rm orb}. \tag{6.16}$$

When computing higher-order derivatives of $\dot{\hat{H}}_{\rm EOB}$, terms involving derivatives of the radiation reaction forces appear. However, we neglect these contributions in our calculations. For instance, in the second derivative we have terms containing $\dot{\hat{\mathcal{F}}}_r$ and $\dot{\hat{\mathcal{F}}}_\varphi$, i.e.

$$\ddot{\hat{H}}_{\rm EOB} = \ddot{r}\hat{\mathcal{F}}_r + \dot{r}\dot{\hat{\mathcal{F}}}_r + \dot{\Omega}\hat{\mathcal{F}}_\varphi + \Omega\dot{\hat{\mathcal{F}}}_\varphi. \tag{6.17}$$

Note that derivatives of $\hat{\mathcal{F}}_\varphi$ are not completely omitted and enter in the equations of motion via derivatives of p_φ, e.g. $\ddot{p}_\varphi = \dot{\hat{\mathcal{F}}}_\varphi$. The first derivative of $\hat{H}_{\rm orb}$, $\hat{H}_{\rm eff}$ and $\hat{H}_{\rm SO}$ are computed as

$$\begin{aligned}
\dot{\hat{H}}_{\rm orb} &= \dot{\hat{H}}_{\rm eff} - \dot{\hat{H}}_{\rm SO}, \\
\dot{\hat{H}}_{\rm eff} &= \frac{E\dot{E}}{\nu} \\
\dot{\hat{H}}_{\rm SO} &= \dot{p}_\varphi \tilde{G} + p_\varphi \left(\dot{r}\tilde{G}' + \dot{p}_{r_*} \frac{\partial \tilde{G}}{\partial p_{r_*}} \right)
\end{aligned} \tag{6.18}$$

and so on for higher-order derivatives. The first derivative of p_{r*} is given by

$$\begin{aligned}
\dot{p}_{r_*} &= \sqrt{\frac{A}{B}} \left(-\frac{\partial \hat{H}_{\rm EOB}}{\partial r} + \hat{\mathcal{F}}_r \right) = \\
&- \sqrt{\frac{A}{B}} \left(\frac{1}{2\nu \hat{H}_{\rm EOB} \hat{H}^{\rm orb}_{\rm eff}} \Big[A' + p_\varphi^2 (A u_c^2)' + (AQ)' \Big] - \frac{1}{\nu \hat{H}_{\rm EOB}} \tilde{G}' p_\varphi \right) + \hat{\mathcal{F}}_r = \\
&- \sqrt{\frac{A}{B}} \left(\frac{1}{2H} \Big[A' + p_\varphi^2 (A u_c^2)' + (AQ)' \Big] - \frac{1}{E} \tilde{G}' p_\varphi \right) + \hat{\mathcal{F}}_r
\end{aligned} \tag{6.19}$$

Higher-order derivatives follow the same procedure and can be found in App. A. After computing the first second and third derivatives of r and Ω, which involve all the derivatives of the quantities described above, we implement the resulting analytical expressions in `TEOBResumS-Dalí` [333] and use them to numerically evaluate the non-circular prefactor $\hat{f}^{\rm Nnc}_{21}$ and quantify its impact on the EOB dynamics and waveform. We focus on the $(2,1)$-mode because it represent the higher-order correction that involves the lowest-order derivatives in Ω, r and p_{r*}. Fig. 6.5 shows the impact of the non-circular correction that we have included. The figure illustrates mismatches between two waveforms emitted by non-spinning binaries computed with and without including $\hat{f}^{\rm Nnc}_{21}$.

For the mismatches we employ `aLIGOAPlusDesignSensitivityT1800042` available as a module of the `pycbc` software [339] corresponding to the approximate sensitivity of the

Advanced LIGO detector [331, 332] with a low frequency cutoff $f_{\rm low} = 1/(\pi r_{\rm start}^{1/2} M_{\rm tot})$, an high frequency cutoff $f_{\rm high} = 4096$ Hz, $r_{\rm start} = 12M$ and $M_{\rm tot} = 70M_{\odot}$. Here we only consider non-spinning binaries and evaluate the mismatches over a range of mass ratios $q \in [1, 100]$ in steps of $\Delta q = 5$. We choose initial eccentricities $e_0 = (0.2, 0.3, 0.5)$ and initial mean anomaly $l_0 = \pi$. We can determine very approximate accuracy requirements for next-generation gravitational wave detectors, such as ET [53, 54], CE [51, 52] and the space-based gravitational wave detector LISA [340] using the distinguishability criterion [50, 341, 342]. For the next-generation detectors, this translates into mismatches on the order of $\sim 10^{-4} - 10^{-5}$, notably higher than the accuracy requirements for the current generation of detectors. A qualitative assessment of Fig. 6.5 suggests that the computed eccentric correction can not be detected by Advanced LIGO and Virgo but can potentially be detected by ET or CE or LISA which are expected to observe louder signals and thus be sensitive to smaller discrepancies between gravitational wave signals. Moreover, the mismatches tend to increase with mass ratio, correlating with the excitation of the (2,1)-mode with increasing mass asymmetry. This emphasises the importance of modelling higher-order contributions to the eccentric flux in preperation for the next-generation of detectors.

Another feature that we observe for eccentricities $e_0 = 0.3$ and $e_0 = 0.5$ (purple and light blue lines) is the presence of spikes at specific values of q. A detailed investigations of these spikes will be carried out in the future but we outline here some considerations that we made while investigating their origin. Fig 6.6 illustrates the trajectories of the binaries with ($r_{\hat{f}_{22}}$) and without ($r_{\hat{f}_{\ell=2}}$) the higher-order eccentric correction. The figure also shows the semi-latus rectum (see Sec. 2.4.2) defined as $p = A(1 - e^2)$ where $A = (r_+ + r_-)/2$ is the semi-major axis and e is the eccentricity, and the separatrix p_s defined as the location separating the bound motion from plunge. For Kerr potentials the transition from stable to unstable orbits occurs when the effective potential in Eq. 2 of [343] has two roots

instead of three. The separatrix p_s that can be found by solving Eq. B6 of [343]

$$p_s^2\left(p_s-6-2e\right)^2+a^4(e-3)^2(1+e)^2-2a^2(1+e)p_s\left[14+2e^2+p_s(3-e)\right]=0 \quad (6.20)$$

where a is the spin magnitude and e is the eccentricity. In the Schwarzschild case the separatrix is given by $p_s = 6 + 2e$. In order to compute p we fit the maxima and minima of $r(t)$ by employing the `findpeaks` function of `scipy` while for the eccentricity we follow the usual procedure outlined in Chapter 5 obtaining

$$\begin{aligned} p &= \frac{(1-e_{\rm gw}^2)(r_+ + r_-)}{2}, \\ p_s &= 6 + 2e_{\rm gw}. \end{aligned} \quad (6.21)$$

We observe that the configuration corresponding to a spike (upper panel) exhibits a noticeable difference in the orbital trajectories during the transition to plunge after crossing the separatrix, a feature that is not present in the case corresponding to the absence of spikes (lower panel). A comprehensive analysis and deeper understanding of the origin of these spikes is left to future work. It is worth noting, however, that the spikes appear periodically by varying the mass ratio q [2].

6.3.3 Energetics: numerical relativity simulations

The analysis of energetics is performed by computing gauge-invariant relationships obtained from the dimensionless binding energy E_b and the total angular momentum j following the approach used in previous works [280, 337]. While such gauge-invariant relations have been previously derived for quasi-circular configurations [280], this work presents their extension to non-circular dynamics. Such gauge-invariant relations for the

[2] Varying the mass ratio q effectively changes the initial frequency and thus the initial true anomaly. Varying other parameters, such as the spin, could in principle lead to similar effects.

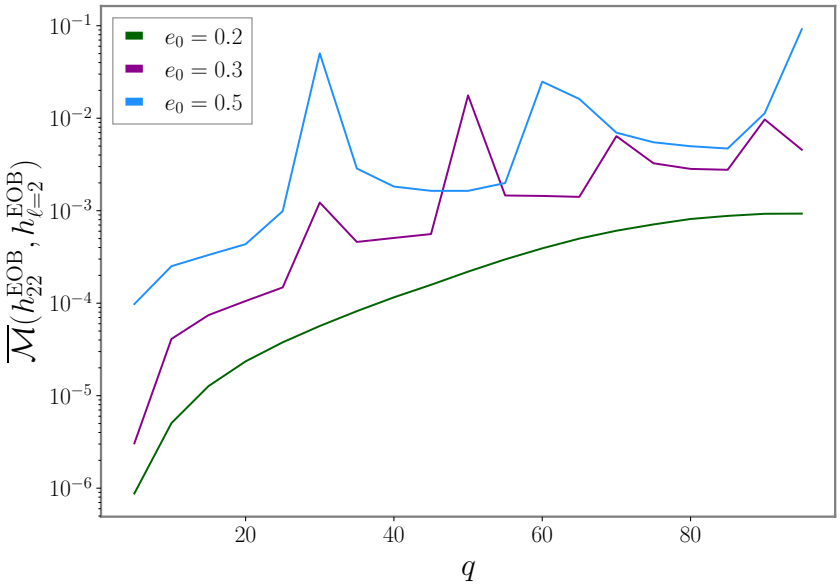


Figure 6.5: Mismatches between two gravitational waveforms computed with `TEOBResumS-Dalí` for non-spinning binaries with different mass ratios q and initial eccentricity e_0. The two waveforms are generated including nonidentical eccentric contributions in the model: we include a non-circular correction $\hat{f} = \hat{f}_{22}^{\rm Nnc}$ in the first waveform and a non-circular correction $\hat{f}^{\rm Nnc} = \hat{f}_{22}^{\rm Nnc} + \hat{f}_{21}^{\rm Nnc}$ in the second waveform. We observe spikes at specific values of q when the initial eccentricity e_0 is $e_0 = 0.3$ and $e_0 = 0.5$ (purple and light blue lines). We observe a general decrease in the agreement between the waveforms for increasing values of q.

scattering-dynamical capture case have been presented in [344]. The binding energy E_b and the total angular momentum j are defined as

$$E_b = \frac{M^0_{\rm ADM} - \Delta E_{\rm rad} - M}{\mu} \tag{6.22}$$

$$j \equiv \frac{J^0_{\rm ADM} - \Delta J_{\rm rad}}{M\mu} \tag{6.23}$$

where $M^0_{\rm ADM}$ and $J^0_{\rm ADM}$ denote the total initial Arnowitt-Deser-Misner (ADM) mass-energy and angular momentum of the system, while $\Delta E_{\rm rad} = \dot{E}$ and $\Delta J_{\rm rad} = \dot{J}$ are the energy and total angular momentum fluxes radiated via gravitational waves, computed from the $(2,2)$-mode of the gravitational waveform and integrated over time. The ini-

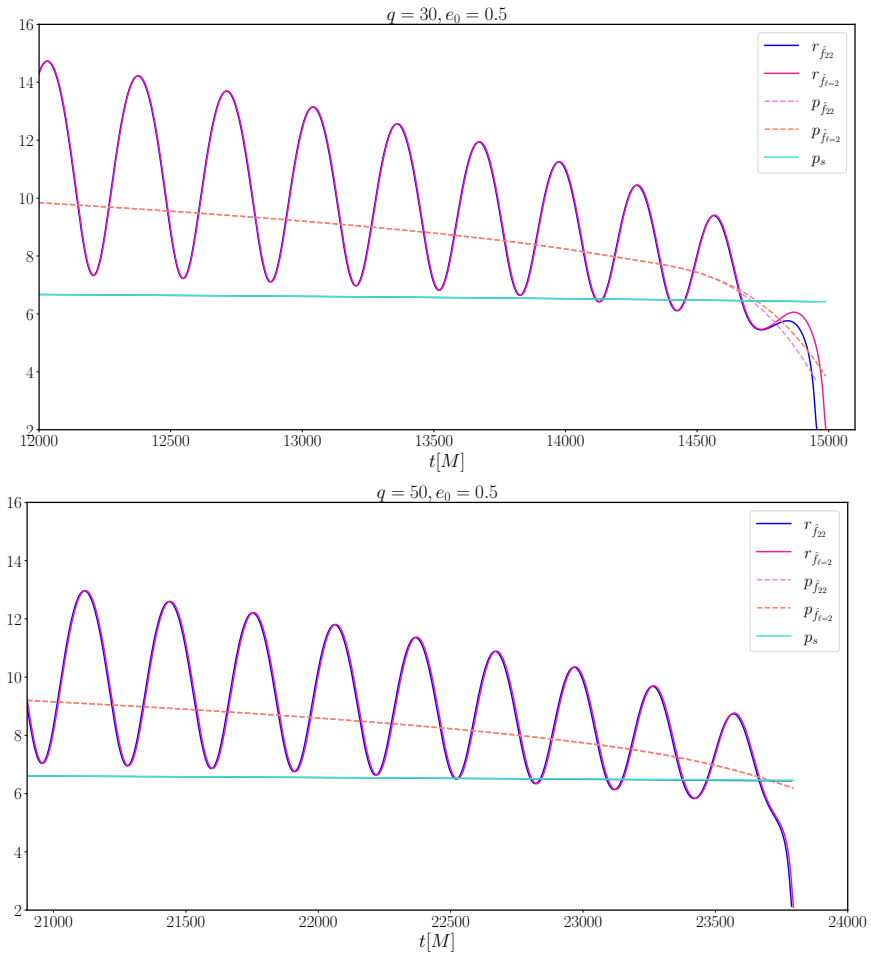


Figure 6.6: Orbital trajectories for non-spinning binaries with $q = 30, e_0 = 0.3$ (upper panel) and $q = 50, e_0 = 0.5$ (bottom panel). The panels also show the semi-latus rectum p and the separatrix p_s. The configurations in the upper panel correspond to a spike in Fig. 6.5 and show noticeable differences in the transition to plunge.

tial conditions for the NR simulations and the corresponding EOB systems are listed in Tab. 6.2 and are given in terms of initial ADM energy $M^0_{\rm ADM}$ and orbital angular momentum $L^0 = P^0_{\rm ADM} D$ where D is the initial separation and $P^0_{\rm ADM}$ is the initial ADM linear momentum. The total angular momentum $J_{\rm ADM}$ is defined as

$$J_{\rm ADM} = L + S \tag{6.24}$$

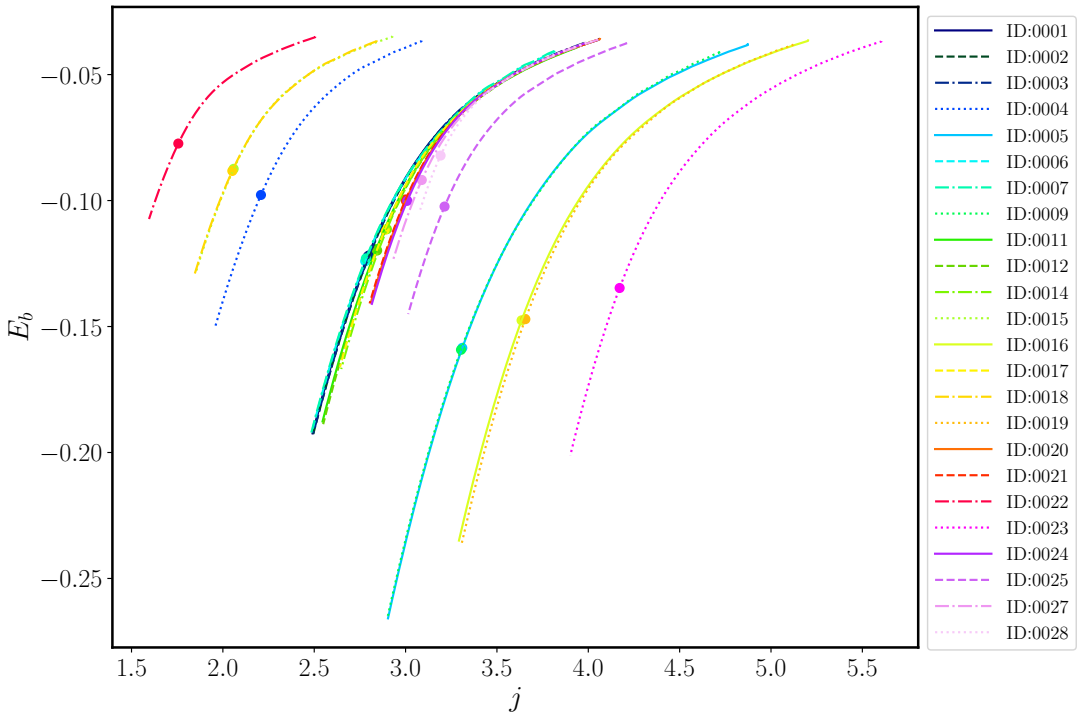


Figure 6.7: Gauge invariat relations between the binding energy E_b and the total angular momentum j of the binary systems.

$$L = P_{\rm ADM} D$$

and includes the contribution of the spin $S = \mu\,(q\,\chi_1 + \chi_2/q)$ where, for non-precessing systems, $\chi_1 = \chi_{1,z}$ and $\chi_2 = \chi_{2,z}$ are the z-components of the dimensionless spins listed in Tab. 5.1. The starting EOB energy and orbital angular momentum are denoted by $E^0_{\rm EOB}$ and $L^0_{\rm EOB} = \mu\, p^0_{\varphi,{\rm EOB}}$. These initial conditions correspond to the ones given in terms of eccentricity and frequency in Tab. 6.1 and illustrated in Fig. 6.1. As previously discussed, oscillations of the order 10^{-5} in these initial conditions lead to noticeable changes in the physical system, significantly affecting its initial energy and angular momentum. The $E_b(j)$ relations for our set of simulations are shown in Fig. 6.7 and their values at merger $E_b^{\rm mrg}(j)$ are indicated by dots. We define the merger as the maximum of the amplitude of h_{22}. The aligned-spin simulation with the highest mass ratio (`ID:0023`) merges at the

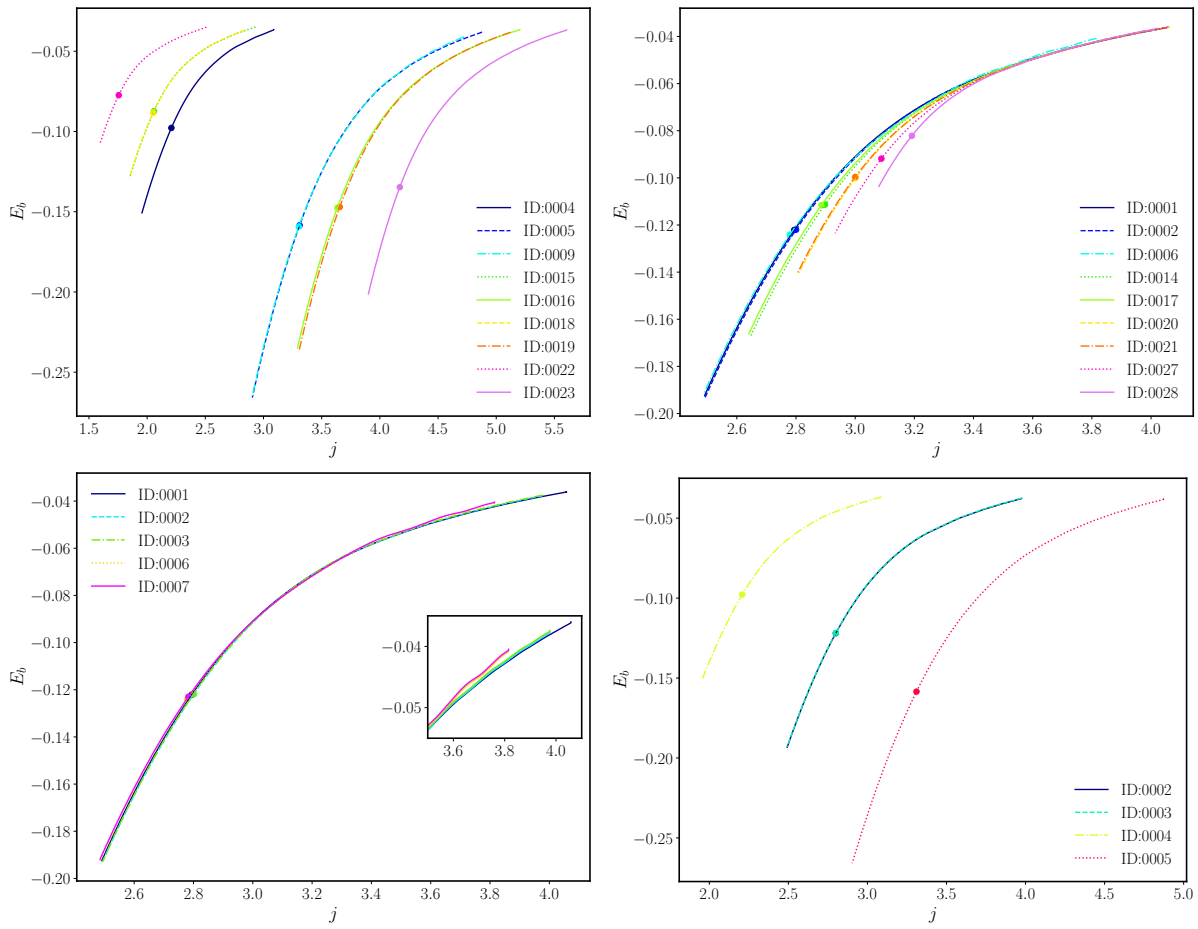


Figure 6.8: Comparisons demonstrating how spin, mass ratio, and eccentricity affect the $E_b(j)$ relations. The first panel (upper left) shows a comparison between simulations with either aligned-spin or anti-aligned spin configurations, $q = 1$ and varying eccentricity. The second panel (upper right) illustrates non-spinning simulations across different q and eccentricities. The third panel (bottom left) displays non-spinning simulations with $q = 1$ and different values of eccentricity. Oscillations appear early in the evolution for higher values of eccentricity. The fourth panel (bottom right) shows curves with the same initial PN eccentricity ($e_{0,\mathrm{PN}} = 0.1$) and different spin configurations showing the impact of spin on the curves.

largest total angular momentum j, while the simulation with anti-aligned spins (`ID:0021`) merges at the lowest j. The data naturally cluster in three distinct groups: aligned-spin configurations merge at higher values of E_b and j with respect the non-spinning and anti-aligned spin cases. This is illustrated in the top left panel of Fig. 6.8. The orbital hang-up

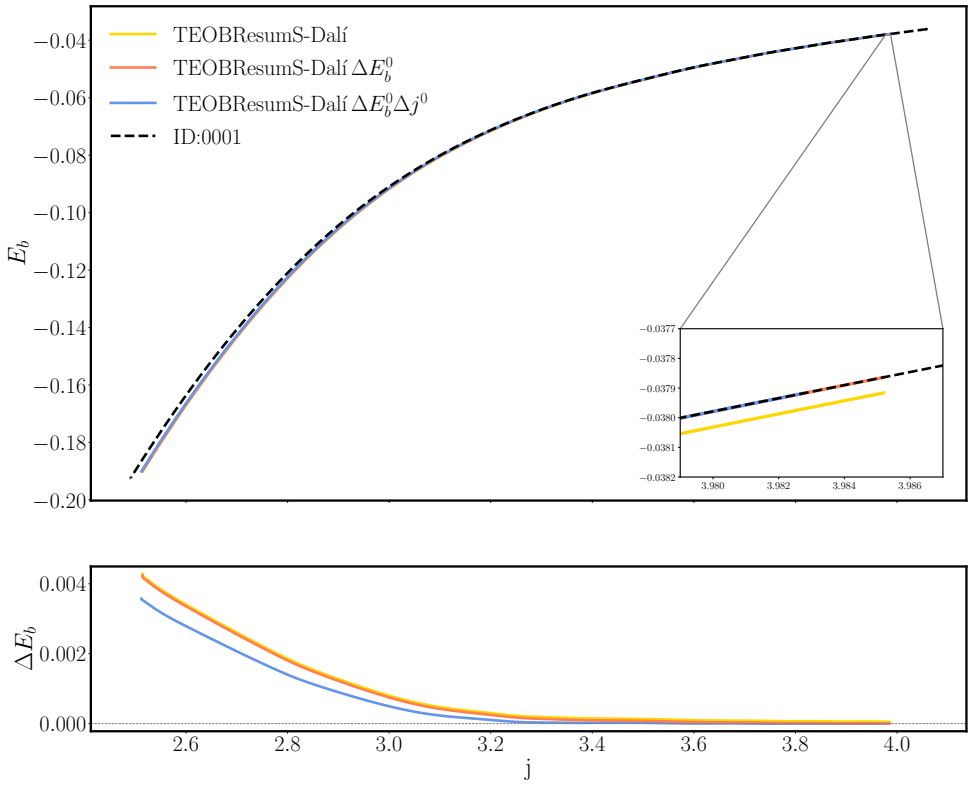


Figure 6.9: Upper panel: $E_b(j)$ relations for `ID:0001`, a non spinning simulation with initial PN eccentricity $e_{0,\mathrm{PN}} = 0.05$ and $q = 1$. We observe a shift in the binding energy of the EOB system of the order 10^{-5} (yellow curve) and we correct the initial conditions by applying a vectorial shift to the binding energy (orange curve) or to both the binding energy and the angular momentum (blue curve). Bottom panel: differences ΔE_b^0 between the NR and EOB $E_b(j)$ relations. Shifting the curves produces a decrease in these differences.

effect [345] is clearly visible: aligned-spin configurations (`ID:0005`, `ID:0009`, `ID:0016`, `ID:0019`, `ID:0023`) undergo slower mergers and radiate more energy, therefore reaching lower values of E_b at merger. In contrast, anti-aligned spin configurations (`ID:0004`, `ID:0015`, `ID:0018`, `ID:0022`) merge more rapidly and emit less energy, merging at higher values of E_b. The top right panel displays non-spinning simulations with varying mass ratios. As q increases, the merger occurrs at progressively higher values of E_b and j. The bottom left panel highlights the effects of eccentricity for systems with $q = 1$ and either non-spinning or equal magnitude spins but opposite in direction. Noticeable oscillations

appear early in the evolution for higher initial eccentricities (`ID:0007`). However, the merging time remains approximately the same. The last panel (bottom right) shows the effect of spin on binaries with $q = 1$ and initial eccentricity[3] $e_{0,\mathrm{PN}} = 0.1$.

6.3.4 Energetics: comparisons between effective-one-body and numerical relativity

Fig. 6.9 shows the $E_b(j)$ EOB relation (yellow) for `ID:0001`, which appears shifted from the NR curve (black). This offset reflects the limitations associated with the the manual computation of initial conditions, as well as numerical noise introduced by junk radiation, i.e. the burst of radiation emitted before the Bowen-York initial data relax and the radiation settles down. We adopt two different strategies to correct the initial conditions. The first procedure to align the NR and EOB curves consists in applying a shift $\Delta E_b^0 = E_{b,\mathrm{NR}}^0 - E_{b,\mathrm{EOB}}^0$ to the binding energy E_b. The second involves applying shifts ΔE_b^0 and Δj^0 to both the binding energy E_b and angular momentum j. In this case, Δj^0 is determined by requiring that the initial total angular momentum of the EOB system $j_{\mathrm{EOB}}^0 = p_{\varphi,\mathrm{EOB}}^0$ matches the total angular momentum of the NR system at the start of the EOB time, meaning $j_{\mathrm{NR}}(t_{\mathrm{EOB}}^0)$. This procedure is performed in two steps. In the first step we perform a shift ΔE_b^0 to align the $E_b(j)$ curves while in the second we shift the EOB angular momentum j introducing

$$\Delta j^0 = j_{\mathrm{NR}}(t_{\mathrm{EOB}}^0) - j_{\mathrm{EOB}}^0 \tag{6.25}$$

where $j_{\mathrm{EOB}}^0 = p_{\varphi,\mathrm{EOB}}^0$. The $E_b(j)$ relations obtained by shifting the curves are illustrated in Fig. 6.9 and in the left panel of Fig. 6.11. The differences ΔE_b are of the order 10^{-3} and decrease, with the exception of `ID:0024`, after correcting the initial conditions.

[3]Initial PN eccentricities are estimated as explained in Sec. 5.2.2.

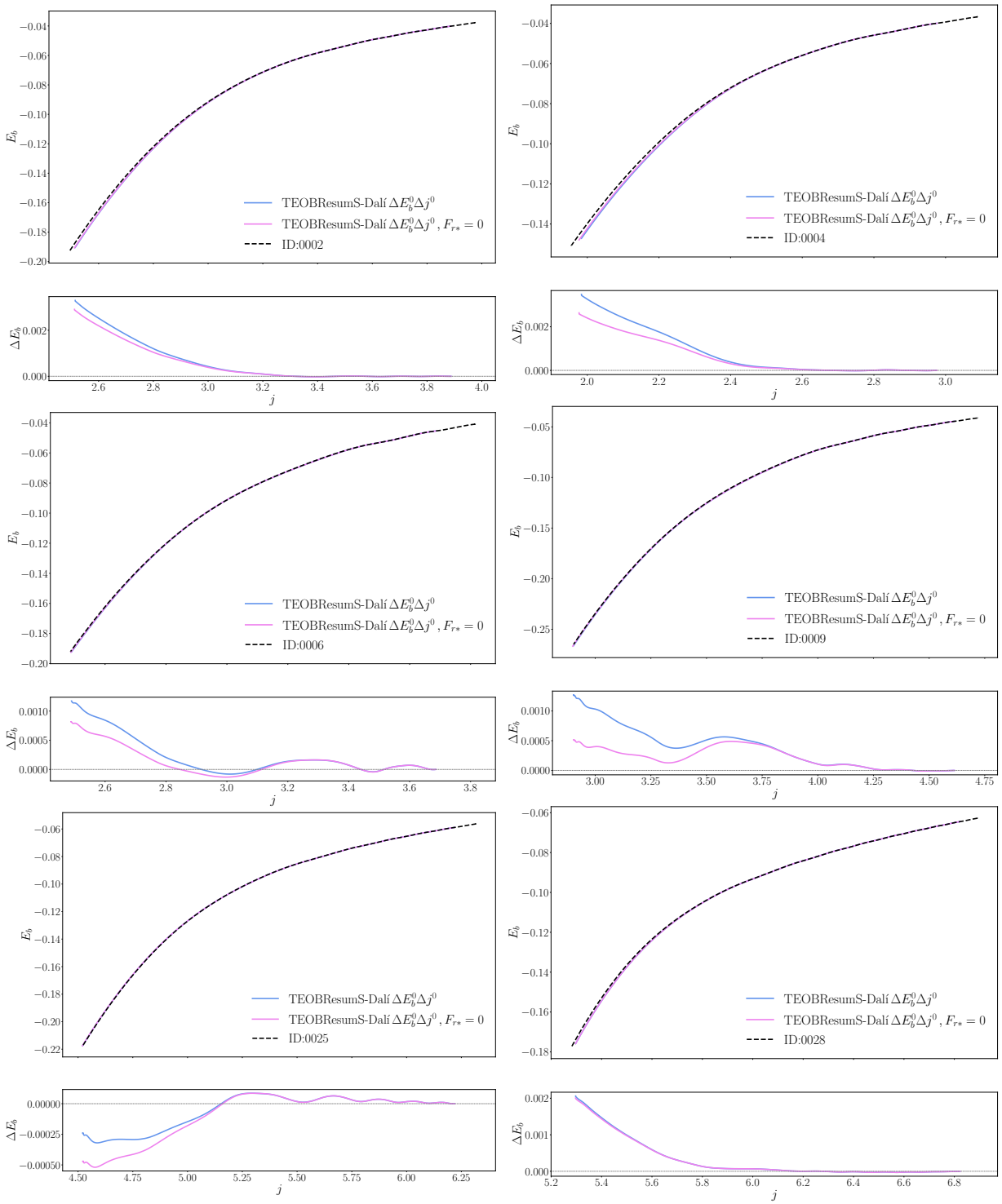


Figure 6.10: Testing the radial component of the radiation reaction $\mathcal{F}_{r*}$. The figure illustrates various systems: non-spinning with $q = 1$ and $e_{0,\mathrm{PN}} = 0.1$ (`ID:0002`), anti-aligned spin with $q = 1$ and $e_{0,\mathrm{PN}} = 0.1$ (`ID:0004`), non-spinning with $q = 1$ and $e_{0,\mathrm{PN}} = 0.2$ (`ID:0006`), spin-aligned with $q = 1$ and $e_{0,\mathrm{PN}} = 0.2$ (`ID:0009`), configuration with $\chi_{1,z} = 0.1$ and $\chi_{2,z} = -0.3$, $q = 3$ and $e_{0,\mathrm{PN}} = 0.1$ (`ID:0025`), non-spinning with $q = 6$ and $e_{0,\mathrm{PN}} = 0.1$ (`ID:0028`). Differences ΔE_b are of the order $\sim 10^{-3}$. The agreement between the EOB and NR $E_b(j)$ relations improves by setting $\mathcal{F}_{r*} = 0$ with the exception of `ID:0025` where the differences are anyway very small (10^{-4}).

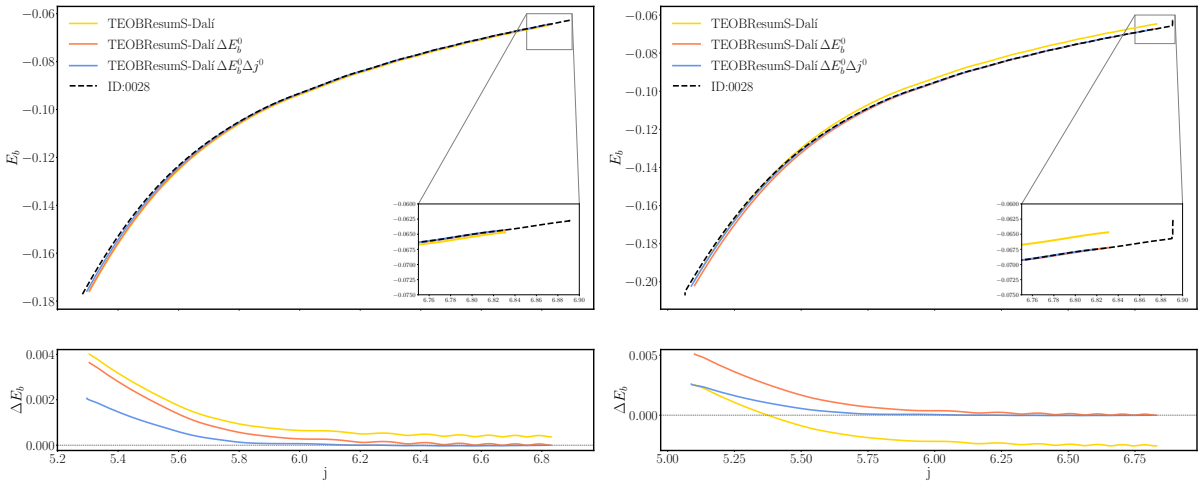


Figure 6.11: Left panel: $E_b(j)$ relations and differences for `ID:0028`, a non-spinning simulation with initial PN eccentricity $e_{0,\mathrm{PN}} = 0.1$ and $q = 6$. As for the $q = 1$ case illustrated in Fig. 6.9, we observe smaller differences after applying the shifts. Right panel: $E_b(j)$ relations and differences for `ID:0028` when we include higher-order modes. We observe larger discrepancies due to numerical noise affecting HM at the start of the simulation. Similarly, we apply ΔE_b^0 and Δj^0 shifts accounting for junk radiation.

The maximum differences between the EOB and NR $E_b(j)$ relations and the shifts ΔE_b^0 and Δj^0 are listed in Tab. 6.3. The shifts are of the order $\sim (10^{-5} - 10^{-4})$ for the energy and $\sim (10^{-3} - 10^{-4})$ for the total angular momentum. After applying these shifts, the maximum observed discrepancy is approximately 0.0078. Tab. 6.3 lists the values corresponding to the corrected EOB initial conditions $E_{\mathrm{EOB}}^{0,\mathrm{new}}$ and $L_{\mathrm{EOB}}^{0,\mathrm{new}}$. Fig. 6.11 shows the impact of higher order modes on the $E(j)$ relations. The figure illustrates that junk radiation becomes more prominent when higher-order multipoles are included As shown in the right panel, the inclusion of higher multipoles, specifically the $(2,1), (3,2), (3,3), (4,4)$ modes, leads to a more pronounced presence of junk radiation. To compensate for this additional unphysical radiation introduced, appropriate shifts along the binding energy and total angular momentum directions must be applied. Ref. [280] similarly observed that the presence of junk radiation impacts the energetics and applied corresponding shifts to both the binding energy and total angular momentum.

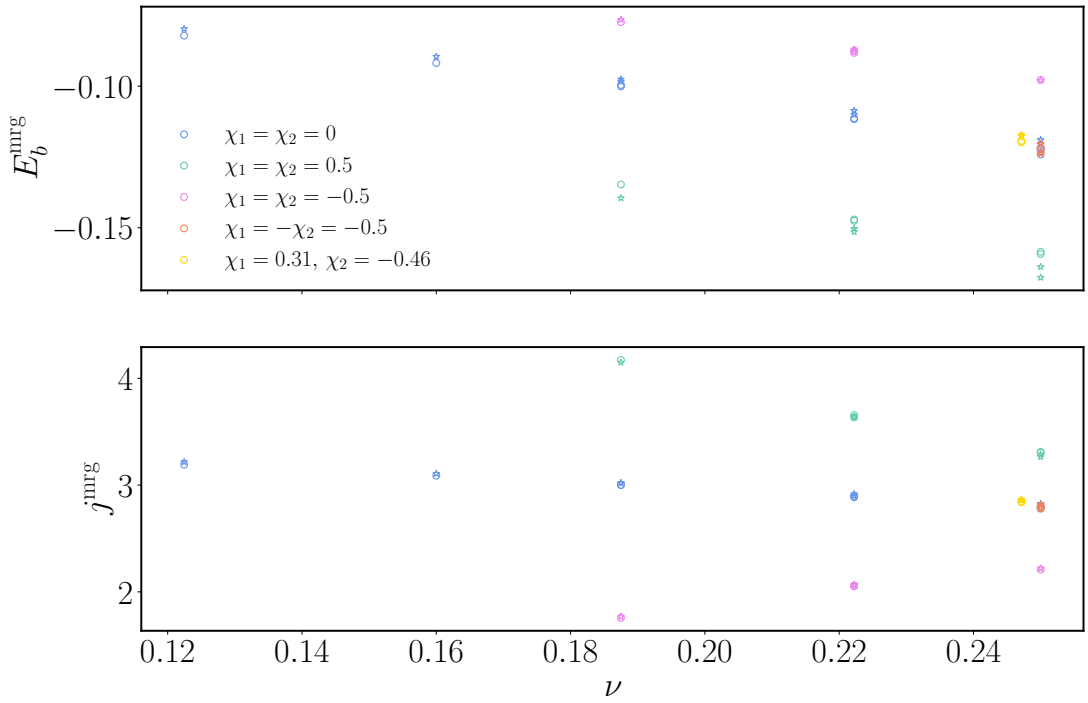


Figure 6.12: Agreement between the NR and EOB predictions for the binding energy E_b and total angular momentum j at merger. The figure displays the binding energy and total angular momentum as a function of the symmetric mass ratio ν. The EOB data are denoted by stars, while NR data by circles with different colors indicating various spin configurations. Overall, there is a good agreement between EOB and NR data, though some discrepancies in E_b are observed for aligned-spin binaries (green).

Testing the radiation reaction: $\hat{\mathcal{F}}_{r*}$

The performance of the radial component of the radiation reaction $\hat{\mathcal{F}}_{r*}$ is illustrated in Fig. 6.10. Similarly to the findings of [280] we find that agreement with the numerical data is greater if we set $\hat{\mathcal{F}}_{r*} = 0$ with the exception of `ID:0025` which has spin $\chi_{1,z} = 0.1$ and $\chi_{1,z} = -0.3$ but the discrepancies remain minimal. This result might suggest that the $\hat{\hat{F}}_{r*}$ overestimates the eccentric contribution, though a detailed analysis is left for future work. We also examined the effect of the horizon flux $\mathcal{F}_H$ and from our comparisons we found that, in this regime, no contributions from the horizon flux are observable.

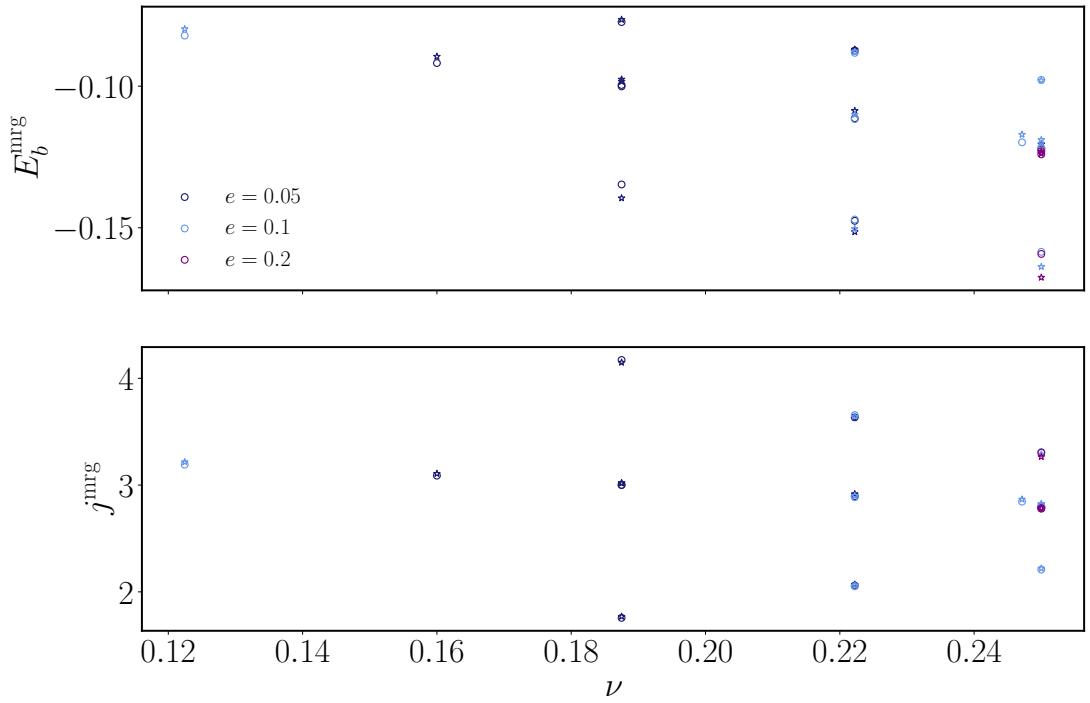


Figure 6.13: Agreement between the NR and EOB predictions for the binding energy E_b and total angular momentum j at merger as in Fig. 6.12 but highlighting the agreement of the data for differen initial PN eccentricities. The data relative to the aligned-spin configuration with larger eccentricity $e_{0,\rm PN} = 0.2$ display the largest disagreement.

Merger: agreement between EOB and NR data

Fig. 6.12 and 6.13 show the agreement between the NR and EOB data relative to the merger states as a function of the symmetric mass ratio ν. The NR data are denoted by circles, while the EOB data by stars. The EOB and NR data show a good agreement, especially for anti-aligned and non-spinning configurations. The aligned-spin configurations show a larger disagreement, in particular for a larger initial PN eccentricity $e_{0,\rm PN} = 0.2$. Future directions will be to compare these data with analytical predictions and study the dependence of the merger states from the spin as done in [280].

6.4 Discussion

In this chapter we presented the first systematic comparisons between an EOB model and NR for non-circular binary configurations, carried out without relying on numerical optimisation. We showed comparisons between the EOB and NR fluxes, incorporating an eccentric correction into the EOB dynamics and we discussed the impact of this correction for next-generation gravitational wave detectors. A qualitative assessment suggests that the correction grows in significance with increasing mass ratio and could be detected by next-generation detectors. Additionally, we carried out the first systematic computation of gauge-invariant relations between the binding energy E_b and total angular momentum j for eccentric, spinning, non-precessing binary systems. The methodology developed in this work introduces a novel approach for comparing EOB and NR data within non-circular dynamics. This represents an important step towards a more comprehensive understanding of non-circular effects and their relations with other physical quantities. We presented a procedure that can serve as baseline for future studies that can be applied to include higher-order eccentric corrections and compare EOB models with NR. Subsequent research will include (i) investigations of the spikes that appear in the mismatches shown in Fig. 6.5 and possible connections with the separatrix; (ii) investigations of the effect of inclusion of Schott energy in the fluxes; (iii) more analysis and investigations of the agreement between the EOB and NR $E_b(j)$ relations and further tests of the radiation reaction and (iv) understanding how the results can be used to inform the model in the strong-field regime. Another possible future direction could be the inclusion of factorised and resummed non-circular 2PN corrections presented in [117].

ID	D [M]	$M^0_{\rm ADM}$	L^0	$E^0_{\rm EOB}$	$L^0_{\rm EOB}$
0001	12.5	0.991003	1.01445586	0.990521	0.996298
0002	12.5	0.990594	0.99385	0.989971	0.972287
0003	12.5	0.990665	0.99381	0.989965	0.971964
0004	12.5	0.990872	1.0219125	0.989966	0.994229
0005	12.5	0.990483	0.96817125	0.989882	0.949132
0006	12.5	0.989820	0.9537775	0.988690	0.921833
0007	12.5	0.989887	0.95373875	0.988688	0.921701
0009	12.5	0.989730	0.92913375	0.988789	0.902731
0011	11.05	0.990378	0.9703668	0.989623	0.947697
0012	12.22	0.990687	0.0803349	0.981692	0.960010
0014	12.1579	0.991832	0.8939169	0.991386	0.877921
0015	12.5	0.992286	0.92839375	0.991743	0.911350
0016	12.5	0.991902	0.8784225	0.991480	0.864751
0017	12.5	0.991651	0.8839275	0.991152	0.866759
0018	12.5	0.991903	0.0727589	0.99118	0.887637
0019	12.5	0.991547	0.0688427	0.991058	0.845447
0020	12.5	0.993277	0.0609532	0.992994	0.751728
0021	12.379	0.993223	0.0613483	0.992944	0.749593
0022	12.379	0.993461	0.0632006	0.993044	0.769997
0023	12.379	0.993117	0.0596535	0.992793	0.728504
0024	12.5	0.992968	0.0597077	0.992596	0.733806
0025	12.5	0.992976	0.0596607	0.992573	0.731737
0027	12.379	0.994227	0.0523838	0.994008	0.640939
0028	12.83	0.995521	0.0383639	0.995380	0.487901

Table 6.2: Table of the NR and EOB initial conditions in terms of initial energy and total angular momentum. The initial energy $M_{\rm ADM}$ and orbital angular momentum L^0 of the NR simulations. The EOB initial energy and orbital angular momentum are denoted by $E^0_{\rm EOB}$ and $L^0_{\rm EOB}$. The initial separations D for the NR simulations are listed in the second column. Their values differ from the EOB initial separations, as the latter are calculated at the time of first apastron, following the procedure outlined in [2].

ID	$\Delta E_b^{\max}$	$\Delta E_b^0(10^{-4})$	Δj^0	$\Delta E^{\max}_{b,\Delta E_b^0}$	$\Delta E^{\max}_{b,\Delta E_b^0,\Delta j^0}$	$E^{0,\mathrm{new}}_{\mathrm{EOB}}$	$L^{0,\mathrm{new}}_{\mathrm{EOB}}$
0001	0.0043	0.525	0.0025	0.0042	0.00357	0.990520	0.995687
0002	0.0038	0.465	0.0018	0.0038	0.00329	0.989973	0.971848
0003	0.0039	2.92	0.0004	0.0036	0.00348	0.990036	0.971859
0004	0.0040	2.31	0.0012	0.0037	0.00349	0.990017	0.993926
0005	0.0026	2.79	0.0006	0.0023	0.00212	0.989949	0.948988
0006	0.0016	−1.23	0.0020	0.0017	0.00117	0.988646	0.921326
0007	0.002	1.18	0.0037	0.0019	0.00093	0.988693	0.920778
0009	0.0010	2.80	−0.0018	0.00071	0.00127	0.988870	0.903180
0011	0.0032	2.96	0.0010	0.0029	0.00262	0.989684	0.947474
0012	0.0038	2.54	0.0004	0.0035	0.00352	0.990065	0.959925
0014	0.0023	1.41	−0.0022	0.0021	0.00265	0.991418	0.878287
0015	0.0027	3.70	0.0004	0.0023	0.00257	0.991809	0.911531
0016	0.0089	4.29	0.0020	0.0084	0.00784	0.864427	0.991545
0017	0.0027	1.16	0.0006	0.0026	0.00245	0.991169	0.866656
0018	0.0022	2.76	−0.0010	0.0019	0.00213	0.991225	0.887804
0019	0.0033	4.48	−0.0010	0.0029	0.00318	0.991136	0.845610
0020	0.0022	2.16	0.0011	0.002	0.00179	0.993018	0.751591
0021	0.0042	2.06	0.0057	0.0040	0.00270	0.992955	0.748880
0022	0.0026	5.10	0.0003	0.0021	0.00206	0.993107	0.769960
0023	0.0007	5.79	−0.0013	0.00007	0.00043	0.992870	0.728662
0024	0.0015	2.14	−0.0029	0.0013	0.00191	0.992631	0.734172
0025	−0.0036	1.98	−0.0153	−0.0038	−0.00024	0.992642	0.733647
0027	0.0020	2.94	0.0016	0.0017	0.00137	0.994034	0.640785
0028	0.0040	3.72	0.0079	0.0036	0.00206	0.995395	0.487336

Table 6.3: The table presents the vectorial shifts applied along the total angular momentum and binding energy directions. These shifts reduce the discrepancies between the NR and EOB values of $E_b(j)$. The largest differences between the NR and EOB curves are indicated by $\Delta E_b^{\max}$ and $\Delta E^{\max}_{b,\Delta E_b^0,\Delta j^0}$.

Chapter 7

Conclusions

To date, more than a hundred gravitational wave events have been observed during the LVK observing runs [12–14], with many additional detections reported during the ongoing O4 run. The majority of these events are consistent with quasi-circular inspirals [15, 17], however growing evidence suggests that some of the detected events exhibit measurable eccentricity when entering the frequency band of gravitational wave detectors [32, 33, 35–40]. Furthermore, enhancing the low-frequency sensitivity of the next-generation ground-based detectors, including Cosmic Explorer [51, 52], Einstein Telescope [53, 54] and of the space-based observatory LISA [340] could yield to significant improvements allowing us to observe binary systems earlier in their inspiral phase before gravitational wave emission has time to circularise their orbit. A non-negligible orbital eccentricity in compact binaries offers key insights into their astrophysical origin, and can be inferred from gravitational-wave detections through its distinct signature on the emitted signal. The imprint of of eccentricity on the gravitational-wave signal can help discriminate between different dynamical formation channels, as binaries formed through dynamical interaction are more likely to retain a non-negligible eccentricity when entering the sensitivity band of gravitational wave detectors. Moreover, a significant fraction of binaries formed

through dynamical interactions are expected to have higher masses, often resulting from hierarchical mergers [323]. Their gravitational-wave signals are typically dominated by the merger and ringdown phases. For this reason it is imperative to develop robust gravitational waveform models capable of accurately describing binary systems in both bound and unbound orbits. Waveform templates based on quasi-circular waveforms suffer significant sensitivity loss to systems moving along non-circular orbits, highlighting the urgent need for robust waveform models that incorporate orbital eccentricity effects [32, 33, 35, 37, 346–352].

On the other hand it is crucial to develop reliable tools to measure eccentricity from gravitational wave data that enable direct comparison across different eccentric waveform models and can be applied to generic waveform data.

In this thesis we addressed two key aspects of gravitational wave modelling and data analysis applied to eccentric binaries. Specifically, (i) we developed a robust pipeline for measuring eccentricity from various types of data; (ii) we extended the available catalogs of NR simulations to cover a wider region of the parameter space; and (iii) we provided accurate eccentric initial conditions to explore the synergies between NR and the EOB formalism with the aim of improving the state-of-the-art of `TEOBResumS-Dalí` and establishing a methodology that can serve as a baseline for future studies.

In Chapter 4 we validated the accuracy of `TEOBResumS-Dalí` and presented a pipeline to measure eccentricity from gravitational wave data. We performed parameter estimation by employing two eccentric parameters, demostrating the efficacy of the model in distinguishing between circular and eccentric gravitational wave signals and investigated correlations between eccentricity and other parameters characterising the binary. In Chapter 5 we presented a new suite of NR simulations with eccentric initial conditions and established a mapping between the eccentricity evolution in EOB and NR waveforms. This mapping is particularly significant, as it offers a reliable method for translating ec-

centric initial conditions from NR data into the EOB framework and enables a consistent pipeline that can be applied across different datasets allowing *apple-to-apple* comparisons. In Chapter 6 we employed the previously developed pipeline and eccentricity mapping to directly compare EOB and NR fluxes and energetics in the comparable-mass regime. This represents an important step towards understanding the role of eccentric corrections on both the dynamics and waveform, particularly within the EOB framework, and exploring the synergies with NR. Future directions include leveraging these comparisons to refine and calibrate `TEOBResumS-Dalí` in the strong-field regime, further investigate the interplay between eccentricity and other physical quantities such as mass ratio and spin, and extending the analysis to incorporate higher-order PN eccentric corrections to the waveform. We aim to further investigate the spikes observe in the mismatches and determine whether similar features arise when varying other quantities, such as spin or the mean anomaly as well as examine the role of the separatrix. Additionally, we plan to inspect the agreement between the EOB and NR predictions for the binding energy and angular momentum at merger and examine whether specific spin configurations lead to greater (smaller) discrepancies. Other potential avenues include the extension of the comparisons to investigate synergies with other approaches, such as post-Minkowskian theory, perturbation theory and gravitational self-force as well as extending the analysis to eccentric spin-precessing systems and higher mass ratios. Ultimately, we want to leverage insights from NR to enhance gravitational waveform models for both current and next-generation of gravitational wave detectors.

Appendix A

Derivatives of r, Ω, p_{r*}

A.1 Second derivatives

$$\ddot{r} = \sqrt{\frac{A}{B}}\Bigg\{\frac{1}{2H}\left(A\frac{\partial^2 Q}{\partial p_{r*}^2}\dot{p}_{r*} + A\frac{\partial^2 Q}{\partial r \partial p_{r*}}\dot{r} + dA\frac{\partial Q}{\partial p_{r*}}\dot{r} + 2\dot{p}_{r*}\right) - \frac{1}{2H^2}\left[\dot{H}\left(A\frac{\partial Q}{\partial p_{r*}} + 2p_{r*}\right)\right] \tag{A.1}$$
$$+ \frac{1}{E^2}\left[\frac{\partial^2 \tilde{G}}{\partial p_{r*}^2}Ep_\varphi\dot{p}_{r*} + \frac{\partial^2 \tilde{G}}{\partial r \partial p_{r*}}Ep_\varphi\dot{r} - \frac{\partial \tilde{G}}{\partial p_{r*}}\dot{E}p_\varphi + \frac{\partial \tilde{G}}{\partial p_{r*}}E\dot{p}_\varphi\right]\Bigg\} + \sqrt{\frac{B}{A}}\left(\sqrt{\frac{A}{B}}\right)'\dot{r}^2$$

$$\ddot{\Omega} = \frac{1}{H^3}\left[Au_c^2\left(H^2\ddot{p}_\varphi - H\ddot{H}p_\varphi - 2H\dot{H}\dot{p}_\varphi + 2\dot{H}^2p_\varphi\right)\right] \tag{A.2}$$
$$+ \frac{1}{E^3}\left[\frac{(Au_c^2)''E^3p_\varphi\dot{r}^2}{H} + \frac{\partial^2 \tilde{G}}{\partial p_{r*}^2}E^2\dot{p}_{r*}^2 + (\tilde{G})''E^2\dot{r}^2 + 2\frac{\partial^2 \tilde{G}}{\partial r \partial p_{r*}}E^2\dot{p}_{r*}\dot{r}\right.$$
$$\left. - 2\dot{E}E\left(\frac{\partial \tilde{G}}{\partial p_{r*}}\dot{p}_{r*} + \tilde{G}'\dot{r}\right) + \frac{\partial \tilde{G}}{\partial p_{r*}}E^2\ddot{p}_{r*} + \tilde{G}'E^2\ddot{r}\right]$$

$$+\frac{1}{E^3}\left[(Au_c)''\left(-\frac{2\dot{H}E^3p_\varphi\dot{r}}{H^2}+\frac{E^3p_\varphi\ddot{r}}{H}+\frac{2E^3\dot{p}_\varphi\dot{r}}{H}\right)\right]+\frac{\tilde{G}}{E^3}\left(2\dot{E}^2-\ddot{E}E\right)$$

$$\begin{aligned}\ddot{p}_{r*}=\frac{1}{2H^2E^2}\Bigg\{&\sqrt{\frac{A}{B}}\Bigg[\frac{1}{r_c^4}\Bigg\{AE^2\Bigg(-Hr_c\left(d2Qr_c^3\dot{r}-2(r_c)''p_\varphi^2\dot{r}+\frac{\partial^2Q}{\partial r\partial p_{r*}}\dot{p}_{r*}r_c^3\right)\\&+dQ\dot{H}r_c^4-6(r_c)'^2Hp_\varphi^2\dot{r}+(r_c)'\left(4Hp_\varphi\dot{p}_\varphi r_c-2\dot{H}p_\varphi^2r_c\right)\Bigg)\Bigg\}\\&+H\left(-d2AE^2\dot{r}\left(\frac{p_\varphi^2}{r_c^2}+Q+1\right)-2HE\left((\tilde{G})''p_\varphi\dot{r}+\frac{\partial^2\tilde{G}}{\partial r\partial p_{r*}}p_\varphi\dot{p}_{r*}+\tilde{G}'\dot{p}_\varphi\right)+2\tilde{G}'\dot{E}Hp_\varphi\right)\\&+dAE^2\left(\dot{H}\left(\frac{p_\varphi^2}{r_c^2}+Q+1\right)-H\left(2dQ\dot{r}+\frac{\partial Q}{\partial p_{r*}}\dot{p}_{r*}+\frac{2p_\varphi\left(\dot{p}_\varphi r_c-2(r_c)'p_\varphi\dot{r}\right)}{r_c^3}\right)\right)\Bigg]\Bigg\}\\&+\sqrt{\frac{B}{A}}\left(\sqrt{\frac{A}{B}}\right)'\dot{p}_{r*}\dot{r}\end{aligned}\tag{A.3}$$

A.2 Third derivatives

$$\begin{aligned}\dddot{r}=\frac{B}{2A}\Bigg\{&\frac{1}{H^3E^3}\Bigg[\sqrt{\frac{A}{B}}^3\Big(AE^3\Big(H\Big(\frac{\partial^3Q}{\partial p_{r*}^3}H\dot{p}_{r*}^2+\frac{\partial^3Q}{\partial p_{r*}\partial r^2}H\dot{r}^2\\&+2\frac{\partial^3Q}{\partial r\partial p_{r*}^2}H\dot{p}_{r*}\dot{r}+\frac{\partial^2Q}{\partial p_{r*}^2}H\ddot{p}_{r*}-2\frac{\partial^2Q}{\partial p_{r*}^2}\dot{H}\dot{p}_{r*}+\frac{\partial^2Q}{\partial r\partial p_{r*}}H\dot{r}\\&-2\frac{\partial^2Q}{\partial r\partial p_{r*}}\dot{H}\dot{r}\Big)+\frac{\partial Q}{\partial p_{r*}}\left(2\dot{H}^2-H\ddot{H}\right)\Big)+H^2E^3\Big((A)''\frac{\partial Q}{\partial p_{r*}}\dot{r}^2\\&+2A'\frac{\partial^2Q}{\partial p_{r*}^2}\dot{p}_{r*}\dot{r}+2A'\frac{\partial^2Q}{\partial r\partial p_{r*}}\dot{r}^2+A'\frac{\partial Q}{\partial p_{r*}}\dot{r}+2\ddot{p}_{r*}\Big)\\&+2H^3E\Big(\frac{\partial^2\tilde{G}}{\partial p_{r*}^2}\left(-2\dot{E}\dot{p}_\varphi\dot{p}_{r*}+E\dot{p}_\varphi\ddot{p}_{r*}+2E\dot{p}_\varphi\dot{p}_{r*}\right)\\&-2\frac{\partial^2\tilde{G}}{\partial r\partial p_{r*}}\dot{E}\dot{p}_\varphi\dot{r}+\frac{\partial^2\tilde{G}}{\partial r\partial p_{r*}}E\dot{p}_\varphi\dot{r}+2\frac{\partial^2\tilde{G}}{\partial r\partial p_{r*}}E\dot{p}_\varphi\dot{r}+2\frac{\partial^3\tilde{G}}{\partial r\partial p_{r*}^2}E\dot{p}_\varphi\dot{p}_{r*}\dot{r}+\frac{\partial\tilde{G}}{\partial p_{r*}^3}E\dot{p}_\varphi\dot{p}_{r*}^2\end{aligned}\tag{A.4}$$

$$
\begin{aligned}
&+\frac{\partial^3\tilde{G}}{\partial p_{r*}\partial r^2}E\dot{p}_\varphi\dot{r}^2\ ) - 2HE^3\ (\ A'\frac{\partial Q}{\partial p_{r*}}\dot{H}\dot{r} + \ddot{H}p_{r*}\\
&+2\dot{H}\dot{p}_{r*}\ ) + 2\frac{\partial\tilde{G}}{\partial p_{r*}}H^3\left[E\left(E\ddot{p}_\varphi - \ddot{E}\dot{p}_\varphi\right) + 2\dot{E}^2\dot{p}_\varphi - 2\dot{E}E\dot{p}_\varphi\right]\\
&+4\dot{H}^2E^3p_{r*}\ )\Big] + 2\left(\sqrt{\frac{A}{B}}\right)''\dot{r}^3\sqrt{\frac{A}{B}} - 2\left(\sqrt{\frac{A}{B}}\right)'^2\left(\dot{r}\dot{r}^2 + \dot{r}^3\right) + 6\left(\sqrt{\frac{A}{B}}\right)'\dot{r}\dot{r}\sqrt{\frac{A}{B}}\Big\}
\end{aligned}
$$

$$
\ddot{\Omega} = \frac{1}{H^4}\Big\{Au_c^2\left(H^3\,\dddot{p}_\varphi - H^2(3\ddot{H}\dot{p}_\varphi + \dddot{H}p_\varphi + 3\dot{H}\ddot{p}_\varphi) + 6H\dot{H}(\ddot{H}p_\varphi + \dot{H}\dot{p}_\varphi) - 6\dot{H}^3p_\varphi\right)\Big\} \tag{A.5}
$$

$$
\begin{aligned}
&+\frac{1}{E^4}\Big\{-\frac{3(Au_c^2)''\dot{H}E^4p_\varphi\dot{r}^2}{H^2} + \frac{3(Au_c^2)''E^4p_\varphi\ddot{r}\dot{r}}{H} + \frac{3(Au_c^2)''E^4\dot{p}_\varphi\dot{r}^2}{H} - 3\dot{E}E^2\ (\ \frac{\partial^2\tilde{G}}{\partial p_{r*}^2}\dot{p}_{r*}^2 + \frac{\partial^2G}{\partial r^2}\dot{r}^2\\
&+2\frac{\partial^2\tilde{G}}{\partial r\partial p_{r*}}\dot{p}_{r*}\dot{r} + \frac{\partial\tilde{G}}{\partial p_{r*}}\ddot{p}_{r*} + \frac{\partial\tilde{G}}{\partial r}\ddot{r}\ ) + 3\frac{\partial^2\tilde{G}}{\partial p_{r*}^2}E^3\ddot{p}_{r*}\dot{p}_{r*} + 3\frac{\partial^2\tilde{G}}{\partial r^2}E^3\ddot{r}\dot{r}\\
&+3\frac{\partial^2\tilde{G}}{\partial r\partial p_{r*}}E^3\ddot{p}_{r*}\dot{r} + 3\frac{\partial^2\tilde{G}}{\partial r\partial p_{r*}}E^3\dot{p}_{r*}\ddot{r} + \frac{(Au_c^2)'''E^4p_\varphi\dot{r}^3}{H} + 3\frac{\partial^3\tilde{G}}{\partial r\partial p_{r*}^2}E^3\dot{p}_{r*}^2\dot{r} + \frac{\partial^3\tilde{G}}{\partial p_{r*}^3}E^3\dot{p}_{r*}^3\\
&+3\frac{\partial^3\tilde{\tilde{G}}}{\partial p_{r*}\partial r^2}E^3\dot{p}_{r*}\dot{r}^2 + \frac{\partial^3\tilde{G}}{\partial r^3}E^3\dot{r}^3 + 6\dot{E}^2E(\frac{\partial\tilde{G}}{\partial p_{r*}}\dot{p}_{r*} + \frac{\partial\tilde{G}}{\partial r}\dot{r}) + \frac{\partial\tilde{G}}{\partial p_{r*}}E^2\left(E\,\dddot{p}_{r*} - 3\ddot{E}\dot{p}_{r*}\right)\\
&-3\frac{\partial\tilde{G}}{\partial r}\ddot{E}E^2\dot{r} + \frac{\partial\tilde{G}}{\partial r}E^3\,\ddot{r}\Big\} + (Au_c^2)'\ (\ \frac{6\dot{H}^2p_\varphi\dot{r}}{H^3} - \frac{3\ddot{H}p_\varphi\dot{r}}{H^2} - \frac{3\dot{H}p_\varphi\ddot{r}}{H^2} - \frac{6\dot{H}\dot{p}_\varphi\dot{r}}{H^2} + \frac{p_\varphi\,\dddot{r}}{H}\\
&+\frac{3\ddot{p}_\varphi\dot{r}}{H} + \frac{3\dot{p}_\varphi\ddot{r}}{H}\ ) + \frac{1}{E^4}\Big\{\tilde{G}\left(6\ddot{E}\dot{E}E - \dddot{E}E^2 - 6\dot{E}^3\right)\Big\}
\end{aligned}
$$

$$
\begin{aligned}
\dddot{p}_{r*} = \frac{1}{H^3}\Big\{\sqrt{\frac{A}{B}}\ (\ A\ (\ &-\frac{1}{2}Q''H^2\ddot{r} + Q''H\dot{H}\dot{r} - 9(r_c)''(r_c)'H^2p_\varphi^2\ddot{r}u_c^4 + 4(r_c)''H^2p_\varphi\dot{p}_\varphi\dot{r}u_c^3 \qquad (A.6)\\
&+(r_c)''H^2p_\varphi^2\ddot{r}u_c^3 - 2(r_c)''H\dot{H}p_\varphi^2\dot{r}u_c^3 - \frac{1}{2}(Q)'''H^2\ddot{r} - \frac{\partial^3Q}{\partial p_{r*}\partial r^2}H^2\dot{p}_{r*}\dot{r} - \frac{1}{2}\frac{\partial^3Q}{\partial r\partial p_{r*}^2}H^2\dot{p}_{r*}^2\\
&+(r_c)'''H^2p_\varphi^2\ddot{r}u_c^3 + \frac{\partial^2Q}{\partial r\partial p_{r*}}H(\dot{H}\dot{p}_{r*} - \frac{1}{2}H\ddot{p}_{r*}) + Q'\left(\frac{1}{2}H\ddot{H} - \dot{H}^2\right) + 12(r_c)'^3H^2p_\varphi^2\ddot{r}u_c^5
\end{aligned}
$$

$$
\begin{aligned}
&- 12(r_c)'^2 H^2 p_\varphi \dot{p}_\varphi \dot{r} u_c^4 - 3(r_c)'^2 H^2 p_\varphi^2 \ddot{r} u_c^4 + 6(r_c)'^2 H \dot{H} p_\varphi^2 \dot{r} u_c^4 \\
&+ 2(r_c)' H^2 p_\varphi \ddot{p}_\varphi u_c^3 + 2(r_c)' H^2 \dot{p}_\varphi^2 u_c^3 - (r_c)' H \ddot{H} p_\varphi^2 u_c^3 - 4(r_c)' H \dot{H} p_\varphi \dot{p}_\varphi u_c^3 + 2(r_c)' \dot{H}^2 p_\varphi^2 u_c^3 \ ) \\
&+ H \ (\ - \frac{3}{2} A'' Q' H \ddot{r} - A'' \frac{\partial Q}{\partial p_{r*}} H \dot{p}_{r*} \dot{r} + 3A''(r_c)' H p_\varphi^2 \ddot{r} u_c^3 - 2A'' H p_\varphi \dot{p}_\varphi \dot{r} u_c^2 - \frac{1}{2} A'' H p_\varphi^2 \ddot{r} u_c^2 \\
&- \frac{1}{2} A'' H Q \ddot{r} - \frac{1}{2} A'' H \ddot{r} + A'' \dot{H} p_\varphi^2 \dot{r} u_c^2 + A'' \dot{H} Q \dot{r} + A'' \dot{H} \dot{r} \\
&+ 2(\tilde{G})'' \dot{E} H^2 E^2 p_\varphi \dot{r} - (\tilde{G})'' H^2 E p_\varphi \ddot{r} - 2(\tilde{G})'' H^2 E \dot{p}_\varphi \dot{r} + \frac{\partial^2 G}{\partial r \partial p_{r*}} H^2 E (2 \dot{E} E p_\varphi \dot{p}_{r*} \\
&- p_\varphi \ddot{p}_{r*} - 2 \dot{p}_\varphi \dot{p}_{r*}) - \frac{1}{2} A'' H p_\varphi^2 \ddot{r} u_c^2 - \frac{1}{2} A'' H Q \ddot{r} - \frac{1}{2} A'' H \ddot{r} - \frac{\partial^3 G}{\partial r \partial p_{r*}} H^2 E p_\varphi \dot{p}_{r*}^2 \\
&- 2 \frac{\partial^3 \tilde{G}}{\partial p_{r*} \partial^2 r} H^2 E p_\varphi \dot{p}_{r*} \dot{r} - \tilde{G}''' H^2 E p_\varphi \ddot{r} + \tilde{G}' H^2 E \ (\ \ddot{E} E p_\varphi - 2 \dot{E}^2 E^2 p_\varphi + 2 \dot{E} E \dot{p}_\varphi - \ddot{p}_\varphi \ ) \ ) \\
&+ A' \ (\ H^2 \ (\ - \frac{3}{2} Q'' \ddot{r} + 3(r_c)'' p_\varphi^2 \ddot{r} u_c^3 - \frac{1}{2} \frac{\partial Q}{\partial p_{r*}} \dot{p}_{r*}^2 - 2 \frac{\partial Q}{\partial r \partial p_{r*}} \dot{p}_{r*} \dot{r} - Q' \ddot{r} - \frac{1}{2} \frac{\partial Q}{\partial p_{r*}} \ddot{p}_{r*} - 9(r_c)'^2 p_\varphi^2 \ddot{r} u_c^4 \\
&+ 8(r_c)' p_\varphi \dot{p}_\varphi \dot{r} u_c^3 + 2(r_c)' p_\varphi^2 \ddot{r} u_c^3 - p_\varphi \ddot{p}_\varphi u_c^2 - \dot{p}_\varphi^2 u_c^2 \ ) + H \dot{H} (2Q' \dot{r} + \frac{\partial Q}{\partial p_{r*}} \dot{p}_{r*} + p_\varphi u_c^2 (2 \dot{p}_\varphi - 4(r_c)' p_\varphi \dot{r} u_c)) \\
&+ H \ddot{H} (\frac{1}{2} p_\varphi^2 u_c^2 + \frac{1}{2} Q + \frac{1}{2}) + \dot{H}^2 (-p_\varphi^2 u_c^2 - Q - 1) \ ) \ ) \Big\} \\
&+ \frac{1}{H^3} \Big\{ \left(\sqrt{\frac{A}{B}} \right)' H^2 \dot{r} \ (\ A \left(- \frac{1}{2} Q'' \dot{r} + (r_c)'' p_\varphi^2 \dot{r} u_c^3 - \frac{1}{2} \frac{\partial Q}{\partial r \partial p_{r*}} \dot{p}_{r*} - 3(r_c)'^2 p_\varphi^2 \dot{r} u_c^4 + 2(r_c)' p_\varphi \dot{p}_\varphi u_c^3 \right) \\
&+ A'' \dot{r} (- \frac{1}{2} p_\varphi^2 u_c^2 - \frac{1}{2} Q - \frac{1}{2}) + A' (- Q' \dot{r} - \frac{1}{2} \frac{\partial Q}{\partial p_{r*}} \dot{p}_{r*} + p_\varphi u_c^2 (2(r_c)' p_\varphi \dot{r} u_c - \dot{p}_\varphi)) \ ) \\
&+ \left(\sqrt{\frac{A}{B}} \right)' H \dot{H} \dot{r} \left(\frac{1}{2} A Q' - A(r_c)' p_\varphi^2 u_c^3 + A' (\frac{1}{2} p_\varphi^2 u_c^2 + \frac{1}{2} Q + \frac{1}{2}) \right) + \left(\sqrt{\frac{A}{B}} \right)' H^3 E \dot{r} (- (\tilde{G})'' p_\varphi \dot{r} \\
&+ \tilde{G}' \dot{E} E p_\varphi - \tilde{G}' \dot{p}_\varphi) - \frac{\partial^2 G}{\partial r \partial p_{r*}} \left(\sqrt{\frac{A}{B}} \right)' H^3 E p_\varphi \dot{p}_{r*} \dot{r} \Big\} + \frac{1}{H^3} \sqrt{\frac{B}{A}} \Big\{ \left(\sqrt{\frac{A}{B}} \right)'' H^3 \dot{p}_{r*} \ddot{r} + \left(\sqrt{\frac{A}{B}} \right)' H^3 \ddot{p}_{r*} \dot{r} \\
&+ \left(\sqrt{\frac{A}{B}} \right)' H^3 \dot{p}_{r*} \ddot{r} \Big\} - \frac{B}{A} \left(\sqrt{\frac{A}{B}} \right)'^2 \dot{p}_{r*} \ddot{r}
\end{aligned}
$$

Bibliography

[1] Alice Bonino et al. “Inferring eccentricity evolution from observations of coalescing binary black holes”. In: *Phys. Rev. D* 107.6 (2023), p. 064024. DOI: 10.1103/PhysRevD.107.064024. arXiv: 2207.10474 [gr-qc].

[2] Alice Bonino, Patricia Schmidt, and Geraint Pratten. “Mapping eccentricity evolutions between numerical relativity and effective-one-body gravitational waveforms”. In: *Phys. Rev. D* 110 (2024), p. 104002. DOI: 10.1103/PhysRevD.110.104002. arXiv: 2404.18875 [gr-qc].

[3] Albert Einstein. “Approximative Integration of the Field Equations of Gravitation”. In: *Sitzungsber. Preuss. Akad. Wiss. Berlin (Math. Phys.)* 1916 (1916), pp. 688–696.

[4] Albert Einstein. “Über Gravitationswellen”. In: *Sitzungsber. Preuss. Akad. Wiss. Berlin (Math. Phys.)* 1918 (1918), pp. 154–167.

[5] R. A. Hulse and J. H. Taylor. “Discovery of a pulsar in a binary system.” In: *Astrophysical Journal* 195 (Jan. 1975), pp. L51–L53. DOI: 10.1086/181708.

[6] B. P. Abbott et al. “LIGO: The Laser interferometer gravitational-wave observatory”. In: *Rept. Prog. Phys.* 72 (2009), p. 076901. DOI: 10.1088/0034-4885/72/7/076901. arXiv: 0711.3041 [gr-qc].

[7] J. Aasi et al. “Advanced LIGO”. In: *Class. Quant. Grav.* 32 (2015), p. 074001. DOI: 10.1088/0264-9381/32/7/074001. arXiv: 1411.4547 [gr-qc].

[8] M. Tse et al. “Quantum-Enhanced Advanced LIGO Detectors in the Era of Gravitational-Wave Astronomy”. In: *Phys. Rev. Lett.* 123.23 (2019), p. 231107. DOI: 10.1103/PhysRevLett.123.231107.

[9] F. Acernese et al. “Advanced Virgo: a second-generation interferometric gravitational wave detector”. In: *Class. Quant. Grav.* 32.2 (2015), p. 024001. DOI: 10.1088/0264-9381/32/2/024001. arXiv: 1408.3978 [gr-qc].

[10] F. Acernese et al. “Increasing the Astrophysical Reach of the Advanced Virgo Detector via the Application of Squeezed Vacuum States of Light”. In: *Phys. Rev. Lett.* 123.23 (2019), p. 231108. DOI: 10.1103/PhysRevLett.123.231108.

[11] B. P. Abbott et al. “Observation of Gravitational Waves from a Binary Black Hole Merger”. In: *Phys. Rev. Lett.* 116.6 (2016), p. 061102. DOI: 10.1103/PhysRevLett.116.061102. arXiv: 1602.03837 [gr-qc].

[12] B. P. Abbott et al. “GWTC-1: A Gravitational-Wave Transient Catalog of Compact Binary Mergers Observed by LIGO and Virgo during the First and Second Observing Runs”. In: *Phys. Rev.* X9.3 (2019), p. 031040. DOI: 10.1103/PhysRevX.9.031040. arXiv: 1811.12907 [astro-ph.HE].

[13] R. Abbott et al. “GWTC-2: Compact Binary Coalescences Observed by LIGO and Virgo During the First Half of the Third Observing Run”. In: *Phys. Rev. X* 11 (2021), p. 021053. DOI: 10.1103/PhysRevX.11.021053. arXiv: 2010.14527 [gr-qc].

[14] R. Abbott et al. “GWTC-3: Compact Binary Coalescences Observed by LIGO and Virgo during the Second Part of the Third Observing Run”. In: *Phys. Rev. X* 13.4 (2023), p. 041039. DOI: 10.1103/PhysRevX.13.041039. arXiv: 2111.03606 [gr-qc].

[15] P. C. Peters and J. Mathews. "Gravitational radiation from point masses in a Keplerian orbit". In: *Phys. Rev.* 131 (1963), pp. 435–439. DOI: 10.1103/PhysRev.131.435.

[16] P. C. Peters. "Gravitational Radiation and the Motion of Two Point Masses". In: *Phys. Rev.* 136 (1964), B1224–B1232. DOI: 10.1103/PhysRev.136.B1224.

[17] P. C. Peters. "Gravitational Radiation and the Motion of Two Point Masses". PhD thesis. Caltech, 1964.

[18] Isobel M. Romero-Shaw, Paul D. Lasky, and Eric Thrane. "Signs of Eccentricity in Two Gravitational-wave Signals May Indicate a Subpopulation of Dynamically Assembled Binary Black Holes". In: *Astrophys. J. Lett.* 921.2 (2021), p. L31. DOI: 10.3847/2041-8213/ac3138. arXiv: 2108.01284 [astro-ph.HE].

[19] Johan Samsing. "Eccentric Black Hole Mergers Forming in Globular Clusters". In: *Phys. Rev. D* 97.10 (2018), p. 103014. DOI: 10.1103/PhysRevD.97.103014. arXiv: 1711.07452 [astro-ph.HE].

[20] Johan Samsing et al. "Single-single gravitational-wave captures in globular clusters: Eccentric deci-Hertz sources observable by DECIGO and Tian-Qin". In: *Phys. Rev. D* 101.12 (2020), p. 123010. DOI: 10.1103/PhysRevD.101.123010. arXiv: 1907.11231 [astro-ph.HE].

[21] Michael Zevin et al. "Implications of Eccentric Observations on Binary Black Hole Formation Channels". In: *Astrophys. J. Lett.* 921.2 (2021), p. L43. DOI: 10.3847/2041-8213/ac32dc. arXiv: 2106.09042 [astro-ph.HE].

[22] Stanislav Babak et al. "Science with the space-based interferometer LISA. V: Extreme mass-ratio inspirals". In: *Phys. Rev. D* 95.10 (2017), p. 103012. DOI: 10.1103/PhysRevD.95.103012. arXiv: 1703.09722 [gr-qc].

[23] Pau Amaro-Seoane et al. *Laser Interferometer Space Antenna*. 2017. arXiv: 1702.00786 [astro-ph.IM].

[24] Christopher P. L. Berry et al. "The unique potential of extreme mass-ratio inspirals for gravitational-wave astronomy". In: (2019). arXiv: 1903.03686 [astro-ph.HE].

[25] William E. East et al. "Observing complete gravitational wave signals from dynamical capture binaries". In: *Phys. Rev. D* 87.4 (2013), p. 043004. DOI: 10.1103/PhysRevD.87.043004. arXiv: 1212.0837 [gr-qc].

[26] Roman Gold and Bernd Brügmann. "Eccentric black hole mergers and zoom-whirl behavior from elliptic inspirals to hyperbolic encounters". In: *Phys. Rev. D* 88.6 (2013), p. 064051. DOI: 10.1103/PhysRevD.88.064051. arXiv: 1209.4085 [gr-qc].

[27] Nicholas Loutrel. "Repeated Bursts: Gravitational Waves from Highly Eccentric Binaries". In: (Sept. 2020). DOI: 10.1007/978-981-15-4702-7_33-1. arXiv: 2009.11332 [gr-qc].

[28] Carl L. Rodriguez et al. "Post-Newtonian Dynamics in Dense Star Clusters: Highly-Eccentric, Highly-Spinning, and Repeated Binary Black Hole Mergers". In: *Phys. Rev. Lett.* 120.15 (2018), p. 151101. DOI: 10.1103/PhysRevLett.120.151101. arXiv: 1712.04937 [astro-ph.HE].

[29] Giacomo Fragione et al. "Black hole and neutron star mergers in galactic nuclei". In: *Mon. Not. Roy. Astron. Soc.* 488.1 (2019), pp. 47–63. DOI: 10.1093/mnras/stz1651. arXiv: 1811.10627 [astro-ph.GA].

[30] J. Samsing et al. "Active Galactic Nuclei as Factories for Eccentric Black Hole Mergers". In: (Oct. 2020). arXiv: 2010.09765 [astro-ph.HE].

[31] Hiromichi Tagawa et al. "Eccentric Black Hole Mergers in Active Galactic Nuclei". In: *Astrophys. J. Lett.* 907.1 (2021), p. L20. DOI: 10.3847/2041-8213/abd4d3. arXiv: 2010.10526 [astro-ph.HE].

[32] V. Gayathri et al. "Eccentricity estimate for black hole mergers with numerical relativity simulations". In: *Nature Astron.* 6.3 (2022), pp. 344–349. DOI: 10.1038/s41550-021-01568-w. arXiv: 2009.05461 [astro-ph.HE].

[33] Isobel M. Romero-Shaw, Paul D. Lasky, and Eric Thrane. "Four eccentric mergers increase the evidence that LIGO–Virgo–KAGRA's binary black holes form dynamically". In: (June 2022). arXiv: 2206.14695 [astro-ph.HE].

[34] Teagan A. Clarke et al. "Gravitational-wave inference for eccentric binaries: the argument of periapsis". In: *Mon. Not. Roy. Astron. Soc.* 517.3 (2022), pp. 3778–3784. DOI: 10.1093/mnras/stac2965. arXiv: 2206.14006 [gr-qc].

[35] Rossella Gamba et al. "GW190521 as a dynamical capture of two nonspinning black holes". In: *Nature Astron.* 7.1 (2023), pp. 11–17. DOI: 10.1038/s41550-022-01813-w. arXiv: 2106.05575 [gr-qc].

[36] Isobel M. Romero-Shaw et al. "GW190521: orbital eccentricity and signatures of dynamical formation in a binary black hole merger signal". In: *Astrophys. J. Lett.* 903.1 (2020), p. L5. DOI: 10.3847/2041-8213/abbe26. arXiv: 2009.04771 [astro-ph.HE].

[37] Nihar Gupte et al. "Evidence for eccentricity in the population of binary black holes observed by LIGO-Virgo-KAGRA". In: (Apr. 2024). arXiv: 2404.14286 [gr-qc].

[38] Gonzalo Morras, Geraint Pratten, and Patricia Schmidt. "Improved post-Newtonian waveform model for inspiralling precessing-eccentric compact binaries". In: *Phys. Rev. D* 111.8 (2025), p. 084052. DOI: 10.1103/PhysRevD.111.084052. arXiv: 2502.03929 [gr-qc].

[39] Maria de Lluc Planas et al. "Eccentric or circular? A reanalysis of binary black hole gravitational wave events for orbital eccentricity signatures". In: (Apr. 2025). arXiv: 2504.15833 [gr-qc].

[40] Maria de Lluc Planas et al. “First eccentric inspiral-merger-ringdown analysis of neutron star-black hole mergers”. In: (June 2025). arXiv: 2506.01760 [astro-ph.HE].

[41] Rossella Gamba et al. “Revisiting GW150914 with a non-planar, eccentric waveform model”. In: *Class. Quant. Grav.* 42.17 (2025), p. 175014. DOI: 10.1088/1361-6382/adfe50. arXiv: 2505.21612 [gr-qc].

[42] R. Abbott et al. “GW190521: A Binary Black Hole Merger with a Total Mass of $150M_\odot$”. In: *Phys. Rev. Lett.* 125.10 (2020), p. 101102. DOI: 10.1103/PhysRevLett.125.101102. arXiv: 2009.01075 [gr-qc].

[43] R. et al. Abbott. “Properties and Astrophysical Implications of the 150 $M_\odot$ Binary Black Hole Merger GW190521”. In: *apjl* 900.1, L13 (Sept. 2020), p. L13. DOI: 10.3847/2041-8213/aba493. arXiv: 2009.01190 [astro-ph.HE].

[44] Giacomo Fragione, Abraham Loeb, and Frederic A. Rasio. “On the Origin of GW190521-like events from repeated black hole mergers in star clusters”. In: *Astrophys. J. Lett.* 902.1 (2020), p. L26. DOI: 10.3847/2041-8213/abbc0a. arXiv: 2009.05065 [astro-ph.GA].

[45] Giacomo Fragione et al. “Repeated Mergers, Mass-gap Black Holes, and Formation of Intermediate-mass Black Holes in Dense Massive Star Clusters”. In: *Astrophys. J.* 927.2 (2022), p. 231. DOI: 10.3847/1538-4357/ac5026. arXiv: 2107.04639 [astro-ph.GA].

[46] Juan Calderón Bustillo et al. “GW190521 as a Merger of Proca Stars: A Potential New Vector Boson of 8.7×10^{-13} eV”. In: *Phys. Rev. Lett.* 126.8 (2021), p. 081101. DOI: 10.1103/PhysRevLett.126.081101. arXiv: 2009.05376 [gr-qc].

[47] Masaru Shibata et al. “Alternative possibility of GW190521: Gravitational waves from high-mass black hole-disk systems”. In: *Phys. Rev. D* 103.6 (2021), p. 063037. DOI: 10.1103/PhysRevD.103.063037. arXiv: 2101.05440 [astro-ph.HE].

[48] Héctor Estellés et al. "A Detailed Analysis of GW190521 with Phenomenological Waveform Models". In: *Astrophys. J.* 924.2 (2022), p. 79. DOI: 10.3847/1538-4357/ac33a0. arXiv: 2105.06360 [gr-qc].

[49] Gonzalo Morras, Geraint Pratten, and Patricia Schmidt. "Orbital eccentricity in a neutron star - black hole binary". In: (Mar. 2025). arXiv: 2503.15393 [astro-ph.HE].

[50] Marcus E. Lower et al. "Measuring eccentricity in binary black hole inspirals with gravitational waves". In: *Phys. Rev. D* 98.8 (2018), p. 083028. DOI: 10.1103/PhysRevD.98.083028. arXiv: 1806.05350 [astro-ph.HE].

[51] David Reitze et al. "Cosmic Explorer: The U.S. Contribution to Gravitational-Wave Astronomy beyond LIGO". In: *Bull. Am. Astron. Soc.* 51 (July 2019), p. 035. arXiv: 1907.04833 [astro-ph.IM].

[52] Matthew Evans et al. "A Horizon Study for Cosmic Explorer: Science, Observatories, and Community". In: (Sept. 2021). arXiv: 2109.09882 [astro-ph.IM].

[53] Michele Maggiore et al. "Science Case for the Einstein Telescope". In: *JCAP* 03 (2020), p. 050. DOI: 10.1088/1475-7516/2020/03/050. arXiv: 1912.02622 [astro-ph.CO].

[54] Adrian Abac et al. "The Science of the Einstein Telescope". In: (Mar. 2025). arXiv: 2503.12263 [gr-qc].

[55] Amber K. Lenon, Duncan A. Brown, and Alexander H. Nitz. "Eccentric binary neutron star search prospects for Cosmic Explorer". In: *Phys. Rev. D* 104.6 (2021), p. 063011. DOI: 10.1103/PhysRevD.104.063011. arXiv: 2103.14088 [astro-ph.HE].

[56] Pankaj Saini. "Resolving the eccentricity of stellar mass binary black holes with next generation gravitational wave detectors". In: (Aug. 2023). arXiv: 2308.07565 [astro-ph.HE].

[57] Katelyn Breivik et al. "Distinguishing Between Formation Channels for Binary Black Holes with LISA". In: *Astrophys. J. Lett.* 830.1 (2016), p. L18. DOI: 10.3847/2041-8205/830/1/L18. arXiv: 1606.09558 [astro-ph.GA].

[58] Atsushi Nishizawa et al. "Constraining stellar binary black hole formation scenarios with eLISA eccentricity measurements". In: *Mon. Not. Roy. Astron. Soc.* 465.4 (2017), pp. 4375–4380. DOI: 10.1093/mnras/stw2993. arXiv: 1606.09295 [astro-ph.HE].

[59] Antoine Klein et al. "The last three years: multiband gravitational-wave observations of stellar-mass binary black holes". In: (Apr. 2022). arXiv: 2204.03423 [astro-ph.HE].

[60] Davide Gerosa et al. "Multiband gravitational-wave event rates and stellar physics". In: *Phys. Rev. D* 99.10 (2019), p. 103004. DOI: 10.1103/PhysRevD.99.103004. arXiv: 1902.00021 [astro-ph.HE].

[61] Becca Ewing et al. "Archival searches for stellar-mass binary black holes in LISA data". In: *Phys. Rev. D* 103.2 (2021), p. 023025. DOI: 10.1103/PhysRevD.103.023025. arXiv: 2011.03036 [gr-qc].

[62] Luc Blanchet. "Gravitational Radiation from Post-Newtonian Sources and Inspiralling Compact Binaries". In: *Living Rev. Relativity* 17 (2014), p. 2. DOI: 10.12942/lrr-2014-2. arXiv: 1310.1528 [gr-qc].

[63] T. Damour and N. Deruelle. "General relativistic celestial mechanics of binary systems. I. The post-Newtonian motion." In: *Annales de L'Institut Henri Poincare Section (A) Physique Theorique* 43.1 (Jan. 1985), pp. 107–132.

[64] Craig W. Lincoln and Clifford M. Will. "Coalescing binary systems of compact objects to (post)$^{5/2}$-Newtonian order: Late-time evolution and gravitational-radiation

emission". In: *Phys. Rev. D* 42 (4 Aug. 1990), pp. 1123–1143. DOI: 10.1103/PhysRevD.42.1123. URL: https://link.aps.org/doi/10.1103/PhysRevD.42.1123.

[65] Thibault Damour, Achamveedu Gopakumar, and Bala R. Iyer. "Phasing of gravitational waves from inspiralling eccentric binaries". In: *Phys. Rev.* D70 (2004), p. 064028. DOI: 10.1103/PhysRevD.70.064028. arXiv: gr-qc/0404128 [gr-qc].

[66] Raoul-Martin Memmesheimer, Achamveedu Gopakumar, and Gerhard Schaefer. "Third post-Newtonian accurate generalized quasi-Keplerian parametrization for compact binaries in eccentric orbits". In: *Phys. Rev. D* 70 (2004), p. 104011. DOI: 10.1103/PhysRevD.70.104011. arXiv: gr-qc/0407049.

[67] Christian Konigsdorffer and Achamveedu Gopakumar. "Phasing of gravitational waves from inspiralling eccentric binaries at the third-and-a-half post-Newtonian order". In: *Phys. Rev. D* 73 (2006), p. 124012. DOI: 10.1103/PhysRevD.73.124012. arXiv: gr-qc/0603056.

[68] Thibault Damour, Piotr Jaranowski, and Gerhard Schäfer. "Conservative dynamics of two-body systems at the fourth post-Newtonian approximation of general relativity". In: *Phys. Rev.* D93.8 (2016), p. 084014. DOI: 10.1103/PhysRevD.93.084014. arXiv: 1601.01283 [gr-qc].

[69] Donato Bini, Thibault Damour, and Andrea Geralico. "Novel approach to binary dynamics: application to the fifth post-Newtonian level". In: *Phys. Rev. Lett.* 123.23 (2019), p. 231104. DOI: 10.1103/PhysRevLett.123.231104. arXiv: 1909.02375 [gr-qc].

[70] Donato Bini, Thibault Damour, and Andrea Geralico. "Binary dynamics at the fifth and fifth-and-a-half post-Newtonian orders". In: *Phys. Rev. D* 102.2 (2020), p. 024062. DOI: 10.1103/PhysRevD.102.024062. arXiv: 2003.11891 [gr-qc].

[71] J. Blümlein et al. "The fifth-order post-Newtonian Hamiltonian dynamics of two-body systems from an effective field theory approach". In: *Nucl. Phys. B* 983 (2022). [Erratum: Nucl.Phys.B 985, 115991 (2022)], p. 115900. DOI: 10.1016/j.nuclphysb.2022.115900. arXiv: 2110.13822 [gr-qc].

[72] Christoph Dlapa et al. "Conservative Dynamics of Binary Systems at Fourth Post-Minkowskian Order in the Large-Eccentricity Expansion". In: *Phys. Rev. Lett.* 128.16 (2022), p. 161104. DOI: 10.1103/PhysRevLett.128.161104. arXiv: 2112.11296 [hep-th].

[73] Quentin Henry and François Larrouturou. "Conservative tail and failed-tail effects at the fifth post-Newtonian order". In: *Phys. Rev. D* 108.8 (2023), p. 084048. DOI: 10.1103/PhysRevD.108.084048. arXiv: 2307.05860 [gr-qc].

[74] K. G. Arun et al. "Tail effects in the 3PN gravitational wave energy flux of compact binaries in quasi-elliptical orbits". In: *Phys. Rev. D* 77 (2008), p. 064034. DOI: 10.1103/PhysRevD.77.064034. arXiv: 0711.0250 [gr-qc].

[75] K. G. Arun et al. "Inspiralling compact binaries in quasi-elliptical orbits: The Complete 3PN energy flux". In: *Phys. Rev. D* 77 (2008), p. 064035. DOI: 10.1103/PhysRevD.77.064035. arXiv: 0711.0302 [gr-qc].

[76] K. G. Arun et al. "Third post-Newtonian angular momentum flux and the secular evolution of orbital elements for inspiralling compact binaries in quasi-elliptical orbits". In: *Phys. Rev. D* 80 (2009), p. 124018. DOI: 10.1103/PhysRevD.80.124018. arXiv: 0908.3854 [gr-qc].

[77] Chandra Kant Mishra, K. G. Arun, and Bala R. Iyer. "Third post-Newtonian gravitational waveforms for compact binary systems in general orbits: Instantaneous terms". In: *Phys. Rev.* D91.8 (2015), p. 084040. DOI: 10.1103/PhysRevD.91.084040. arXiv: 1501.07096 [gr-qc].

[78] Nicholas Loutrel and Nicolas Yunes. "Hereditary Effects in Eccentric Compact Binary Inspirals to Third Post-Newtonian Order". In: *Class. Quant. Grav.* 34.4 (2017), p. 044003. DOI: 10.1088/1361-6382/aa59c3. arXiv: 1607.05409 [gr-qc].

[79] Yannick Boetzel et al. "Gravitational-wave amplitudes for compact binaries in eccentric orbits at the third post-Newtonian order: Tail contributions and post-adiabatic corrections". In: *Phys. Rev. D* 100.4 (2019), p. 044018. DOI: 10.1103/PhysRevD.100.044018. arXiv: 1904.11814 [gr-qc].

[80] Michael Ebersold et al. "Gravitational-wave amplitudes for compact binaries in eccentric orbits at the third post-Newtonian order: Memory contributions". In: *Phys. Rev. D* 100.8 (2019), p. 084043. DOI: 10.1103/PhysRevD.100.084043. arXiv: 1906.06263 [gr-qc].

[81] Mohammed Khalil et al. "Radiation-reaction force and multipolar waveforms for eccentric, spin-aligned binaries in the effective-one-body formalism". In: *Phys. Rev. D* 104.2 (2021), p. 024046. DOI: 10.1103/PhysRevD.104.024046. arXiv: 2104.11705 [gr-qc].

[82] Kaushik Paul and Chandra Kant Mishra. "Spin effects in spherical harmonic modes of gravitational waves from eccentric compact binary inspirals". In: *Phys. Rev. D* 108.2 (2023), p. 024023. DOI: 10.1103/PhysRevD.108.024023. arXiv: 2211.04155 [gr-qc].

[83] Nicolas Yunes et al. "Post-Circular Expansion of Eccentric Binary Inspirals: Fourier-Domain Waveforms in the Stationary Phase Approximation". In: *Phys. Rev. D* 80.8 (2009). [Erratum: Phys.Rev.D 89, 109901 (2014)], p. 084001. DOI: 10.1103/PhysRevD.80.084001. arXiv: 0906.0313 [gr-qc].

[84] Manuel Tessmer and Gerhard Schaefer. "Full-analytic frequency-domain 1pN-accurate gravitational wave forms from eccentric compact binaries". In: *Phys. Rev. D* 82 (2010), p. 124064. DOI: 10.1103/PhysRevD.82.124064. arXiv: 1006.3714 [gr-qc].

[85] Sashwat Tanay, Maria Haney, and Achamveedu Gopakumar. "Frequency and time domain inspiral templates for comparable mass compact binaries in eccentric orbits". In: *Phys. Rev. D* 93.6 (2016), p. 064031. DOI: 10.1103/PhysRevD.93.064031. arXiv: 1602.03081 [gr-qc].

[86] Antoine Klein et al. "Fourier domain gravitational waveforms for precessing eccentric binaries". In: *Phys. Rev. D* 98.10 (2018), p. 104043. DOI: 10.1103/PhysRevD.98.104043. arXiv: 1801.08542 [gr-qc].

[87] Blake Moore and Nicolás Yunes. "A 3PN Fourier Domain Waveform for Non-Spinning Binaries with Moderate Eccentricity". In: *Class. Quant. Grav.* 36.18 (2019), p. 185003. DOI: 10.1088/1361-6382/ab3778. arXiv: 1903.05203 [gr-qc].

[88] Srishti Tiwari and Achamveedu Gopakumar. "Combining post-circular and Padé approximations to compute Fourier domain templates for eccentric inspirals". In: *Phys. Rev. D* 102.8 (2020), p. 084042. DOI: 10.1103/PhysRevD.102.084042. arXiv: 2009.11333 [gr-qc].

[89] Seth Hopper, Chris Kavanagh, and Adrian C. Ottewill. "Analytic self-force calculations in the post-Newtonian regime: eccentric orbits on a Schwarzschild background". In: *Phys. Rev. D* 93.4 (2016), p. 044010. DOI: 10.1103/PhysRevD.93.044010. arXiv: 1512.01556 [gr-qc].

[90] Erik Forseth, Charles R. Evans, and Seth Hopper. "Eccentric-orbit extreme-mass-ratio inspiral gravitational wave energy fluxes to 7PN order". In: *Phys. Rev. D* 93.6 (2016), p. 064058. DOI: 10.1103/PhysRevD.93.064058. arXiv: 1512.03051 [gr-qc].

[91] Donato Bini and Thibault Damour. "Gravitational scattering of two black holes at the fourth post-Newtonian approximation". In: *Phys. Rev.* D96.6 (2017), p. 064021. DOI: 10.1103/PhysRevD.96.064021. arXiv: 1706.06877 [gr-qc].

[92] Chris Kavanagh et al. "Spin-orbit precession along eccentric orbits for extreme mass ratio black hole binaries and its effective-one-body transcription". In: *Phys. Rev. D* 96.6 (2017), p. 064012. DOI: 10.1103/PhysRevD.96.064012. arXiv: 1706.00459 [gr-qc].

[93] Christopher Munna. "Analytic post-Newtonian expansion of the energy and angular momentum radiated to infinity by eccentric-orbit nonspinning extreme-mass-ratio inspirals to the 19th order". In: *Phys. Rev. D* 102.12 (2020), p. 124001. DOI: 10.1103/PhysRevD.102.124001. arXiv: 2008.10622 [gr-qc].

[94] Philip Lynch, Maarten van de Meent, and Niels Warburton. "Eccentric self-forced inspirals into a rotating black hole". In: *Class. Quant. Grav.* 39.14 (2022), p. 145004. DOI: 10.1088/1361-6382/ac7507. arXiv: 2112.05651 [gr-qc].

[95] Angelica Albertini et al. "Effective-one-body waveforms for extreme-mass-ratio binaries: Consistency with second-order gravitational self-force quasicircular results and extension to nonprecessing spins and eccentricity". In: *Phys. Rev. D* 109.4 (2024), p. 044022. DOI: 10.1103/PhysRevD.109.044022. arXiv: 2310.13578 [gr-qc].

[96] Antoni Ramos-Buades et al. "First survey of spinning eccentric black hole mergers: Numerical relativity simulations, hybrid waveforms, and parameter estimation". In: *Phys. Rev. D* 101.8 (2020), p. 083015. DOI: 10.1103/PhysRevD.101.083015. arXiv: 1909.11011 [gr-qc].

[97] U. Sperhake et al. "Amplification of superkicks in black-hole binaries through orbital eccentricity". In: *Phys. Rev. D* 101.2 (2020), p. 024044. DOI: 10.1103/PhysRevD.101.024044. arXiv: 1910.01598 [gr-qc].

[98] Antoni Ramos-Buades et al. "Eccentric binary black holes: Comparing numerical relativity and small mass-ratio perturbation theory". In: *Phys. Rev. D* 106.12 (2022), p. 124040. DOI: 10.1103/PhysRevD.106.124040. arXiv: 2209.03390 [gr-qc].

[99] James Healy and Carlos O. Lousto. "Fourth RIT binary black hole simulations catalog: Extension to eccentric orbits". In: *Phys. Rev. D* 105.12 (2022), p. 124010. DOI: 10.1103/PhysRevD.105.124010. arXiv: 2202.00018 [gr-qc].

[100] Abhishek V. Joshi et al. "Numerical relativity higher order gravitational waveforms of eccentric, spinning, nonprecessing binary black hole mergers". In: *Phys. Rev. D* 107.6 (2023), p. 064038. DOI: 10.1103/PhysRevD.107.064038. arXiv: 2210.01852 [gr-qc].

[101] Deborah Ferguson et al. "Second MAYA Catalog of Binary Black Hole Numerical Relativity Waveforms". In: (Sept. 2023). arXiv: 2309.00262 [gr-qc].

[102] Tousif Islam et al. "Eccentric binary black hole surrogate models for the gravitational waveform and remnant properties: comparable mass, nonspinning case". In: (Jan. 2021). arXiv: 2101.11798 [gr-qc].

[103] E. A. Huerta et al. "Eccentric, nonspinning, inspiral, Gaussian-process merger approximant for the detection and characterization of eccentric binary black hole mergers". In: *Phys. Rev.* D97.2 (2018), p. 024031. DOI: 10.1103/PhysRevD.97.024031. arXiv: 1711.06276 [gr-qc].

[104] Ian Hinder, Lawrence E. Kidder, and Harald P. Pfeiffer. "An eccentric binary black hole inspiral-merger-ringdown gravitational waveform model from numerical relativity and post-Newtonian theory". In: (2017). arXiv: 1709.02007 [gr-qc].

[105] Gihyuk Cho et al. "Generalized quasi-Keplerian solution for eccentric, non-spinning compact binaries at 4PN order and the associated IMR waveform". In: (Oct. 2021). arXiv: 2110.09608 [gr-qc].

[106] Abhishek Chattaraj et al. "High accuracy PN and NR comparisons involving higher modes for eccentric BBHs and a dominant mode eccentric IMR model". In: (Apr. 2022). arXiv: 2204.02377 [gr-qc].

[107] A. Buonanno and T. Damour. "Effective one-body approach to general relativistic two-body dynamics". In: *Phys. Rev.* D59 (1999), p. 084006. DOI: 10.1103/PhysRevD.59.084006. arXiv: gr-qc/9811091.

[108] Alessandra Buonanno and Thibault Damour. "Transition from inspiral to plunge in binary black hole coalescences". In: *Phys. Rev.* D62 (2000), p. 064015. DOI: 10.1103/PhysRevD.62.064015. arXiv: gr-qc/0001013.

[109] Thibault Damour, Piotr Jaranowski, and Gerhard Schaefer. "On the determination of the last stable orbit for circular general relativistic binaries at the third postNewtonian approximation". In: *Phys. Rev.* D62 (2000), p. 084011. DOI: 10.1103/PhysRevD.62.084011. arXiv: gr-qc/0005034 [gr-qc].

[110] Thibault Damour. "Coalescence of two spinning black holes: An effective one-body approach". In: *Phys. Rev.* D64 (2001), p. 124013. DOI: 10.1103/PhysRevD.64.124013. arXiv: gr-qc/0103018.

[111] Donato Bini and Thibault Damour. "Gravitational radiation reaction along general orbits in the effective one-body formalism". In: *Phys.Rev.* D86 (2012), p. 124012. DOI: 10.1103/PhysRevD.86.124012. arXiv: 1210.2834 [gr-qc].

[112] Tanja Hinderer and Stanislav Babak. "Foundations of an effective-one-body model for coalescing binaries on eccentric orbits". In: *Phys. Rev.* D96.10 (2017), p. 104048. DOI: 10.1103/PhysRevD.96.104048. arXiv: 1707.08426 [gr-qc].

[113] Zhoujian Cao and Wen-Biao Han. "Waveform model for an eccentric binary black hole based on the effective-one-body-numerical-relativity formalism". In: *Phys. Rev.* D96.4 (2017), p. 044028. DOI: 10.1103/PhysRevD.96.044028. arXiv: 1708.00166 [gr-qc].

[114] Xiaolin Liu, Zhoujian Cao, and Lijing Shao. "Validating the Effective-One-Body Numerical-Relativity Waveform Models for Spin-aligned Binary Black Holes along Eccentric Orbits". In: (2019). arXiv: 1910.00784 [gr-qc].

[115] Danilo Chiaramello and Alessandro Nagar. "Faithful analytical effective-one-body waveform model for spin-aligned, moderately eccentric, coalescing black hole binaries". In: *Phys. Rev. D* 101.10 (2020), p. 101501. DOI: 10.1103/PhysRevD.101.101501. arXiv: 2001.11736 [gr-qc].

[116] Alessandro Nagar, Alice Bonino, and Piero Rettegno. "Effective one-body multipolar waveform model for spin-aligned, quasicircular, eccentric, hyperbolic black hole binaries". In: *Phys. Rev. D* 103.10 (2021), p. 104021. DOI: 10.1103/PhysRevD.103.104021. arXiv: 2101.08624 [gr-qc].

[117] Andrea Placidi et al. "Exploiting Newton-factorized, 2PN-accurate waveform multipoles in effective-one-body models for spin-aligned noncircularized binaries". In: *Phys. Rev. D* 105.10 (2022), p. 104030. DOI: 10.1103/PhysRevD.105.104030. arXiv: 2112.05448 [gr-qc].

[118] Angelica Albertini et al. "Waveforms and fluxes: Towards a self-consistent effective one body waveform model for nonprecessing, coalescing black-hole binaries for third generation detectors". In: (Nov. 2021). arXiv: 2111.14149 [gr-qc].

[119] Simone Albanesi et al. "Assessment of Effective-One-Body Radiation Reactions for Generic Planar Orbits". In: (Feb. 2022). arXiv: 2202.10063 [gr-qc].

[120] Simone Albanesi et al. "New avenue for accurate analytical waveforms and fluxes for eccentric compact binaries". In: *Phys. Rev. D* 105.12 (2022), p. L121503. DOI: 10.1103/PhysRevD.105.L121503. arXiv: 2203.16286 [gr-qc].

[121] Antoni Ramos-Buades et al. "Effective-one-body multipolar waveforms for eccentric binary black holes with nonprecessing spins". In: *Phys. Rev. D* 105.4 (2022), p. 044035. DOI: 10.1103/PhysRevD.105.044035. arXiv: 2112.06952 [gr-qc].

[122] Xiaolin Liu, Zhoujian Cao, and Zong-Hong Zhu. "A higher-multipole gravitational waveform model for an eccentric binary black holes based on the effective-one-body-numerical-relativity formalism". In: (Feb. 2021). arXiv: 2102.08614 [gr-qc].

[123] Qianyun Yun et al. "Surrogate model for gravitational waveforms of spin-aligned binary black holes with eccentricities". In: *Phys. Rev. D* 103.12 (2021), p. 124053. DOI: 10.1103/PhysRevD.103.124053. arXiv: 2104.03789 [gr-qc].

[124] Quentin Henry and Mohammed Khalil. "Spin effects in gravitational waveforms and fluxes for binaries on eccentric orbits to the third post-Newtonian order". In: *Phys. Rev. D* 108.10 (2023), p. 104016. DOI: 10.1103/PhysRevD.108.104016. arXiv: 2308.13606 [gr-qc].

[125] Xiaolin Liu, Zhoujian Cao, and Lijing Shao. "Upgraded waveform model of eccentric binary black hole based on effective-one-body-numerical-relativity for spin-aligned binary black holes". In: *Int. J. Mod. Phys. D* 32.04 (2023), p. 2350015. DOI: 10.1142/S0218271823500153. arXiv: 2306.15277 [gr-qc].

[126] Alessandro Nagar and Piero Rettegno. "Next generation: Impact of high-order analytical information on effective one body waveform models for noncircularized, spin-aligned black hole binaries". In: *Phys. Rev. D* 104.10 (2021), p. 104004. DOI: 10.1103/PhysRevD.104.104004. arXiv: 2108.02043 [gr-qc].

[127] Simone Albanesi, Alessandro Nagar, and Sebastiano Bernuzzi. "Effective one-body model for extreme-mass-ratio spinning binaries on eccentric equatorial orbits: Testing radiation reaction and waveform". In: *Phys. Rev. D* 104.2 (2021), p. 024067. DOI: 10.1103/PhysRevD.104.024067. arXiv: 2104.10559 [gr-qc].

[128] Alessandro Nagar et al. "Effective-one-body waveforms from dynamical captures in black hole binaries". In: *Phys. Rev. D* 103.6 (2021), p. 064013. DOI: 10.1103/PhysRevD.103.064013. arXiv: 2009.12857 [gr-qc].

[129] Xiaolin Liu, Zhoujian Cao, and Zong-Hong Zhu. "Effective-One-Body Numerical-Relativity waveform model for Eccentric spin-precessing binary black hole coalescence". In: (Oct. 2023). arXiv: 2310.04552 [gr-qc].

[130] Alessandro Nagar et al. "Time-domain effective-one-body gravitational waveforms for coalescing compact binaries with nonprecessing spins, tides and self-spin effects". In: *Phys. Rev. D* 98.10 (2018), p. 104052. DOI: 10.1103/PhysRevD.98.104052. arXiv: 1806.01772 [gr-qc].

[131] Alessandro Nagar et al. "Analytic systematics in next generation of effective-one-body gravitational waveform models for future observations". In: *Phys. Rev. D* 108.12 (2023), p. 124018. DOI: 10.1103/PhysRevD.108.124018. arXiv: 2304.09662 [gr-qc].

[132] J. B. Hartle. *Gravity: An introduction to Einstein's general relativity*. 2003. ISBN: 978-0-8053-8662-2.

[133] Bernard F. Schutz. *A FIRST COURSE IN GENERAL RELATIVITY*. Cambridge, UK: Cambridge Univ. Pr., 1985. ISBN: 978-0-511-98418-1. DOI: 10.1017/CBO9780511984181.

[134] Charles W. Misner, K. S. Thorne, and J. A. Wheeler. *Gravitation*. San Francisco: W. H. Freeman, 1973. ISBN: 978-0-7167-0344-0, 978-0-691-17779-3.

[135] Robert M. Wald. *General Relativity*. Chicago, USA: Chicago Univ. Pr., 1984. DOI: 10.7208/chicago/9780226870373.001.0001.

[136] A. Einstein. "Die Grundlage der allgemeinen Relativitätstheorie". In: *Annalen der Physik* 354.7 (Jan. 1916), pp. 769–822. DOI: 10.1002/andp.19163540702.

[137] Karl Schwarzschild. "Über das Gravitationsfeld eines Massenpunktes nach der Einsteinschen Theorie". In: *Sitzungsberichte der Königlich Preussischen Akademie der Wissenschaften* (Jan. 1916), pp. 189–196.

[138] Roy P. Kerr. "Gravitational field of a spinning mass as an example of algebraically special metrics". In: *Phys. Rev. Lett.* 11 (1963), pp. 237–238. DOI: 10.1103/PhysRevLett.11.237.

[139] E. T. Newman and A. I. Janis. "Note on the Kerr spinning particle metric". In: *J. Math. Phys.* 6 (1965), pp. 915–917. DOI: 10.1063/1.1704350.

[140] E T. Newman et al. "Metric of a Rotating, Charged Mass". In: *J. Math. Phys.* 6 (1965), pp. 918–919. DOI: 10.1063/1.1704351.

[141] G. Nordström. "On the Energy of the Gravitation field in Einstein's Theory". In: *Koninklijke Nederlandse Akademie van Wetenschappen Proceedings Series B Physical Sciences* 20 (Jan. 1918), pp. 1238–1245.

[142] H. Reissner. "Über die Eigengravitation des elektrischen Feldes nach der Einsteinschen Theorie". In: *Annalen Phys.* 355.9 (1916), pp. 106–120. DOI: 10.1002/andp.19163550905.

[143] A. Friedmann. "Über die Krümmung des Raumes". In: *Zeitschrift fur Physik* 10 (Jan. 1922), pp. 377–386. DOI: 10.1007/BF01332580.

[144] Michele Maggiore. *Gravitational Waves. Vol. 1: Theory and Experiments*. Oxford University Press, 2007. ISBN: 978-0-19-171766-6, 978-0-19-852074-0. DOI: 10.1093/acprof:oso/9780198570745.001.0001.

[145] Kip S. Thorne. "Multipole expansions of gravitational radiation". In: *Rev. Mod. Phys.* 52 (2 Apr. 1980), pp. 299–339. DOI: 10.1103/RevModPhys.52.299.

[146] Jun John Sakurai and Jim Napolitano. *Modern Quantum Mechanics*. 3rd ed. Quantum physics, quantum information and quantum computation. Cambridge University Press, Oct. 2020. ISBN: 978-0-8053-8291-4, 978-1-108-52742-2, 978-1-108-58728-0. DOI: 10.1017/9781108587280.

[147] Eric Poisson and Clifford M. Will. *Gravity*. 2014.

[148] H. A. Lorentz and J. Droste. "The Motion of a System of Bodies under the Influence of their Mutual Attraction, According to Einstein's Theory". In: *Collected Papers: Volume V*. Dordrecht: Springer Netherlands, 1937, pp. 330–355. ISBN: 978-94-015-3445-1. DOI: 10.1007/978-94-015-3445-1_11. URL: https://doi.org/10.1007/978-94-015-3445-1_11.

[149] A. Einstein, L. Infeld, and B. Hoffmann. "The Gravitational Equations and the Problem of Motion". In: *Annals of Mathematics* 39.1 (1938), pp. 65–100. ISSN: 0003486X, 19398980. URL: http://www.jstor.org/stable/1968714 (visited on 06/12/2025).

[150] William L. Burke and Kip S. Thorne. "Gravitational Radiation Damping". In: *Relativity*. Ed. by Moshe Carmeli, Stuart I. Fickler, and Louis Witten. Boston, MA: Springer US, 1970, pp. 209–228. ISBN: 978-1-4684-0721-1.

[151] W. L. Burke. "Gravitational radiation damping of slowly moving systems calculated using matched asymptotic expansions." In: *Journal of Mathematical Physics* 12 (Jan. 1971), pp. 401–418. DOI: 10.1063/1.1665603.

[152] J. L. Anderson et al. "DIVERGENT INTEGRALS OF POSTNEWTONIAN GRAVITY: NONANALYTIC TERMS IN THE NEAR ZONE EXPANSION OF A GRAV-

ITATIONALLY RADIATING SYSTEM FOUND BY MATCHING". In: *Phys. Rev. D* 25 (1982), pp. 2038–2048. DOI: 10.1103/PhysRevD.25.2038.

[153] Olivier Poujade and Luc Blanchet. "PostNewtonian approximation for isolated systems calculated by matched asymptotic expansions". In: *Phys. Rev. D* 65 (2002), p. 124020. DOI: 10.1103/PhysRevD.65.124020. arXiv: gr-qc/0112057.

[154] Eanna E. Flanagan and Scott A. Hughes. "The Basics of gravitational wave theory". In: *New J. Phys.* 7 (2005), p. 204. DOI: 10.1088/1367-2630/7/1/204. arXiv: gr-qc/0501041.

[155] B. S. Sathyaprakash and B. F. Schutz. "Physics, Astrophysics and Cosmology with Gravitational Waves". In: *Living Rev. Rel.* 12 (2009), p. 2. DOI: 10.12942/lrr-2009-2. arXiv: 0903.0338 [gr-qc].

[156] R. Abbott et al. "Diving below the Spin-down Limit: Constraints on Gravitational Waves from the Energetic Young Pulsar PSR J0537-6910". In: *Astrophys. J.* 913 (2021), p. L27. DOI: 10.3847/2041-8213/abffcd. arXiv: 2012.12926 [astro-ph.HE].

[157] R. Abbott et al. "Narrowband Searches for Continuous and Long-duration Transient Gravitational Waves from Known Pulsars in the LIGO-Virgo Third Observing Run". In: *Astrophys. J.* 932.2 (2022), p. 133. DOI: 10.3847/1538-4357/ac6ad0. arXiv: 2112.10990 [gr-qc].

[158] Nelson Christensen. "Stochastic Gravitational Wave Backgrounds". In: *Rept. Prog. Phys.* 82.1 (2019), p. 016903. DOI: 10.1088/1361-6633/aae6b5. arXiv: 1811.08797 [gr-qc].

[159] Gabriella Agazie et al. "The NANOGrav 15 yr Data Set: Observations and Timing of 68 Millisecond Pulsars". In: *Astrophys. J. Lett.* 951.1 (2023), p. L9. DOI: 10.3847/2041-8213/acda9a. arXiv: 2306.16217 [astro-ph.HE].

[160] J. Antoniadis et al. "The second data release from the European Pulsar Timing Array - IV. Implications for massive black holes, dark matter, and the early Universe". In: *Astron. Astrophys.* 685 (2024), A94. DOI: 10.1051/0004-6361/202347433. arXiv: 2306.16227 [astro-ph.CO].

[161] Heng Xu et al. "Searching for the Nano-Hertz Stochastic Gravitational Wave Background with the Chinese Pulsar Timing Array Data Release I". In: *Res. Astron. Astrophys.* 23.7 (2023), p. 075024. DOI: 10.1088/1674-4527/acdfa5. arXiv: 2306.16216 [astro-ph.HE].

[162] R. Abbott et al. "Tests of General Relativity with GWTC-3". In: (Dec. 2021). arXiv: 2112.06861 [gr-qc].

[163] Vitor Cardoso and Paolo Pani. "Testing the nature of dark compact objects: a status report". In: *Living Rev. Rel.* 22.1 (2019), p. 4. DOI: 10.1007/s41114-019-0020-4. arXiv: 1904.05363 [gr-qc].

[164] Curt Cutler and Eanna E. Flanagan. "Gravitational waves from merging compact binaries: How accurately can one extract the binary's parameters from the inspiral wave form?" In: *Phys. Rev. D* 49 (1994), pp. 2658–2697. DOI: 10.1103/PhysRevD.49.2658. arXiv: gr-qc/9402014.

[165] B. P. Abbott et al. "Properties of the Binary Black Hole Merger GW150914". In: *Phys. Rev. Lett.* 116.24 (2016), p. 241102. DOI: 10.1103/PhysRevLett.116.241102. arXiv: 1602.03840 [gr-qc].

[166] Dirk Brouwer and Gerald M. Clemence. *Methods of celestial mechanics*. 1961.

[167] T. Damour and Gerhard Schäfer. "HIGHER ORDER RELATIVISTIC PERIASTRON ADVANCES AND BINARY PULSARS". In: *Nuovo Cim.* B101 (1988), p. 127. DOI: 10.1007/BF02828697.

[168] Gerhard Schäfer and Norbert Wex. "Second post-Newtonian motion of compact binaries". In: *Physics Letters A* 174.3 (Mar. 1993), pp. 196–205. DOI: 10.1016/0375-9601(93)90758-R.

[169] Norbert Wex. "The second post-Newtonian motion of compact binary-star systems with spin". In: *Classical and Quantum Gravity* 12.4 (Apr. 1995), pp. 983–1005. DOI: 10.1088/0264-9381/12/4/009.

[170] J. Weber. "Observation of the Thermal Fluctuations of a Gravitational-Wave Detector". In: *Phys. Rev. Lett.* 17 (1966), pp. 1228–1230. DOI: 10.1103/PhysRevLett.17.1228.

[171] J. Weber. "Evidence for discovery of gravitational radiation". In: *Phys. Rev. Lett.* 22 (1969), pp. 1320–1324. DOI: 10.1103/PhysRevLett.22.1320.

[172] Kentaro Somiya. "Detector configuration of KAGRA: The Japanese cryogenic gravitational-wave detector". In: *Class. Quant. Grav.* 29 (2012). Ed. by Mark Hannam et al., p. 124007. DOI: 10.1088/0264-9381/29/12/124007. arXiv: 1111.7185 [gr-qc].

[173] Yoichi Aso et al. "Interferometer design of the KAGRA gravitational wave detector". In: *Phys. Rev. D* 88.4 (2013), p. 043007. DOI: 10.1103/PhysRevD.88.043007. arXiv: 1306.6747 [gr-qc].

[174] Albert Abraham Michelson and Edward Williams Morley. "On the Relative Motion of the Earth and the Luminiferous Ether". In: *Am. J. Sci.* 34 (1887), pp. 333–345. DOI: 10.2475/ajs.s3-34.203.333.

[175] Benjamin P. Abbott et al. "Sensitivity of the Advanced LIGO detectors at the beginning of gravitational wave astronomy". In: *Phys. Rev. D* 93.11 (2016). [Addendum: Phys.Rev.D 97, 059901 (2018)], p. 112004. DOI: 10.1103/PhysRevD.93.112004. arXiv: 1604.00439 [astro-ph.IM].

[176] Benjamin P Abbott et al. "A guide to LIGO–Virgo detector noise and extraction of transient gravitational-wave signals". In: *Class. Quant. Grav.* 37.5 (2020), p. 055002. DOI: 10.1088/1361-6382/ab685e. arXiv: 1908.11170 [gr-qc].

[177] Joseph D. Romano and Neil J. Cornish. "Detection methods for stochastic gravitational-wave backgrounds: a unified treatment". In: *Living Rev. Rel.* 20.1 (2017), p. 2. DOI: 10.1007/s41114-017-0004-1. arXiv: 1608.06889 [gr-qc].

[178] Thomas Bayes Rev. "An essay toward solving a problem in the doctrine of chances". In: *Phil. Trans. Roy. Soc. Lond.* 53 (1764), pp. 370–418. DOI: 10.1098/rstl.1763.0053.

[179] W. K. Hastings. "Monte Carlo Sampling Methods Using Markov Chains and Their Applications". In: *Biometrika* 57 (1970), pp. 97–109. DOI: 10.1093/biomet/57.1.97.

[180] Nicholas Metropolis et al. "Equation of State Calculations by Fast Computing Machines". In: *jcp* 21.6 (June 1953), pp. 1087–1092. DOI: 10.1063/1.1699114.

[181] John Skilling. "Nested sampling for general Bayesian computation". In: *Bayesian Anal.* 1.4 (Dec. 2006), pp. 833–859. DOI: 10.1214/06-BA127. URL: https://doi.org/10.1214/06-BA127.

[182] Matteo Breschi, Rossella Gamba, and Sebastiano Bernuzzi. "Bayesian inference of multimessenger astrophysical data: Methods and applications to gravitational waves". In: *Phys. Rev. D* 104.4 (2021), p. 042001. DOI: 10.1103/PhysRevD.104.042001. arXiv: 2102.00017 [gr-qc].

[183] Joshua S Speagle. "dynesty: a dynamic nested sampling package for estimating Bayesian posteriors and evidences". In: *Monthly Notices of the Royal Astronomical Society* 493.3 (Feb. 2020), 3132?3158. ISSN: 1365-2966. DOI: 10.1093/mnras/staa278. URL: http://dx.doi.org/10.1093/mnras/staa278.

[184] M. Alcubierre. *Introduction to 3+1 Numerical Relativity*. Ed. by M. Alcubierre. Oxford University Press, 2008.

[185] Eric Gourgoulhon. *3+1 formalism and bases of numerical relativity*. Lecture notes in physics. Berlin: Springer, 2012. arXiv: gr-qc/0703035 [GR-QC].

[186] Michele Maggiore. *Gravitational Waves. Vol. 2: Astrophysics and Cosmology*. Oxford University Press, Mar. 2018. ISBN: 978-0-19-857089-9.

[187] Thibault Damour, Bala R. Iyer, and Alessandro Nagar. "Improved resummation of post-Newtonian multipolar waveforms from circularized compact binaries". In: *Phys. Rev.* D79 (2009), p. 064004. DOI: 10.1103/PhysRevD.79.064004. arXiv: 0811.2069 [gr-qc].

[188] Alessandro Nagar et al. "Effective-one-body waveform model for noncircularized, planar, coalescing black hole binaries. II. High accuracy by improving logarithmic terms in resummations". In: *Phys. Rev. D* 111.6 (2025), p. 064050. DOI: 10.1103/PhysRevD.111.064050. arXiv: 2407.04762 [gr-qc].

[189] Thibault Damour and Alessandro Nagar. "New effective-one-body description of coalescing nonprecessing spinning black-hole binaries". In: *Phys.Rev.* D90.4 (2014), p. 044018. DOI: 10.1103/PhysRevD.90.044018. arXiv: 1406.6913 [gr-qc].

[190] Thierry Mora and Clifford M. Will. "Numerically generated quasiequilibrium orbits of black holes: Circular or eccentric?" In: *Phys. Rev. D* 66 (2002), p. 101501. DOI: 10.1103/PhysRevD.66.101501. arXiv: gr-qc/0208089.

[191] Antoni Ramos-Buades et al. "Validity of common modeling approximations for precessing binary black holes with higher-order modes". In: *Phys. Rev. D* 101.10 (2020), p. 103014. DOI: 10.1103/PhysRevD.101.103014. arXiv: 2001.10936 [gr-qc].

[192] Md Arif Shaikh et al. "Defining eccentricity for gravitational wave astronomy". In: (Feb. 2023). arXiv: 2302.11257 [gr-qc].

[193] Nicolas Chartier et al. “A comparison between best-fit eccentricity definitions and the standardized definition of eccentricity”. In: (Mar. 2025). arXiv: 2503.19538 [gr-qc].

[194] J. R. Oppenheimer and G. M. Volkoff. “On massive neutron cores”. In: *Phys. Rev.* 55 (1939), pp. 374–381. DOI: 10.1103/PhysRev.55.374.

[195] A. Friedmann. “Über die Möglichkeit einer Welt mit konstanter negativer Krümmung des Raumes”. In: *Zeitschrift fur Physik* 21.1 (Dec. 1924), pp. 326–332. DOI: 10.1007/BF01328280.

[196] Luc Blanchet. “Gravitational radiation from post-Newtonian sources and inspiralling compact binaries”. In: *Living Rev. Rel.* 9 (2006), p. 4.

[197] Thibault Damour. “Gravitational scattering, post-Minkowskian approximation and Effective One-Body theory”. In: *Phys. Rev. D* 94.10 (2016), p. 104015. DOI: 10.1103/PhysRevD.94.104015. arXiv: 1609.00354 [gr-qc].

[198] Thibault Damour. “High-energy gravitational scattering and the general relativistic two-body problem”. In: *Phys. Rev. D* 97.4 (2018), p. 044038. DOI: 10.1103/PhysRevD.97.044038. arXiv: 1710.10599 [gr-qc].

[199] Thibault Damour. “Classical and quantum scattering in post-Minkowskian gravity”. In: *Phys. Rev. D* 102.2 (2020), p. 024060. DOI: 10.1103/PhysRevD.102.024060. arXiv: 1912.02139 [gr-qc].

[200] Mathias Driesse et al. “Conservative Black Hole Scattering at Fifth Post-Minkowskian and First Self-Force Order”. In: *Phys. Rev. Lett.* 132.24 (2024), p. 241402. DOI: 10.1103/PhysRevLett.132.241402. arXiv: 2403.07781 [hep-th].

[201] Mathias Driesse et al. “Emergence of Calabi–Yau manifolds in high-precision black-hole scattering”. In: *Nature* 641.8063 (2025), pp. 603–607. DOI: 10.1038/s41586-025-08984-2. arXiv: 2411.11846 [hep-th].

[202] Gregor Kälin and Rafael A. Porto. "Post-Minkowskian Effective Field Theory for Conservative Binary Dynamics". In: *JHEP* 11 (2020), p. 106. DOI: 10.1007/JHEP11(2020)106. arXiv: 2006.01184 [hep-th].

[203] Gregor Kälin, Jakob Neef, and Rafael A. Porto. "Radiation-reaction in the Effective Field Theory approach to Post-Minkowskian dynamics". In: *JHEP* 01 (2023), p. 140. DOI: 10.1007/JHEP01(2023)140. arXiv: 2207.00580 [hep-th].

[204] Gregor Kälin, Zhengwen Liu, and Rafael A. Porto. "Conservative Dynamics of Binary Systems to Third Post-Minkowskian Order from the Effective Field Theory Approach". In: *Phys. Rev. Lett.* 125.26 (2020), p. 261103. DOI: 10.1103/PhysRevLett.125.261103. arXiv: 2007.04977 [hep-th].

[205] Christoph Dlapa et al. "Dynamics of binary systems to fourth Post-Minkowskian order from the effective field theory approach". In: *Phys. Lett. B* 831 (2022), p. 137203. DOI: 10.1016/j.physletb.2022.137203. arXiv: 2106.08276 [hep-th].

[206] Christoph Dlapa et al. "Radiation Reaction and Gravitational Waves at Fourth Post-Minkowskian Order". In: *Phys. Rev. Lett.* 130.10 (2023), p. 101401. DOI: 10.1103/PhysRevLett.130.101401. arXiv: 2210.05541 [hep-th].

[207] Zvi Bern et al. "Scattering Amplitudes and the Conservative Hamiltonian for Binary Systems at Third Post-Minkowskian Order". In: *Phys. Rev. Lett.* 122.20 (2019), p. 201603. DOI: 10.1103/PhysRevLett.122.201603. arXiv: 1901.04424 [hep-th].

[208] Zvi Bern et al. "Spinning black hole binary dynamics, scattering amplitudes, and effective field theory". In: *Phys. Rev. D* 104.6 (2021), p. 065014. DOI: 10.1103/PhysRevD.104.065014. arXiv: 2005.03071 [hep-th].

[209] Zvi Bern et al. "Scattering Amplitudes and Conservative Binary Dynamics at $\mathcal{O}(G^4)$". In: *Phys. Rev. Lett.* 126.17 (2021), p. 171601. DOI: 10.1103/PhysRevLett.126.171601. arXiv: 2101.07254 [hep-th].

[210] Zvi Bern et al. "Scattering Amplitudes, the Tail Effect, and Conservative Binary Dynamics at O(G4)". In: *Phys. Rev. Lett.* 128.16 (2022), p. 161103. DOI: 10.1103/PhysRevLett.128.161103. arXiv: 2112.10750 [hep-th].

[211] Gustav Mogull, Jan Plefka, and Jan Steinhoff. "Classical black hole scattering from a worldline quantum field theory". In: *JHEP* 02 (2021), p. 048. DOI: 10.1007/JHEP02(2021)048. arXiv: 2010.02865 [hep-th].

[212] Gustav Uhre Jakobsen et al. "Classical Gravitational Bremsstrahlung from a Worldline Quantum Field Theory". In: *Phys. Rev. Lett.* 126.20 (2021), p. 201103. DOI: 10.1103/PhysRevLett.126.201103. arXiv: 2101.12688 [gr-qc].

[213] Gustav Uhre Jakobsen et al. "All things retarded: radiation-reaction in worldline quantum field theory". In: *JHEP* 10 (2022), p. 128. DOI: 10.1007/JHEP10(2022)128. arXiv: 2207.00569 [hep-th].

[214] Adam Pound. "Motion of small objects in curved spacetimes: An introduction to gravitational self-force". In: *Fund. Theor. Phys.* 179 (2015). Ed. by Dirk Pützfeld, Claus Lämmerzahl, and Bernard Schutz, pp. 399–486. DOI: 10.1007/978-3-319-18335-0_13. arXiv: 1506.06245 [gr-qc].

[215] Theodore C. Quinn and Robert M. Wald. "An Axiomatic approach to electromagnetic and gravitational radiation reaction of particles in curved space-time". In: *Phys.Rev.* D56 (1997), pp. 3381–3394. DOI: 10.1103/PhysRevD.56.3381. arXiv: gr-qc/9610053 [gr-qc].

[216] Yasushi Mino, Misao Sasaki, and Takahiro Tanaka. "Gravitational radiation reaction to a particle motion". In: *Phys.Rev.* D55 (1997), pp. 3457–3476. DOI: 10.1103/PhysRevD.55.3457. arXiv: gr-qc/9606018 [gr-qc].

[217] Adam Pound. "Second-order gravitational self-force". In: *Phys. Rev. Lett.* 109 (2012), p. 051101. DOI: 10.1103/PhysRevLett.109.051101. arXiv: 1201.5089 [gr-qc].

[218] Samuel E. Gralla. "Second Order Gravitational Self Force". In: *Phys. Rev. D* 85 (2012), p. 124011. DOI: 10.1103/PhysRevD.85.124011. arXiv: 1203.3189 [gr-qc].

[219] Marina De Amicis et al. "Dynamical quasinormal mode excitation". In: (June 2025). arXiv: 2506.21668 [gr-qc].

[220] Shahar Hadar. "Post-ISCO ringdown amplitudes in extreme mass ratio inspiral". In: *Nucl. Phys. B Proc. Suppl.* 216 (2011). Ed. by Laurent Baulieu et al., pp. 229–230. DOI: 10.1016/j.nuclphysbps.2011.04.164.

[221] Alejandro Bohé et al. "Improved effective-one-body model of spinning, nonprecessing binary black holes for the era of gravitational-wave astrophysics with advanced detectors". In: *Phys. Rev.* D95.4 (2017), p. 044028. DOI: 10.1103/PhysRevD.95.044028. arXiv: 1611.03703 [gr-qc].

[222] Roberto Cotesta et al. "Enriching the Symphony of Gravitational Waves from Binary Black Holes by Tuning Higher Harmonics". In: *Phys. Rev.* D98.8 (2018), p. 084028. DOI: 10.1103/PhysRevD.98.084028. arXiv: 1803.10701 [gr-qc].

[223] Serguei Ossokine et al. "Multipolar Effective-One-Body Waveforms for Precessing Binary Black Holes: Construction and Validation". In: *Phys. Rev. D* 102.4 (2020), p. 044055. DOI: 10.1103/PhysRevD.102.044055. arXiv: 2004.09442 [gr-qc].

[224] Jonathan E. Thompson et al. "PhenomXO4a: a phenomenological gravitational-wave model for precessing black-hole binaries with higher multipoles and asymmetries". In: *Phys. Rev. D* 109.6 (2024), p. 063012. DOI: 10.1103/PhysRevD.109.063012. arXiv: 2312.10025 [gr-qc].

[225] Jonathan Blackman et al. "A Surrogate Model of Gravitational Waveforms from Numerical Relativity Simulations of Precessing Binary Black Hole Mergers". In: *Phys. Rev. D* 95.10 (2017), p. 104023. DOI: 10.1103/PhysRevD.95.104023. arXiv: 1701.00550 [gr-qc].

[226] Jonathan Blackman et al. "Numerical relativity waveform surrogate model for generically precessing binary black hole mergers". In: *Phys. Rev. D* 96.2 (2017), p. 024058. DOI: 10.1103/PhysRevD.96.024058. arXiv: 1705.07089 [gr-qc].

[227] P. Ajith et al. "Inspiral-merger-ringdown waveforms for black-hole binaries with non-precessing spins". In: *Phys.Rev.Lett.* 106 (2011), p. 241101. DOI: 10.1103/PhysRevLett.106.241101. arXiv: 0909.2867 [gr-qc].

[228] L. Santamaria et al. "Matching post-Newtonian and numerical relativity waveforms: systematic errors and a new phenomenological model for non-precessing black hole binaries". In: *Phys. Rev. D* 82 (2010), p. 064016. DOI: 10.1103/PhysRevD.82.064016. arXiv: 1005.3306 [gr-qc].

[229] Mark Hannam et al. "Simple Model of Complete Precessing Black-Hole-Binary Gravitational Waveforms". In: *Phys. Rev. Lett.* 113.15 (2014), p. 151101. DOI: 10.1103/PhysRevLett.113.151101. arXiv: 1308.3271 [gr-qc].

[230] Sascha Husa et al. "Frequency-domain gravitational waves from nonprecessing black-hole binaries. I. New numerical waveforms and anatomy of the signal". In: *Phys. Rev.* D93.4 (2016), p. 044006. DOI: 10.1103/PhysRevD.93.044006. arXiv: 1508.07250 [gr-qc].

[231] Sebastian Khan et al. "Frequency-domain gravitational waves from nonprecessing black-hole binaries. II. A phenomenological model for the advanced detector era". In: *Phys. Rev.* D93.4 (2016), p. 044007. DOI: 10.1103/PhysRevD.93.044007. arXiv: 1508.07253 [gr-qc].

[232] Cecilio García-Quirós et al. "Multimode frequency-domain model for the gravitational wave signal from nonprecessing black-hole binaries". In: *Phys. Rev. D* 102.6 (2020), p. 064002. DOI: 10.1103/PhysRevD.102.064002. arXiv: 2001.10914 [gr-qc].

[233] Héctor Estellés et al. "Time-domain phenomenological model of gravitational-wave subdominant harmonics for quasicircular nonprecessing binary black hole coalescences". In: *Phys. Rev. D* 105.8 (2022), p. 084039. DOI: 10.1103/PhysRevD.105.084039. arXiv: 2012.11923 [gr-qc].

[234] Geraint Pratten et al. "Setting the cornerstone for a family of models for gravitational waves from compact binaries: The dominant harmonic for nonprecessing quasicircular black holes". In: *Phys. Rev. D* 102.6 (2020), p. 064001. DOI: 10.1103/PhysRevD.102.064001. arXiv: 2001.11412 [gr-qc].

[235] Theocharis A. Apostolatos et al. "Spin induced orbital precession and its modulation of the gravitational wave forms from merging binaries". In: *Phys. Rev. D* 49 (1994), pp. 6274–6297. DOI: 10.1103/PhysRevD.49.6274.

[236] Alessandra Buonanno, Yan-bei Chen, and Michele Vallisneri. "Detecting gravitational waves from precessing binaries of spinning compact objects: Adiabatic limit". In: *Phys. Rev. D* 67 (2003). [Erratum: Phys.Rev.D 74, 029904 (2006)], p. 104025. DOI: 10.1103/PhysRevD.67.104025. arXiv: gr-qc/0211087.

[237] Patricia Schmidt et al. “Tracking the precession of compact binaries from their gravitational-wave signal”. In: *Phys. Rev. D* 84 (2011), p. 024046. DOI: 10.1103/PhysRevD.84.024046. arXiv: 1012.2879 [gr-qc].

[238] Patricia Schmidt, Mark Hannam, and Sascha Husa. “Towards models of gravitational waveforms from generic binaries: A simple approximate mapping between precessing and non-precessing inspiral signals”. In: *Phys. Rev. D* 86 (2012), p. 104063. DOI: 10.1103/PhysRevD.86.104063. arXiv: 1207.3088 [gr-qc].

[239] Eleanor Hamilton et al. “Model of gravitational waves from precessing black-hole binaries through merger and ringdown”. In: *Phys. Rev. D* 104.12 (2021), p. 124027. DOI: 10.1103/PhysRevD.104.124027. arXiv: 2107.08876 [gr-qc].

[240] Sarp Akcay, Rossella Gamba, and Sebastiano Bernuzzi. “A hybrid post-Newtonian – effective-one-body scheme for spin-precessing compact-binary waveforms”. In: *Phys. Rev. D* 103.2 (2021), p. 024014. DOI: 10.1103/PhysRevD.103.024014. arXiv: 2005.05338 [gr-qc].

[241] Rossella Gamba et al. “Effective-one-body waveforms for precessing coalescing compact binaries with post-Newtonian Twist”. In: (Nov. 2021). arXiv: 2111.03675 [gr-qc].

[242] Rossella Gamba, Danilo Chiaramello, and Sayan Neogi. “Toward efficient effective-one-body models for generic, nonplanar orbits”. In: *Phys. Rev. D* 110.2 (2024), p. 024031. DOI: 10.1103/PhysRevD.110.024031. arXiv: 2404.15408 [gr-qc].

[243] Antoni Ramos-Buades et al. “Next generation of accurate and efficient multipolar precessing-spin effective-one-body waveforms for binary black holes”. In: *Phys. Rev. D* 108.12 (2023), p. 124037. DOI: 10.1103/PhysRevD.108.124037. arXiv: 2303.18046 [gr-qc].

[244] Yi Pan et al. “Inspiral-merger-ringdown waveforms of spinning, precessing black-hole binaries in the effective-one-body formalism”. In: *Phys.Rev.* D89 (2014), p. 084006. DOI: 10.1103/PhysRevD.89.084006. arXiv: 1307.6232 [gr-qc].

[245] Stanislav Babak, Andrea Taracchini, and Alessandra Buonanno. “Validating the effective-one-body model of spinning, precessing binary black holes against numerical relativity”. In: *Phys. Rev.* D95.2 (2017), p. 024010. DOI: 10.1103/PhysRevD.95.024010. arXiv: 1607.05661 [gr-qc].

[246] Sebastian Khan et al. “Phenomenological model for the gravitational-wave signal from precessing binary black holes with two-spin effects”. In: *Phys. Rev.* D100.2 (2019), p. 024059. DOI: 10.1103/PhysRevD.100.024059. arXiv: 1809.10113 [gr-qc].

[247] Frank Loffler et al. “The Einstein Toolkit: A Community Computational Infrastructure for Relativistic Astrophysics”. In: *Class. Quant. Grav.* 29 (2012), p. 115001. DOI: 10.1088/0264-9381/29/11/115001. arXiv: 1111.3344 [gr-qc].

[248] Steven R. Brand et al. *The Einstein Toolkit*. Version The "Katherine Johnson" release, ET_2021_11. Dec. 2021. DOI: 10.5281/zenodo.5770803. URL: https://zenodo.org/records/5770803.

[249] Y. Foures-Bruhat. “Theoreme d’existence pour certains systemes derivees partielles non lineaires”. In: *Acta Mat.* 88 (1952), pp. 141–225. DOI: 10.1007/BF02392131.

[250] Richard L. Arnowitt, Stanley Deser, and Charles W. Misner. “The Dynamics of general relativity”. In: *Gen. Rel. Grav.* 40 (2008), pp. 1997–2027. DOI: 10.1007/s10714-008-0661-1. arXiv: gr-qc/0405109 [gr-qc].

[251] Frans Pretorius. “Evolution of binary black hole spacetimes”. In: *Phys. Rev. Lett.* 95 (2005), p. 121101. DOI: 10.1103/PhysRevLett.95.121101. arXiv: gr-qc/0507014.

[252] Manuela Campanelli et al. "Accurate Evolutions of Orbiting Black-Hole Binaries Without Excision". In: *Phys. Rev. Lett.* 96 (2006), p. 111101. DOI: 10.1103/PhysRevLett.96.111101. arXiv: gr-qc/0511048.

[253] James W. York Jr. "Kinematics and Dynamics of General Relativity". In: *Workshop on Sources of Gravitational Radiation*. 1978, pp. 83–126.

[254] M. Shibata and T. Nakamura. "Evolution of three-dimensional gravitational waves: Harmonic slicing case". In: *Phys. Rev.* D52 (1995), pp. 5428–5444. DOI: 10.1103/PhysRevD.52.5428.

[255] Thomas W. Baumgarte and Stuart L. Shapiro. "On the numerical integration of Einstein's field equations". In: *Phys. Rev.* D59 (1999), p. 024007. DOI: 10.1103/PhysRevD.59.024007. arXiv: gr-qc/9810065.

[256] Pedro Marronetti et al. "High-spin binary black hole mergers". In: *Phys.Rev.* D77 (2008), p. 064010. DOI: 10.1103/PhysRevD.77.064010. arXiv: 0709.2160 [gr-qc].

[257] Jeffrey M. Bowen and James W. York Jr. "Time asymmetric initial data for black holes and black hole collisions". In: *Phys. Rev.* D21 (1980), pp. 2047–2056. DOI: 10.1103/PhysRevD.21.2047.

[258] Steven Brandt and Bernd Brügmann. "A Simple construction of initial data for multiple black holes". In: *Phys. Rev. Lett.* 78 (1997), pp. 3606–3609. DOI: 10.1103/PhysRevLett.78.3606. arXiv: gr-qc/9703066.

[259] Bernd Bruegmann et al. "Calibration of Moving Puncture Simulations". In: *Phys. Rev. D* 77 (2008), p. 024027. DOI: 10.1103/PhysRevD.77.024027. arXiv: gr-qc/0610128.

[260] D. Christodoulou. "Reversible and irreversible transforations in black hole physics". In: *Phys. Rev. Lett.* 25 (1970), pp. 1596–1597. DOI: 10.1103/PhysRevLett.25.1596.

[261] Marcus Ansorg, Bernd Brügmann, and Wolfgang Tichy. "A single-domain spectral method for black hole puncture data". In: *Phys. Rev.* D70 (2004), p. 064011. DOI: 10.1103/PhysRevD.70.064011. arXiv: gr-qc/0404056.

[262] Carles Bona et al. "A New formalism for numerical relativity". In: *Phys. Rev. Lett.* 75 (1995), pp. 600–603. DOI: 10.1103/PhysRevLett.75.600. arXiv: gr-qc/9412071.

[263] C. Bona et al. "New Formalism for Numerical Relativity". In: *Phys. Rev. Lett.* 75 (1995), pp. 600–603. eprint: gr-qc/9412071.

[264] Miguel Alcubierre et al. "Gauge conditions for long term numerical black hole evolutions without excision". In: *Phys.Rev.* D67 (2003), p. 084023. DOI: 10.1103/PhysRevD.67.084023. arXiv: gr-qc/0206072 [gr-qc].

[265] T. Damour and G. Schafer. "Higher-order relativistic periastron advances and binary pulsars." In: *Nuovo Cimento B Serie* 101B.2 (Jan. 1988), pp. 127–176. DOI: 10.1007/BF02828697.

[266] Thibault Damour and Gerhard Schäfer. "Lagrangians for n point masses at the second post-Newtonian approximation of general relativity". In: *Gen. Rel. Grav.* 17 (1985), pp. 879–905. DOI: 10.1007/BF00773685.

[267] T. Ohta et al. "Higher order gravitational potential for many-body system". In: *Prog. Theor. Phys.* 51 (1974), pp. 1220–1238. DOI: 10.1143/PTP.51.1220.

[268] Alessandro Nagar et al. "Effective-one-body waveform model for noncircularized, planar, coalescing black hole binaries: The importance of radiation reaction". In: *Phys. Rev. D* 110.8 (2024), p. 084001. DOI: 10.1103/PhysRevD.110.084001. arXiv: 2404.05288 [gr-qc].

[269] Thibault Damour, Piotr Jaranowski, and Gerhard Schäfer. "Effective one body approach to the dynamics of two spinning black holes with next-to-leading order

spin-orbit coupling". In: *Phys.Rev.* D78 (2008), p. 024009. DOI: 10.1103/PhysRevD.78.024009. arXiv: 0803.0915 [gr-qc].

[270] Thibault Damour and Alessandro Nagar. "Faithful Effective-One-Body waveforms of small-mass-ratio coalescing black-hole binaries". In: *Phys. Rev.* D76 (2007), p. 064028. DOI: 10.1103/PhysRevD.76.064028. arXiv: 0705.2519 [gr-qc].

[271] Thibault Damour and Alessandro Nagar. "Comparing Effective-One-Body gravitational waveforms to accurate numerical data". In: *Phys. Rev. D* 77 (2008), p. 024043. DOI: 10.1103/PhysRevD.77.024043. arXiv: 0711.2628 [gr-qc].

[272] Ryuichi Fujita and Bala R. Iyer. "Spherical harmonic modes of 5.5 post-Newtonian gravitational wave polarizations and associated factorized resummed waveforms for a particle in circular orbit around a Schwarzschild black hole". In: *Phys. Rev.* D82 (2010), p. 044051. DOI: 10.1103/PhysRevD.82.044051. arXiv: 1005.2266 [gr-qc].

[273] Alessandro Nagar and Abhay Shah. "Factorization and resummation: A new paradigm to improve gravitational wave amplitudes". In: *Phys. Rev.* D94.10 (2016), p. 104017. DOI: 10.1103/PhysRevD.94.104017. arXiv: 1606.00207 [gr-qc].

[274] Francesco Messina, Alberto Maldarella, and Alessandro Nagar. "Factorization and resummation: A new paradigm to improve gravitational wave amplitudes. II: the higher multipolar modes". In: *Phys. Rev.* D97.8 (2018), p. 084016. DOI: 10.1103/PhysRevD.97.084016. arXiv: 1801.02366 [gr-qc].

[275] Thibault Damour and Alessandro Nagar. "An improved analytical description of inspiralling and coalescing black-hole binaries". In: *Phys. Rev.* D79 (2009), p. 081503. DOI: 10.1103/PhysRevD.79.081503. arXiv: 0902.0136 [gr-qc].

[276] Kashif Alvi. "Energy and angular momentum flow into a black hole in a binary". In: *Phys. Rev. D* 64 (2001), p. 104020. DOI: 10.1103/PhysRevD.64.104020. arXiv: gr-qc/0107080.

[277] Alessandro Nagar and Sarp Akcay. "Horizon-absorbed energy flux in circularized, nonspinning black-hole binaries and its effective-one-body representation". In: *Phys. Rev. D* 85 (2012), p. 044025. DOI: 10.1103/PhysRevD.85.044025. arXiv: 1112.2840 [gr-qc].

[278] Alessandro Nagar et al. "Multipolar effective one body waveform model for spin-aligned black hole binaries". In: *Phys. Rev. D* 102.2 (2020), p. 024077. DOI: 10.1103/PhysRevD.102.024077. arXiv: 2001.09082 [gr-qc].

[279] Gunnar Riemenschneider et al. "Assessment of consistent next-to-quasicircular corrections and postadiabatic approximation in effective-one-body multipolar waveforms for binary black hole coalescences". In: *Phys. Rev. D* 104.10 (2021), p. 104045. DOI: 10.1103/PhysRevD.104.104045. arXiv: 2104.07533 [gr-qc].

[280] Alessandro Nagar et al. "Energetics and phasing of nonprecessing spinning coalescing black hole binaries". In: *Phys. Rev.* D93.4 (2016), p. 044046. DOI: 10.1103/PhysRevD.93.044046. arXiv: 1506.08457 [gr-qc].

[281] Alessandro Nagar et al. "A Multipolar Effective One Body Model for Non-Spinning Black Hole Binaries". In: (2019). arXiv: 1904.09550 [gr-qc].

[282] *SXS Gravitational Waveform Database*. https://data.black-holes.org/waveforms/index.html.

[283] Thibault Damour, Alessandro Nagar, and Sebastiano Bernuzzi. "Improved effective-one-body description of coalescing nonspinning black-hole binaries and its numerical-relativity completion". In: *Phys.Rev.* D87 (2013), p. 084035. DOI: 10.1103/PhysRevD.87.084035. arXiv: 1212.4357 [gr-qc].

[284] Michael Boyle et al. "The SXS Collaboration catalog of binary black hole simulations". In: *Class. Quant. Grav.* 36.19 (2019), p. 195006. DOI: 10.1088/1361-6382/ab34e2. arXiv: 1904.04831 [gr-qc].

[285] Aaron Buikema et al. "Sensitivity and performance of the Advanced LIGO detectors in the third observing run". In: *Phys. Rev. D* 102.6 (2020), p. 062003. DOI: 10.1103/PhysRevD.102.062003. arXiv: 2008.01301 [astro-ph.IM].

[286] Jacob Lange, Richard O'Shaughnessy, and Monica Rizzo. "Rapid and accurate parameter inference for coalescing, precessing compact binaries". In: (2018). arXiv: 1805.10457 [gr-qc].

[287] Alessandro Nagar and Piero Rettegno. "Efficient effective one body time-domain gravitational waveforms". In: *Phys. Rev.* D99.2 (2019), p. 021501. DOI: 10.1103/PhysRevD.99.021501. arXiv: 1805.03891 [gr-qc].

[288] Eamonn O'Shea and Prayush Kumar. "Correlations in parameter estimation of low-mass eccentric binaries: GW151226 & GW170608". In: (July 2021). arXiv: 2107.07981 [astro-ph.HE].

[289] Agata Trovato. "GWOSC: Gravitational Wave Open Science Center". In: *PoS* Asterics2019 (2020), p. 082. DOI: 10.22323/1.357.0082.

[290] *Parameter estimation sample release for GWTC-1*. https://doi.org/10.7935/KSX7-QQ51.

[291] Isobel M. Romero-Shaw, Paul D. Lasky, and Eric Thrane. "Searching for Eccentricity: Signatures of Dynamical Formation in the First Gravitational-Wave Transient Catalogue of LIGO and Virgo". In: *Mon. Not. Roy. Astron. Soc.* 490.4 (2019), pp. 5210–5216. DOI: 10.1093/mnras/stz2996. arXiv: 1909.05466 [astro-ph.HE].

[292] H. L. Iglesias et al. 2022. arXiv: 2208.01766 [gr-qc].

[293] Benjamin P. Abbott et al. "Effects of waveform model systematics on the interpretation of GW150914". In: *Class. Quant. Grav.* 34.10 (2017), p. 104002. DOI: 10.1088/1361-6382/aa6854. arXiv: 1611.07531 [gr-qc].

[294] Thierry Mora and Clifford M. Will. "A PostNewtonian diagnostic of quasiequilibrium binary configurations of compact objects". In: *Phys. Rev.* D69 (2004). [Erratum: Phys. Rev.D71,129901(2005)], p. 104021. DOI: 10.1103/PhysRevD.71.129901,10.1103/PhysRevD.69.104021. arXiv: gr-qc/0312082 [gr-qc].

[295] A. M. Knee et al. 2022. arXiv: 2207.14346 [gr-qc].

[296] Nicholas Loutrel et al. "The eccentric behavior of inspiralling compact binaries". In: *Class. Quant. Grav.* 36.2 (2019), p. 025004. DOI: 10.1088/1361-6382/aaf2a9. arXiv: 1810.03521 [gr-qc].

[297] Adam G. M. Lewis, Aaron Zimmerman, and Harald P. Pfeiffer. "Fundamental frequencies and resonances from eccentric and precessing binary black hole inspirals". In: *Class. Quant. Grav.* 34.12 (2017), p. 124001. DOI: 10.1088/1361-6382/aa66f4. arXiv: 1611.03418 [gr-qc].

[298] R. Abbott et al. "The population of merging compact binaries inferred using gravitational waves through GWTC-3". In: (Nov. 2021). arXiv: 2111.03634 [astro-ph.HE].

[299] *Prospects for Observing and Localizing Gravitational-Wave Transients with Advanced LIGO, Advanced Virgo and KAGRA*. https://dcc.ligo.org/LIGO-P1200087/public.

[300] Aditya Vijaykumar, Alexandra G. Hanselman, and Michael Zevin. "Consistent eccentricities for gravitational wave astronomy: Resolving discrepancies between astrophysical simulations and waveform models". In: (Feb. 2024). arXiv: 2402.07892 [astro-ph.HE].

[301] John G. Baker et al. "Gravitational wave extraction from an inspiraling configuration of merging black holes". In: *Phys. Rev. Lett.* 96 (2006), p. 111102. DOI: 10.1103/PhysRevLett.96.111102. arXiv: gr-qc/0511103.

[302] *Cactus*. URL: http://www.cactuscode.org.

[303] *Cactus Thorns*. URL: https://einsteintoolkit.org/documentation/ThornGuide.php.

[304] H. O. Kreiss and J.. Oliger. *Methods for the approximate solution of time dependent problems*. Geneva: International Council of Scientific Unions, World Meteorological Organization, 1973.

[305] Jonathan Thornburg. "Black hole excision with multiple grid patches". In: *Class.Quant.Grav.* 21 (2004), pp. 3665–3692. DOI: 10.1088/0264-9381/21/15/004. arXiv: gr-qc/0404059 [gr-qc].

[306] Abhay Ashtekar and Badri Krishnan. "Dynamical horizons and their properties". In: *Phys. Rev. D* 68 (2003), p. 104030. DOI: 10.1103/PhysRevD.68.104030. arXiv: gr-qc/0308033.

[307] Olaf Dreyer et al. "Black hole spectroscopy: Testing general relativity through gravitational wave observations". In: *Class. Quant. Grav.* 21 (2004), pp. 787–804. DOI: 10.1088/0264-9381/21/4/003. arXiv: gr-qc/0309007 [gr-qc].

[308] Erik Schnetter, Badri Krishnan, and Florian Beyer. "Introduction to dynamical horizons in numerical relativity". In: *Phys. Rev. D* 74 (2006), p. 024028. DOI: 10.1103/PhysRevD.74.024028. arXiv: gr-qc/0604015.

[309] Erik Schnetter, Scott H. Hawley, and Ian Hawke. "Evolutions in 3-D numerical relativity using fixed mesh refinement". In: *Class.Quant.Grav.* 21 (2004), pp. 1465–1488. DOI: 10.1088/0264-9381/21/6/014. arXiv: gr-qc/0310042 [gr-qc].

[310] Denis Pollney et al. "High accuracy binary black hole simulations with an extended wave zone". In: *Phys. Rev.* D83 (2011), p. 044045. DOI: 10.1103/PhysRevD.83.044045. arXiv: 0910.3803 [gr-qc].

[311] C. Reisswig et al. "Three-Dimensional General-Relativistic Hydrodynamic Simulations of Binary Neutron Star Coalescence and Stellar Collapse with Multipatch

Grids". In: *Phys. Rev.* D87.6 (2013), p. 064023. DOI: 10.1103/PhysRevD.87.064023. arXiv: 1212.1191 [astro-ph.HE].

[312] Ezra Newman and Roger Penrose. "An Approach to gravitational radiation by a method of spin coefficients". In: *J. Math. Phys.* 3 (1962), pp. 566–578. DOI: 10.1063/1.1724257.

[313] Christian Reisswig and Denis Pollney. "Notes on the integration of numerical relativity waveforms". In: *Class.Quant.Grav.* 28 (2011), p. 195015. DOI: 10.1088/0264-9381/28/19/195015. arXiv: 1006.1632 [gr-qc].

[314] Michael Boyle and Abdul H. Mroue. "Extrapolating gravitational-wave data from numerical simulations". In: *Phys. Rev.* D80 (2009), p. 124045. DOI: 10.1103/PhysRevD.80.124045. arXiv: 0905.3177 [gr-qc].

[315] Ian Hinder et al. "Error-analysis and comparison to analytical models of numerical waveforms produced by the NRAR Collaboration". In: *Class.Quant.Grav.* 31 (2013), p. 025012. DOI: 10.1088/0264-9381/31/2/025012. arXiv: 1307.5307 [gr-qc].

[316] Hiroyuki Nakano et al. "Perturbative extraction of gravitational waveforms generated with Numerical Relativity". In: *Phys. Rev. D* 91.10 (2015), p. 104022. DOI: 10.1103/PhysRevD.91.104022. arXiv: 1503.00718 [gr-qc].

[317] Antoni Ramos-Buades, Sascha Husa, and Geraint Pratten. "Simple procedures to reduce eccentricity of binary black hole simulations". In: *Phys. Rev. D* 99.2 (2019), p. 023003. DOI: 10.1103/PhysRevD.99.023003. arXiv: 1810.00036 [gr-qc].

[318] Xisco Jiménez-Forteza et al. "Hierarchical data-driven approach to fitting numerical relativity data for nonprecessing binary black holes with an application to final spin and radiated energy". In: *Phys. Rev.* D95.6 (2017), p. 064024. DOI: 10.1103/PhysRevD.95.064024. arXiv: 1611.00332 [gr-qc].

[319] Milton Ruiz et al. “Multipole expansions for energy and momenta carried by gravitational waves”. In: *Gen. Rel. Grav.* 40 (2008), p. 2467. DOI: 10.1007/s10714-007-0570-8. arXiv: 0707.4654 [gr-qc].

[320] David Keitel et al. “The most powerful astrophysical events: Gravitational-wave peak luminosity of binary black holes as predicted by numerical relativity”. In: *Phys. Rev.* D96.2 (2017), p. 024006. DOI: 10.1103/PhysRevD.96.024006. arXiv: 1612.09566 [gr-qc].

[321] Abdul H. Mroue et al. “Measuring orbital eccentricity and periastron advance in quasi-circular black hole simulations”. In: *Phys. Rev. D* 82 (2010), p. 124016. DOI: 10.1103/PhysRevD.82.124016. arXiv: 1004.4697 [gr-qc].

[322] Antoni Ramos-Buades, Alessandra Buonanno, and Jonathan Gair. “Bayesian inference of binary black holes with inspiral-merger-ringdown waveforms using two eccentric parameters”. In: (Sept. 2023). arXiv: 2309.15528 [gr-qc].

[323] Gregorio Carullo et al. “Unveiling the Merger Structure of Black Hole Binaries in Generic Planar Orbits”. In: *Phys. Rev. Lett.* 132.10 (2024), p. 101401. DOI: 10.1103/PhysRevLett.132.101401. arXiv: 2309.07228 [gr-qc].

[324] Michael Purrer, Sascha Husa, and Mark Hannam. “An Efficient iterative method to reduce eccentricity in numerical-relativity simulations of compact binary inspiral”. In: *Phys. Rev. D* 85 (2012), p. 124051. DOI: 10.1103/PhysRevD.85.124051. arXiv: 1203.4258 [gr-qc].

[325] Tullio Regge and John A. Wheeler. “Stability of a Schwarzschild singularity”. In: *Phys. Rev.* 108 (1957), pp. 1063–1069.

[326] Frank J. Zerilli. “Effective potential for even parity Regge-Wheeler gravitational perturbation equations”. In: *Phys. Rev. Lett.* 24 (1970), pp. 737–738. DOI: 10.1103/PhysRevLett.24.737.

[327] Olivier Sarbach and Manuel Tiglio. "Gauge invariant perturbations of Schwarzschild black holes in horizon-penetrating coordinates". In: *Phys. Rev.* D64 (2001), p. 084016. eprint: gr-qc/0104061.

[328] Wolfram Research Inc. *Mathematica, Version 14.0*. Champaign, IL, 2024. URL: https://www.wolfram.com/mathematica.

[329] Ian Hinder et al. "Comparisons of eccentric binary black hole simulations with post-Newtonian models". In: *Phys. Rev. D* 82 (2010), p. 024033. DOI: 10.1103/PhysRevD.82.024033. arXiv: 0806.1037 [gr-qc].

[330] Alan M. Knee et al. "A Rosetta Stone for Eccentric Gravitational Waveform Models". In: *Astrophys. J.* 936.2 (2022), p. 172. DOI: 10.3847/1538-4357/ac8b02. arXiv: 2207.14346 [gr-qc].

[331] B. P. Abbott et al. "Prospects for observing and localizing gravitational-wave transients with Advanced LIGO, Advanced Virgo and KAGRA". In: *Living Rev. Rel.* 21.1 (2020), p. 3. DOI: 10.1007/s41114-020-00026-9. arXiv: 1304.0670 [gr-qc].

[332] LIGO Scientific Collaboration, Virgo Collaboration, and KAGRA Collaboration. *Noise curves used for Simulations in the update of the Observing Scenarios Paper*. Tech. rep. LIGO-T2000012-v2. 2022. URL: https://dcc.ligo.org/LIGO-T2000012/public.

[333] S. Bernuzzi, A. Nagar, et al. *TEOBResumS Bitbucket Respository*. 2024. URL: https://bitbucket.org/teobresums/teobresums/commits/7de8c4d0497824c580335a5d90aed760

[334] Simulation Tools. *Simulation Tools*. https://simulationtools.org.

[335] Guglielmo Faggioli et al. "Testing eccentric corrections to the radiation-reaction force in the test-mass limit of effective-one-body models". In: *Phys. Rev. D* 111.4 (2025), p. 044036. DOI: 10.1103/PhysRevD.111.044036. arXiv: 2405.19006 [gr-qc].

[336] Alessandro Nagar and Luciano Rezzolla. "Gauge-invariant non-spherical metric perturbations of Schwarzschild black-hole spacetimes". In: *Class. Quant. Grav.* 22 (2005). [Erratum: Class.Quant.Grav. 23, 4297 (2006)], R167. DOI: 10.1088/0264-9381/22/16/R01. arXiv: gr-qc/0502064.

[337] Thibault Damour et al. "Energy versus Angular Momentum in Black Hole Binaries". In: *Phys.Rev.Lett.* 108 (2012), p. 131101. DOI: 10.1103/PhysRevLett.108.131101. arXiv: 1110.2938 [gr-qc].

[338] S. Bernuzzi, A. Nagar, et al. *TEOBResumS Bitbucket Respository*. 2024. URL: https://bitbucket.org/teobresums/teobresums/src/Dali-f21/Mathematica/Derivatives_checked.nb.

[339] Alex Nitz et al. *gwastro/pycbc: v2.3.3 release of PyCBC*. Version v2.3.3. Jan. 2024. DOI: 10.5281/zenodo.10473621.

[340] Monica Colpi et al. "LISA Definition Study Report". In: (Feb. 2024). arXiv: 2402.07571 [astro-ph.CO].

[341] Lee Lindblom, Benjamin J. Owen, and Duncan A. Brown. "Model Waveform Accuracy Standards for Gravitational Wave Data Analysis". In: *Phys. Rev. D* 78 (2008), p. 124020. DOI: 10.1103/PhysRevD.78.124020. arXiv: 0809.3844 [gr-qc].

[342] Michael Pürrer and Carl-Johan Haster. "Gravitational waveform accuracy requirements for future ground-based detectors". In: *Phys. Rev. Res.* 2.2 (2020), p. 023151. DOI: 10.1103/PhysRevResearch.2.023151. arXiv: 1912.10055 [gr-qc].

[343] Richard W. O'Shaughnessy. "Transition from inspiral to plunge for eccentric equatorial Kerr orbits". In: *Phys. Rev. D* 67 (2003), p. 044004. DOI: 10.1103/PhysRevD.67.044004. arXiv: gr-qc/0211023.

[344] Simone Albanesi et al. “Scattering and dynamical capture of two black holes: Synergies between numerical and analytical methods”. In: *Phys. Rev. D* 111.2 (2025), p. 024069. DOI: 10.1103/PhysRevD.111.024069. arXiv: 2405.20398 [gr-qc].

[345] Manuela Campanelli, C.O. Lousto, and Y. Zlochower. “Spinning-black-hole binaries: The orbital hang up”. In: *Phys.Rev.* D74 (2006), p. 041501. DOI: 10.1103/PhysRevD.74.041501. arXiv: gr-qc/0604012 [gr-qc].

[346] Giulia Fumagalli et al. “Residual eccentricity as a systematic uncertainty on the formation channels of binary black holes”. In: *Phys. Rev. D* 110.6 (2024), p. 063012. DOI: 10.1103/PhysRevD.110.063012. arXiv: 2405.14945 [astro-ph.HE].

[347] Marc Favata et al. “Constraining the orbital eccentricity of inspiralling compact binary systems with Advanced LIGO”. In: *Phys. Rev. D* 105.2 (2022), p. 023003. DOI: 10.1103/PhysRevD.105.023003. arXiv: 2108.05861 [gr-qc].

[348] Bhooshan Gadre et al. “Detectability of eccentric binary black holes with matched filtering and unmodeled pipelines during the third observing run of LIGO-Virgo-KAGRA”. In: *Phys. Rev. D* 110.4 (2024), p. 044013. DOI: 10.1103/PhysRevD.110.044013. arXiv: 2405.04186 [gr-qc].

[349] Pankaj Saini, Marc Favata, and K. G. Arun. “Systematic bias on parametrized tests of general relativity due to neglect of orbital eccentricity”. In: *Phys. Rev. D* 106.8 (2022), p. 084031. DOI: 10.1103/PhysRevD.106.084031. arXiv: 2203.04634 [gr-qc].

[350] Purnima Narayan, Nathan K. Johnson-McDaniel, and Anuradha Gupta. “Effect of ignoring eccentricity in testing general relativity with gravitational waves”. In: *Phys. Rev. D* 108.6 (2023), p. 064003. DOI: 10.1103/PhysRevD.108.064003. arXiv: 2306.04068 [gr-qc].

[351] Md Arif Shaikh, Sajad A. Bhat, and Shasvath J. Kapadia. "A study of the inspiral-merger-ringdown consistency test with gravitational-wave signals from compact binaries in eccentric orbits". In: *Phys. Rev. D* 110.2 (2024), p. 024030. DOI: 10.1103/PhysRevD.110.024030. arXiv: 2402.15110 [gr-qc].

[352] Sajad A. Bhat et al. "Parametrized tests of general relativity using eccentric compact binaries". In: *Phys. Rev. D* 110.12 (2024), p. 124062. DOI: 10.1103/PhysRevD.110.124062. arXiv: 2408.14132 [gr-qc].